Novel $LiMnPO_4$ Nanocomposite Material for High-Power Lithium Battery Cathodes

Adiel Nathan Gounder

B. Sc. (Honours)

B. Sc. (Forensic Science)

Thesis submitted in fulfilment of the requirements for admission to the degree of

DOCTOR OF PHILOSOPHY

IN CHEMICAL SCIENCE

Western Sydney University

School of Science and Health

2016

Abstract

Lithium ion batteries are emerging as one of the most promising technology for high powered energy storage applications. $LiMnPO_4$, is currently one of the most promising cathode materials for lithium batteries considering its low cost, environmental safety, high theoretical capacity and operating voltage (4.1 V *vs* Li/Li^+), achievable within the stability window of conventional carbonate ester-based electrolytes. The practical use of $LiMnPO_4$ is however limited by several intrinsic obstacles: (1) low electrical and ionic conductivity; (2) kinetic limits of Li^+ diffusion and; (3) large volume change between $LiMnPO_4$ and $MnPO_4$ phases during charge/discharge cycles. In this dissertation, a novel sol-gel procedure has been developed to produce $LiMnPO_4$ and carbon coating derived from the *in-situ* addition of sucrose. This work has shown how the purity of the prepared materials can be modulated by the temperature and atmosphere used. Focusing on how the inclusion of a two-step heating regime can help produce phase pure $LiMnPO_4$ at a lower temperature. Results have shown that variations in the thermal treatment of the dried gel precursor can produce pure $LiMnPO_4$ or produce an impure phase such as $Mn_2P_2O_7$. It also shows that the temperature at which pure, stable and highly crystalline $LiMnPO_4$ is produced can be reduced significantly (400°C instead of 900ºC). The electrochemical performance was best at when tested under higher temperatures of 40°C and for products synthesised with the final heating step at 700°C. Further, when analysing $LiMnPO_4$/carbon composite, the G band peak shifted to a lower wavenumber with increased temperature due to the increase in delocalised π electrons caused by the transformation of alkenic C=C chains to aromatic hexagonal rings. It was found that the I_D/I_G ratios of the carbon increased with temperature, confirming an increase in D band peak intensity, attributed to the material being in a pyrolysis state. This is critical information as it indicates that the material is not yet in a graphitised stage and that the I_D/I_G ratio does not imply the extent of graphitisation but confirms that the carbon is approaching the state of graphitisation. Because of the close link between the electric conductivity and delocalisation of the π electrons, this study shows that the optimisation of the heat-treatment of the $LiMnPO_4$/carbon composite is critical to the rate capability of the cathode material.

Acknowledgement

I would like to express my sincere gratitude and thanks to my supervisors Dr. Adriyan Milev and Associate Professor Kamali Kannangara for their constant encouragement and support during this research. Their patience, motivation and knowledge have been invaluable to this research. I would also like to extend my gratitude to Dr Laurel George who spent a lot of time helping me work through the vast amount of electrochemical data.

I would like to acknowledge the financial support from Western Sydney University in the form of the Western Sydney University International Postgraduate Research Scholarship (IPRS). I also would like to acknowledge the University for access to facilities and resources, especially the Advanced Characteristics Materials Facility (AMC) and for providing funding for travel to both international and domestic conferences. I would also like to thank Dr Richard Wuhrer who is in charge of the AMC facility and Tim Murphy for all the help using the instruments and accommodating me whenever I needed a booking.

Also, would like to thank all the people who have been with me on my PhD journey: Audrey, Solomon, Manish, Hai, Lin and all the great mates I have met while living on campus. Lastly, to my parents who have had to watch me study for a very long time and have always been there to provide love and support during my most challenging times.

Declaration

The work presented in this thesis is, to the best of my knowledge and belief, original except as acknowledged in the text. I hereby declare that I have not submitted this material, either in full or in part, for a degree at this or any other institution.

Adiel Nathan Gounder

31.08.2016

Table of Contents

List of Figures

List of Tables

Abbreviations and Symbols

Symbols / Units

α	Alpha
°C	Degrees Celsius
$\overline{\mu}_A$	Electrode potential of anode
$\overline{\mu}_C$	Electrode potential of cathode
η	Electrode polarisation
ΔG	Gibbs free energy
ΔG^{θ}	Standard state free energy change
ΔH	Change in the enthalpy released by the reaction
ΔS	Change in the entropy or measure of disorder
A.h kg^{-1}	Specific capacity
a.u.	Absorbance unit
g mol^{-1}	Concentration
kDa	Kilo Dalton
λ	Wavelength
σ	Sigma
mA.h g^{-1}	Specific capacity
mg	milligram
mL	millilitre
mm	millimetre
mV	millivolts
Ω	Omega
Ωs^{-1}	Warburg factor
π	Pi

A

A	Ampere
AC	Alternating current
Al	Aluminium
Al_2O_3	Alumina
As	Astatine

Ar	Argon

B

BET	Brunauer-Emmett-Teller

C

$Ca(C_2H_3O_2)_2$	Calcium acetate
C_{DL}	Double layer capacitance
$C_2H_6O_2$	Ethylene glycol
CE	Counter electrode
CH_2	Methylene
CH_3COOH	Acetic acid
CMC	Carboxy methyl cellulose
Co	Cobalt
CO_2	Carbon dioxide
CoO_2	Cobalt oxide
CPE	Constant phase element
Cr	Chromium
CV	Cyclic voltammetry

D

DC	Direct current
DHP	Diethyl hydrogen phosphonate
DMC	Dimethyl carbonate
DSC	Differential Scanning Calorimetry
DTGS	Deuterated Tri Glycine Sulfate

E

E^{θ}	Standard state electrochemical potential in Volts
EC	Ethylene carbonate
EGA	Evolved gas analysis
EIS	Electrochemical impedance spectroscopy
E_{OCV}	Equilibrium potential / open circuit voltage

E_T	Terminal Voltage
EV	Electric vehicle
eV	Electron volts

F

F	Faraday
Fe	Iron
FE-SEM	Field emission scanning electron microscopy
$Fe_2(SO_4)_3$	Iron sulphate

G

Ge	Germanium

H

HEV	Hybrid electric vehicle
HOMO	Highest Occupied Molecular Orbital
H_z	Hertz

I

I	Infrared
ICDD	International Centre for Diffraction Data
IR-ATR	Infrared attenuated total reflective

K

K	Kelvin
KBr	Potassium bromide
KOH	Potassium hydroxide

L

Li	Lithium
LiC_6	Lithiated graphite
Li^+	Lithium ion
$LiCoO_2$	Lithium cobalt oxide
$LiFePO_4$	Lithium iron phosphate

$LiMPO_4$	Lithium transition-metal phosphate
$LiMnPO_4$	Lithium manganese phosphate
$LiMn_2O_4$	Lithium manganese oxide
$LiMO_2$	Lithium transition-metal oxide
$LiNiO_2$	Lithium nickel oxide
$LiOOCCH_3$	Lithium acetate
$LiPF_6$	Lithium hexaflorophosphate
LUMO	Lowest Unoccupied Molecular Orbital

M

MCT	Mercury-Cadmium-Telluride detector
Mn	Manganese
$Mn[CH_3COO]_2 \cdot 4H_2O$	Manganese (II) acetate tetrahydrate
MnO	Manganese oxide
$MnPO_4$	Manganese phosphate
$Mn_2P_2O_7$	Manganese pyrophosphate
MoO_4	

N

n	Number of electrons transferred per mole of reactants
nm	nanometre
Ni	Nickel
Ni-Cd	Nickle cadmium
Ni-MH	Nickle metal-hydride
NiO(OH)	Nickel oxyhydroxide

O

$(O_2)^{2-}$	Peroxide ion

P

P	Phosphorus
PDF	Powder Diffraction File

PEG	Polyethylene glycol
PITT	Potentiostatic Intermittent Titration Technique
Pb-acid	Lead-acid
$(PO_4)^{3-}$	Phosphate ion
PXRD	Powder X-ray diffraction

R

R	Rate constant
R	Resistance
R_{CT}	Charge-transfer resistance
RE	Reference electrode
R_{Ω}	Ohmic resistance
rpm	Revolutions per minute

S

SEI	Solid electrolyte interface
SEM	Scanning electron microscopy
SHE	Standard hydrogen electrode
SLI	Start-up, lighting and ignition
SO_4^{2-}	Sulphate ion
SWCNT	Single walled carbon nanotubes

T

T	Temperature in Kelvin
TGA	Thermogravimetric
TiS_2	Titanium disulphide

U

U	Finite energy

V

V	Volts / Voltage
V	Vanadium

V_{ch}	Cell potential
V_{dis}	Output Voltage

W

W	Watts
WE	Working electrode
W.h	Watt hours

X

XRD	X-ray diffraction

Z

Z	Impedance
Z_{imag}	Imaginary impedance
Z_{real}	Real impedance
ZrO_2	Zirconium dioxide

CHAPTER 1

Introduction to Lithium ion batteries

The purpose of this chapter is to provide context and a general introduction to rechargeable lithium ion (Li-ion) batteries. It begins with a broad introduction which sets into perspective the significance of energy storage devices with a focus on Li-ion batteries, in enhancing the practical use of other technology such as mobile devices. The fundamental principles of how batteries operate and selection criteria of potential electrode materials will also be discussed. This will look at the kinetic and thermodynamic principles behind battery operation and the theoretical considerations behind the combination of lithium, transition metal and polyanions in cathode materials. Furthermore, this chapter will briefly highlight the limitations to current commercial and matured Li-ion battery technology and lithium manganese phosphate ($LiMnPO_4$) as a potential next generation cathode material to address these. Finally, the chapter finishes with the aims of the project and the outline of the subsequent chapters in the thesis.

1.1. Introduction

The most widely used, flexible and convenient form of energy is electrical energy. Electrical energy storage has become a critical issue and is essential in realising the potential of other technologies. Electricity is a secondary source of energy; direct storage is extremely challenging. To allow for more convenient storage, it has to be converted into other forms of energy, and when required, converted back to electrical energy.

Among the myriad of technologies available to store electricity, electrochemical storage solutions offer a wider range of functionality when compared to other systems that have specific limitations. For example, excess electricity produced from hydropower dams can be stored using pumped hydroelectric systems; however, this is dependent on the availability of land with specific geographical constraints [1]. Electrochemical storage devices, on the other hand, can be developed for specific applications without necessarily being dependent on location. Out of the three most established electrochemical systems (batteries, super-capacitors and fuel cells); batteries are the most flexible and hold the most promise. Currently, most energy storage research is based on batteries [1, 2]. They are portable, robust and can be applied to a range of applications by using different chemistries or engineering specifications.

Consumerism has led to greater demand for more portable devices such as laptops and mobile phones with improved speed, processing power and functionality; while expecting battery performance to continuously improve. Li-ion batteries are now the dominant technology used for these applications. There is now a need for better batteries in more demanding applications such as for renewable energies or utility companies and for automotive applications. It has been identified that the lack of suitable and affordable batteries is the biggest limiting factor in these industries.

Concerns surrounding the effects of climate change have led to an increased focus on developing renewable energy sources and displacing the use of fossil fuels in transportation. For renewable energy, an integral part of realising its potential is the storage of energy produced, which cannot be produced 'on demand' because it is dependent on the availability of resources. These intermittent sources of energy include solar, wind and hydropower which have daily or seasonal variations. Also, grid infrastructure is built to meet peak demands; hence, this infrastructure is not continuously used at full capacity. However, cost effective, large-scale stationary battery storage, will allow providers to store excess electricity produced when demand is low, which can then be used when demand increases, instead of building excessive infrastructure.

The use of batteries in transportation is arguably a more challenging application. The use of all-electric vehicles (EVs) powered by batteries such as the Tesla Model S and BMW i3, is increasingly becoming popular. Batteries operate with higher efficiencies by directly converting chemical energy into electrical energy unlike combustion engines whose efficiency is limited by the Carnot Cycle [3]. Other advantages of EVs include low maintenance of the vehicle and cheaper cost of electricity when compared to petroleum. For instance, an economic evaluation of the benefits of using EVs by the Department of Transport in Victoria, concluded that EVs incur a cost of $0.03/km when compared to an equivalent vehicle using an internal combustion engine (ICE), which would incur more than $0.10/km [4]. However, widespread adoption of EVs is hindered by higher cost, limited range and longer refuelling (charging) times of EVs, all of which are dependent on the battery. The complexities are increased by the need to balance technical specifications of the battery such as low weight, high energy and power density, portability, durability, longevity and safety.

1.2. The electrochemical cell: principle and definitions

A battery consists of one or more electrochemical cells, each of which converts chemical energy contained in its active materials into electrical energy by means of an oxidation and a reduction (redox) reaction during discharge/charge cycles (Figure 1.1). Each cell has three major components: (1) a positive electrode or cathode (the oxidising electrode) which is reduced during the discharge cycle when accepting electrons from the external circuit; (2) a negative electrode or anode (the reducing electrode) which is oxidised during discharge cycle and gives electrons to the external circuit and; (3) electrolyte which is an ionic conductive material that completes and balances the circuit by allowing ions to travel between the anode and cathode while at the same time being an electrical insulator [5]. A separator, which is usually a permeable membrane, prevents the anode and cathode from contact and shorting out the circuit, while allowing ions to permeate through. In a secondary or rechargeable battery, the reactions can be reversed (charged) *via* an external direct current (DC) power supply which drives a reverse current through the cell [5] (Figure 1.1).

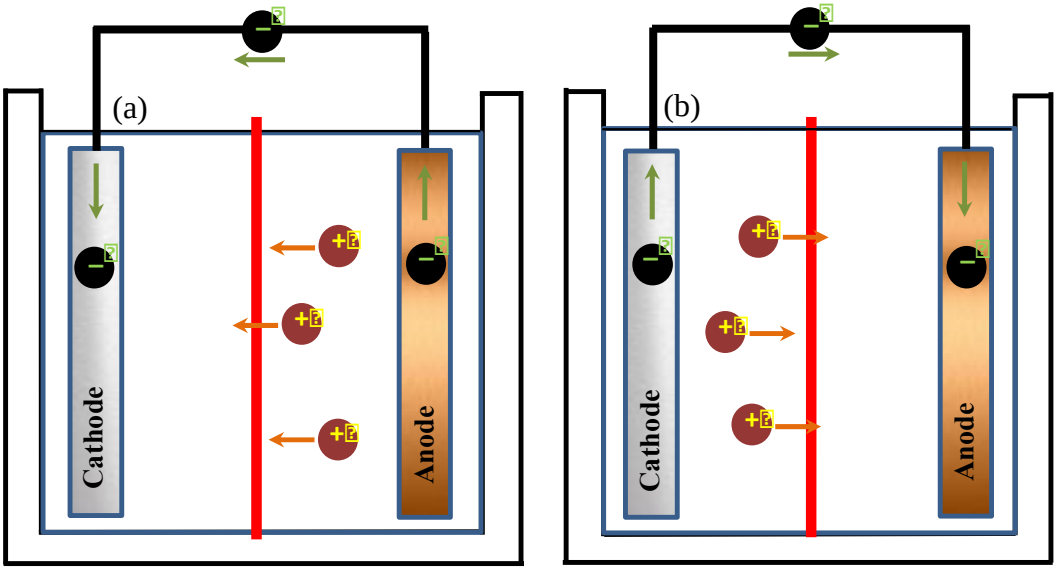

Figure 1.1: Simplified schematic of an electrochemical cell. (a) Discharging: ions and electrons move from the anode towards the cathode through the electrolyte and circuit, respectively; (b) Charging: external current forces the ions and electrons towards the anode to charge the cell.

While the fundamental physical principles behind battery operation remain the same, the nature of the reactants and other materials present in an electrochemical cell determine its characteristics and performance. Li-ion batteries for intensive applications would require interrelated properties to be simultaneously optimised. Firstly, the energy density of a cell which is typically measured in Watt hours (W.h). The specific energy density can be given by mass or volume (W.h kg^{-1} and W.h L^{-1} respectively). Specific power density (W kg^{-1}) refers to how rapidly stored energy can be dissipated. Typically, electrode combinations with the best weight to volume ratio along with a high cell voltage and capacity to give high energy density and good rate capability are preferred. This energy density is directly proportional to the product of the cell capacity (mA.h g^{-1}) and the voltage (V). The former refers to the amount of lithium ions that can be stored while the latter refers to how much energy is stored per lithium ions. Another important parameter is the power density (W). However, not all cells may be practical due to toxicity, cost, susceptibility to side reactions and whether its characteristics fall within the specifications of other cell components.

1.3. Types of batteries

Studies have been done on numerous battery chemistries, however, only a limited number of these batteries discussed in this section have been commercialised. Within these battery systems, incremental improvements and variations have continuously been made.

1.3.1. Lead-acid

Lead-acid (Pb-acid) batteries are the oldest battery technology and have been in use for over 100 years [6]. A Pb-acid cell consists of lead and lead oxide as the anode and cathode respectively with diluted sulphuric acid as the electrolyte [7]. These low-cost systems are easy to maintain and have low self-discharge rates making these batteries ideal for long-term storage [8]. It is used in conventional vehicles for start-up, lighting and ignition (SLI), however, due to its low energy density, very low specific energy density and cycle life would not allow it to be used in more demanding applications such as in electric vehicles [7].

1.3.2. Nickel cadmium (Ni-Cd)

Nickel cadmium (Ni-Cd) batteries use nickel oxyhydroxide (NiO(OH)) for the positive electrode and metallic cadmium for the negative electrode with potassium hydroxide (KOH) as the electrolyte [6, 7]. Its energy density and cycle life outperform that of Pb-acid batteries and has excellent high power rate capabilities making it suitable for use in power tools [3, 7]. However, Ni-Cd battery chemistry suffers from 'memory effect' and the toxicity of cadmium which requires complex recycling procedures [7]. For these reasons, it was replaced by nickel metal-hydride (Ni-MH) as the battery of choice.

1.3.3. Nickel metal-hydride (Ni-MH)

Nickel metal-hydride (Ni-MH) cells use nickel oxyhydroxide as the anode and potassium hydroxide (KOH) as electrolyte similar to the Ni-Cd cell but eliminates the use of cadmium with a metal halide cathode [7]. These have been the batteries of choice for hybrid electric vehicles (HEVs) and EVs for the past 20 years because of its high-power density, safety, abuse tolerance, low maintenance and better lifetime [7]. However, it has a relatively high self-discharge rate [7]. The potential for further cost reduction is limited by the cost of raw materials (e.g. the price of nickel) [9].

1.3.4. Lithium ion (Li-ion)

The Ni-MH batteries were quickly displaced by Li-ion batteries as the dominant energy storage solution for mass produced consumer electronics such as laptops and mobile phones, and they are poised to take over the HEV and EV market provided costs are significantly reduced and energy density is further increased [7, 8]. Lithium has the largest electrochemical potential (-3.04 V *vs* the Standard Hydrogen Electrode, SHE), the lowest physical density and exceptional energy to weight ratio (theoretical capacity of 3862 A.h kg^{-1} to an atomic mass of 6.94 g mol^{-1}) [10-12]. Li-ion batteries have double the specific energy density of Ni-Cd and Ni-MH batteries as well as being comparatively smaller and lighter without any 'memory effect' [7, 13] (Figure 1.2). A comparison of Li-ion technology to the other common battery technologies are summarised in Table 1.

Table 1.1: Comparison of the important properties of Pb-acid, Ni-Cd, NiMH and Li-ion batteries

Battery Type	Cycle efficiency (%)	Specific Energy Density (W.h kg-1)	Specific Power Density (W kg-1)	Lifetime Cycles	Self-discharge per day (%)	Capital ($ kW-1)
Pb-acid	70-90	30-50	75-300	500-800	0.1-0.3	100-200
Ni-Cd	70-90	50-75	150-300	2000-2500	0.2-0.6	800-1000
Ni-MH	85-90	66	250-1000	500-1000	0.5-1.0	450-1000
Li-ion	90-100	> 90	250-340	1000-10000+	0.1-0.3	600-2500

Li-ion technology has usurped established technology and is now the material of choice for the above applications that require rechargeable battery systems [2]. However, since the commercialisation of the lithium cobalt oxide ($LiCoO_2$) based battery in 1991 by Sony Corporation, which is still the current standard formulation, improvements have been relatively modest and is limited by the characteristics of the materials used. However, to be widely adopted in more demanding applications such as in EVs, batteries would need to be substantially improved.

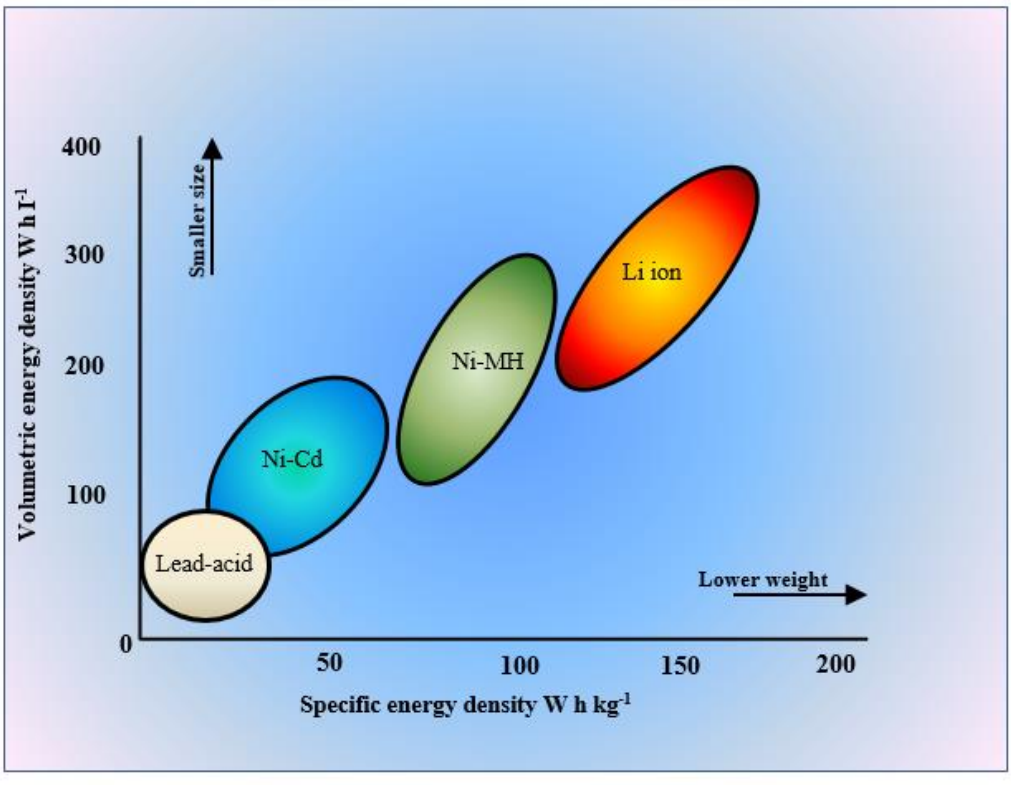

Figure 1.2: Comparison of different battery technologies in terms of volumetric (Wh L^{-1}) and specific gravimetric energy density (Wh kg^{-1}). Li-ion batteries are comparatively lighter and smaller than Pb-acid, Ni-Cd and Ni-MH batteries. Adapted from Tarascon and Armand [14].

Battery technology has not yet achieved the requirements of reduction in weight and volume, charging time and cost and enhancement increases in energy and power density and high cycling capacity to compete with conventional internal combustion engines [15]. Based on a comprehensive theoretical study by Gerssen-Gondelach and Faaij [16], the only battery type that could attain the requirements needed for EVs in the short to medium term, are Li-ion batteries. However, due to the price and safety concerns, its practical use is still restricted.

1.4. Theoretical background of electrochemical cells

Electricity in the form of current (movement of charge) is generated during an electrochemical reaction. Current flows in the form of electrons which carry charge through the external circuit. For every electron that goes through the external circuit, a corresponding quantity of ionic charge moves between the electrodes. An electrochemical reaction in a cell requires the understanding of both thermodynamic and kinetics principles. Thermodynamics is responsible for the driving force behind the reactions and the movement of ions inside the cell. On the other hand, the rates of reaction that occur at the respective electrodes are dependent on kinetic factors. The simultaneous involvement of these competing phenomena makes the mechanism of an electrochemical cell rather complicated. Hence, the thermodynamic and kinetic parameters play a major role in determining the energy density and power output of electrochemical cells.

The fundamental limitations to a battery potential and key requirements and criteria for materials to be used as a cathode or anode in various batteries have been discussed in several excellent comprehensive reviews [12, 17-22]. Goodenough *et al.* [12, 17-19, 23] and Whittingham *et al.* [20-22] have discussed the relationship between the thermodynamics and kinetics of an electrochemical reaction to its energy storage capability and power output. These concepts are briefly summarised in the following section with an emphasis on Li-battery cathodes.

1.4.1. Thermodynamics

To understand how a battery works, an understanding of the free energy driving force behind the reactions is essential. This driving force will give the electric potential or voltage that is attainable from the cell. Consequently, by knowing the thermodynamics of a given reaction, the voltage that can theoretically be produced from the cell can be determined. The fundamental thermodynamic equation for a reversible electrochemical reaction is given as:

$$\Delta G = G\ after\ process - G\ before\ process$$

$$\Delta G = \Delta H - T\Delta S \quad \text{(Equation 1.1)}$$

Where:

ΔG = available Gibbs free energy for useful work

ΔH = change in the enthalpy or the energy released by the reaction

ΔS = change in the entropy or measure of disorder

T = the absolute temperature

$T\Delta S$ = the heat associated with the organisation/disorganisation of materials.

If the change in Gibbs free energy (ΔG) is < 0, a reaction will proceed spontaneously. In this regard, the more negative the value of ΔG is, the more a reaction will proceed. Applied to electrochemical cells, it is advantageous to use materials that react to give a large negative ΔG value, since this will push electrons through a large potential drop in order to make the reaction occur, thus giving higher energy density. On the other hand, if the value of ΔG is > 0 or = 0, then the reverse reaction will occur spontaneously or an equilibrium state is achieved respectively. In the case of an equilibrium state, there is no driving force to go either side of the reaction.

As explained above, there is a direct relationship between a large negative change in free energy, ΔG, and a higher voltage. A standard potential or voltage (at constant pressure and temperature) can be defined by the following equation.

$$E^{\theta} = \frac{-\Delta G^{\theta}}{nF} \qquad \text{(Equation 1.2)}$$

Where:

E^{θ} = standard state electrochemical potential measured in Volts

ΔG^{θ} = standard state free energy change

n = the number of electrons transferred per mole of reactants

F = the Faraday constant, equal to the charge of one mole of electrons

In electrical terms, ΔG represents the net available electrical energy from a reaction in a cell. Therefore, by rearranging the above equation, the ΔG in a cell is given by:

$$\Delta G = -nFE \qquad \text{(Equation 1.3)}$$

The voltage, *E*, is dependent on the combination of anode and cathode material used. The quantity of electricity produced, *nF*, is determined by the total amount of active material available for the reaction, which determines the capacity, while the cell voltage can be considered to be an intensity factor. The product of capacity and cell voltage gives the energy density of the material. To determine the experimental thermodynamic quantities for the active materials in a cell reaction, the cell voltage is monitored as the temperature is varied.

1.4.2. The open circuit voltage (E_{OCV})

The equilibrium potential or open circuit voltage, E_{OCV}, is the voltage across the positive and negative electrodes without discharging any current to a load. The working ions, Li-ion in this case, flows from the anode to the cathode to charge the cathode positively and the anode negatively until, at equilibrium, the electrochemical potentials of the two electrodes are equal ($\bar{\mu}_A = \bar{\mu}_C$). The free energy change associated with the transfer of one mole of Li between the two electrodes is equivalent to the difference in the chemical potential of Li in the two electrodes. The cell potential, V, is determined by this difference, thus:

$$E_{OCV} = -\frac{\overline{\mu}_C^{Li} - \overline{\mu}_A^{Li}}{nF} \qquad \text{(Equation 1.4)}$$

where $\overline{\mu}_A^{Li}$ and $\overline{\mu}_C^{Li}$, are the chemical potentials of lithium in the anode and in the cathode electrodes at equilibrium. Ideally, the E_{OCV} of the cell should be large to maximise theoretical energy density. This voltage range that can be utilised in practise is limited by two factors: (1) compatibility of the electrodes with the electrolyte and; (2) intrinsic voltage limits of the electrodes.

1.4.3. Kinetics

The detailed mechanism of reactions occurring within an electrochemical cell often involves a series of physical, chemical, and electrochemical stages. While thermodynamics can show the likelihood of a cell reaction occurring and the theoretical potential difference, the rate of reaction is limited by kinetics. Under operating conditions, the cell moves away from equilibrium and the voltage differs from the E_{OCV} due to kinetic limitations with the reaction occurring. The electrodes undergo a series of steps including charge-transfer and charge-transport reactions, which determine the actual voltage of the cell [3, 12, 17, 22].

During charge/discharge cycling, the limited kinetics lead to polarisation loss during discharge and overvoltage on charge. On discharge, the internal cell resistance to the ionic current reduces the output voltage, V_{dis}, from the open circuit or equilibrium voltage, E_{OCV}, by electrode polarisation, η, so:

$$V_{dis} = E_{OCV} - \eta \qquad \text{(Equation 1.5)}$$

In contrast, on the charging cycle, the internal battery resistance to the ionic current flow increases the cell potential, V_{ch}, by an overvoltage, η, so:

$$V_{ch} = E_{OCV} + \eta \qquad \text{(Equation 1.6)}$$

According to Winter and Brodd [3], the total polarisation, η, of an electrode has three contributing kinetic effects (activation polarisation, ohmic polarisation and concentration polarisation) and is given by:

$$\eta = E_{OCV} - E_T \qquad \text{(Equation 1.7)}$$

where, E_T is the terminal voltage, that is the cell voltage with current flowing. The effects of the three polarisations on the voltage of the cell can be summarised as follows:

Activation polarisation is related to the charge-transfer reaction taking place at the electrolyte/electrode interfaces of the anode and cathode. In treating this type of kinetics, it is assumed that the rate-determining step is the dissociation of an activated complex [3]. The rate of a charge-transfer reaction is given by the Butler-Volmer equation:

$$i = i_0 exp\left(\frac{\alpha F\eta}{RT}\right) - exp\left[\frac{(1-\alpha)F\eta}{RT}\right] \qquad \text{(Equation 1.8)}$$

Where η is the polarisation during discharge (or over potential), α is the transfer coefficient, which describes how much of the over potential is used at the electrolyte/electrode interface in lowering the free energy barrier for charge-transfer to occur. The exchange current density, i_0, is the current in the absence of net electrolysis and zero potential. Considering a cell at equilibrium (open circuit), electron transfer still occurs at the electrode/electrolyte interface of both anode and cathode, but is completely balanced ($i_a = i_c$). The exchange current density is this background current which is used to normalise the net current. The Tafel equation is used to describe the activation polarisation and is derived from the Butler-Volmer equation:

$$\eta = a - b\left[log\left(\frac{i}{i_o}\right)\right] \qquad \text{(Equation 1.9)}$$

where *a* and *b* are constants.

Ohmic polarisation gives the total resistance experienced by the charge carriers as they move between the two electrodes. There is an (i) electronic component due to resistivity of the cell components (electrodes, current collectors and contacts on the terminals) and an (ii) ionic component due to resistance of electrolyte within the ionic solution, the separator, and the electrodes and the contact between particles of the active mass. The Ohm's law relationship is used to describe this type of polarisation:

$$\eta = IR \qquad \text{(Equation 1.10)}$$

where I is the current and R is the resistance. Ohmic polarisation appears and disappears instantaneously ($< 10^{-6}$ s) when current flows and ceases respectively.

Concentration polarisation arises from the difference between the rate of reactions on the electrode and the rate of ion migration through the electrolyte to the electrode surface [12, 18, 19]. If there is limited diffusion in the electrolyte, the concentration polarisation can be given as:

$$\eta = \left(\frac{RT}{n}\right) ln \left(\frac{C}{C_0}\right) \qquad \text{(Equation 1.11)}$$

where the concentration of the ion at the electrolyte surface and in the bulk are, C and C_0, respectively.

During discharge, the effects of the three polarisations on the voltage of the cell during discharge are shown in Figure 1.3. The faster a cell is discharged, the more rapid the voltage drop compared to that from equilibrium where the reactants are uniformly distributed. Subsequently, the ionic current density of the electrolyte and electrodes, including the rate of ion transfer across the electrode/electrolyte interface, is much smaller than the electronic current density [12, 18, 19].

For practical electrochemical cells, to minimise polarisation, cell electrodes can be made of a highly porous network of an interconnected network of small particles. This increases the surface area contact between the electrodes and the electrolytes. Despite this, at higher current rates, the ionic motion within an electrode or across an electrode/electrolyte interface is too slow for the charge distribution to reach equilibrium.

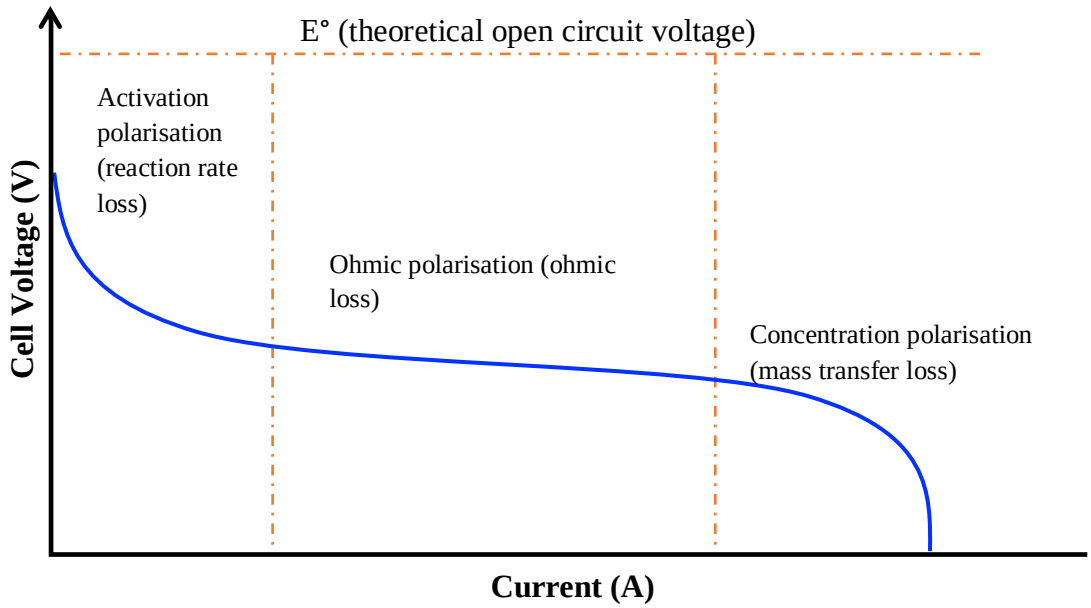

Figure 1.3: Typical polarisation curve of a battery showing the activation, Ohmic and concentration polarisation regions [24].

Thus, the specific capacity decreases as the electronic current, *I*, increases because the chemical reaction at the cathode depends on the relatively slow diffusion rate of the Li ion into its structure as well as in the electrolyte. Producing materials that can handle high current densities while maintaining its specific capacity is essential for its use in EVs.

1.5. Electrode-electrolyte compatibility

The energy or band gap, E_g, between the lowest unoccupied and highest occupied molecular orbitals (LUMO and HOMO) of a liquid electrolyte is known as the stability window of the electrolyte [19]. For a solid electrolyte, the LUMO and HOMO is analogous to the bottom of the conduction band and top of the valence band, respectively. This can be equated as:

$$E_g = E_{LUMO} - E_{HOMO} \qquad \text{(Equation 1.12)}$$

The concept of this stability window describes the useful potential range of an electrolyte. This window is important when determining the combination of electrodes since their electrochemical potentials, $\overline{\mu}_A$ and $\overline{\mu}_C$ (i.e. their Fermi levels, E_F) should be within the E_{LUMO} and E_{HOMO} (or energy gap) of the electrolyte to be thermodynamically stable (Figure 1.4) [17, 25].

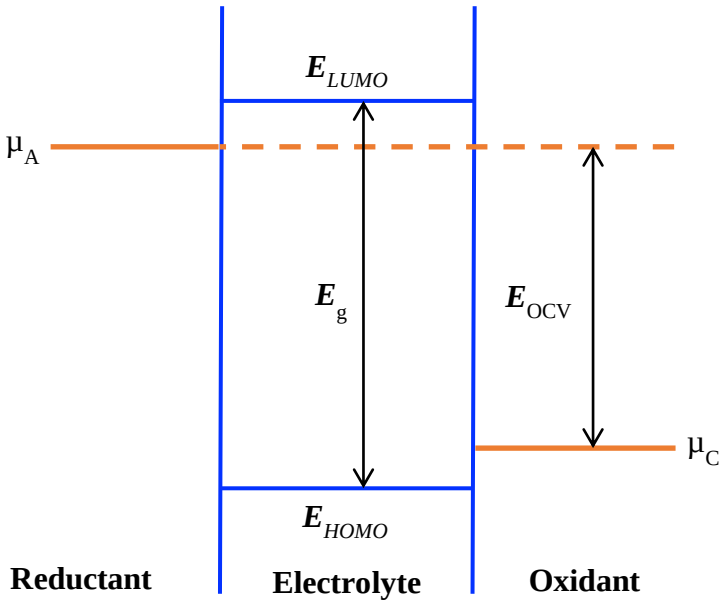

Figure 1.4: Relative energies of the electrolyte window E_g and the electrode electrochemical potentials $\overline{\mu}_A$ and $\overline{\mu}_C$. Adapted from reference [19].

Thus, the open circuit voltage, E_{OCV}, of a battery cell is limited to this window and is described as:

$$E_{OCV} = \frac{\overline{\mu}_A - \overline{\mu}_C}{e} \leq E_g \qquad \text{(Equation 1.13)}$$

where *e* is the magnitude of the electron charge. The electrolyte must be stable in the presence of both the reducing and oxidising conditions applied by the anode and cathode respectively. Hence, if $\overline{\mu}_A$ is above the E_{LUMO}, the electrolyte is reduced by electrons from the anode and similarly, if $\overline{\mu}_C$ is located below the E_{HOMO}, the electrolyte is oxidised by losing electrons to the cathode [19].

Lithium offers the highest anodic electrochemical potential energy, $\overline{\mu}_A$. Lithium salts (e.g. $LiPF_6$) can be dissolved in aprotic organic carbonates to give a Li-ion conductivity of more than 10^{-2} S cm^{-1}. In an electrochemical cell, the electrolyte will need to be an electric isolator to prevent short circuiting but allow fast diffusion of the Li ions. Organic carbonates have the E_{LUMO} and an E_{HOMO} at approximately 1.0 and 4.3 eV, respectively, an energy gap, E_g of 3.3 eV. Usually, the electrolyte blend contains more than one type of carbonate. These formulations are discussed comprehensively in literature [26-28].

1.6. Intrinsic voltage limit of electrodes

Given that the voltage of Li in the anode, $\overline{\mu}_A^{Li}$, is fixed, to maximise the theoretical cell voltage, E_{OCV}, a cathode material with a low $\overline{\mu}_C^{Li}$ and a high stability (low energy) for Li-ion in its sites is required [29]. The cathode material of a Li-ion cell is usually an intercalation transition-metal compound including oxides, chalcogenides and phosphates. As Li-ion ions are inserted/extracted from the host structure, a corresponding charge of electrons enters or leaves the *d* states of the transition-metal cations (e.g. Fe, Mn, Co, Ni). Thus, the voltage of the Li in the cathode is the sum of the chemical potentials of the Li-ion and e^- :

$$\overline{\mu}_C^{Li} = \overline{\mu}_C^{Li^+} + \overline{\mu}_C^{e^-} \qquad \text{(Equation 1.14)}$$

where, $\mu_C^{Li^+}$ and $\mu_C^{e^-}$ represent the chemical potentials of Li-ion and e^-, respectively. On insertion of electrons into the cathode, they will enter at the Fermi level, E_F, and this is the electron energy level of significance because:

$$E_F = \overline{\mu}_e \qquad \text{(Equation 1.15)}$$

where, $\overline{\mu}_e$ is the electrochemical potential for electrons [29]. Therefore, the chemical potential of the cathode, $\overline{\mu}_C$, which is directly related to the theoretical voltage, E_{OCV}, and the specific capacity of the cell, will depend on the energy of the electrons and the Li-ion ions in the cathode structure [19, 29].

As mentioned. the site energy for Li-ion in the cathode is the main factor determining the ionic contribution to the overall energy of the cell. To maximise the E_{OCV}, the cathode material should have low energy and thus high stability at the Fermi level (maximum energy occupied by an electron at 0 K) where the electrons enter/leave the *d* states of the transition metal. The lowest practically achievable Fermi level and the limiting effect of the cathode's anion structure on the battery voltage and battery stability are comprehensively discussed by Goodenough *et al.* [12, 17-19, 23, 30-32] and is illustrated schematically in Figure 1.5 a-c.

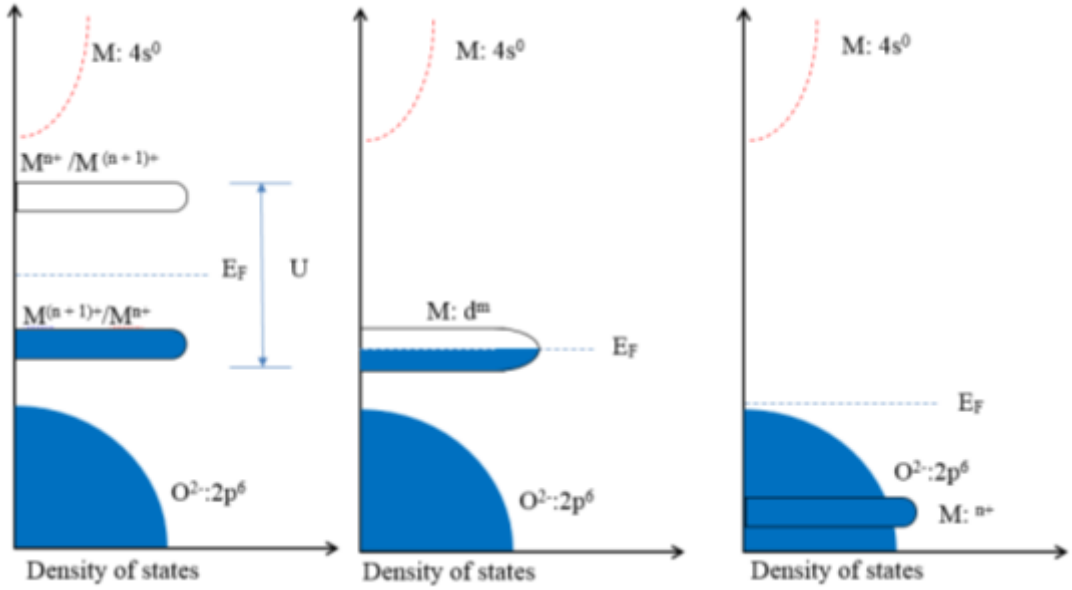

Figure 1.5: Schematic of the energy vs. density of states for the transition-metal redox couples and the O anion-p bands relative to the cathode Fermi level. Adapted from ref [19, 30].

The *d* states of the transition metal $M^{n/(n+1)}$ redox couple into/from which the electrons move, have energies above or at the top of the anion-*p* bands of the cathode compound. If the *d* electrons are localised at the transition metal cation, the *d*-electron manifold represents a redox couple that is separated by a finite energy, *U*, from the next formal valence state (Figure 1.5a). If a redox couple approaches the top of the anion *p* bands, the covalent admixture of the anion-*p* and cation-*d* orbitals is large enough for the *d* states to become itinerant, and the cathode Fermi level $E_{FC} = \mu_C$ becomes pinned at the top of the anion-*p* bands on oxidation (Figure 1.5b). If, the *d*-states lie well below the top of the anion-*p* bands, oxidation of the cathode on the Li-ion removal introduces *p*-band holes that can be trapped irreversibly in anti-bonding states of an anion-anion bond, for example, in the peroxide $(O_2)^{2-}$ ion in the CoO_2 host (Figure 1.4c). The evolution of oxygen gas would increase the pressure inside the cell leading to thermal runway.

The redox-couple $M^{n/(n+1)}$ at the top of an anion *p* band stabilises occupied states at the expense of empty states and provides an inherent voltage limit for a cathode or the lowest practical $\overline{\mu}_C$ [12, 30]. Alternatively, the intrinsic voltage limit of a cathode material occurs where E_F touches the top of the anion-*p* bands [25]. In oxides, the top of the O:*2p* band lies at a significantly lower energy than the top of the S:*3p* band in sulphides [18, 19, 29, 30]. Consequently, Fermi levels in oxides can be more than 2 eV lower, that is, having potentials of between 4 V to 5 V *vs*. the Li/Li^+. This explains why the modern lithium batteries use oxide cathodes rather than chalcogenides such as TiS_2 (Li/TiS_2; 2.2 V whereas Li/CoO_2; 3.7 V - 3.9 V). Therefore, oxide, sulphide and polyanionic structures alter the energy at the Fermi level of the transition metal redox couple differently which enables the design of new cathode materials with higher voltages.

To summarise, electrolytes require specific criteria to be met (1) a non-aqueous electrolyte allowing high Li-ion ion conductivity ($>10^{-3}$ S cm^{-1}) over the practical temperature range of -40˚C to 60˚C; (2) has an electrochemical stability window allowing a thermodynamically stable open circuit potential, $E_{OCV} > 4$ V; and (3) an anode and cathode with their $\overline{\mu}_A$ and $\overline{\mu}_C$ values within the window of the electrolyte.

1.7. Anodes and cathodes in an electrochemical cell

The anode is selected on the basis that it is a good reducing agent, or can be oxidised easily (gives up electrons during discharge), has a high columbic output (A.h g^{-1}), excellent conductivity and stability to be able to withstand multiple charge and discharge cycles. For commercialisation purposes, it should also be cost-effective to manufacture and environmentally friendly. The elemental Li^0 would be the ideal anode material, however, the $\overline{\mu}_A$ (i.e. the Fermi level, E_F) of Li^0 lies above the E_{LUMO} of many common electrolytes resulting in the formation of dendrites that can grow across the electrolyte and short-circuit an electrochemical cell.

Presently, lithiated graphite (Li_xC_6) is used as the intercalation material of choice for Li-ion batteries as it is safer than pure lithium metal. LiC_6, however, has a $\overline{\mu}_A \sim 0.1 – 0.3$ eV below $\overline{\mu}_A$ of Li^0, and thus its cell potential decreases by 100 – 300 mV. A detailed discussion on anodes is beyond the scope of this dissertation and readers are directed to detailed reviews of different types of anode materials [33-37].

Consider the commercial $Li_xC_6/Li_{1-x}CoO_2$ cell shown in Figure 1.9, the voltage between the anode and cathode is related to the work the cell can deliver on transferring electrons around the external circuit and to the free energy change on transferring Li ions from one electrode to the other [29]. On discharge, Li is transferred from a state of high $\overline{\mu}_A^{Li}$(high energy, less stable) in the negative anode to one of low $\overline{\mu}_C^{Li}$ (low energy, high stability) in the cathode; resulting in work being done (Figure 1.6).

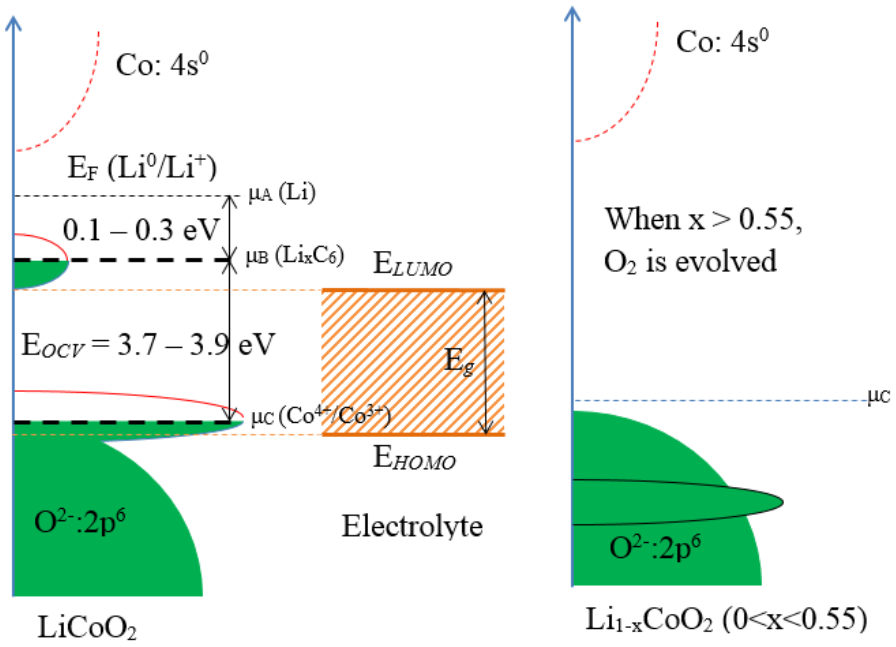

Figure 1.6: Schematic of the energy *vs.* density of states for the Co^{4+}/Co^{3+} redox couple at the top of O:2p bands relative to the cathode Fermi level. (a) The litigated graphite anode imposes penalty of +0.1 to +0.3 V compared to metallic Li. (b) At a critical O:2p component in the antibonding hole states, peroxide ions are formed. Adapted from reference [19, 38].

The schematic energy diagram (Figure 1.6), also shows the $\overline{\mu}_A(Li)$, $\overline{\mu}_A(Li_xC_6)$ and $\overline{\mu}_C(Li_{1-x}CoO_2)$ and their relative energy positions with respect to the E_{HOMO} and E_{LUMO} of a carbonate-based electrolyte. E_{LUMO} is below $\overline{\mu}_A(Li)$ and $\overline{\mu}_A(Li_xC_6)$ of anode, hence it is not well matched to the anode. The $\overline{\mu}_C$ of $Li_{1-x}CoO_2$, on the other hand, is within the carbonate E_{HOMO}, but the intrinsic voltage limit restricts the capacity of the cell.

Since the practical E_{HOMO} of the currently used organic liquid carbonate electrolytes in Li-batteries is at 4.3 eV below $\overline{\mu}_A$(Li) or 4.0 eV below $\overline{\mu}_A(Li_xC_6)$, the voltage of the $Li_{1-x}CoO_2$ layered oxides is also self-limited (intrinsic voltage limit) by the energy of the top of the O:2p bands. As shown in section 1.2.4, the intrinsic voltage limit of a cathode occurs where $\overline{\mu}_C$ (Fermi level) is pinned at the top of the anion-*p* bands. For $Li_{1-x}CoO_2$, this phenomenon is illustrated in Figure 1.5b. On oxidation of the (Co^{4+}/Co^{3+}) couple, as the energy of the *d*-electron redox couple is lowered below the top of the O:2*p* bands, holes introduced by oxidation of the redox couple by the Li-ion, occupy antibonding states at the top of the bonding O:2*p* states [17, 31]. At a critical fraction of anion-*p* character, the holes become trapped in surface di-anion molecules, e.g., peroxide $(O_2)^{2-}$ ion in CoO_2 host [17, 31]. The peroxide ions readily lose gaseous O_2 in the reaction:

$$2(O_2)^{2-} = 2O^{2-} + O_2 \uparrow \qquad \text{(Equation 1.16)}$$

The loss of O_2 from the cathode reflects the intrinsic voltage limit of these layered oxides. As a result, the $Li_{1-x}CoO_2$ cathode evolves oxygen or inserts protons on removing Li-ion beyond x > 0.55 [39]. The oxygen gas evolution would increase the pressure inside the cell and may lead to explosion. This limits the practical capacity of Li batteries with CoO_2 cathodes to ~ 50% of the theoretical capacity.

1.8. Kinetic Stability of the Cell, Solid/Electrolyte-Interphase

As mentioned in Section 1.2.3 and 1.2.4, thermodynamic stability and cell safety require locating the electrode electrochemical potentials, $\overline{\mu}_A$ and $\overline{\mu}_C$, within the stability window of the electrolyte, E_g. However, as shown in Figure 1.6, the $\overline{\mu}_A$ of LiC_6 lies ~ 1.0 eV above the E_{LUMO} of the carbonate electrolyte used in the Li-batteries. Consequently, the electrolyte would be reduced by electrons from the anode during cycling. During the first charge/discharge cycle however, chemical reactions involving the decomposition of the electrolyte may occur between the anode and the electrolyte to form a passivation layer at the interface of the anode and electrolyte known as the solid electrolyte interphase (SEI) [40]. This prevents further reaction and is also an ionic conductor.

While thermodynamically $\overline{\mu}_A$ and E_{LUMO} are not well matched, the formation of the layer may provide the kinetic stability required at the expense of capacity loss. This occurs according to the following mechanism. The rechargeable Li-ion cells are fabricated in their discharged state. During charging, Li ions from the cathode are inserted into a discharged anode. Since the Fermi level $\overline{\mu}_A$ of the charged anode is above the E_{LUMO} of the electrolyte, as is the case with a graphite anode, a fraction of the lithium from the cathode is consumed irreversibly on the initial charge in the passivating layer that forms on the anode surface. The formation of this SEI protective layer provides kinetic stability at the graphitic anode/electrolyte interface. Consequently, a cell can operate at higher voltages than that theoretically predicted.

Alternatively, the SEI layer can increase the impedance of Li-ion ions transfer across the anode/electrolyte interface, and the SEI layer changes with successive cycling to contribute to a capacity fade [12]. Moreover, during a fast charge, the concentration of Li-ion may build up on the surface of the SEI layer and, where a change in volume of the electrode breaks the SEI layer, Li^0 may be plated out before the break is restored. The Li^0 plating can result in dendrites that grow across the electrolyte, possibly short-circuiting the cell. Therefore, the use of LiC_6 as an anode is only possible because a passivating SEI layer is formed; but on repeated charge/discharge cycles, breaking of the SEI layer results in the formation of dendrites that may grow across the electrolyte to short-circuit a cell of the battery.

Ideally, the passivating SEI layer should self-heal rapidly when broken by the changes in electrode volume that occur in a charge/ discharge cycle; the SEI layer must also permit a fast Li-ion -ion transfer between the electrode and the electrolyte without blocking electron transfer between the active particle and the current collector. Therefore, it is essential to identify a solvent and electrode system that spontaneously forms a very thin SEI electronically isolating layer on the surface of both anode and cathode, while allowing fast ionic transport through the layer. One such group of solvents are organic solvents such as cyclic alkyl carbonates. This forms an effective SEI layer on the anode that ensures good cycling stability of the negative electrode. Cyclic alkyl carbonates, with ethylene carbonate additive, form a passivating SEI layer on the anode that is permeable to Li-ion ions but impermeable to electrons [40-42]. To improve the stability and lower the impedance of the SEI layer, replacement of ethylene carbonate by other additives to the electrolyte, e.g. fluoro-ethylene carbonate has been investigated [41].

To summarise, this chapter has highlighted several possible ways to increase E_{OCV} of an electrochemical cell, the specific cell capacity as well as the limitations of the current electrolyte/electrode systems. If $\overline{\mu}_{\mathrm{A}}$ is above the E_{LUMO}, the electrolyte is reduced by electrons from the anode unless the anode−electrolyte reaction becomes blocked by the formation of a SEI layer. Similarly, if $\overline{\mu}_{\mathrm{C}}$ is located below the E_{HOMO}, the electrolyte is oxidised by transferring electrons to the cathode unless the reaction is blocked by an SEI layer. Battery performance, irreversible charge "loss", rate capability, cyclability, and safety are highly dependent on the quality of the SEI. The development of organic carbonate electrolytes that can dissolve a sufficient amount of Li salt and have E_{LUMO} and E_{HOMO} at about 1.0 and 4.3 eV respectively, and the formation of the passivating SEI layer, were the breakthrough that enabled commercialisation of Li-ion batteries.

Therefore, the development of novel electrochemical cells would require the design of an anode with an $\overline{\mu}_A$ matched to the E_{LUMO} of the electrolyte as well as a cathode with a μ_C matched to the E_{HOMO} of the electrolyte. It is worth noting that the anode and cathode modulate each-others Fermi levels. This means that E_{OCV} is a measure of the potential difference between the cathode and anode only when they are in a cell i.e. in mutual contact with each other mediated by the electrolyte. Selecting a cathode or an anode solely based on their individual Fermi levels in isolation will not yield the desired cell voltage [29].

In summary, increasing the cell voltage involves decreasing the chemical potential of lithium, $\overline{\mu}_C^{Li}$ in the cathode, which can be done by tailoring the energy of the redox couple in two broad ways: (1) the oxidation state of the transition-metal ion should be high enough since the redox energy is lower (or the operating voltage is higher) for higher oxidation states, and (2) modifying the iono-covalent character of the transition metal-oxygen bond either through the inductive effect or structural features.

The practical application of these approaches is discussed in the Section 1.10 Alternatively, to achieve larger capacities we need to identify materials with the capability of reversibly accepting more than one lithium/electron per transition-metal ion. However, the latter approach is beyond the scope of this Thesis.

1.9. Past developments in lithium ion technology

The specific energy density of a cell is limited largely by the cathode materials. Accordingly, the research efforts have been on finding cathodes with larger specific capacities and greater operating potentials.

In 1976, the pioneering work of Stan Whittingham at Exxon Laboratories in studying intercalation compounds as potential electrode materials [20, 43, 44], led to the development of a layered titanium disulphide (TiS_2) cathode that could store Li-ions within its sheets (Figure 1.7). Intercalation chemistry deals with the insertion and extraction of guest species into a lamellar or layered host with little or no changes to the structural features of the host [45]. This allowed the lithium ions to shuttle or intercalate from the anode to cathode and *vice versa*, during discharge and charge cycles, respectively.

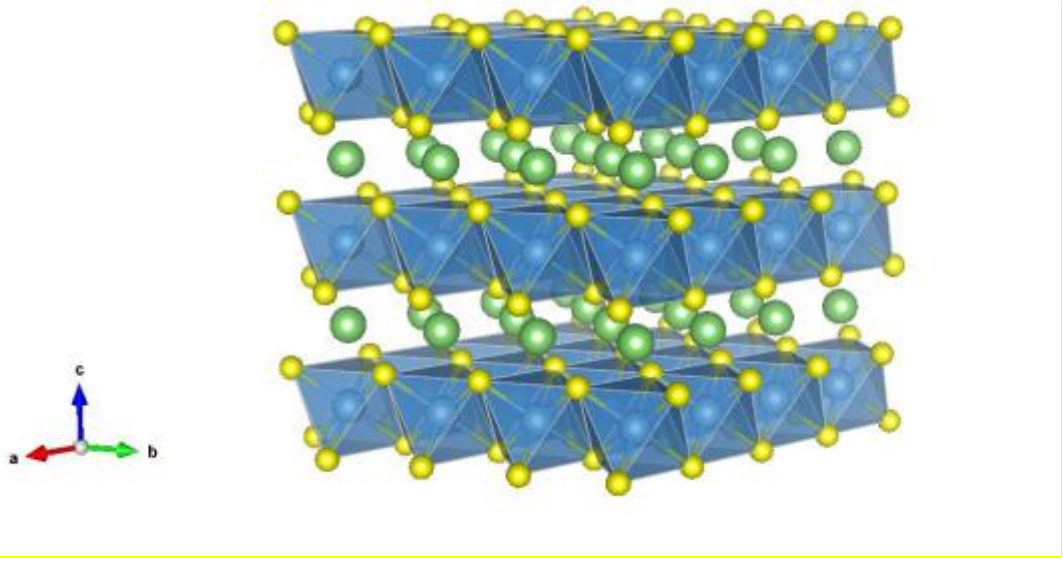

Figure 1.7: Crystalline structure of layered $LiTiS_2$. This structure allows 2-D diffusion of Li-ions (green atoms). Blue polyhedral shows Ti as the central atom bonded to two unshared and four shared S (yellow atoms) and green is Li. Drawn using VESTA 3.

The TiS_2 cathode material showed excellent reversibility over a single-phase intercalation reaction where one Li per transition metal could be extracted and inserted, however, it had a low voltage of 2 V. This development, led to increasing interest in the use of intercalation compounds as electrode materials.

In 1981, Bell Labs developed a graphite anode as a safer alternative to metallic Li anode. This lithiated graphite (LiC_6) could accommodate the Li ions within its layers with a minimal reduction in cell capacity. Following this work, a major breakthrough was made with the discovery of the $LiCoO_2$ cathode material in the early 1980s by Goodenough [32, 46]. Eventually, in 1991, Sony commercialised the first Li-ion battery by combining two intercalation electrodes, $LiCoO_2$ cathode with a graphite anode (Figure 1.8 a & b).

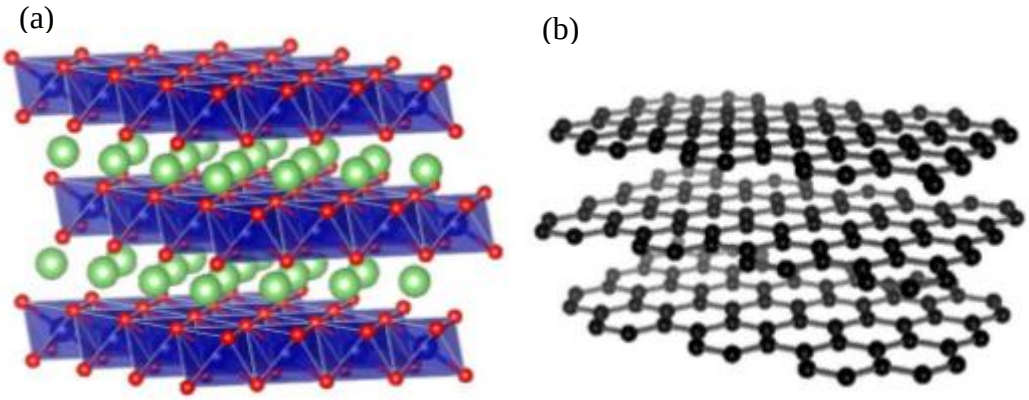

Figure 1.8: (a) $LiCoO_2$ cathode. Blue atoms represent Co, red – O and green is Li. This structure allows 2-D diffusion of lithium. The lithium intercalates into the octahedral sites between the edge sharing CoO_2 layers (b) stacked graphene layers of graphite anode. Drawn using VESTA 3.

This system was the first widely adopted Li-ion battery and still dominates the market today. This electrochemical cell has a $LiCoO_2$ cathode material (positive electrode) and graphite as the anode (negative electrode) layered onto an aluminium and copper current collector, respectively (Figure 1.9).

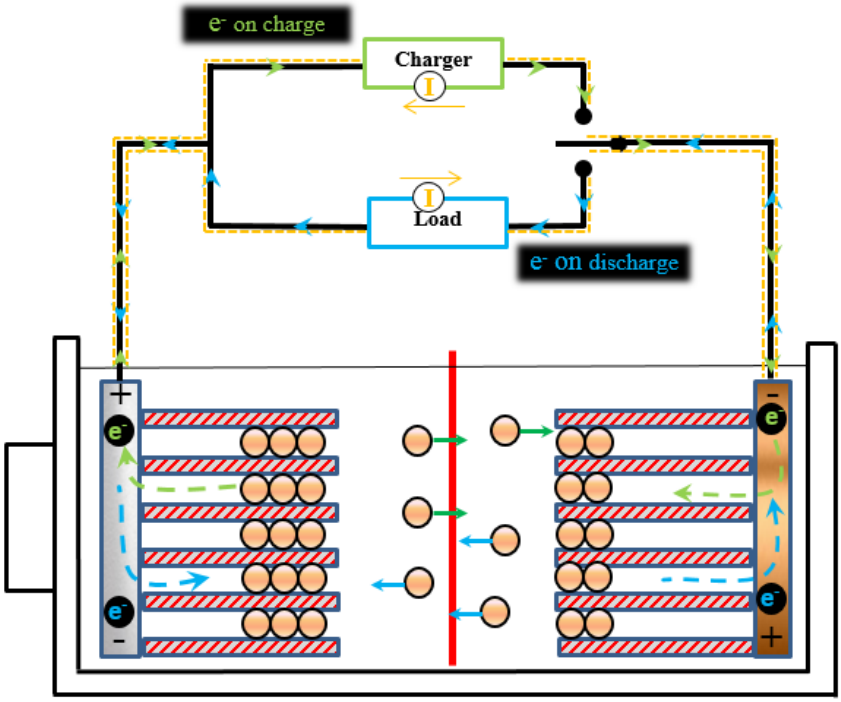

Figure 1.9: Schematic illustration of a typical $LiCoO_2$ cell.

The two electrodes are immersed in an organic electrolyte which usually contains a lithium hexafluorophosphate ($LiPF_6$) salt dissolved in a mixture of carbonates such as dimethyl carbonate (DMC) and ethylene carbonate (EC). The $LiPF_6$ salt is inert to strong reducing agents (anode is a reducing agent) and it also acts as a protective 'coating' for the aluminium current collector which is prone to oxidation [47]. The mixed electrolyte is expected to have high ionic conductivity to allow the Li ions to move across but low electronic conductivity to prevent the electrons from shorting the cell. DMC or other linear carbonates decrease the viscosity of the electrolytic solution and disperses easily into the separators. The EC has a high dielectric constant; hence, it is responsible for providing a medium that has high ionic conductivity [47]. This also allows the formation of the stable solid electrolyte interface (SEI) film at the graphite anode and electrolyte interface [47]. Further, a porous polymer membrane is placed between the electrodes to prevent the electrodes from contacting and short circuiting the cell while allowing the Li ions to permeate through.

Charging the cell enables the diffusion of Li ions from between the layered $LiCoO_2$, across the electrolyte and the separator and into the graphene layers. When the cell is discharged, the Li ions are removed from the anode and inserted into the Li_xCoO_2 crystalline structure. While the Li ions flow through the electrolyte between the electrodes, the circuit is completed by the free electrons from the Co^{3+}/Co^{4+} redox reaction that carry charge through the external circuit to perform work. Li-ion batteries are assembled in discharged state where the Li ions are available in cathode. The discharge reaction for the $LiCoO_2$/graphite cell is shown below.

Positive electrode:	$Li_{1-x}Co^{3+}O_2 + xLi\text{-ion} + xe^- \rightarrow LiCo^{2+}O_2$
Negative electrode:	$Li_xC_6 \rightarrow xLi\text{-ion} + C_6 + xe^-$
Total reaction:	$Li_{1-x}Co^{3+}O_2 + Li_xC_6 \leftrightarrow LiCo^{2+}O_2 + C_6$

The rate at which the reaction proceeds is dependent on the rate of lithium diffusion into and out of the electrodes' crystalline structure since this is the slowest step. In a $LiCoO_2$ cell, lithium diffusion is two dimensional. Batteries based on this configuration were a huge step up from the commonly used chemistry at that time, that is, Ni-Cd and Ni-MH, and it enabled the widespread adoption of portable technology such as laptops and mobile phones. Each cell had a potential of around 3.7 V whereas Ni-Cd and Ni-MH have an operating voltage of around 1.2 V. However, the use of these batteries to more energy intensive applications is limited because (1) only half of the lithium per transition metal is able to take part in the electrochemical reaction without damaging the structural integrity of $LiCoO_2$ layers, resulting in a lower practical capacity than theoretically possible; (2) oxygen is released at high temperatures which can undergo an exothermic reaction with the organic electrolyte; (3) Co is costly because of limited availability; and (4) Co is toxic. Considering the above issues with $LiCoO_2$ as the cathode material, it would lack the necessary characteristics for large scale applications where increased safety and energy density are even more important.

Other lithium metal oxides ($LiMO_2$) have been used including $LiNiO_2$ and spinel $LiMn_2O_4$ (Figure 1.10) [48-50].

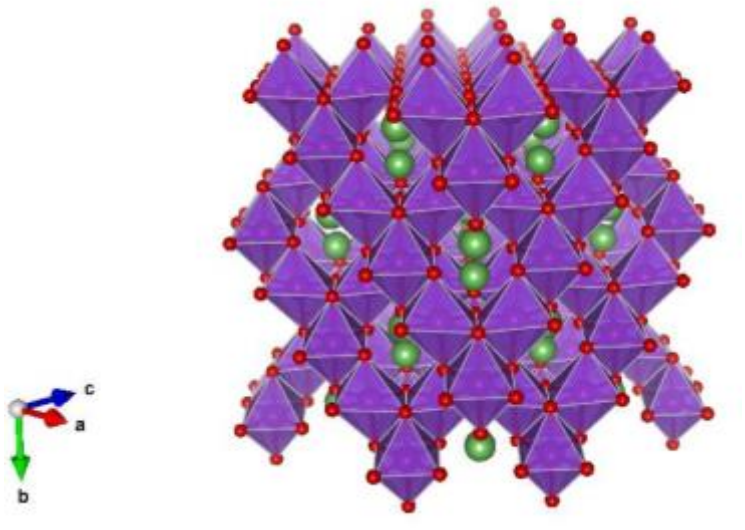

Figure 1.10: Crystalline structure of spinel $LiMn_2O_4$. The 3-D structure allows diffusion of Li-ions along all three axes. Drawn using VESTA 3.

The main disadvantage of all these oxides is that they are unstable and can decompose and release O_2 at higher temperatures which can ignite the organic solvents in the electrolyte [48]. These oxide materials as well as substituted variations have been extensively studied as cathode materials.

Major increases in battery performance metrics while concurrently lowering costs are required to meet the demand of the renewable energy and transportation sectors. Nevertheless, considering the challenges involved, a lot of fundamental and practical progress has been made in the fabrication and design of these batteries.

1.10. Development of Polyanionic Cathode Materials

As already discussed in Section 1.6 and 1.7 both the nature of the transition metal and the anion structure of the cathode compound strongly influence the energy at the Fermi level (i.e. $\overline{\mu}_C$) and the stability of the electrochemical cell.

1.10.1. Nature of the Transition Metal in the Polynomic Cathode Materials

The voltage of a given cathode material is determined by the location of the $M^{(n+1)+}/M^{n+}$ redox couple relative to that of the Li^0/Li-ion couple. The lowest *d* levels are associated with cations from the centre or right of the first transition series, i.e. Cr, Fe, Mn, Co, Ni, V; all exhibit oxidation states corresponding to *d* levels which lie close to the top of the anion-*p* bands [30]. Environmental and toxicity concerns have precluded the development of most V or Cr-containing materials, although electro-active compounds containing these metals exist. Therefore, the requirement for high specific capacity generally restricts choices to compounds containing first-row transition metals (usually Fe, Mn, Co, and Ni). The effect of the nature of the transition metal, in a phosphate anion environment, on *Eocv* is illustrated in Figure 1.11 *a* and *b*.

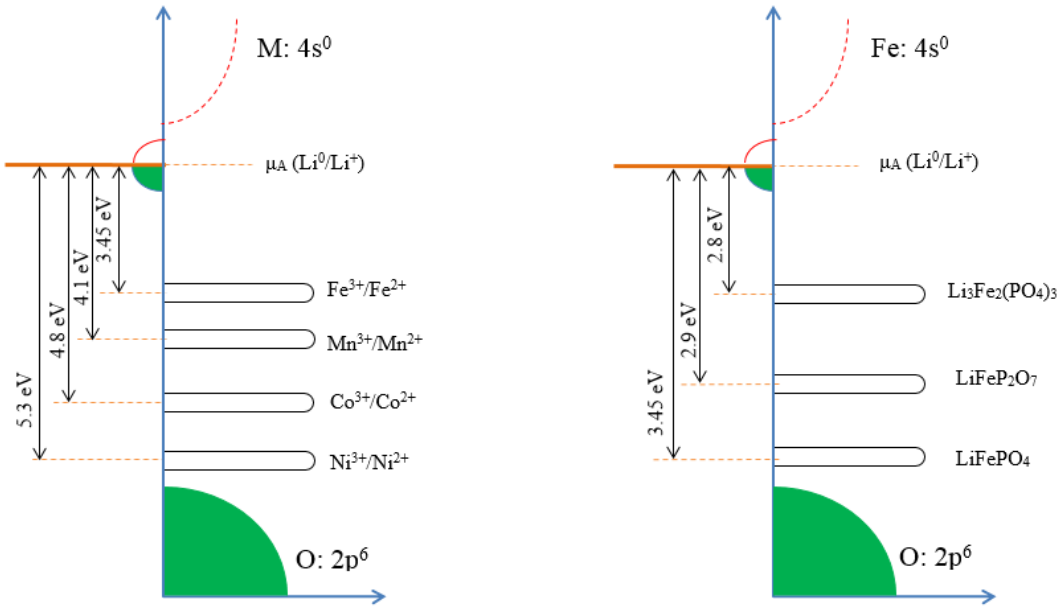

Figure 1.11: Effect of nature of the transition metal and effect of transition metal coordination on E_{ocv} relative to the Fermi level of Li-ion/Li^0. (a) Position of $M^{3+/2+}$ redox couples of various transition metals. (b) Effect of anion structure on the position of the Fe^{3+}/Fe^{2+}redox couple. Adapted from ref. [12].

The voltage of a cell is determined by the energy position, *E*, of the $M^{(n+1)+}/M^{n+}$ redox couple (for example, $M^{(n+1)+}/M^{n+}$ = Co^{3+}/Co^{2+}, Fe^{3+}/Fe^{2+} etc.) relative to that of the Li^0/Li-ion couple. The energy position of the redox couple varies with the nature of the transition metal, as well as the voltage of the cell Figure 1.12a. The discharge potential values are 3.45 V (Fe), 4.1 V (Mn), and 4.8 V (Co). Although the top of the O: 2p band of a cathode host material can be lowered to more than 5 eV below μ_A^{Li} by replacing an oxide ion with a polyanion, as in $LiNiPO_4$, investigation of these high voltage cathodes has been limited because the organic liquid carbonate electrolytes used in the Li-batteries decompose at a voltage V > 4.5 – 5 V.

1.10.2. Transition metal coordination

The energy of a redox couple depends not only on the formal valence state of the transition metal cation, but also is influenced by the nearest-neighbour bonding structure (Figure 1.11b). The ability of an anion to shift the transition metal redox couple, known as inductive effect, was originally used to explain the increased voltages of the polyanion cathodes, such as phosphate compared to their oxide analogues. The strength of the inductive effect can be exemplified by comparison of the energy position of the $Co^{3+/}Co^{2+}$ redox pair in $LiCoPO_4$ shown in Figure 1.12a and the energy position of Co^{4+}/Co^{3+} redox pair in $LiCoO_2$ shown in Figure 1.11a in the previous section. In a phosphate anion environment, the voltage of the cell is about 0.8 V higher than in an oxide anion environment.

The position of the $M^{n+/(n+1)+}$ redox couple can be modulated by changing the bond character of the M-O bond. A more covalent polyanion lowers the $M^{n+/(n+1)+}$ redox couple more effectively (lowers, E_F and hence μ_C^{Li}) compared to that in an oxide, resulting in a higher cell voltage *vs.* Li^0/Li-ion [12, 19, 30]. For example, the voltage increases from 3.0 to 3.6 V on going from $Fe_2(MoO_4)_3$ to $Fe_2(SO_4)_3$, which have similar crystal structures, due to a larger covalence of the SO_4 units compared to the MoO_4 units arising from the higher electronegativity of sulphur [12, 17-19, 30, 31].

The strength of the inductive effect can be modulated by using more electronegative counter-cations X in the M-O-X structure (X = B, Si, P, As, Mo, W) in the form of XO_4^{y-}, $X_2O_7^{y-}$ and other polyanions [25, 51-53]. The influence of structure is exemplified by the comparison in Figure 1.12a of the voltages from the Fe^{3+}/Fe^{2+} redox couple in various phosphate anions modulated through the inductive effect. Goodenough *et al*. [51, 53, 54] provided guidance as to how structural differences may shift the Fe^{3+}/Fe^{2+}redox energies. Most lithium metal phosphate compounds containing FeO_6 octahedra as the redox centre have potentials in the range of 2.8 – 3.45 V versus Li-ion/Li^0 due to the inductive effect [53].

The structural and compositional varieties are of paramount importance to design poly-oxyanion cathode materials. For example, it was pointed out that edge sharing of the FeO_6 octahedra within the $LiFePO_4$ structure further increases the voltage compared to compounds that do not have edge sharing. This suggests that it may be useful to analyse how edge sharing between polyhedra affects the voltage of the new polyanion chemistries including the Mn, Co and Ni phosphates. Particularly, polymorphic differences of the crystal structure often cause drastic changes of the properties (e.g. Fermi level energy position and thermal stability).

1.11. $LiMPO_4$ (M = Fe, Mn, Co, Ni) as next generation cathode material

In 1997, a breakthrough was made by Padhi *et al.* who demonstrated the potential of poly-anionic compounds, particularly lithium transition metal phosphates ($LiMPO_4$, M = Fe, Mn, Co, Ni), with an olivine structure as cathode materials [54]. From this class of materials, $LiFePO_4$ is already a mature technology and has the advantage of safety compared to $LiCoO_2$. This structure does restrict the Li ions to diffuse in a one-dimensional direction whereas in $LiCoO_2$ the diffusion is two-dimensional (Figure 1.12).

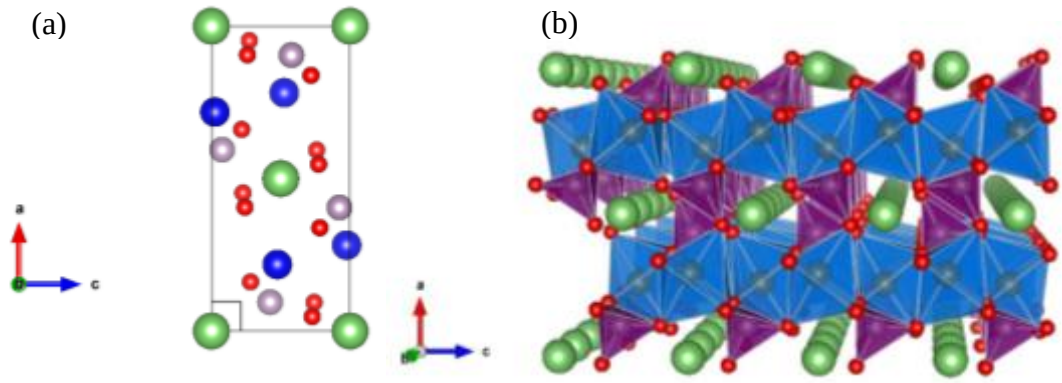

Figure 1.12: Crystalline structure of olivine $LiFePO_4$. Atomic distribution (a) unit cell of olivine $LiFePO_4$ looking towards the b direction which is the one-dimensional Li diffusion channel (b) framework showing Li-ion tunnels. Blue atoms represent Fe, purple – P, red – O and green is Li. Drawn using VESTA 3.

$LiFePO_4$ has a theoretical capacity of 170 mA.h g^{-1} and shows a flat voltage curve, with a plateau at around 3.4 V vs Li/Li-ion compared with about 3.7 V for $LiCoO_2$ and 4.1 V for $LiMn_2O_4$ [55-57]. Consequently, due to this lower working voltage, it has an energy density less than $LiCoO_2$. Research interest is now shifting towards the more challenging but potentially better Mn, Co and Ni containing structures of $LiMPO_4$ that have higher operating voltages. $LiCoPO_4$ and $LiNiPO_4$ are less attractive because cobalt is expensive and toxic and both $LiCoPO_4$ and $LiNiPO_4$ require the development of an electrolyte that works at higher voltages [58]. Therefore, research is focussed on $LiMnPO_4$ to be the next potential generation of Li-ion batteries, since the existing electrolyte formulations meet the voltage requirements of $LiMnPO_4$ (more detail is provided in Chapter 2).

1.12. Research aims

The $LiMnPO_4$ cathode material thus far has not been commercialised but can be used with existing electrolyte formulations unlike Co and Ni based phosphate materials. However, there are several drawbacks with this material. Similar to the other members of the olivine family, $LiMnPO_4$ has very poor electrochemical properties which are related to its (1) low ionic and electronic conductivity; (2) low diffusivity of Li- ions; (3) anisotropic lattice distortions and interface strains caused by the large volume change between $LiMn^{2+}PO_4$ (discharged) and $Mn^{3+}PO_4$ (charged) states, a phenomenon that is partially related to the Jahn-Teller effect. Further research is required to understand $LiMnPO_4$ cathode material from a fundamental and applied point of view to enhance its electrochemical performance. Thus, the motivation of this study is to synthesise $LiMnPO_4$ using a novel synthetic approach and to investigate its electrochemical properties and link its performance or lack of to its physical characteristics.

The broad aim of this research is to use a novel and modified sol-gel procedure to prepare $LiMnPO_4$ with different carbon loadings obtained from the *in-situ* pyrolysis of sucrose. Concurrently, the aim is to synthesis pure $LiMnPO_4$ at significantly lower temperatures than currently done using classic sol-gel methods. The specific aims are:

- To develop and optimise a modified sol-gel method and produce pure samples (i.e. crystalline phase purity where the product consists of a single phase rather than a mixture of crystalline phases) by the manipulation of temperature, heating regimes and atmosphere.

- To reduce the final temperature required to produce pure $LiMnPO_4$.

- To determine the effect of different amounts of carbon on the physical characteristics and electrochemical performance of the cathode material.

- To determine the electrochemical performance and subsequent mechanisms behind the performance of a cell using various electrochemical methods such as Cyclic Voltammetry, Charge Discharge measurements, and electrochemical impedance spectroscopy (EIS).

1.13. Thesis outline

The next chapter (Chapter 2) will provide a review on the development of Li-ion battery cathodes with an emphasis on $LiMnPO_4$. It highlights the recent developments specifically for $LiMnPO_4$ cathode materials and remaining challenges. It will summarise the work done to improve the performance of this material: 1) describing the synthetic methods reported in literature; 2) effect of reducing particle size; 3) and the importance and types of conductive coatings used.

Chapter 3 will look at firstly the synthetic method (modified sol-gel) used for the preparation of $LiMnPO_4$ materials. Further, it will show how the purity of stoichiometric amounts of Li, Mn and phosphate used in the synthesis can be modulated by varying the temperature, atmosphere and by including an intermediate or pre-decomposition temperature.

Chapter 4 discusses the synthesis of the material with varying amounts of carbon coating obtained from the decomposition of sucrose. A comparison is made between the physical and electrochemical characteristics of 'carbon free', 3% carbon and 5% carbon samples. This section will also include cyclic voltammetry and charge/discharge experiments to evaluate the basic electrochemical performance of the prepared samples.

Chapter 5 investigates the sources of polarisation in selected electrochemical cells using electrochemical impedance spectroscopy (EIS).

Chapter 6 will summarise the general conclusions derived from the prior chapters and ideas on what further studies can be done to optimise the performance of the newly developed cathode material.

1.14. References

1. Dunn B, Kamath H, Tarascon J. Electrical energy storage for the grid: a battery of choices. Science. 2011;334(6058):928-35.

2. Lindley D. The energy storage problem. Nature. 2010;463(7277):18-20.

3. Winter M, Brodd R. What are batteries, fuel cells, and supercapacitors? Chemical Reviews. 2004;104(10):4245-70.

4. AECOM. Forecast uptake and economic evaluation of electric vehicles in Victoria. Department of Transport 2011.

5. Chen H, Cong T, Yang W, Tan C, Li Y, Ding Y. Progress in electrical energy storage system: a critical review. Progress in Natural Science. 2009;19(3):291-312.

6. Evans A, Strezov V, Evans T. Assessment of utility energy storage options for increased renewable energy penetration. Renewable and Sustainable Energy Reviews. 2012;16(6):4141-7.

7. Vazquez S, Lukic S, Galvan E, Franquelo L, Carrasco J. Energy storage systems for transport and grid applications. IEEE Transactions on Industrial Electronics. 2010;57(12):3881-95.

8. Hadjipaschalis I, Poullikkas A, Efthimiou V. Overview of current and future energy storage technologies for electric power applications. Renewable and Sustainable Energy Reviews. 2009;13(6–7):1513-22.

9. Karden E, Ploumen S, Fricke B, Miller T, Snyder K. Energy storage devices for future hybrid electric vehicles. Journal of Power Sources. 2007;168(1):2-11.

10. Armand M, Tarascon J. Building better batteries. Nature. 2008;451(7179):652-7.

11. Scrosati B, Garche J. Lithium batteries: status, prospects and future. Journal of Power Sources. 2010;195(9):2419-30.

12. Goodenough J, Park K. The Li-ion rechargeable battery: a perspective. Journal of the American Chemical Society. 2013;135(4):1167-76.

13. Liu C, Li F, Ma L, Cheng H. Advanced materials for energy storage. Advanced Materials. 2010;22(8):E28-62.

14. Tarascon J, Armand M. Issues and challenges facing rechargeable lithium batteries. Nature. 2001;414(6861):359-67.

15. Semadeni M. Storage of energy, overview. In: Cleveland CJ, editor. Encyclopedia of Energy. 5. Amsterdam: Elsevier; 2004. p. 719-38.

16. Gerssen-Gondelach S, Faaij A. Performance of batteries for electric vehicles on short and longer term. Journal of Power Sources. 2012;212:111-29.

17. Goodenough J. Rechargeable batteries: challenges old and new. Journal of Solid State Electrochemistry. 2012;16(6):2019-29.

18. Goodenough J. Evolution of strategies for modern rechargeable batteries. Accounts of Chemical Research. 2013;46(5):1053-61.

19. Goodenough J, Kim Y. Challenges for rechargeable Li batteries†. Chemistry of Materials. 2009;22(3):587-603.

20. Whittingham M. Lithium batteries and cathode materials. Chemical Reviews. 2004;104(10):4271-301.

21. Whittingham M. Materials challenges facing electrical energy storage. MRS Bulletin. 2008;33(04):411-9.

22. Whittingham M, Zawodzinski T. Introduction: batteries and fuel cells. Chemical Reviews. 2004;104(10):4243-4.

23. Zaghib K, Mauger A, Goulet H, Goodenough J, Julien C. Advanced electrodes for high power Li-ion batteries. Materials. 2013;6(3):1028.

24. Saha B, Goebel K, editors. Modeling Li-ion battery capacity depletion in a particle filtering framework. Proceedings of the annual conference of the prognostics and health management society; 2009.

25. Yuan L, Wang Z, Zhang W, Hu X, Chen J, Huang Y, et al. Development and challenges of $LiFePO_4$ cathode material for lithium-ion batteries. Energy & Environmental Science. 2011;4(2):269-84.

26. Aurbach D, Chusid O. Secondary batteries - lithium rechargeable systems | electrolytes: additives. In: Garche J, editor. Encyclopedia of Electrochemical Power Sources. Amsterdam: Elsevier; 2009. p. 92-111.

27. Kühnel R, Böckenfeld N, Passerini S, Winter M, Balducci A. Mixtures of ionic liquid and organic carbonate as electrolyte with improved safety and performance for rechargeable lithium batteries. Electrochimica Acta. 2011;56(11):4092-9.

28. Lewandowski A, Świderska-Mocek A. Ionic liquids as electrolytes for Li-ion batteries: an overview of electrochemical studies. Journal of Power Sources. 2009;194(2):601-9.

29. Bruce P. Solid-state chemistry of lithium power sources. Chemical Communications. 1997(19):1817-24.

30. Goodenough J, Kim Y. Locating redox couples in the layered sulfides with application to $Cu[Cr_2]S_4$. Journal of Solid State Chemistry. 2009;182(10):2904-11.

31. Goodenough J. Cathode materials: a personal perspective. Journal of Power Sources. 2007;174(2):996-1000.

32. Mizushima K, Jones P, Wiseman P, Goodenough J. Li_xCoO_2 ($0<x<-1$): a new cathode material for batteries of high energy density. Materials Research Bulletin. 1980;15(6):783-9.

33. Goriparti S, Miele E, De Angelis F, Di Fabrizio E, Proietti Zaccaria R, Capiglia C. Review on recent progress of nanostructured anode materials for Li-ion batteries. Journal of Power Sources. 2014;257(0):421-43.

34. Zhang W. A review of the electrochemical performance of alloy anodes for lithium-ion batteries. Journal of Power Sources. 2011;196(1):13-24.

35. Fauteux D, Koksbang R. Rechargeable lithium battery anodes: alternatives to metallic lithium. Journal of Applied Electrochemistry. 1993;23(1):1-10.

36. de las Casas C, Li W. A review of application of carbon nanotubes for lithium ion battery anode material. Journal of Power Sources. 2012;208(0):74-85.

37. Ji L, Lin Z, Alcoutlabi M, Zhang X. Recent developments in nanostructured anode materials for rechargeable lithium-ion batteries. Energy & Environmental Science. 2011;4(8):2682-99.

38. Goodenough J, Park K. The Li-ion rechargeable battery: a perspective. Journal of the American Chemical Society. 2013;135(4):1167-76.

39. Gupta R, Manthiram A. Chemical extraction of lithium from layered $LiCoO_2$. Journal of Solid State Chemistry. 1996;121(2):483-91.

40. Verma P, Maire P, Novák P. A review of the features and analyses of the solid electrolyte interphase in Li-ion batteries. Electrochimica Acta. 2010;55(22):6332-41.

41. Choi N, Yew K, Lee K, Sung M, Kim H, Kim S. Effect of fluoroethylene carbonate additive on interfacial properties of silicon thin-film electrode. Journal of Power Sources. 2006;161(2):1254-9.

42. Fong R, von Sacken U, Dahn J. Studies of lithium intercalation into carbons using nonaqueous electrochemical cells. Journal of The Electrochemical Society. 1990;137(7):2009-13.

43. Whittingham M. Electrical energy storage and intercalation chemistry. Science. 1976;192(4244):1126-7.

44. Whittingham M. Chalcogenide battery. Google Patents; 1977.

45. Whittingham M, Chianelli R. Layered compounds and intercalation chemistry: an example of chemistry and diffusion in solids. Journal of Chemical Education. 1980;57(8):569.

46. Mizushima K, Jones P, Wiseman P, Goodenough J. Li_xCoO_2 ($0<x\leqslant1$): a new cathode material for batteries of high energy density. Solid State Ionics. 1981;3:171-4.

47. Zhang S, Jow T, Amine K, Henriksen G. $LiPF_6$–EC–EMC electrolyte for Li-ion battery. Journal of Power Sources. 2002;107(1):18-23.

48. Liu C, Wu X, Wu W, Cai J, Liao S. Preparation of nanocrystalline $LiMnPO_4$ via a simple and novel method and its isothermal kinetics of crystallization. Journal of Materials Science. 2011;46(8):2474-8.

49. Thackeray M, David W, Bruce P, Goodenough J. Lithium insertion into manganese spinels. Materials Research Bulletin. 1983;18(4):461-72.

50. Thackeray M, Johnson P, de Picciotto L, Bruce P, Goodenough J. Electrochemical extraction of lithium from $LiMn_2O_4$. Materials Research Bulletin. 1984;19(2):179-87.

51. Padhi A, Manivannan V, Goodenough J. Tuning the position of the redox couples in materials with NASICON structure by anionic substitution. Journal of The Electrochemical Society. 1998;145(5):1518-20.

52. Padhi A, Nanjundaswamy K, Masquelier C, Goodenough J. Mapping of transition metal redox energies in phosphates with NASICON structure by lithium intercalation. Journal of The Electrochemical Society. 1997;144(8):2581-6.

53. Padhi A, Nanjundaswamy K, Masquelier C, Okada S, Goodenough JB. Effect of structure on the Fe^{3+} / Fe^{2+} redox couple in iron phosphates. Journal of The Electrochemical Society. 1997;144(5):1609-13.

54. Padhi A, Nanjundaswamy K, Goodenough J. Phospho-olivines as positive-electrode materials for rechargeable lithium batteries. Journal of The Electrochemical Society. 1997;144(4):1188-94.

55. Ni J, Kawabe Y, Morishita M, Watada M, Sakai T. Improved electrochemical activity of $LiMnPO_4$ by high-energy ball-milling. Journal of Power Sources. 2011;196(19):8104-9.

56. Anderson A, Kalska B, Haggstrom L, Thomas J. Lithium extraction/insertion in $LiFePO_4$: an X-ray diffraction and Mossbauer spectroscopy study. Solid State Ionics. 2000;130(1):41-52.

57. Zhang S, Meng F, Wu Q, Liu F, Gao H, Zhang M, et al. Synthesis and characterization of $LiMnPO_4$ nanoparticles prepared by a citric acid assisted sol-gel method. International Journal of Electrochemical Science. 2013;8(5):6603-9.

58. Xiao J, Xu W, Choi D, Zhang J. Synthesis and characterisation of lithium manganese phosphate by a precipitation method. Journal of The Electrochemical Society. 2012;157(2):142-7.

CHAPTER 2

$LiMnPO_4$: Recent developments and challenges

Development of low cost, environmentally friendly, and high energy density cathodes containing polyoxyanionic structural units became attractive due to their operating voltage located inside of the electrochemical stability window of conventional organic electrolytes and safety due to the presence of strong covalent bonds in the anionic unit. This chapter summarises current progress on the development of cathodes based on poly-oxy-anionic materials, such as olivine-structured transition metal-phosphates Li*M*PO_4 (*M* = Fe, Mn, Co, Ni) with focus on materials containing $LiMnPO_4$, with the drawbacks of using this material compared to the already commercialised $LiFePO_4$. These problems are summarised followed by description of the efforts made to minimise or solve their effect on the battery performance by: (1) various synthetic methods reported in the literature; (2) manipulating the particle size; (3) addition of conductive coating; and (4) doping. Finally, the chapter highlights the need for further research to realise the full potential of $LiMnPO_4$ cathodes.

2.1. Introduction

The performance of the rechargeable battery strongly depends on the active materials employed in both anodes and cathodes for ion storage. The cathode is the most expensive part and limits the battery performance, since it has a significantly lower specific capacity (140 – 170 mA.h g^{-1}) than the most common anode material, lithiated graphite, LiC_6 (372 mAh g^{-1}). Therefore, most research is currently focussed on new and improvements to current cathode materials.

There are three types of cathode materials that can be categorised according to the dimensionality of the Li ion motion in them: one-dimensional, olivine $LiMPO_4$ (M = Fe, Mn, Ni, Co), two-dimensional, layered transition-metal oxides $LiMO_2$ (M = Co, Ni) and three-dimensional, spinel frameworks ($LiMn_2O_4$). The layered cathodes such as $LiCoO_2$ and $LiNiO_2$ with highly oxidized redox couples ($Co^{3+/4+}$ and $Ni^{3+/4+}$) can offer high cell potentials (around 3.7 – 4.2 V *vs.* Li^0/Li^+) are used as cathodes for high-energy Li-ion batteries [1, 2]. However, the relatively high cost, rarity, toxicity, chemical instability and along with safety issues discussed in Chapter 1 (Section 1.7) arising from a significant overlap of the $Co^{3+/4+}$:3d band with the top of the O_2: 2p band limits the possible usage of cobalt-containing materials in large-scale batteries [3]. Manganese is five times cheaper than cobalt and is found in abundance in nature. The spinel $LiMn_2O_4$, with operation voltage of ~ 4.1 – 4.2 V *vs.* Li^0/Li^+ although possessing about 10% less capacity than $LiCoO_2$, has been considered in the case of high-power Li-ion batteries has an advantage in terms of cost and is perceived as being 'green' (non-toxic and from abundant material source) [4, 5]. However, the $LiMn_2O_4$ cathodes suffer from serious capacity loss at elevated temperatures due to the dissolution of Mn ions from the lattice and the consequent reaction of the solvated Mn atoms with the carbon containing anodes, resulting in an increase in cell impedance [6-8].

From 1997 to present, continuous efforts have been devoted by Goodenough [9-14] to propose and study polyoxyanionic compounds such as olivine based on transition-metal element with a focus to those structures that favour large mobility of the Li-ions in order to transfer energy during the redox reaction. One of the main drawbacks with using these materials is their poor electronic conductivity, and this limitation had to be overcome through various materials processing approaches. The polyoxyanion materials are discussed in the subsequent sections.

2.2. Polyoxyanion framework materials

Polyoxyanionic structures possess M–O–X bonds; altering the nature of X will change (through an inductive effect) the iono-covalent character of the M–O bonding. In this way, it is possible to modulate transition metal redox potentials (for more details see Chapter 1 (Section 1.6). Initially, Goodenough *et al.* [9-13] focused on the development of polyanionic framework materials, which comprise oxygen in tetrahedral sites, such as XO_4^{2-} (X = S, Mo, and W). They found that the voltage of the $Fe^{2+/3+}$ couple increases from ~2.5 V in oxide Fe_2O_3 to 3.6 and 3.0 V, respectively, in polyanion-containing $Fe_2(SO_4)_3$ and $Fe_2(MoO_4)_3$ [12, 14, 15]. The stronger S-O or Mo-O covalent bonds weaken the Fe-O covalency due to the inductive effect and thereby lower the position of the $Fe^{2+/3+}$ couple, resulting in an increase in the cell voltage. Likewise, the 600 mV increase in going from $Fe_2(MoO_4)_3$ to $Fe_2(SO_4)_3$ is due to an increase in the covalency of the S-O bond compared to the Mo-O bond. This lowers the covalency of the M-O bond and is referred to as the M-O-X inductive effect [16]. That is, the presence of the polyanion with strong X-O covalent bonds lowers the Fermi level of the redox couple, M^{3+}/M^{2+}, and thus increases the cell voltage, because of the strong polarisation of oxygen ions toward the X cation (See also Chapter 1 Section 1.7) [9, 12, 13]. Therefore, the electronegativity of X and the strength of the X-O bond play a role in controlling the redox energies of metal ions in polyanion containing samples [12, 13, 17, 18]. Also, the strong covalent X-O bond of the polyanion also minimises the oxygen loss that occur in the layered or spinel oxides which can lead to thermal runaway [19].

2.3. Development of olivine cathode materials

Since 1997, with the discovery of the electrochemical properties of olivine by Padhi *et al*. [20] there has been considerable interest in developing other poly-anion based cathodes of the form XO_4^{3-} (where X = P and As). The olivine structured mixed lithium-transition metal phosphates $LiMPO_4$ (M = Fe, Mn, Co, Ni) have many advantages over the layered oxides (e.g. $LiCoO_2$ and $LiNiO_2$) cathodes that are used in commercial batteries. With theoretical specific capacity of 170 mAh g^{-1} at moderate current densities, $LiFePO_4$ is considered as potential positive electrode material for use in lithium batteries; it is inexpensive, not toxic with high thermal stability, three determinant advantages with respect to cobalt-oxide-based materials for large-scaled applications such as hybrid electric vehicles (HEV). Also, the Fe^{2+}/Fe^{3+} couple operates around 3.45 V *vs.* Li^0/Li^+ which gives an individual cell a higher specific energy density (3.45 V x 170 mA.h g^{-1} = 586 W.h kg^{-1}) comparable to those of $LiCoO_2$ (3.9 V x 140 mA.h g^{-1} = 546 W.h kg^{-1}) and spinel $LiMn_2O_4$ (4.1 V x 100 – 120 mA.h g^{-1} = 410 – 492 W.h kg^{-1}).

The $LiMPO_4$ materials have been found to be more stable to lithium extraction compared to the oxide materials [21]. This is attributed to the presence of strong phosphorus-oxygen (P-O) bond that give it a higher thermal stability than $LiCoO_2$ and the other oxides used as cathode materials [22]. The strong covalent bond between oxygen and phosphorus ions forming $(PO_4)^{3-}$ units allows greater stabilization of the structure when compared to oxide cathodes and prevents O_2 release [22]. This chemical stability allows it to retain performance during cycling and tolerance to overcharge, making $LiFePO_4$ the most stable commercial cathode material. Its stability extends to temperatures of up to 400°C, resulting in better charge-discharge performance and operational safety at elevated temperatures than $LiCoO_2$ which decomposes at 250°C [23].

Despite the excellent cycling performance of $LiFePO_4$, the key drawbacks of the pure material are its low energy density due to its relatively lower voltage (E_{OCV} of 3.4 V *vs.* 3.7 – 4.0 V for $LiCoO_2$ and 4.0 – 4.2 V for $LiMn_2O_4$), one-dimensional Li-ion diffusion rate (10^{-14} cm^2 s^{-1}) and poor intrinsic electronic conductivity (10^{-9} $S.cm^{-1}$) [24, 25], which are quite low for high power applications [26, 27]. To overcome these difficulties, many processing methods to decrease the particle size and realise conductive coatings have been pursued in recent years. A reversible capacity ≈160 mA.h g^{-1} is delivered by the nano-structured particles coated with carbon. Without carbon coating, the specific capacity is lower than 100 mA.h g^{-1}, while a 3-nm thick carbon film deposited onto 500 nm sized particle enhances the discharge capacity to 141 mA.h g^{-1} at a C/12 rate [15, 28]. This result is attributed to the high quality of the "optimised" $LiFePO_4$, impurity-free materials used as positive electrodes.

Other approaches involved creating lithium rich or deficient sites and partial substitution of either isovalent or aliovalent cations which significantly improved the conductivity thereby enabling better battery performance and approaching the theoretical capacity. Although the $LiFePO_4$ shows an acceptably large capacity, the insertion and extraction reactions of Li-ion take place at lower potentials than with $LiCoO_2$ which remains the key disadvantage of the $LiFePO_4$ based cathodes [9, 13, 25].

2.4. Transport properties of $LiMnPO_4$

As already shown in Chapter 1, Section 1.6 and Figure 1.5, the nature of transition metal affects the open circuit voltage, E_{OCV}. In the case of $LiMPO_4$, the polyanion, PO_4, is fixed, so the shifts in the redox potential can only be associated with the changes in the M^{2+} cations. The shifts in the redox potentials have been explained by the changes in the M-O covalence (inductive effect) caused by the changes in the electronegativity of M or M-O bond length [29]. Therefore, replacing the transition-metal ion Fe^{2+} by Mn^{2+}, Co^{2+}, and Ni^{2+} increases the redox potential significantly from 3.4 V in $LiFePO_4$ to 4.1, 4.8, and 5.1 V, respectively, in $LiMnPO_4$, $LiCoPO_4$, and $LiNiPO_4$ because of the changes in the positions of the respective redox couples [25, 30, 31].

However, the voltages of the last two exceed the stability window of the conventional carbonate-based electrolytes presently available, so attention has been focused primarily on $LiMnPO_4$ due to the favourable position of the $Mn^{2+/3+}$ redox couple at 4.1 V vs Li/Li^+, which is compatible with most of the electrolytes [32-38]. An interesting point is that $LiFePO_4$ exhibits a lower voltage (3.43 V) than $LiMnPO_4$ (4.13 V) despite Fe being to the right of Mn in the periodic table as the upper-lying t_{2g} of $Fe^{2+}: t_{2g}^4 e_g^2$ is the redox active band (due to the pairing of the sixth electron in the t_{2g} orbital) compared to the lower-lying e_g of $Mn^{2+}: t_{2g}^3 e_g^2$ (Figure 2.1).

The difference between the covalence of the Fe-O and Mn-O bonds is rather insignificant, so the difference between the electronegativity of Fe and Mn plays a much weaker role than the changes in the M-O bond lengths. Furthermore, $LiMnPO_4$ is of particular interest because of the environmentally benign manganese and its larger theoretical specific energy density (701 Wh kg^{-1}, *vs* 586 Wh kg^{-1} in $LiFePO_4$) and compatibility with conventional oxide-based cathode materials ($LiMO_2$ M= Co, Ni and $LiMn_2O_4$) [33].

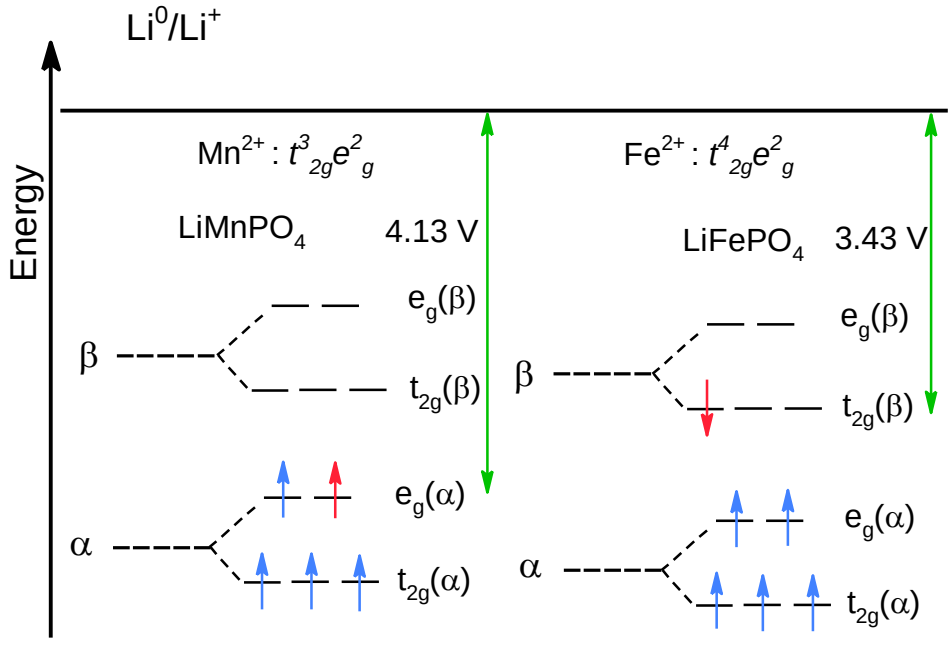

Figure 2.1: Crystal field splitting and 3*d*-orbital energy level diagram for the high-spin Fe^{2+} and Mn^{2+}ions in olivine $LiMPO_4$. The electron involved in the redox reaction is shown with a red arrow.

Its practical performance is however, limited, due to the large lattice distortions induced by Jahn-Teller active Mn^{3+} ions (see section 2.4.2), the much inferior electronic conductivity (10^{-12} – 10^{-14} S cm^{-1}) of $LiMnPO_4$ compared to $LiFePO_4$ (~10^{-9} S cm^{-1}) and kinetics limitations of Li ion diffusion [30, 39-42]. Therefore, these challenges in achieving a high-quality product with the required performance metrics must be overcome for commercial use. To date, we have not reached the same level of understanding and comprehension of $LiMnPO_4$ as we have for $LiFePO_4$ which has been thoroughly studied.

2.4.1. Lithium transport

In the same manner as $LiFePO_4$ (triphylite), $LiMnPO_4$ (lithiophilite) falls into the category of olivine, space group #62 (*Pnma*) [25, 30, 31, 43]. The olivine-type structure contains a distorted hexagonal close-packing (hcp) of oxygen anions, with three types of cations occupying the interstitial sites: (1) corner-sharing MO_6 (*M* = Fe, Mn, Co, Ni etc.) octahedra, which are nearly co-planar to form a distorted two-dimensional square lattice perpendicular to the *a* axis; (2) edge-sharing LiO_6 octahedra aligned in parallel chains along the *b* axis; and (3) tetrahedral PO_4 groups connecting neighbouring planes or arrays. The three-dimensional framework of an olivine is stabilised by the strong covalent bonds between oxygen ions and the P^{5+} resulting in PO_4^{3-} tetrahedral polyanions. The PO_4 tetrahedra share one edge with a MnO_6 octahedron and two edges with LiO_6 octahedra as shown in Figure 2.2a. The presence of the polyanion (PO_4) with strong P-O covalent bonds increases the potential because of the strong polarisation of oxygen ions toward the P cation, which lowers the covalency of the Mn-O bond and increases the voltage [11, 44-45]. Consequently, olivine lithium metal phosphate materials do not undergo a structural re-arrangement during lithiation and de-lithiation. This means that they do not experience the capacity fade during cycling suffered by lithium transition metal oxides such as $LiCoO_2$, $LiNiO_2$, and $LiMn_2O_4$.

Corner-shared MnO_6 octahedra are linked together in the *bc*-plane, while LiO_6 octahedra form edge-sharing chains along the *b*-axis. The tetrahedral PO_4 groups bridge neighbouring layers of MnO_6 octahedra by sharing a common edge with one MnO_6 octahedra and two edges with LiO_6 octahedra. Tetrahedral PO_4 units are also responsible for the rigidity of the lattice which links Mn-O planes together and gives room for Li diffusion along the [010] direction. This $LiMnPO_4$ structure illustrated in Figure 2.2b shows the channels *via* which the Li-ions can diffuse down the [010] direction. Lithium diffusion, primarily within the host electrode and at the electrode/electrolyte interface, is a key factor that determines the charge or discharge rate of an electrochemical cell.

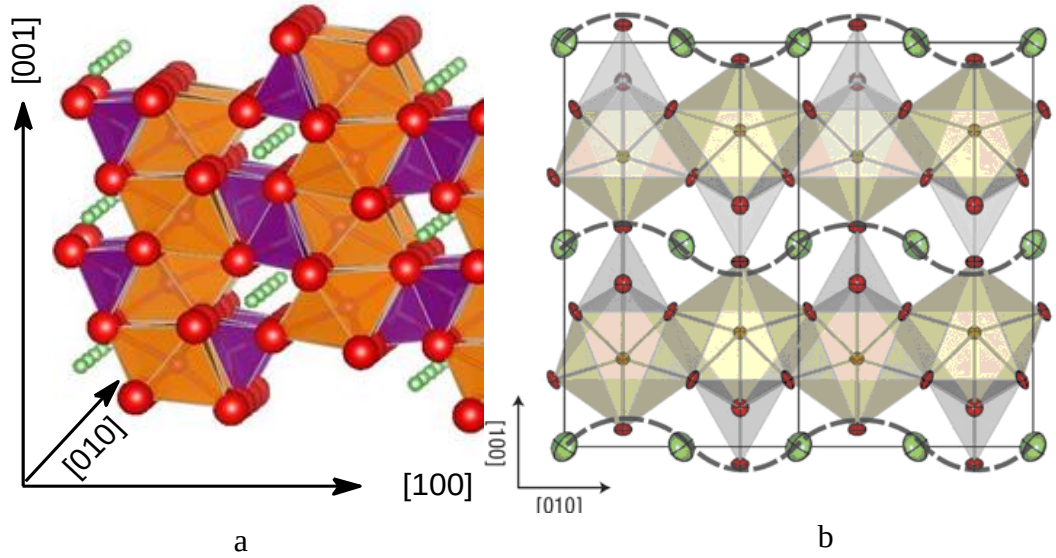

Figure 2.2: (a) The olivine structure of $LiMnPO_4$: showing the MnO_6 octahedra (orange), PO_4 tetrahedra (purple), and the one-dimensional tunnels in which the Li ions reside (green). (b) Visualisation of one-dimensional diffusion Li diffusion path in the phosphate structure. Ellipsoids and dashed curved lines show the diffusion path of Li ions along *b*-direction. Adapted from ref. [46].

Likewise, the other members of the olivine family, the Li-ion diffusion in $LiMnPO_4$ is possible only along the [010] direction, whereby the transportation of Li ion into/out of the crystals is restricted *via* their facets facing the *b*-axes. The one-dimensional tunnels are particularly susceptible to blockage by defects and impurities which limits the rate performance and the energy density of the material. Thus, the theoretical energy density predicted cannot be achieved as Li-ion inaccessible areas remain inactive, especially under high current [22].

The interface strains due to a larger volume change between the $LiMnPO_4$ – $MnPO_4$ phases (8.9 %) in comparison with the $LiFePO_4$ – $FePO_4$ phases (7.0 %) also contribute to the poor ionic conductivity of $LiMnPO_4$ ($<10^{-16}$ – 10^{-14} cm^2 s^{-1}) [47, 48]. According to Nie *et al*. [49], the large volume change can be partially attributed to the Jahn-Teller distortion around the Mn^{3+} ions due to the asymmetric electronic configuration of Mn^{3+} ions in the $MnPO_4$ end-member. This is discussed in more detail in the following Section 2.4.2.

2.4.2. Electronic conductivity

All Li*M*PO_4 materials suffer from low electronic conductivity and low ionic diffusivity which is linked to the presence of covalent bonding in the phosphate ion [22, 30]. At ambient temperature, the electrochemical performance of native $LiMnPO_4$ is several orders of magnitude lower than that of $LiFePO_4$ [50-52]. This is in part due to the poor electronic conductivity of $LiMnPO_4$. While the $LiFePO_4$ is a semi-conductor with a crystal field band gap of approximately 0.3 eV, the $LiMnPO_4$, has a spin exchange band gap of about 2 eV, making it an insulator [53].

This band gap is primarily responsible for the inferior electronic conductivity of the pristine $LiMnPO_4$ phase [53-56]. However, there are other factors which control the electronic conductivity in olivines. Theoretical studies by Maxisch *et al.* [57] have provided evidence that electronic conductivity in olivines is governed by a polaron mechanism. The barriers to movement of hole and electron polarons in $LiMnPO_4$ have been calculated to be significantly higher than that of $LiFePO_4$ resulting in poorer conductivity. Yamada *et al.* [58-60] postulated that a large polaron effective mass in the Mn olivine due to the Jahn-Teller (JT) active Mn^{3+} ion is the likely explanation for the observed low electronic conductivities.

Yamada *et al.* [58-60] also suggested large local lattice deformation during phase transformation to be a further factor limiting the intrinsic kinetics in $LiMnPO_4$. Recently, Piper *et al.* [61] verified experimentally Yamada *et al.* [58-60] suggestion that the pseudo JT distortion is responsible for increasing the activation energy for polaron migration and the formation energy of the electron (hole) lithium ion (vacancy) complex, thereby accounting for the slow intrinsic kinetics of the Mn olivine compared to the Fe olivine.

The Jahn-Teller effect is a geometric distortion of a non-linear molecular system that reduces its symmetry and energy. This distortion is typically observed among octahedral complexes where the two axial bonds can be shorter or longer than those of the equatorial bonds. This effect is dependent on the electronic state of the system. For a perfect octahedron, the five *d* atomic orbitals are split into two degenerate sets; a t_{2g} triplet (d_{xy}, d_{xz}, d_{yz}) and an e_g doublet (d_z^2 and $d_x^2 - d_y^2$) corresponding to the degree of orbital overlap in the direction of the ligands. When a structural unit possesses such a degenerate electronic ground state, it will distort (JT distortion) to remove the degeneracy and form a lower energy and also lower symmetry system. The octahedral complex then will either elongate or contract along the z direction as shown in Figure 2.3. Elongation distortion occurs when the degeneracy is broken by the stabilization (lowering in energy) of the *d* orbitals **with** a *z* component (d_z^2, d_{xz}, d_{yz}), while the orbitals without a *z* component ($d_x^2 - d_y^2$ and d_{xy}) are destabilized (higher in energy) as shown in Figure 2.3 A. This is due to the d_{xy} and $d_x^2 - d_y^2$ orbitals having greater overlap with the ligand orbitals, resulting in the orbitals being higher in energy.

In contrast, contraction distortion occurs when the degeneracy is broken by the stabilisation (lowering in energy) of the *d* orbitals **without** a z component ($d_{x^2} - d_{y^2}$, and d_{xy}), while the orbitals with a z component (d_{z^2}, d_{xz} and d_{yz}) are destabilized (higher in energy) as shown in Figure 2.3 B. Likewise, during elongation, this is due to the *z*-component *d* orbitals having greater overlap with the ligand orbitals, resulting in the orbitals being higher in energy. As far as $LiMnPO_4$ is concerned, de-lithiation results in a volume shrinkage associated with the reduction of the ionic radius of manganese from the 2^+ to the 3^+ ion [49]. The hole is then localised on the MnO_6 in a such a way to distort the ion from Mn^{2+} to Mn^{3+} (i.e., hole polaron). The removal of an electron in going from Mn^{2+} to the Mn^{3+} charge state results in the removal of the degeneracy formed in the e_g state, whereby changes in bond lengths effectively reduce the coordination number from 6 to 4 and further split both the t_{2g} and the e_g state. This is accompanied with an elongation of the axial Mn−O bond lengths with the contraction of the equatorial Mn−O bond lengths, resulting in the preferred de-occupation of the $d_{x^2-y^2}$state, as shown schematically in Figure 2.3 b.

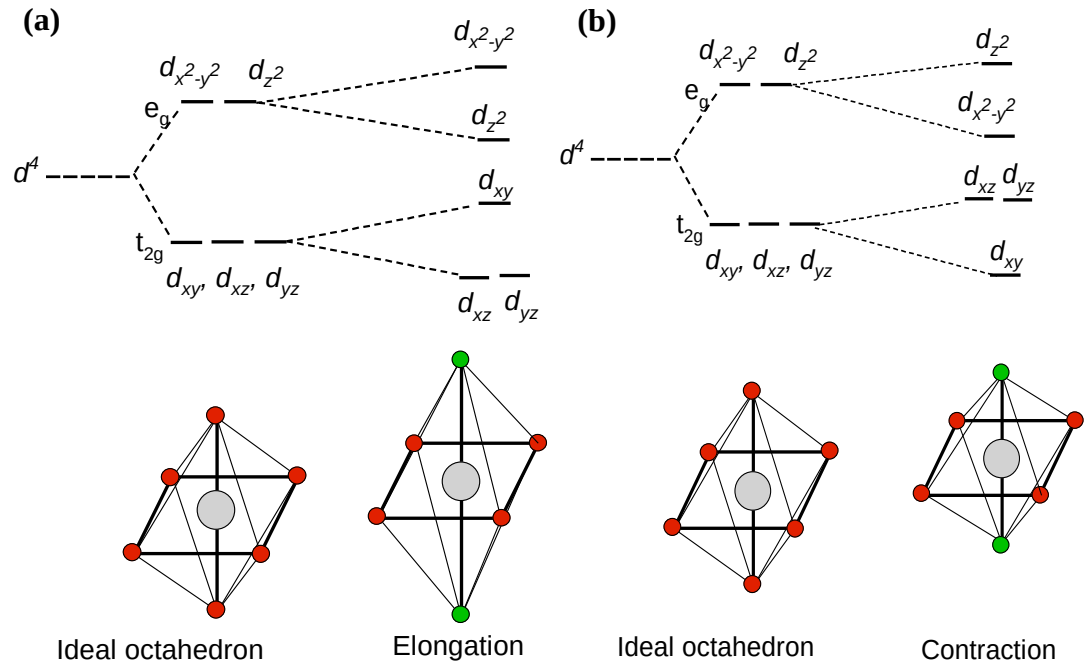

Figure 2.3: Schematic representation of a Jahn−Teller distortion $3d^4$ ($t_{2g}^3e_g^1$) involving the elongation/contraction of the axial Mn−O bonds to lift the orbital degeneracy of the Mn^{3+} configuration. (a) Elongation, (b) Compression.

Similarly, lithiating $MnPO_4$ will form an electron polaron [61, 62]. In this sense, the polaron formation in Fe and Mn olivines is the same [63]. However, the Mn^{3+} ion is considered JT active due to its high spin$t_{2g}^3(\uparrow)\ e_g^1(\uparrow)$ configuration, whereupon removing the electron will lead to an additional distortion in order to lift the degeneracy of the e_g manifold. These changes are thought to be attributable to a greater energy barrier against the charge and Li ion transfers through the significantly misfit crystalline boundary between reduced and oxidized phase of $LiMnPO_4$, [36] and an inactive polaron migration in their phases, which would relate to the JT distortion of high-spin Mn^{3+} ions ($t_{2g}^3(\uparrow)\ e_g^1(\uparrow)$) in the delithiated phase [49, 56]. Nie *et al.* [49] concluded that although the JT effect was harmful to the structural stability, it was helpful for electrical conduction in partially lithiated Li_xMnPO_4 phase. Yamada *et al.* [53, 55, 64] highlighted that the extraction of Li-ion from the pure $LiMnPO_4$ is complicated because of its insulating behaviour, which together with the JT deformation around Mn^{3+} lead to a huge polarization during the charging/discharging cycle.

In summary, during charging/discharging, the MnO_6 octahedra will elongate or compress respectively, thus contributing to the larger volume difference between the $LiMnPO_4$ and $MnPO_4$ end-members compared with $LiFePO_4$ and $FePO_4$ counterparts. The larger volume difference contributes to a greater energy barrier against the Li ion transfers through the significantly misfit crystalline boundary between lithiated and de-lithiated end members, which would relate to the JT distortion of high-spin Mn^{3+} ions in the de-lithiated phase [49, 56]. In other words, the JT deformation accompanied with the large lattice misfit between $LiMnPO_4$ and $MnPO_4$ phases also adversely affects the structural integrity of the lattice, thus leading to lower electrochemical activity than theoretically predicted [24, 52]. The practical use is inhibited by several intrinsic obstacles of $LiMnPO_4$ material:

i. More than five orders of magnitude lower electronic conductivity of $LiMnPO_4$ compared to that of $LiFePO_4$ at room temperature.

ii. Low ionic diffusivity due to large kinetic barrier at the mismatched interface of $MnPO_4/LiMnPO_4$ (<10-16 – 10-12 $cm^2\ s^{-1}$),

iii. Lattice misfit during charge and discharge and polarisation caused by Jahn-Teller deformation around Mn^{3+},

iv. Significant volume changes during the charge/discharge process, which increase energy barrier to Li-ion diffusion across phase interfaces.

Nevertheless, it seems that $LiMnPO_4$, or its derivatives, has the potential to be the next generation of Li-ion cathode material. It has outstanding thermal stability, is environmentally friendly and prices of raw materials are relatively low or similar to $LiFePO_4$ [65]. Efforts to improve electrochemical performance of electrodes made from this material have been focussed on tailoring particle size to reduce the ionic and electronic path length, preparation of porous material, and enhancing electronic conductivity with surface carbon coating layers and cation doping [9, 30, 66-71]. These strategies are discussed in the following Sections.

2.5. Synthesis methods

There are several broad approaches to address the low Li-ion diffusion rate and low electric conductivity of $LiMnPO_4$ that have proved successful for $LiFePO_4$ cathodes including:

- Reduction of $LiMnPO_4$ particle size to a nanometre level which would consequently lead to a reduction in the diffusion path length in the phosphate structure for both electrons and Li-ion ions,
- Production of $LiMnPO_4$ particles coated with a conductive phase, such as carbon, to improve the electronic contact between the particles,
- Carbon coating may also suppress the crystallite and particle growth and therefore may offer an indirect electrochemical advantage as it limits the Li-ion diffusion distance,
- Various synthetic methods that can impact morphology, particle size and conductivity,
- Doping and ionic substitutions.

Two broad synthetic strategies have been employed to achieve the above goals; (1) solid-state methods where all precursor materials are in the solid state, mixed by different mechanical means such as ball milling to improve homogeneity of the product [24, 72-74], and (2) solution methods, in which the precursors are dissolved in a suitable liquid medium to ensure better homogeneity [58, 75-79]. Common aim is a low-cost strategy to produce nanosized particles containing or being coated with a conductive phase.

2.5.1. Solid-state methods

The solid-state reaction to synthesise $LiMnPO_4$ is a conventional simple method which has the ease of upscaling for industrial mass production, utilising a two-step heating regime, including the first firing in a temperature range of 300˚C – 400˚C and subsequently one between 600˚C and 800˚C [24, 72, 73]. The need for high temperature during synthesis however, increases the cost of production. Also, the method produces a product with larger crystal sizes which impacts the electrochemical performance of the material [35, 38, 78]. Due to this, post-processing of the material is required to reduce the particle and crystal size. This is usually done through mechanical methods such as high-energy ball milling which can also help improve the homogeneity of the material. However, this approach could also lead to amorphisation of the material. Other measures to circumvent these problems include addition of carbon during the solid-state reaction which can in turn inhibit crystal growth.

2.5.2. Wet chemistry methods

Unlike solid-state methods, wet chemical methods have several advantages which include better mixing of precursors, better homogeneity, and more regular and consistent morphology, but also at the expense of higher production cost. The methods described here are by no means exhaustive but give an indication of the differences between the most common methods.

2.5.2.1. Spray pyrolysis

Spray pyrolysis is an effective method to produce well crystalline and pure phase fine particles within a short time [72, 73, 80]. Compared to the solid-state method, the particle size distribution is more controllable [81]. In this method, solutions containing precursor colloidal particles are used to generate droplets which act as nucleation centres around which well crystallised, dense and pure particles can be formed [82]. These droplets are typically sprayed into a pyrolysis furnace by a carrier gas [82]. This process produces uniform particles with a short synthesis time. It has been successfully applied to the synthesis of $LiMnPO_4$. Bakenov and Taniguchi's groups [72, 73, 75, 81, 83] have done numerous studies using spray pyrolysis to synthesise $LiMnPO_4$ with combinations of dry or wet ball milling with carbon to produce carbon composites ($LiMnPO_4$/C) where they were able to achieve close to theoretical values for selected samples. Oh *et al.* [80] also used ultrasonic spray pyrolysis investigating the effect of the final calcination temperature achieving discharge capacity of 118 mA.h g^{-1}.

2.5.2.2. Hydrothermal and solvothermal

This method of synthesis involves a chemical process in a precursor containing aqueous solution heated above the boiling point of water (hydrothermal) [77, 84-86] or other solvent (solvothermal) in non-aqueous systems [48, 87, 88]. The advantage of this technique is the possibility of obtaining pure products direct from the solution without the extra calcination step required in other synthetic methods. This reaction is typically carried out in a closed system, where the heated water/co-solvent increases the diffusion of particles and hence leads to faster crystal growth. The structure of the final product can be modulated by manipulating the temperature and therefore, the pressure and amount of precursor compounds in the pressurised vessel. Fang *et al*. [89, 90] successfully prepared $LiMnPO_4$ with a plate-like morphology (thickness 100 nm – 200 nm) using a simple hydrothermal method in a basic aqueous medium at 200°C for 10 hours. The resulting material delivered a discharge capacity 68 mA.h g^{-1} between 3 V – 4.5 V [89, 90].

2.5.2.3. Sol-gel

The sol-gel technique is a well-established colloidal chemistry technique which allows the production of material with smaller particle sizes than solid-state methods. It is a relatively simple and low cost process. The 'sol' component comprises of colloidal particles with sizes less than 500 nm usually in the range of 200 – 300 nm dispersed in a liquid phase whereas the 'gel' is the three-dimensional network in the liquid phase produced *via* the agglomeration of the colloidal particles. Essentially, the reaction process involves the chemical transformation of the liquid phase containing the precursor components into a gel-like state, with subsequent drying at ambient pressures (to produce a xerogel) [35]. It can be used to prepare materials with different morphology such as porous structures (e.g. aerogel), thin fibres or thin films. Depending on the final material required, further post-processing of the material can then be done.

Yang and Xu [43] utilised an ethylene glycol based sol-gel method to produce carbon-coated $LiMnPO_4$ with uniform size distribution. Analysis of the material demonstrated that *in situ* carbon covered the surface after the $LiMnPO_4$ phase formation at 700˚C in a N_2 atmosphere. They reported reversible capacities of 85 and 42 mA.h g^{-1} using 0.01 and 0.05 C rates respectively [43]. Other organic solvents have been employed to manipulate the particle size of the product and act as a source of conductive carbon formed *in situ* during high temperature pyrolysis.

Doi *et al.* [76] used long chain oleic acid to manipulate the particle sizes of the $LiMnPO_4$ product in addition to using it as the carbon source. The obtained $LiMnPO_4$/carbon composite delivered a discharge capacity of 6 mA.h g^{-1} between 3 and 4.5 V at 0.01C. Kwon *et al.* [91] used a similar approach to prepare nanosized $LiMnPO_4$ particles with sizes in the range 130 – 140 nm. Post synthesis, the $LiMnPO_4$ powder was ball milled with 20 wt% carbon to enable carbon coating. The cycling profiles demonstrated a maximum of 92 % of reversible capacity at 1 C.

The effect of particle size on the electrochemical behaviour of carbon coated LiMnPO4 was reported by Drezen *et al.* [35] using a conventional sol–gel technique followed by dry ball milling with 20% carbon. During the synthesis, increasing the temperature led to an increase of the particle sizes from nanometres (~140 nm) to sub-micrometres (~ 800 nm), simultaneously the specific capacity decreased from 134 to 60 mA.h g^{-1} respectively, at 0.1 C rate.

In summary, the solution chemical preparation routes, such as sol–gel, co-precipitation methods and hydrothermal (solvothermal) methods, have an advantage over solid-state reactions in achieving better homogeneity and mixing of the starting compounds on a molecular level. However, these require significant amount of energy to evaporate the solvents and do not always guarantee pure product.

2.6. Improving transport properties

2.6.1. Effect of particle and crystallite size on the transport properties

Reducing the particle size or designing the architecture of the electrode material to the nanoscale level is one of the options abovementioned and can lead to improvement in the electrochemical performance [74, 88, 91, 92]. The shorter diffusion path length for Li^+ ions and electrons increase particularly the rate of charge or discharge as the characteristic time constant, τ, for diffusion is proportional to the square of the diffusion length, L and the diffusion coefficient of Li-ion in the host lattice, D [93].

$$\tau \approx \frac{L^2}{4\pi D} \qquad \text{Equation 2.1}$$

As an example, for 2-μm $LiFePO_4$ particles τ = 83 h, while decreasing the particle to 40 nm reduces τ to 13 s. Also, the greater surface to volume ratio ensure greater contact between the cathode and electrolyte [93]. These both enable a higher charge and discharge rate [35, 36, 73, 75, 77, 82, 94]. Besides improving Li ion diffusion kinetics, nanosized particles can also accommodate the volume changes caused by Li-ion insertion/extraction due to faster strain relaxation [75, 82, 86, 91, 94]. Delacourt *et al.* [95] synthesized 100 nm diameter particles of $LiMnPO_4$, which enhanced the reversible capacity to 70 mA.h g^{-1} at C/20 from only 35 mA.h g^{-1} for 1 μm diameter particles. Yonemura *et al.* [59] reached 150 mA.h g^{-1} of discharge capacity at C/100 with small particles. Thus, it is apparent that particle size is a critical factor in determining useful lithium capacity and charge/discharge rates [96].

However, the goal is not only to prepare nanosized material but also to produce electrodes with a specific microstructure and morphology [74, 77]. The purpose is multifaceted as it can help reduce particle size, which in turn can improve the electronic and ionic transport properties of the material [92]. Ideally, the morphological structure produced may be able to introduce a flexible three-dimensional network that can withstand the expansion and contractions with successive charge and discharge cycles. It is important to realise that the resulting higher surface areas can also increase the likelihood of adverse by-reactions with the electrolyte, hence, the size has to be optimised in relation to increasing Li ion diffusion while preventing any unwanted side reactions. Not only can the higher surface area lead to reactions with the electrolyte, it can also lead to greater self-discharge, poor cycling, calendar life and lower volumetric energy densities [93].

2.6.2. Addition of conductive phase

Ravet *et al*. [25] was the first to show that efficient carbon coating on $LiFePO_4$ allowed the theoretical capacity of 170 mA.h g^{-1} to be achieved. Prior to this, the capacity of $LiFePO_4$ was limited, even at higher temperatures, due to its inherent low electronic conductivity. Dominko *et al*. [97-99] estimated that electrical point-contacts of the particles of $LiFePO_4$ with added carbon black are sufficient to ensure electron conduction if the contacts of the Li-ions with the active material are sufficiently secured. Considering the much lower electronic conductivity of $LiMnPO_4$, a conductive additive is therefore essential to achieve better electrochemical performance. A thin carbon layer may provide a good electrical contact between particles and current collector, a path for electrons to flow to and from the phosphate particles without blocking access for the diffusion of Li-ions [24, 100]. The effectiveness of carbon depends on the type (sp^2 or sp^3), thickness and amount of carbon used [101-103]. According to Fergus [100], graphitic like carbon containing mainly sp^2 bonded carbons arranged in hexagons provides a higher conductivity than coatings containing mostly sp^3 bonded carbon, and therefore carbon coatings with large sp^2/sp^3 ratios are generally preferred [102, 104]. It is important to note that the electro-conductive carbon layers, however, could be barriers against the transportation of the Li-ions, unless they have sufficient defects allowing permeation of electrolyte to ensure the Li-ion conducting routes, especially when they are thick [97].

Carbon coating on the $LiMnPO_4$ particles can be applied either by ball milling [81, 83, 103, 105] or by pyrolysis of carbon precursors [106, 107]. To this end, it is preferred that carbon or carbon precursors are added during synthesis, before the formation of the crystalline phase. It can also help in preventing recrystallisation and agglomeration of nanoparticles thus keeping the particles small. Also, the amount of carbon coating has to be optimised considering it reduces the volumetric energy density of the cathode.

Li *et al.* [108] demonstrated the reversible extraction and insertion of Li-ions from $LiMnPO_4$/carbon composite cathodes, prepared *via* a solid-state route comprising ~10 wt% carbon. During charging to 4.5 V *vs.* Li^0/Li^+, a capacity of 162 mA.h g^{-1} was observed. The cell delivered a first discharge capacity of 146 mA.h g^{-1} and a stable reversible capacity of 140 mA.h g^{-1} was noted in subsequent cycles. The authors also charged the cell to 4.8 V *vs.* Li^0/Li^+ for complete removal of Li-ions from the lattice. In that situation, the first charge capacity approaches the theoretical value (171 mA.h g^{-1}) but the capacity faded to 152 mA.h g^{-1} during the subsequent discharge, perhaps due to the decomposition of the electrolyte used [108]. A citric acid assisted one step solvothermal procedure was adopted by Wang *et al.* [87, 88] to synthesize $LiMnPO_4$ at 300˚C with spherical morphology. After mixing with glucose followed by pyrolysis, the $LiMnPO_4$ cell displayed a discharge a capacity of 107 mA.h g^{-1} at 0.01 C with an appreciable plateau around 4.1 V *vs.* Li^0/Li^+.

Dettlaff-Weglikowska *et al.* [109] reported the preparation of $LiMnPO_4$ composites with single walled carbon nanotubes (SWCNTs). The addition of 1 wt.% nanotubes contributed to the increase in surface area of the resulting $LiMnPO_4$/SWCNT composite. This indicated that the presence of SWCNTs during the formation of crystallites increases the number of nucleation sites and leads to a reduction in the size of the particle. Further, electrical conductivity could be improved by five orders of magnitude through *in situ* addition of 1 wt% of SWCNTs. Battery performance revealed that 68 – 83% of theoretical capacity can be achieved at 0.1 C rate.

2.7. Summary and outlook

After the commercialisation of $LiFePO_4$, the $LiMnPO_4$ may be considered as a next generation cathode material for high capacity Li-ion batteries. This material is not considered as dangerous or poisonous, and its elements are abundant in the earth's crust. It has the same theoretical specific capacity as $LiFePO_4$, 170 mA.h g^{-1}, a flat potential profile at 4.1 V *vs.* Li^0/Li^+, which is ~0.65 V higher than that of $LiFePO_4$ which increases the specific energy by about 15%. This relatively high redox potential of $LiMnPO_4$ falls well within the potential windows of the existing electrolyte solutions.

However, the higher energy density of $LiMnPO_4$ can only be achieved at a very slow rate. The disappointing performance has been attributed to poor transport properties in the bulk $LiMnPO_4$ or $MnPO_4$ phases, the instability of the $MnPO_4$ phase itself, the distortion of the Jahn–Teller active Mn^{3+} ion, the large volumetric change between $LiMnPO_4$ and $MnPO_4$ during charge/discharge, or the high activation barrier for Li-ion to cross the surface. Thus, in contrast to $LiFePO_4$, which is successfully commercialised by improving its low electro-conductivity with simple carbon coating, electrochemically less active $LiMnPO_4$ has not been practically used. Another way to improve the electrochemical performance of the $LiMnPO_4$ phase is the transition metal site doping (Mn sites with isovalent or aliovalent substitutions) or Li-site doping. Both Mn and Li-site doping provides improved battery performance irrespective of the testing temperature. In Mn site substitution, Fe is found to be attractive (compared to Mg, Zn, Cu, Zr, V, Gd, Ti and Ni) and its concentration beyond 10% subsequently leads to the formation of a solid-solution between two olivine compounds ($LiMnPO_4$ and $LiFePO_4$). This is beyond the scope of study here so is not included in the literature review.

The $LiMnPO_4$ synthetic method has a major impact on the electrochemical performance of the cathode material. Nano structuring and/or conductive coatings may overcome kinetic and electronic limitations, allowing materials that would once have been thought of as unsuitable for electrodes to be considered. For $LiMnPO_4$ small particle size, with relatively larger surface area along the *b*-axis and uniform carbon coating of this active mass enable one to overcome the intrinsic poor electronic and ionic conductivity of the material. The shortened diffusion distances for Li-ion in nanoparticles may enable high rate capability in powders that appear to have severe rate limitations when micron-sized or larger. However, some reports are available for nanostructured morphologies that exhibit poor electrochemical properties even when the applied current rate exceeds C/2. The best results reported so far have been for carbon-coated $LiMnPO_4$ with small sizes prepared either by the solvo-thermal polyol process or sol-gel process, 145 mA.h g^{-1} and 134 mA.h g^{-1}, respectively at C/10 and at room temperature.

2.8. References

1. Mizushima K, Jones P, Wiseman P, Goodenough J. Li_xCoO_2 (0<x<-1): a new cathode material for batteries of high energy density. Materials Research Bulletin. 1980;15(6):783-9.

2. Thackeray M, Johnson P, de Picciotto L, Bruce P, Goodenough J. Electrochemical extraction of lithium from LiMn2O4. Materials Research Bulletin. 1984;19(2):179-87.

3. Balakrishnan P, Ramesh R, Prem Kumar T. Safety mechanisms in lithium-ion batteries. Journal of Power Sources. 2006;155(2):401-14.

4. Tarascon J, Armand M. Issues and challenges facing rechargeable lithium batteries. Nature. 2001;414(6861):359-67.

5. Tarascon J, Grugeon S, Laruelle S, Larcher D, Poizot P. The key role of nanoparticles in reactivity of 3D metal oxides toward lithium. In: Nazri G, Pistoia G, editors. Lithium Batteries Science and Technology. 1 ed. New York: Springer US; 2003. p. 220-46.

6. Fu L, Liu H, Li C, Wu Y, Rahm E, Holze R, et al. Electrode materials for lithium secondary batteries prepared by sol–gel methods. Progress in Materials Science. 2005;50(7):881-928.

7. Egashira M, Kanetomo A, Yoshimoto N, Morita M. Charge–discharge rate of spinel lithium manganese oxide and olivine lithium iron phosphate in ionic liquid-based electrolytes. Journal of Power Sources. 2011;196(15):6419-24.

8. Park M, Zhang X, Chung M, Less G, Sastry A. A review of conduction phenomena in Li-ion batteries. Journal of Power Sources. 2010;195(24):7904-29.

9. Armand M, Goodenough J, Padhi A, Nanjundaswamy K, Masquelier C, inventors; Board of Regents, The University of Texas, Austin, assignee. Cathode materials for secondary (rechargeable) batteries. United States patent 6,514,640. 1999 Feb 4.

10. Goodenough J. Cathode materials: a personal perspective. Journal of Power Sources. 2007;174(2):996-1000.

11. Goodenough J, Kim Y. Challenges for rechargeable Li batteries. Chemistry of Materials. 2009;22(3):587-603.

12. Manthiram A, Goodenough J. Lithium insertion into $Fe_2(SO_4)_3$ frameworks. Journal of Power Sources. 1989;26(3–4):403-8.

13. Padhi A, Nanjundaswamy K, Masquelier C, Okada S, Goodenough J. Effect of structure on the Fe^{3+} / Fe^{2+} redox couple in iron phosphates. Journal of The Electrochemical Society. 1997;144(5):1609-13.

14. Zaghib K, Mauger A, Gendron F, Julien C, Goodenough J. Secondary batteries – lithium rechargeable systems – lithium-ion | positive electrode: lithium iron phosphate. In: Editor-in-Chief: Jürgen G, editor. Encyclopedia of Electrochemical Power Sources. Amsterdam: Elsevier; 2009. p. 264-96.

15. Zaghib K, Mauger A, Groult H, Goodenough J, Julien C. Advanced electrodes for high power Li-ion batteries. Materials. 2013;6(3):1028.

16. Anderson A, Kalska B, Haggstrom L, Thomas J. Lithium extraction/insertion in $LiFePO_4$: an X-ray diffraction and Mossbauer spectroscopy study. Solid State Ionics. 2000;130(1):41-52.

17. Masquelier C, Padhi A, Nanjundaswamy K, Goodenough J. New cathode materials for rechargeable lithium batteries: the 3-D framework structures $Li_3Fe_2(XO_4)_3$ (X=P, As). Journal of Solid State Chemistry. 1998;135(2):228-34.

18. Padhi A, Nanjundaswamy K, Masquelier C, Goodenough J. Mapping of transition metal redox energies in phosphates with NASICON structure by lithium intercalation. Journal of The Electrochemical Society. 1997;144(8):2581-6.

19. Ni J, Kawabe Y, Morishita M, Watada M, Sakai T. Improved electrochemical activity of LiMnPO4 by high-energy ball-milling. Journal of Power Sources. 2011;196(19):8104-9.

20. Padhi A, Nanjundaswamy K, Goodenough J. Phospho-olivines as positive-electrode materials for rechargeable lithium batteries. Journal of The Electrochemical Society. 1997;144(4):1188-94.

21. Thackeray M. Batteries, transport applications. In: Cleveland CJ, editor. Encyclopedia of Energy. Amsterdam: Elsevier; 2004. p. 117-26.

22. Zhang W. Structure and performance of $LiFePO_4$ cathode materials: A review. Journal of Power Sources. 2011;196(6):2962-70.

23. Cairns E. Batteries, overview. In: Cleveland CJ, editor. Encyclopedia of Energy. 1. Amsterdam: Elsevier; 2004. p. 117-26.

24. Wolfenstine J. Electrical conductivity of doped $LiCoPO_4$. Journal of Power Sources. 2006;158(2):1431-5.

25. Ravet N, Chouinard Y, Magnan J, Besner S, Gauthier M, Armand M. Electroactivity of natural and synthetic triphylite. Journal of Power Sources. 2001;97:503-7.

26. Julien C, Mauger A, Zaghib K, Gendron F, editors. High performance of lithium iron phosphates for HEV with quality control made by magnetometry. Proceedings of the Materials Research Society 2006; Boston, Massachusetts.

27. Wang Y, He P, Zhou H. Olivine $LiFePO_4$: development and future. Energy & Environmental Science. 2011;4(3):805-17.

28. Azib T, Ammar S, Nowak S, Lau-Truing S, Groult H, Zaghib K, et al. Crystallinity of nano C-$LiFePO_4$ prepared by the polyol process. Journal of Power Sources. 2012;217(0):220-8.

29. Muraliganth T, Manthiram A. Understanding the shifts in the redox potentials of olivine $LiM_{1-y}M_yPO_4$ (M = Fe, Mn, Co, and Mg) solid solution cathodes. The Journal of Physical Chemistry C. 2010;114(36):15530-40.

30. Delacourt C, Laffont L, Bouchet R, Wurm C, Leriche J, Morcrette M, et al. Toward understanding of electrical limitations (electronic, ionic) in $LiMPO_4$ (M = Fe, Mn) electrode materials. Journal of The Electrochemical Society. 2005;152(5):A913-21.

31. Okada S, Sawa S, Egashira M, Yamaki J, Tabuchi M, Kageyama H, et al. Cathode properties of phospho-olivine $LiMPO_4$ for lithium secondary batteries. Journal of Power Sources. 2001;97:430-2.

32. Howard W, Spotnitz R. Theoretical evaluation of high-energy lithium metal phosphate cathode materials in Li-ion batteries. Journal of Power Sources. 2007;165(2):887-91.

33. Aravindan V, Gnanaraj J, Lee Y, Madhavi S. $LiMnPO_4$ - A next generation cathode material for lithium-ion batteries. Journal of Materials Chemistry. 2013;1(11):3518-39.

34. Dong Y, Xie H, Song J, Xu M, Zhao Y, Goodenough J. The prepared and electrochemical property of Mg doped $LiMnPO_4$ nanoplates as cathode materials for lithium-ion batteries. Journal of The Electrochemical Society. 2012;159(7):A995-8.

35. Drezen T, Kwon N, Bowen P, Teerlinck I, Isono M, Exnar I. Effect of particle size on $LiMnPO_4$ cathodes. Journal of Power Sources. 2007;174(2):949-53.

36. Liu C, Wu X, Wu W, Cai J, Liao S. Preparation of nanocrystalline $LiMnPO_4$ via a simple and novel method and its isothermal kinetics of crystallization. Journal of Materials Science. 2011;46(8):2474-8.

37. Rao B, Venkateswarlu M, Satyanarayana N. Structural, electrical and dielectric studies of nanocrystalline $LiMnPO_4$ particles. Ionics. 2014;20(7):927-34.

38. Xiao J, Chernova N, Upreti S, Chen X, Li Z, Deng Z, et al. Electrochemical performances of $LiMnPO_4$ synthesized from non-stoichiometric Li/Mn ratio. Physical Chemistry Chemical Physics. 2011;13(40):18099-106.

39. Kang B, Ceder G. Electrochemical performance of $LiMnPO_4$ synthesized with off-stoichiometry. Journal of The Electrochemical Society. 2010;157(7):A808-11.

40. Morgan D, Van der Ven A, Ceder G. Li conductivity in $LixMPO_4$ (M = Mn, Fe, Co, Ni) olivine materials. Electrochemistry Solid State Letters. 2004;7(2):A30-2.

41. Zhou H, Upreti S, Chernova N, Hautier G, Ceder G, Whittingham M. Iron and manganese pyrophosphates as cathodes for lithium-ion batteries. Chemistry of Materials. 2011;23(2):293-300.

42. Zhou F, Kang K, Maxisch T, Ceder G, Morgan D. The electronic structure and band gap of $LiFePO_4$ and $LiMnPO_4$. Solid State Communications. 2004;132(3):181-6.

43. Yang J, Xu J. Synthesis and characterization of carbon-coated lithium transition metal phosphates $LiMPO_4$ (M = Fe, Mn, Co, Ni) prepared via a nonaqueous sol-gel route. Journal of The Electrochemical Society. 2006;153(4):A716-23.

44. Goodenough J. Evolution of strategies for modern rechargeable batteries. Accounts of Chemical Research. 2013;46(5):1053-61.

45. Yuan L, Wang Z, Zhang W, Hu X, Chen J, Huang Y, et al. Development and challenges of $LiFePO_4$ cathode material for lithium-ion batteries. Energy & Environmental Science. 2011;4(2):269-84.

46. Nishimura S-i, Kobayashi G, Ohoyama K, Kanno R, Yashima M, Yamada A. Experimental visualization of lithium diffusion in $LixFePO_4$. Nature Materials. 2008;7(9):707-11.

47. Li L, Liu J, Chen L, Xu H, Yang J, Qian Y. Effect of different carbon sources on the electrochemical properties of rod-like $LiMnPO_4$-C nanocomposites. RSC Advances. 2013;3(19):6847-52.

48. Yang S, Ma R, Hu M, Xi L, Lu Z, Chung C. Solvothermal synthesis of nano-$LiMnPO_4$ from Li_3PO_4 rod-like precursor: reaction mechanism and electrochemical properties. Journal of Materials Chemistry. 2012;22(48):25402-8.

49. Nie Z, Ouyang C, Chen J, Zhong Z, Du Y, Liu D, et al. First principles study of Jahn–Teller effects in $LixMnPO_4$. Solid State Communications. 2010;150(1–2):40-4.

50. Xiao J, Xu W, Choi D, Zhang J. Synthesis and characterisation of lithium manganese phosphate by a precipitation method. Journal of The Electrochemical Society. 2012;157(2):142-7.

51. Chen C, Yuan A, Zhao H, Xu J. Electrochemical behavior of olivine-type $LiMnPO_4$-based material in a mild aqueous electrolyte. Ionics. 2012;18(7):635-41.

52. Bramnik N, Ehrenberg H. Precursor-based synthesis and electrochemical performance of $LiMnPO_4$. Journal of Alloys and Compounds. 2008;464(1–2):259-64.

53. Yamada A, Hosoya M, Chung S, Kudo Y, Hinokuma K, Liu K, et al. Olivine-type cathodes: achievements and problems. Journal of Power Sources. 2003;119:232-8.

54. Kope¢ M, Yamada A, Kobayashi G, Nishimura S, Kanno R, Mauger A, et al. Structural and magnetic properties of Lix(MnyFe1−y)PO_4 electrode materials for Li-ion batteries. Journal of Power Sources. 2009;189(2):1154-63.

55. Yamada A. Electrochemical, magnetic, and structural investigation of the Lix(Mn_yFe_{1-y})PO_4 phases. Chemistry of Materials. 2006;18(3):804-13.

56. Yamada A, Kudo Y, Liu K. Reaction mechanism of the olivine-type Lix($Mn_{0.6}Fe_{0.4}$)PO_4(0<x<1). Journal of Electrochemistry Society. 2001;148(7):A747-54.

57. Maxisch T, Zhou F, Ceder G. Ab initio study of the migration of small polarons in olivine Lix$FePO_4$ and their association with lithium ions and vacancies. Physical Review B. 2006;73(10):104301.

58. Yamada A, Kudo Y, Liu K. Phase diagram of $Li_x(Mn_yFe_{1-y})PO_4$ (0<x,y<1). Journal of Electrochemistry Society. 2001;148(10):A1153-8.

59. Yonemura M, Yamada A, Takei Y, Sonoyama N, Kanno R. Comparative kinetic study of olivine LixMPO_4 (M = Fe , Mn). Journal of The Electrochemical Society. 2004;151(9):A1352-6.

60. McDowall J. Understanding lithium-ion technologies. The Battcon 2008 Proceedings; Marco Island, FL: Battcon/Albercorp; 2008. p. 1-9.

61. Piper L, Quackenbush N, Sallis S, Scanlon D, Watson G, Nam K, et al. Elucidating the nature of pseudo Jahn–Teller distortions in Lix$MnPO_4$: combining density functional theory with soft and hard x-ray spectroscopy. The Journal of Physical Chemistry C. 2013;117(20):10383-96.

62. Huang Y, Fang J, Omenya F, O'Shea M, Chernova N, Zhang R, et al. Understanding the stability of $MnPO_4$. Journal of Materials Chemistry A. 2014;2(32):12827-34.

63. Ong S, Chevrier V, Ceder G. Comparison of small polaron migration and phase separation in olivine $LiMnPO_4$ and $LiFePO_4$ using hybrid density functional theory. Physical Review B. 2011;83(7):075112.

64. Yamada A, Chung S. Crystal chemistry of the olivine-type Li(Mn_yFe_{1-y})PO_4 and (Mn_yFe_{1-y})PO_4 as possible 4V cathode materials for lithium batteries. Electrochemical and Solid-State Letters. 2001;148(8):A960-7.

65. Hautier G, Jain A, Ong S, Kang B, Moore C, Doe R, et al. Phosphates as lithium-ion battery cathodes: an evaluation based on high-throughput ab initio calculations. Chemistry of Materials. 2011;23(15):3495-508.

66. Meethong N, Huang H, Speakman S, Carter W, Chiang Y. Strain accommodation during phase transformations in olivine-based cathodes as a materials selection criterion for high-power rechargeable batteries. Advanced Functional Materials. 2007;17(7):1115-23.

67. Meethong N, Kao Y, Carter W, Chiang Y. Comparative study of lithium transport kinetics in olivine cathodes for Li-ion batteries. Chemistry of Materials. 2010;22(3):1088-97.

68. Meethong N, Kao Y, Tang M, Huang H, Carter W, Chiang Y. Electrochemically induced phase transformation in nanoscale olivines $Li_{1-x}MPO_4$ (M = Fe, Mn). Chemistry of Materials. 2008;20(19):6189-98.

69. Huang H, Yin S, Nazar L. Approaching theoretical capacity of $LiFePO_4$ at room temperature at high rates. Electrochemical and Solid-State Letters. 2001;4(10):A170-2.

70. Yang S, Song Y, Ngala K, Zavalij P, Whittingham M. Performance of $LiFePO_4$ as lithium battery cathode and comparison with manganese and vanadium oxides. Journal of Power Sources. 2003;119–121(0):239-46.

71. Chung S, Bloking J, Chiang Y. Electronically conductive phospho-olivines as lithium storage electrodes. Nature Materials. 2002;1(2):123-8.

72. Doan T, Bakenov Z, Taniguchi I. Preparation of carbon coated $LiMnPO_4$ powders by a combination of spray pyrolysis with dry ball-milling followed by heat treatment. Advanced Powder Technology. 2010;21(2):187-96.

73. Doan T, Taniguchi I. Cathode performance of $LiMnPO_4$/C nanocomposites prepared by a combination of spray pyrolysis and wet ball-milling followed by heat treatment. Journal of Power Sources. 2011;196(3):1399-408.

74. Wang F, Yang J, Gao P, NuLi Y, Wang J. Morphology regulation and carbon coating of $LiMnPO_4$ cathode material for enhanced electrochemical performance. Journal of Power Sources. 2011;196(23):10258-62.

75. Bakenov Z, Taniguchi I. Synthesis of spherical $LiMnPO_4$/C composite microparticles. Materials Research Bulletin. 2011;46(8):1311-4.

76. Doi T, Yatomi S, Kida T, Okada S, Yamaki J. Liquid-phase synthesis of uniformly nanosized $LiMnPO_4$ particles and their electrochemical properties for lithium-ion batteries. Crystal Growth & Design. 2009;9(12):4990-2.

77. Ji H, Yang G, Ni H, Roy S, Pinto J, Jiang X. General synthesis and morphology control of $LiMnPO_4$ nanocrystals via microwave-hydrothermal route. Electrochimica Acta. 2011;56(9):3093-100.

78. Liu J, Hu D, Huang T, Yu A. Synthesis of flower-like $LiMnPO_4$/C with precipitated $NH_4MnPO_4 \cdot H_2O$ as precursor. Journal of Alloys and Compounds. 2012;518(0):58-62.

79. Ramar V, Saravanan K, Gajjela S, Hariharan S, Balaya P. The effect of synthesis parameters on the lithium storage performance of $LiMnPO_4$/C. Electrochimica Acta. 2013;105(0):496-505.

80. Oh S, Oh S, Myung S, Lee S, Sun Y. The effects of calcination temperature on the electrochemical performance of $LiMnPO_4$ prepared by ultrasonic spray pyrolysis. Journal of Alloys and Compounds. 2010;506(1):372-6.

81. Bakenov Z, Taniguchi I. Electrochemical performance of nanocomposite $LiMnPO_4$/C cathode materials for lithium batteries. Electrochemistry Communications. 2010;12(1):75-8.

82. Satyavani T, Srinivas Kumar A, Subba Rao P. Methods of synthesis and performance improvement of lithium iron phosphate for high rate Li-ion batteries: a review. Engineering Science and Technology, an International Journal. 2016;19(1):178-88.

83. Bakenov Z, Taniguchi I. Physical and electrochemical properties of $LiMnPO_4$/C composite cathode prepared with different conductive carbons. Journal of Power Sources. 2010;195(21):7445-51.

84. Chen J, Vacchio M, Wang S, Chernova N, Zavalij P, Whittingham M. The hydrothermal synthesis and characterization of olivines and related compounds for electrochemical applications. Solid State Ionics. 2008;178(31–32):1676-93.

85. Gao Z, Pan X, Li H, Xie S, Yi R, Jin W. Hydrothermal synthesis and electrochemical properties of dispersed $LiMnPO_4$ wedges. CrystEngComm. 2013;15(38):7808-14.

86. Kotobuki M. Improved performance of hydrothermally synthesized $LiMnPO_4$ by ball-milling as a positive electrode for Li ion battery. ISRN Electrochemistry. 2013:1-5.

87. Wang Y, Yang Y, Yang Y, Shao H. Fabrication of microspherical $LiMnPO_4$ cathode material by a facile one-step solvothermal process. Materials Research Bulletin. 2009;44(11):2139-42.

88. Wang Y, Yang Y, Yang Y, Shao H. Enhanced electrochemical performance of unique morphological cathode material prepared by solvothermal method. Solid State Communications. 2010;150(1–2):81-5.

89. Fang H, Li L, Li G. Hydrothermal Synthesis of Electrochemically Active $LiMnPO_4$. Chemistry Letters. 2007;36(3):436-7.

90. Fang H, Li L, Yang Y, Yan G, Li G. Carbonate anions controlled morphological evolution of $LiMnPO_4$ crystals. Chemical Communications. 2008(9):1118-20.

91. Kwon N, Drezen T, Exnar I, Teerlinck I, Isono M, Graetzel M. Enhanced electrochemical performance of mesoparticulate $LiMnPO_4$ for lithium ion batteries. Electrochemical and Solid-State Letters. 2006;9(6):A277-80.

92. Zhao M, Fu Y, Xu N, Li G, Wu M, Gao X. High performance $LiMnPO_4$/C prepared by a crystallite size control method. Journal of Materials Chemistry A. 2014;2(36):15070-7.

93. Arico A, Bruce P, Scrosati B, Tarascon J, Van Schalkwijk W. Nanostructured materials for advanced energy conversion and storage devices. Nature Materials. 2005;4(5):366-77.

94. Kim T, Park H, Lee M, Lee S, Song H. Restricted growth of $LiMnPO_4$ nanoparticles evolved from a precursor seed. Journal of Power Sources. 2012;210(0):1-6.

95. Delacourt C, Poizot P, Morcrette M, Tarascon J, Masquelier C. One-step low-temperature route for the preparation of electrochemically active $LiMnPO_4$ powders. Chemistry of Materials. 2004;16(1):93-9.

96. Martha S, Grinblat J, Haik O, Zinigrad E, Drezen T, Miners J, et al. $LiMn_{0.8}Fe_{0.2}PO_4$: An advanced cathode material for rechargeable lithium batteries. Angewandte Chemie International Edition. 2009;48(45):8559-63.

97. Dominko R, Bele M, Gaberscek M, Remskar M, Hanzel D, Pejovnik S, et al. Impact of the carbon coating thickness on the electrochemical performance of $LiFePO_4$ / C composites. Journal of The Electrochemical Society. 2005;152(3):A607-10.

98. Dominko R, Gaberscek M, Bele M, Mihailovic D, Jamnik J. Carbon nanocoatings on active materials for Li-ion batteries. Journal of the European Ceramic Society. 2007;27(2–3):909-13.

99. Pejovnik S, Dominko R, Bele M, Gaberscek M, Jamnik J. Electrochemical binding and wiring in battery materials. Journal of Power Sources. 2008;184(2):593-7.

100. Fergus J. Recent developments in cathode materials for lithium ion batteries. Journal of Power Sources. 2010;195(4):939-54.

101. Guo P, Song H, Chen X, Ma L, Wang G, Wang F. Effect of graphene nanosheet addition on the electrochemical performance of anode materials for lithium-ion batteries. Analytica Chimica Acta. 2011;688(2):146-55.

102. Milev A, Tran N, Kannangara G, Wilson M. Unoccupied electronic structure of ball-milled graphite. Physical Chemistry Chemical Physics. 2010;12(25):6685-91.

103. Nien Y, Carey J, Chen J. Physical and electrochemical properties of $LiFePO_4$/C composite cathode prepared from various polymer-containing precursors. Journal of Power Sources. 2009;193(2):822-7.

104. Milev A, Dissanayake D, Kannangara G, Kumarasinghe A. Defect induced electronic states and magnetism in ball-milled graphite. Physical Chemistry Chemical Physics. 2013;15(38):16294-302.

105. Wang D, Buqa H, Crouzet M, Deghenghi G, Drezen T, Exnar I, et al. High-performance, nano-structured $LiMnPO_4$ synthesized via a polyol method. Journal of Power Sources. 2009;189(1):624-8.

106. Kumar P, Venkateswarlu M, Misra M, Mohanty A, Satyanarayana N. Carbon coated $LiMnPO_4$ nanorods for lithium batteries. Journal of The Electrochemical Society. 2011;158(3):A227-30.

107. Choi D, Wang D, Bae I, Xiao J, Nie Z, Wang W, et al. $LiMnPO_4$ nanoplate grown via solid-state reaction in molten hydrocarbon for Li-ion battery cathode. Nano Letters. 2010;10(8):2799-805.

108. Li G, Azuma H, Tohda H. $LiMnPO_4$ as a cathode for Li-ion batteries. Electrochemistry Solid State Letters. 2002;5(6):A135-7.

109. Dettlaff-Weglikowska U, Sato N, Yoshida J, Roth S. Preparation and electrochemical characterization of $LiMnPO_4$/single-walled carbon nanotube composites as cathode material for Li-ion battery. physica status solidi (b). 2009;246(11-12):2482-5.

CHAPTER 3

Synthesis of phase-pure $LiMnPO_4$ using a novel phosphonate sol-gel route

This chapter looks at the synthesis of phase-pure $LiMnPO_4$ using a novel sol-gel approach incorporating metal acetate precursors, two different non-aqueous solvents and a new phosphate source. The use of an intermediate phosphonate species to prepare $LiMnPO_4$ has never been attempted before. Firstly, the synthetic method and materials used are described and discussed. Here, the novelty and development of the synthetic method will be highlighted which has never been employed to synthesise $LiMnPO_4$. A brief section looks at the formation of the $LiMnPO_4$ precursor at 24 hour intervals during the sol-gel process. The $LiMnPO_4$ precursor derived from the sol-gel process is then characterised by vibrational spectroscopy (infrared and Raman), powder x-ray diffraction and electron microscopy. Following this, the thermal profile of the precursor in air and argon is determined. Finally, the development of phase pure $LiMnPO_4$ from the dried and densified gel is discussed, highlighting key points on how the phase purity of the final product can be modulated by temperature and atmosphere.

3.1. Introduction

The synthesis method used has a significant influence on the particle morphology, crystal size, crystallisation temperature, specific surface area, metal cation distribution and physical properties of the final product. These properties subsequently influence the electrochemical properties of the material produced. Liquid phase or wet chemical synthesis uses a bottom-up approach to produce nanoparticles with a more uniform nanostructure with the added advantage to be able to control morphology. Moreover, solution methods can lower the temperature needed to produce crystalline materials. Materials can be made through kinetically controlled synthesis rather than a purely thermodynamic controlled synthesis as it is with solid-state reactions, to produce novel materials with structure different to that favoured by thermodynamics. In contrast, conventional solid-state methods require much higher temperatures to produce phase pure crystalline material and are usually more heterogeneous in structure. Therefore, new low-temperature synthesis methods for $LiMnPO_4$ need to be studied and innovated further.

The synthetic procedure used in this study is a novel, non-aqueous sol-gel process to prepare crystalline $LiMnPO_4$. The sol-gel technique has been well-known for decades to prepare mixed metal-oxides, nanomaterials with different architectures and organic-inorganic hybrid materials [1, 2]. Fundamentally, this method involves production of the sol (colloidal solution), from precursors generally consisting of metal alkoxides, followed by the gelation of the sol giving rise to the gel, with subsequent solvent removal by evaporation or rapid extraction under supercritical conditions to produce a xerogel or aerogel, respectively [1-3].

The sol-gel method can produce materials with excellent purity using milder synthetic conditions when compared to conventional solid-state routes. It also permits better mixing of the starting materials or constituent cations, better control of the stoichiometry and thus excellent chemical homogeneity in the final product [1]. Moreover, the molecular level mixing, self-assembly and subsequent formation of extended networks, facilitate the structural evolution, thereby lowering the required crystallisation temperature [1, 2]. To expatiate, due to the intimate mixing, phase pure materials can be made without the need for long range solid-state diffusion of atoms. This reduction in the diffusion distances leads to shorter reaction times and/or lower reaction temperatures when preparing the final crystalline product.

The sol-gel process is separated into different steps that are generally representative of these systems: (i) the formation of stable solutions of solvated metal precursors (the sol); (ii) increase in the viscosity of the solution and forms a gel by polycondensation or polyesterification reactions; (iii) ageing of the gel where the reactions continue, followed by contraction of the gel network and removal of solvent from gel pores; (iv) drying of the gel to remove volatile liquids from the gel network; (v) annealing at higher temperatures to remove the remaining organic ligands and grow crystalline particles [5]. The main advantage over other solution routes such as precipitation routes is the lower tendency for cations to segregate during the process of gelation and subsequent pyrolysis of the resulting gel. Also, it is a relatively facile and inexpensive technique to employ which makes it promising for industrial upscaling. Interested readers are directed to the following resources for more detailed studies and reviews on the sol-gel process [3-6].

Chelating agents are often used to adjust the hydrolysis rates of the metal precursors and hence to control the stoichiometry of mixed metal oxides prepared by the sol-gel method. Specifically, it is a derivative of the Pechini form of sol-gel where there is a chelating agent (acid) and a polymerisation agent (polyhydroxyl alcohol) as described by Cushing *et al.* [5]. Complexing agents in this case are usually acids, for example, acetic acid. The use of various acids as complexing agents has been used successfully by other research groups when synthesising sol-gel derived materials of electrochemical interest [7-9]. As discussed in Chapter 2, Ma *et al* [8] showed that increasing the ratio of citric acid to Fe reduced the average crystallite size from 59.6 nm to 43.1 nm. Acetic acid has been used before as a chelating agent, although only a few reported studies have used it to make lithium transition metal phosphates. Yan *et al.* [10] used the sol-gel method with different chelating agents including acetic acid, ethanediol, oxalic acid, and ethylenediamine. They found out that the electrochemical performance of the $LiFePO_4$ made using acetic acid showed the best results with an initial discharge capacity of 161 mA.h g^{-1} [10].

Ethylene glycol is used as the dispersing agent which provides alcohol groups for esterification. Duncan *et al.* [11] used both acetic acid and ethylene glycol to prepare $LiMn_{1.5}Ni_{0.5}O_4$. Based on the temperature, they obtained crystallites with sizes varying from 21 nm to 400 nm [11]. Pan *et al.* [12, 13] compared the impact of adding a dispersing agent (polyethylene glycol) when preparing LiV_3O_8 on the size and shape of the particles with oxalic acid as the chelating agent. Without the polyethylene glycol, nanorods were formed whereas including it formed nanosheets with the distance between the sheets less than 50 nm [12, 13]. While the capacity of both the materials were similar, the capacity retention of the latter was significantly better [12, 13]. This was attributed to the ease of ion diffusion into the nanosheet material and the ability of the nanosheets to withstand the structural stresses and strains caused by volume expansion resulting from repeated insertion and expulsion charge and discharge cycles [12, 13]. The authors claim that the nanosheets were a result of the decomposition of polyethylene glycol (PEG) and concluded that in the gel, the PEG would have adopted a lamellar morphology. There is no reported comparison for $LiMnPO_4$.

The impetus to employ a sol-gel technique to synthesise $LiMnPO_4$ here is derived from the novel synthetic route developed for hydroxyapatite, $Ca_5(PO_4)_3(OH)$ at Western Sydney University, which was fabricated using a metal salt (calcium ethoxide) and diethyl hydrogen phosphate (DHP) as the phosphorous containing compound, dissolved in a solvent mixture containing a 1:1 molar ratio of ethylene glycol and acetic acid [14-17]. During this reaction at 70°C, an intermediate, acetyl 2-hydroxyethyl phosphonate was identified as the major component along with other esters and water, formed during esterification [14]. This ligand has an inorganic end which undergoes substitution with Ca^{2+} from calcium ethoxide to form stable chelates [14]. Its organic end is weakly attracted through hydrophobic interactions to another organic end. This results in the formation of lamellar structures where the metal ions and phosphonate oxygen atoms lie in sheets (Figure 3.1).

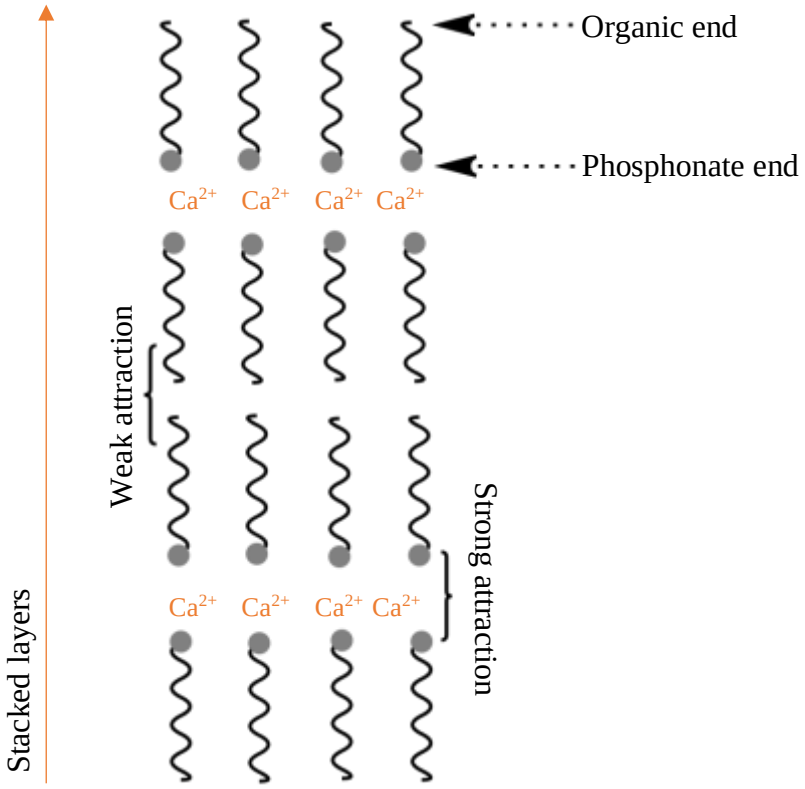

Figure 3.1: A schematic representation of the lamellar structure of phosphonate salt chelated to Ca^{2+}. The Ca^{2+} ions and the phosphonate oxygen atoms lie in packed sheets, while the organic ends are arranged above and below the plane of the inorganic layer, thus forming bi-layers.

It is possible for Ca^{2+} to form complexes with acetate ion from acetic acid as well as the intermediary phosphonate [15]. This intermediate also ensures that P is contained within the system to maintain the molar ratio without being removed due to the high volatility of DHP. The gel dried at 130°C, was found to have a lamellar morphology, which was retained at elevated temperatures to form pure hydroxyapatite, mimicking the biogenic bone material [15, 17]. A later study, eliminated the need for calcium ethoxide which is hygroscopic and instead used calcium acetate, which was an intermediate product characterised in the earlier studies, and is much easier to handle [16, 17].

Hence, the motivation to use the metal acetates of Li and Mn in a modified sol-gel process to prepare $LiMnPO_4$ with DHP as the phosphate source in a mixed solvent system of acetic acid and ethylene glycol. The presence of bimetals adds more complexity to the reaction mixture. The chemistry of the system is the main controlling factor that determines the final physical parameters of the nanostructure and the use of this combination of reagents with this phosphonate source has, never been attempted to synthesise a bimetallic material such as $LiMnPO_4$. The varied chemistry of the organometallic precursors, phosphonate and mixed solvents along with the synthetic parameters, together lends to the novelty of this study.

3.2. Experimental

This section will describe the experimental procedures to prepare $LiMnPO_4$ precursor from a modified novel sol-gel method. The synthesis transformations are monitored by liquid-state vibrational spectroscopic techniques (IR and Raman) at 24 hour intervals. Solid-state IR and Raman spectroscopic techniques are used to investigate the local structure of precursor material. The long-range order of the precursor is determined by Powder X-ray diffraction (PXRD) and the morphology by field emission scanning electron microscopy (FE-SEM). Lastly, the thermal decomposition profiles of the precursor in air and argon environments were examined by simultaneous Thermogravimetric/Differential Scanning Calorimetry and Evolved Gas Analysis (EGA) *via* a coupled Infrared Spectrometer (TGA/DSC/IR).

3.2.1. Materials

Anhydrous, lithium acetate ($LiOOCCH_3$, purity > 99.95% w/w), manganese (II) acetate tetrahydrate ($Mn[CH_3COO]_2 \cdot 4H_2O$), purity > 99.99% w/w), diethyl hydrogen phosphonate, DHP ($C_4H_{11}O_3P$, purity > 98% v/v), acetic acid (CH_3COOH, purity > 99.7%), and ethylene glycol ($C_2H_6O_2$, purity > 99.5%) used to prepare the lithium manganese phosphate ($LiMnPO_4$) precursor, were purchased from Sigma-Aldrich Pty. Ltd (Castle Hill, NSW).

3.2.2. Synthesis route to $LiMnPO_4$ precursor via modified sol-gel method

The $LiMnPO_4$ precursor was prepared using stoichiometric amounts of $LiOOCCH_3$ (13.45 g, 0.2 mol), $Mn(CH_3COO)_2 \cdot 4H_2O$ (50.00 g, 0.2 mol) and DHP (28.20 g, 0.2 mol) dissolved in a mixed solvent containing in excess 240 g of acetic acid and 250 g of ethylene glycol in a 1:1 molar ratio. This excess of solvent is necessary to increase the solubility of different metal-salts in the early stage of the process. A large quantity was prepared to have enough precursor material to produce a range of materials at higher temperatures.

The metal acetates were first dissolved in the solvent mixture by magnetic stirring at ambient temperature. To this mixture, the required amount of DHP was added under constant stirring. The resulting solution of organometallic compounds and solvent was placed in an oven set at 70°C for 96 hours in a closed reagent bottle. The solution was periodically stirred to aid chemical homogeneity. After this period had elapsed, the bottle was opened to start the evaporation process at ambient pressure of excess solvent at 70°C for several days. The resulting gel was then transferred to a crystallising dish and heated at 130°C in air to remove the unreacted volatile solvents and by-products. After this, the dried material was collected and ground in an agate mortar and drying at 130°C was continued. To ensure that it was consistently ground, the oven-dried precursor was dry balled milled at 400 rpm in a planetary ball mill (Fritsch pulverisette 6) for one hour, in an 80 mL zirconium oxide (ZrO_2) jar with ~100 g of 5 mm ZrO_2 balls. Finally, the material was placed in a vacuum oven and dried at 130°C to remove any residual solvent. The resulting material is the $LiMnPO_4$ precursor. An illustration of the process is shown below (Figure 3.2).

A separate sample was made in a smaller quantity (reduced by a factor of 10) to briefly look at the process occurring during the sol-gel process. This required a stoichiometric ratio of 0.02 moles for each of Li, Mn and P. An aliquot was taken every 24 hours and placed in a vial for liquid-state IR and Raman spectroscopic analyses.

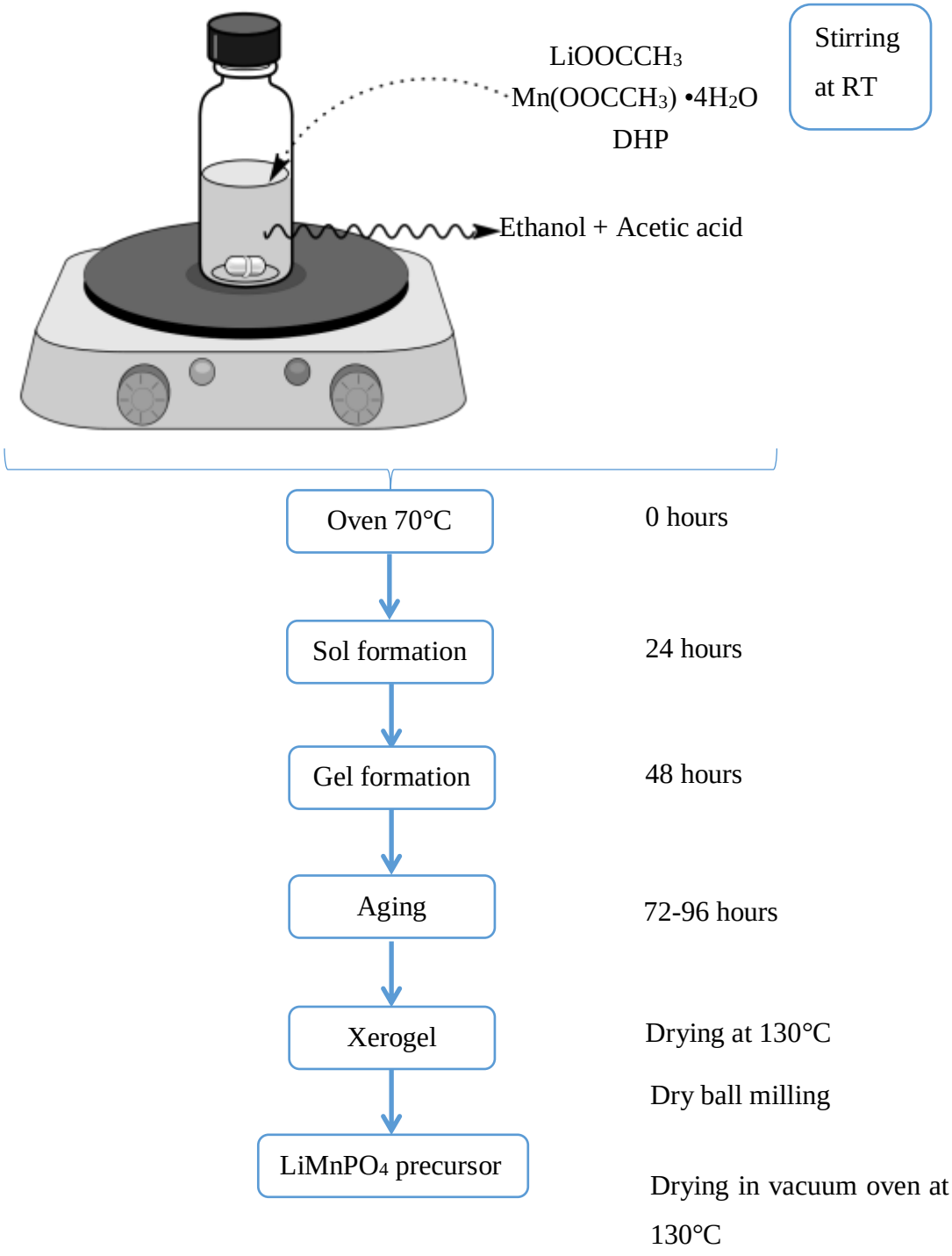

Figure 3.2: Schematic of the modified sol-gel procedure and steps along the sol-gel process to prepare $LiMnPO_4$ precursor.

3.3. Results and Discussion

This section deals with firstly a discussion and observation of the synthetic process followed by the liquid-state vibrational spectroscopic analysis of the sol-gel solution at 24-hour intervals. Next, the thermal decomposition studies of $LiMnPO_4$ precursor are discussed followed by the characterisation of the precursor using XRD, solid-state IR, Raman and FE-SEM. Finally, details on how the phase purity of the final $LiMnPO_4$ product can be modulated are described.

3.3.1. The synthesis process

The first step of the procedure involved dissolving the Li, Mn and P precursors into a solution of ethylene glycol and acetic acid. This resulted in a clear lightly pink solution (Figure 3.3b).

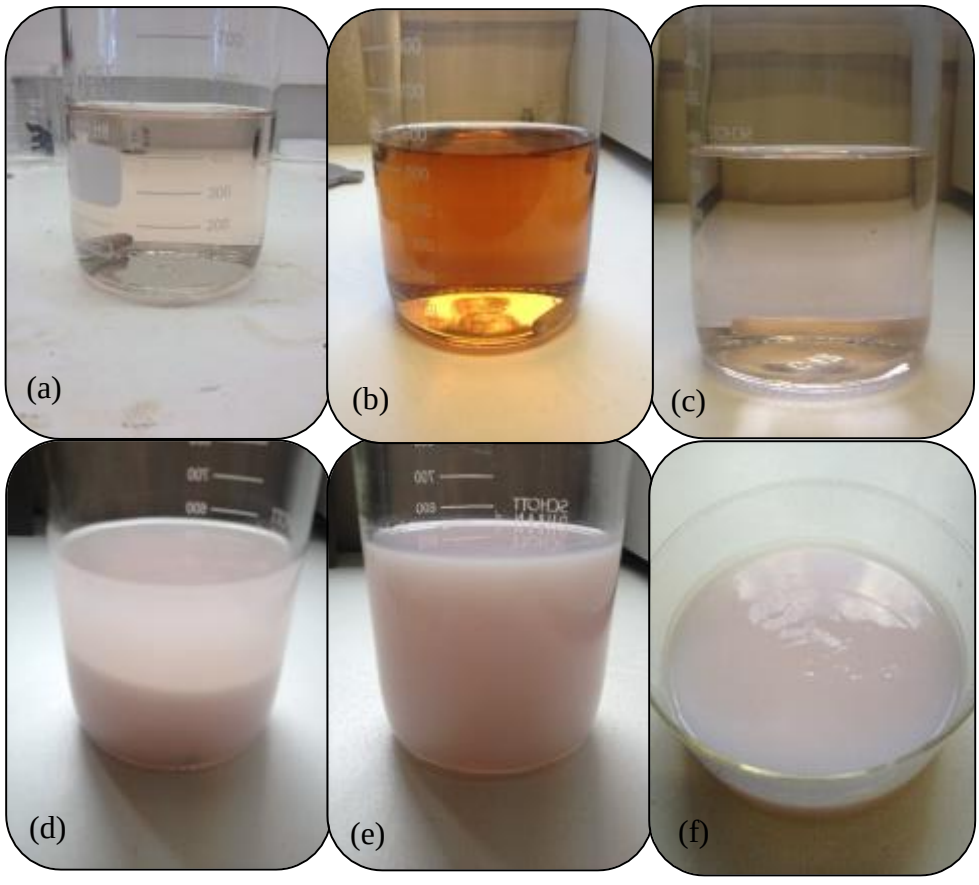

Figure 3.3: The sol-gel process. (a) Li, Mn and P precursors dissolved at RT; (b) at 70°C for 0 hours; (c) after 24 hours at 70°C; (d) after 48 hours at 70°C; (e) after 72 hours at 70°C; (f) gel transferred to crystallising dish after 96 hours.

When it was placed in the oven set at 70°C, the colour changed to brown which slowly disappeared after several hours (Figure 3.3b). After 24 hours at 70°C, the solution turned slightly murky (Figure 3.3c). After 48 hours, it can be clearly seen that a gel phase is starting to form (Figure 3.3d). After 72 hours an opaque gel phase has fully engulfed the liquid phase (Figure 3.3e). This was aged till 96 hours had elapsed and the bottle was opened to allow evaporation of the solvent. The high temperature aging step of the gel is important to complete ligand substitution and complex formation process [14, 15]. Next, the reaction vessel was opened and the solvent was allowed to evaporate at 70°C for 24 hours. Subsequently, it was transferred to a crystallising dish and dried at 130°C (Figure 3.3f). At first, contraction with removal of liquid from the pores of the gel occurs. Eventually, evaporation at 130ºC and at ambient pressure leads to so-called xerogels which has much greater shrinkage than aerogels. The dried samples were dry ball-milled giving a fine light brown powder as the $LiMnPO_4$ precursor material (Figure 3.4).

Figure 3.4: Dried at 130ºC, $LiMnPO_4$ precursor material produced with stoichiometric amounts of lithium, manganese and phosphorous chemicals. The material was ground at 400 rpm for 1 hour to produce a fine powder.

3.3.2. Vibrational spectroscopic analysis of evolution of the gel over 96 hours

A basic study of the constituents of the sol-gel process was done to get an idea of the type of compounds being formed. As such, 3 mL aliquots were taken from a separately prepared reaction vessel at 24-hour intervals up to 96 hours. The temperature of the reaction samples was reduced in a freezer (-5°C) to minimise the progress of any reactions. These samples were denoted as: LMP-0, LMP-24, LMP-48, LMP-72 and LMP-96, were analysed using liquid-state Fourier transform infrared and Fourier transform Raman spectroscopy (FT-IR and FT-Raman). The regression and evolution of the phosphorus peak(s) can be monitored over the sol-gel process. Though no definite structural conclusions can be drawn based exclusively on IR and Raman spectroscopic data of the sol-gel mixture samples, many of the band assignments can be rationalised through comparison with assignments determined on known structures. As such, IR and Raman spectra of the solid $LiOOCCH_3$, $Mn(CH_3COO)_2 \cdot 4H_2O$, and liquid DHP were also acquired.

3.3.2.1. FT-IR analysis

FT-IR spectroscopic analysis was carried out on a Bruker Vertex 70 FT-IR spectrometer to determine the fundamental vibrations of the sol-gel mixtures over a period of 96 hours, at 24-hour intervals. This technique uses the ability of bonds to respond or absorb radiation of frequency similar to its fundamental vibrations when irradiated with infrared radiation. This response is detected and interpreted into a graphical representation called a spectrum. The absorbance spectrum is preferred over the transmittance. The data was acquired at a resolution of 4 cm^{-1} from 4000 cm^{-1} to 400 cm^{-1} and averaged for 256 scans to establish an acceptable signal to noise ratio. A background spectrum is first obtained using the same parameters to account for any contribution from moisture (peaks at about 3600 cm^{-1} and 1600 cm^{-1}) and carbon dioxide (anti-symmetric stretch; doublet at around 2360 cm^{-1} and bending mode; sharp peak at 667 cm^{-1}) which is present in the atmosphere. The IR spectra were all baseline corrected and normalised to 2.0 absorbance units (a.u.).

The KBr disk method was used because of its wider spectral range in the mid-IR region: 400 cm^{-1} to 4000 cm^{-1} (in wavenumbers) or 2.5 µm to 25 µm (in wavelength; λ) to monitor the resonance of chemical bonds at lower frequencies. KBr is also optically transparent over this range of wavelengths so the absorption bands will only be from the analyte while offering superior resolution. Approximately 200 mg of spectroscopic grade KBr powder was used to prepare the pellets. For the powdered raw materials, approximately 1 wt. % of sample (2 mg) was mixed and ground with 99 wt. % KBr powder (200 mg) before being pressed into a pellet using a KBr hydraulic hand press. To minimise band distortion due to scattering of radiation the KBr and sample were ground thoroughly. The other samples were all in a liquid/gel phase, so two neat KBr pellets were prepared and the samples deposited in between them. The IR spectra for $LiOOCCH_3$, $Mn(CH_3COO)_2 \cdot 4H_2O$, and DHP are shown in Figure 3.5 along with the spectrum for LMP-0 in Figure 3.6 for comparison.

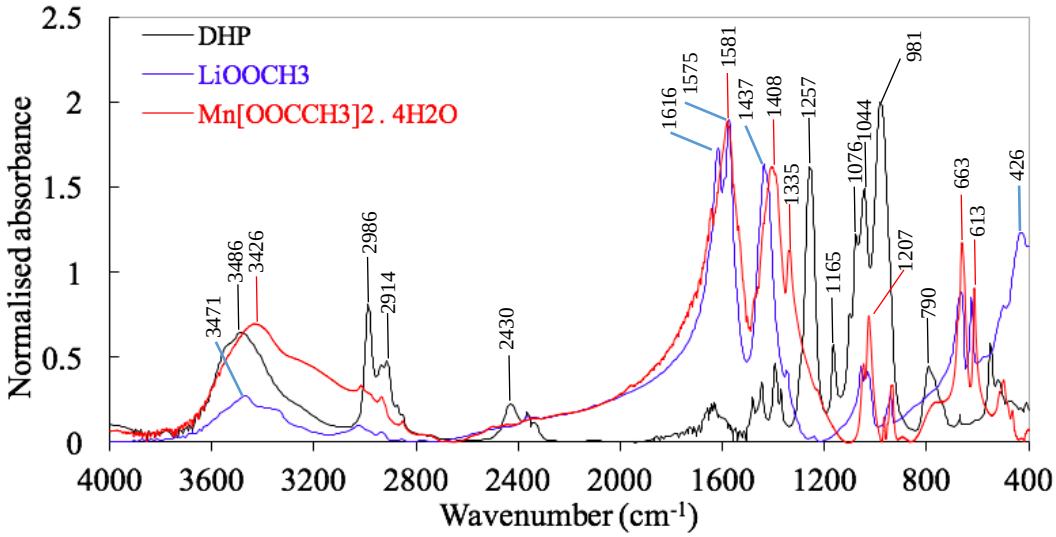

Figure 3.5: IR spectra of the Li, Mn and P precursors

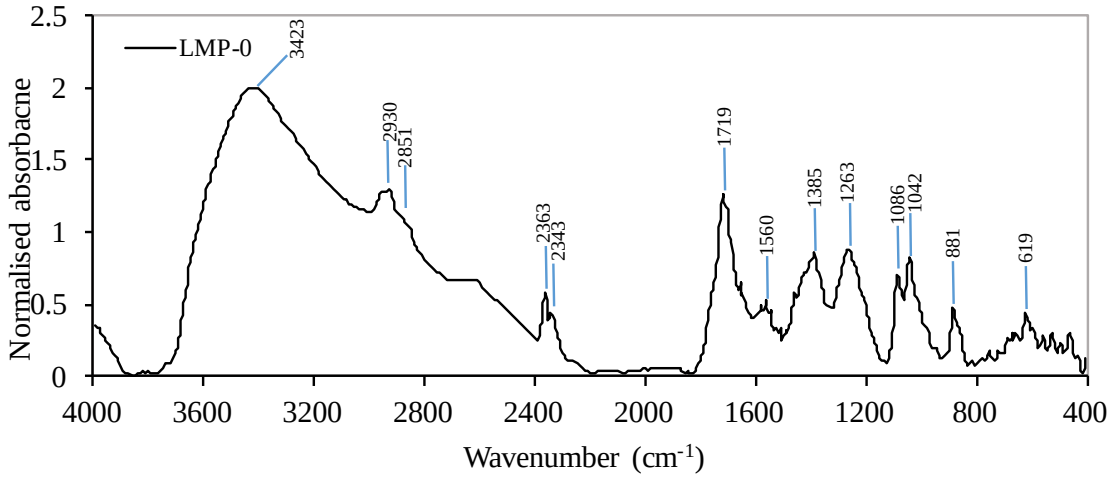

Figure 3.6: IR spectra of the freshly prepared mixture, LMP-0

Table 3.1: Assignment of IR bands to chemical bonds in LMP-0

Peak	Frequency range (cm^{-1})	Peak Assignment	Intensity	Mode
1	3423	O-H (H-bonded, broad)	strong	stretch
2	2930	C-H (CH_3 group, sharp)	strong	anti-symmetric stretch
3	2851	C-H (CH_3 group, sharp)	weak	symmetric stretch
4	2363	C-O (CO_2 group, sharp)	weak	anti-symmetric stretch
5	2343	C-O (CO_2 group, sharp)	weak	symmetric stretch
6	1719	C=O (sharp)	strong	stretch
7	1560	C=O (conjugation, sharp)	weak	stretch
8	1385	C=O (conjugation, sharp)	medium	stretch
9	1263	C-O (acid group, sharp)	medium	stretch
10	1086	C-O (alcohol, sharp)	medium	stretch
11	1042	C-O (alcohol, sharp)	medium	stretch
12	881	unassigned	medium	–
13	619	unassigned	weak	–

The solution mixture contained $LiOOCCH_3$, $Mn(CH_3COO)_2 \cdot 4H_2O$, and DHP as the raw materials in excess amounts of acetic acid and ethylene glycol. This combination produces a very complicated IR spectrum with overlapping peaks (Figure 3.6). The IR spectrum of LMP-0, where the solution was mixed at ambient temperature and before the reaction was subjected to 70°C, compares well to the IR spectra of the raw materials; however, the excess solvents conceal some of the bands. The structures of the compounds in the mixture are shown below for ease of comparison.

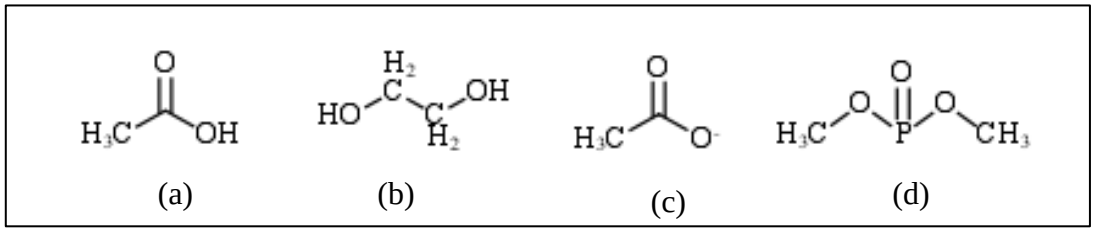

Figure 3.7: Structure of (a) acetic acid; (b) ethylene glycol; (c) acetate ion from the Li or Mn salt precursors; diethyl hydrogen phosphonate

The IR spectra of $LiOOCCH_3$ and $Mn(CH_3COO)_2 \cdot 4H_2O$ are almost identical with respect to the number of the IR active bands (Figure 3.5). It is important to note that the $LiOOCH_3$ and $Mn(CH_3COO)_2 \cdot 4H_2O$ were in solid form but in the sol-gel mixture it is dissolved. The IR spectra of the solid metal acetates can be different depending on the type of coordination of the acetate anion to the metallic ions and compared to the acetate ions dissolved in the mixture [18-20]. The interactions between them can also cause shifts in the frequencies [20]. The DHP spectrum shows the phosphorus containing characteristic bands such as P=O and P-H for comparison with LMP-0 (Figure 3.5).

Considering the LMP-0 spectrum, the strong and very broad peak centred at 3423 cm^{-1} is attributed to the O-H group which is a combination of the water in the solution, and the O-H groups of acetic acid and ethylene glycol. Also, the hygroscopic nature of the KBr pellets could also have contributed slightly to this broad peak. Typically, the acidic O-H group is very broad and relatively lower intensity from 2400 cm^{-1} to 3400 cm^{-1} centring at around 3000 cm^{-1} whereas the peak from alcohol O-H is less broad at a higher intensity with a more distinct peak and at higher frequencies (> 3400 cm^{-1}). This leads to the odd shaped, broad peak in LMP-0. Strongly bound O-H groups would have a very sharp band however; the broad shape here is typical of the presence of hydrogen bonding between the O-H groups. The presence of this acidic O-H group overlaps/superimposes the anti-symmetrical C-H stretching mode of CH_3 around 2930 cm^{-1}. The weaker vibration at around 2851 cm^{-1} is assigned to the respective symmetric C-H stretches that originate from the CH_3 groups of both acetate and ethoxy methyl. The weaker peaks of the anti-symmetrical and symmetrical stretch of C-H in methylene, CH_2 moiety from ethylene glycol and ethoxy groups are also expected to be within this range but cannot be seen here. The deformation mode of C-H which appears at 1340 cm^{-1}, 1346 cm^{-1} and 1369 cm^{-1} as a weak shoulder for $Mn(CH_3COO)_2 \cdot 4H_2O$, $LiOOCCH_3$ and DHP respectively is not detected here.

The weak sharp peaks at 2363 cm^{-1} and 2343 cm^{-1} are typical of gaseous CO_2. Due to relatively low concentration of DHP, it is difficult to assign the characteristic stretches due to the P-H bond. However, when comparing with the spectrum of DHP (Figure 3.5), the same peaks which has been assigned to CO_2 (2363 cm^{-1} and 2343 cm^{-1}) are present with an additional peak (weak, broad) at 2430 cm^{-1}. This band is typical of the P-H bond. This peak cannot be distinguished in the reaction mixture because of the very broad band of the carboxylic acid O-H group.

The fundamental frequency of vibration for acetic acid is the carbonyl stretching mode, C=O. This intense stretching mode of the carbonyl group is attributed to the peak at around 1719 cm^{-1}. The possible effect of resonance and conjugation on the acetate anion can further complicate the location of the carbonyl peaks. According to Keeler [21], the carboxylate anion gives two absorptions at around 1575 cm^{-1} and 1430 cm^{-1}. The formation of mono-dentate or bidentate chelates with the present metal ions (Li^{+} and Mn^{2+}) in solution is also known to modulate the spectral positions of those peaks. Hence, the peaks at 1560 cm^{-1} and around 1400 cm^{-1} could account for this phenomenon. The peak at 1263 cm^{-1} may possibly be the C-O stretch of carboxylic acid although the frequency of its stretching mode is variable and difficult to assign. Considering that DHP has an absorbance band at 1256 cm^{-1} attributed to the P=O stretching mode of the phosphonate group, it is also possible at 1263 cm^{-1} could belong to the P=O bond. Due to the amount of the acetic acid, it is more likely that this band is a result of the C-O stretching mode which overlaps the P=O band.

DHP also has a weak peak at around 1165 cm^{-1} which is attributed to the weak P-O stretch where the P-O is attached to a methyl group ($-CH_3$). This weak peak is not present in the combined spectrum. DHP has two relatively strong bands at 980 cm^{-1} and 1043 cm^{-1} possibly attributed to stretching modes of the P-O group. However, due to the greater quantity of solvent in the mixture, the C-O stretches of alcohol appearing at 1086 cm^{-1} and 1042 cm^{-1} obscure it. Many other additional bands appear usually at lower wavenumbers because of the appearance of overtones, combinations of fundamental frequencies, coupling interactions between the fundamental vibrations and overtones or combination bands resulting from Fermi resonance.

The reaction was carried out in a closed system at 70°C for 96 hours. The IR spectra obtained from aliquots taken at 24 hours, 48 hours, 72 hours and 96 hours are shown in Figure 3.8.

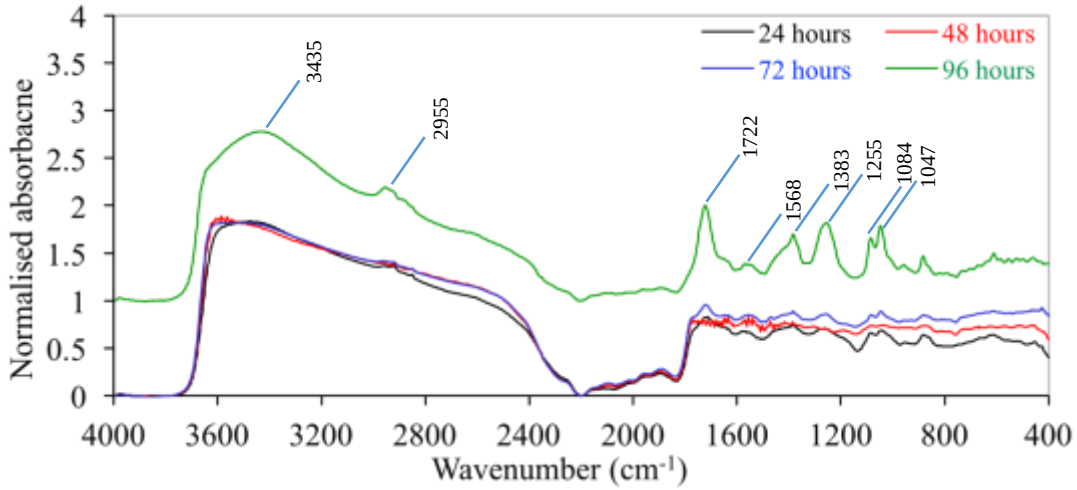

Figure 3.8: IR spectra of the sol-gel system held at 70°C for 24 hours (LMP-24), 48 hours (LMP-48), 72 hours (LMP-72) and 96 hours (LMP-96). For clarity, the latter spectrum is stacked on top of the other overlaid spectra.

Table 3.2: Assignment of IR bands to chemical bonds in LMP-24, LMP-48, LMP-72 and LMP-96.

Peak	Frequency range (cm^{-1})	Peak Assignment	Intensity	Mode
1	3435	O-H (H-bonded, broad)	strong	stretch
2	2955	C-H (CH_3 group, sharp)	weak	anti-symmetric stretch
3	1722	C=O (acid group, sharp)	medium	symmetric stretch
4	1568	C=O (conjugation, sharp)	weak	stretch
5	1383	O-H (broad)	medium	deformation
6	1255	C-O (acid group, sharp)	medium	stretch
7	1084	C-O (alcohol group, sharp)	medium	stretch
8	1047	C-O (alcohol group, sharp)	medium	stretch

The IR spectra shown in Figure 3.8 are almost identical. The peaks for the samples from 24 to 72 hours are fairly broad with the peaks of lower intensity. At 96 hours, the peaks are more intense and are easily identified. As discussed above, the strong broad peak at 3435 cm^{-1} is due to the O-H bond of carboxylic acid, alcohol and glycol functional groups, similar to that of LMP-0. However, there would be contribution from the water molecules produced during the esterification by-reactions between acetic acid and ethylene glycol and perhaps between the acetic acid and the ethoxy groups from DHP. The anti-symmetrical and symmetrical bands of C-H appear at around 2955 cm^{-1}. The doublet at 2363 cm^{-1} and 2343 cm^{-1} of gaseous CO_2 is not present here as well as the P-H bond due to the broad O-H band. The strong stretching mode of the carboxylic acid carbonyl group, C=O, is at 1722 cm^{-1}. The medium deformation of the O-H group is present here as well at 1383 cm^{-1}. The peak at 1255 cm^{-1} is most probably the carboxylic acid C-O stretch or the stretching mode of the P=O group which appears at a similar frequency. The C-O stretches of alcohol appear at 1084 cm^{-1} and 1047 cm^{-1}.

Aside from minor shifts in the absorbance frequencies, the IR spectra of the samples LMP-0, LMP-24, LMP-48, LMP-72 and LMP-96 are similar because of the presence of the solvents which remain even after the formation of the gel. This is expected as the gel ‘traps’ the solvent within its network and the solvents have strong fundamental vibrations in the infrared region. Visual observation of the sol-gel reaction (Figure 3.3) clearly shows the formation of the gel. However, due to the intense bands from the solvents in the reaction (acetic acid and ethylene glycol) which were added in excess, any co-ordination of metals to the phosphonates could not be determined at this stage from IR spectroscopy.

3.3.2.2. Raman analysis

FT-Raman spectroscopic analysis was carried out on a Bruker Vertex 70 with an attached Ram II module equipped with a liquid nitrogen cooled germanium (Ge) detector allowing a spectral range of 3600 cm^{-1} to 50 cm^{-1} (Stokes shift). Raman spectra was acquired by exposing the samples to 250 mW of the 1064 nm line of a Nd:YAG laser as the excitation source at a resolution of 4 cm^{-1} over 256 scans. All the acquired data were baseline corrected and normalised to a Raman intensity of 2.0. The liquid sol-gel samples are held in a special quartz (non-fluorescence glass) cuvette with a mirrored back.

This technique relies on the scattering of light by vibrating molecules and relies inherently on the change in polarisation in contrast to IR spectroscopy which relies on the absorption of light by vibrating molecules and the change in dipole moments [22, 23]. Generally, molecular bonds that have large changes in polarisation are strong Raman scatterers and usually have no or lower change in dipole moments. Consequently, these techniques can provide complimentary data. The advantage of using Raman in this context is the relatively weak stretches of the O-H group which appear strong and broad in an IR spectrum as indicated in Section 3.2.2.1.

The Raman spectra for $LiOOCH_3$, $Mn(CH_3COO)_2 \cdot 4H_2O$ are shown in Figure 3.9. The spectra for the time dependant sol-gel mixtures over 96 hours at 70ºC are shown in Figure 3.10.

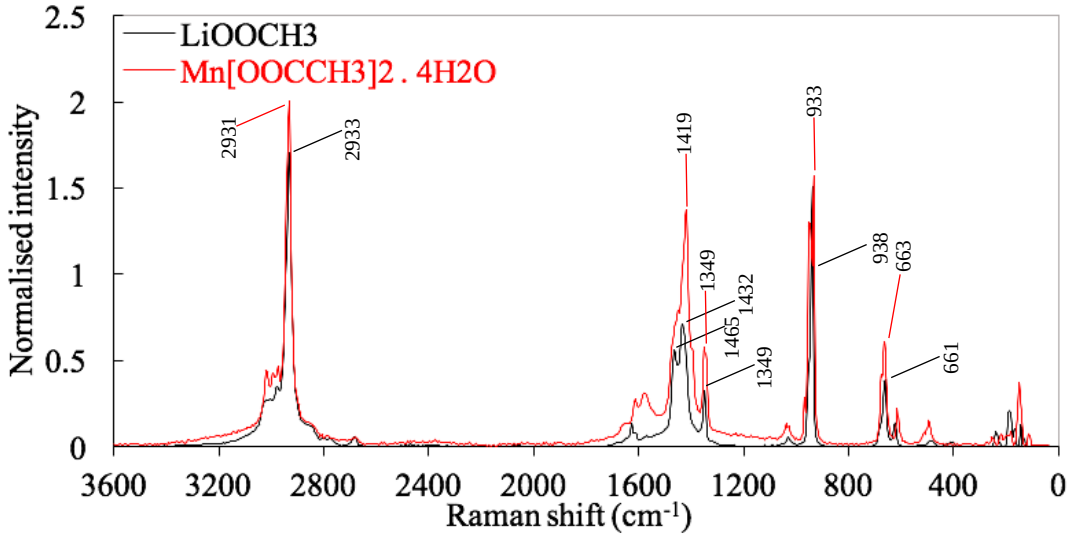

Figure 3.9: Raman spectra of the Li and Mn precursors.

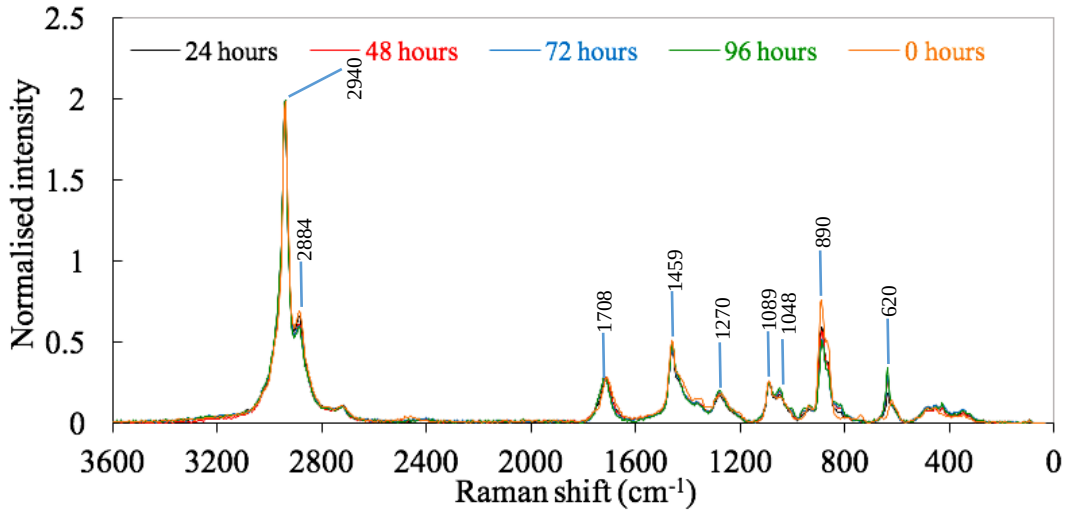

Figure 3.10: Raman spectra of the sol-gel system as 0 hours (LMP-0), 24 hours (LMP-24), 48 hours (LMP-48), 72 hours (LMP-72) and 96 hours (LMP-96).

Table 3.3: Assignment of Raman bands to chemical bonds in LMP-24, LMP-48, LMP-72 and LMP-96.

Peak	Frequency range (cm^{-1})	Peak Assignment	Intensity	Mode
1	2940	C-H (CH_3 group, sharp)	strong	symmetric stretch
2	2884	C-H (CH_3 group, shoulder)	weak	anti-symmetric stretch
3	1708	C=O (sharp)	weak	stretch
4	1459	C-H (CH_3 group, sharp)	medium	deformation
5	1270	unassigned	weak	–
6	1089	C-O (sharp)	weak	stretch
7	1048	C-O (sharp)	weak	stretch
8	890	unassigned	medium	–
9	620	unassigned	weak	–

The symmetrical aliphatic ν(C-H) stretching vibrations are shown at 2940 cm^{-1} with the weaker anti-symmetrical ν(C-H) at 2884 cm^{-1}. The peak at 1459 cm^{-1} is the anti-symmetric deformation of C-H. The weak band at 1708 cm^{-1} is characteristic of C=O stretching. The stretching vibrations of C-O are assigned to the weak band at 1089 cm^{-1} and 1048 cm^{-1}. The P-H stretch would typically be between 2450 cm^{-1} and 2270 cm^{-1} [23]. This peak was not detected in the corresponding IR spectra but seems to give rise to two very weak bands between 2400 and 2500 cm^{-1}. The weak band at 1254 cm^{-1} may be attributed to the P=O group. The effect of having a complex solution such as this means making assignments is extremely difficult and the relatively large amounts of solvents conceal any phosphorous related peaks. Overall, the Raman spectra are consistent with the IR spectra in Section 3.3.2.1.

3.3.3. Characterisation of the $LiMnPO_4$ precursor dried at 130°C

As mentioned, the material obtained after 96 hours at 70°C in a closed system was dried at 130°C to remove the excess solvent. The material was dry ball-milled and dried further in a vacuum oven to remove any remaining residual solvents. The $LiMnPO_4$ precursor was characterised by solid-state IR and Raman spectroscopy, X-ray diffraction and scanning electron microscopy.

3.3.3.1. Interpretation of the vibrational characteristics of the $LiMnPO_4$ precursor using solid-state infrared spectroscopy

The same procedure as described in Section 3.3.2.1 was used to acquire the IR spectrum of $LiMnPO_4$. This spectrum is shown in Figure 3.11 below.

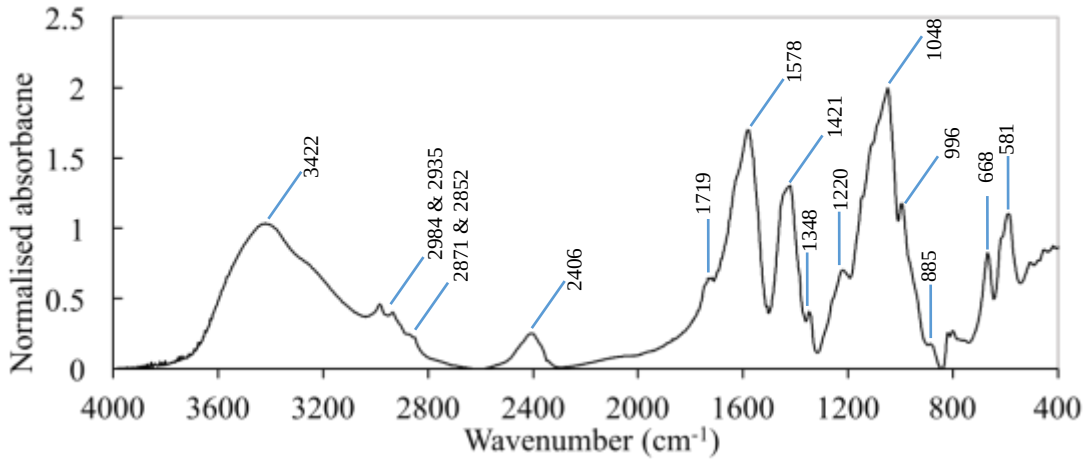

Figure 3.11: IR spectra of the $LiMnPO_4$ precursor dried at 130°C.

Table 3.4: Assignment of IR bands of the $LiMnPO_4$ precursor dried at 130°C.

Peak	Frequency range (cm^{-1})	Peak Assignment	Intensity	Mode
1	3422	O-H (H-bonded, broad)	strong	stretch
2	2984	C-H (CH_3 group, sharp)	weak	anti-symmetric stretch
3	2935	C-H (CH_3 group, shoulder)	weak	symmetric stretch
4	2871	C-H (CH_3 group, sharp)	weak	anti-symmetric stretch
5	2852	C-H (CH_3 group, shoulder)	weak	symmetric stretch
6	2406	P-H (broad)	medium	stretch
7	1719	C=O (acid group, sharp)	weak	stretch
8	1578	C=O (conjugation, sharp)	strong	anti-symmetric stretch
9	1421	C-O (acid group, sharp)	strong	symmetric stretch
10	1348	C-H (CH_3 group, shoulder)	weak	deformation
11	1220	P=O (shoulder)	weak	stretch
12	1048	P-O-C (sharp)	strong	anti-symmetric stretch
13	996	P-H (shoulder)	weak	symmetric stretch
14	885	unassigned	weak	–
15	668	unassigned	medium	–
16	581	unassigned	medium	–

The broad band at 3422 cm^{-1} is attributed to the O-H group of alcohol and acetic acid. The peak is less broad here than in the wet sample at 96 hours (Figure 3.8). This suggests that this band is mainly consists of O-H vibrations of hydrogen bonded hydroxyl groups, which are sharper with a distinctive maximum unlike the O-H band of carboxylic acid which is very broad ranging from 2400 cm^{-1} to 3400 cm^{-1}. Hence, the aliphatic C-H stretching modes can be observed here. Also, the ratio of the O-H band compared to the other bands has decreased significantly unlike in Figure 3.8, where it was the most prominent peak. There could also be a small amount of adsorbed water in the sample. The peaks appearing at 2984 cm^{-1}, 2871 cm^{-1}, 2935 cm^{-1} and 2852 cm^{-1} are assigned to the anti-symmetrical and symmetrical stretches of the C-H of methyl and methylene moieties, respectively.

The doublet at 1578 cm^{-1} and 1421 cm^{-1} are attributed to the anti-symmetrical and symmetrical stretches of the C=O of the carboxylate group participating in various chelates. Usually, C=O has an intense band between 1690 cm^{-1} to 1760 cm^{-1} typical of monomeric carboxylic acids or free carboxylate ligands. IR spectra of samples obtained during the sol-gel reaction had this peak at around 1719 cm^{-1} (Figure 3.6 and 3.8). However, when dried at 130°C to remove the solvents, the bands are split similar to the IR spectra of solid $LiOOCCH_3$ and $Mn(CH_3COO)_2 \cdot 4H_2O$ (Figure 3.5). This doublet for the anti-symmetrical and symmetrical C=O stretching mode appears at 1575 cm^{-1} and 1437 cm^{-1} for $LiOOCCH_3$ and at 1581 cm^{-1} and 1408 cm^{-1} for $Mn(CH_3COO)_2 \cdot 4H_2O$, respectively.

This interesting observation is consistent with formation of metal complexes with the carboxylate ligands. It is known that the coordination *via* the formation of metal carboxylate complexes can influence the wavenumber and the difference in wavenumber of anti-symmetrical and symmetrical carboxylate stretching vibrations [24, 25]. Coordination of a carboxylic ligand to a metal ion can also lead to the appearance of new bands and splitting of existing ones due to lowering of the symmetry. Carboxylate ligands can form complexes with metals in different bonding modes which include ionic type interactions, monodentate coordination, bidentate chelating or the particularly strong tendency for bidendate bridging interactions [24, 25].

Nakamoto [25] proposed that the difference between the wavenumbers of the anti-symmetric and symmetric stretch for the carboxylate peaks could be used as an indication of the nature of the bonding mode in a carboxylate metal complex ligand (Figure 3.12). He indicated that most literature reports which investigated the spectral properties of carboxylates concur that a difference ranging from 150 to 180 cm^{-1} between the anti-symmetric and symmetric vibrations of C=O-O correspond to bridging bidentate carboxylate ligands interactions [25].

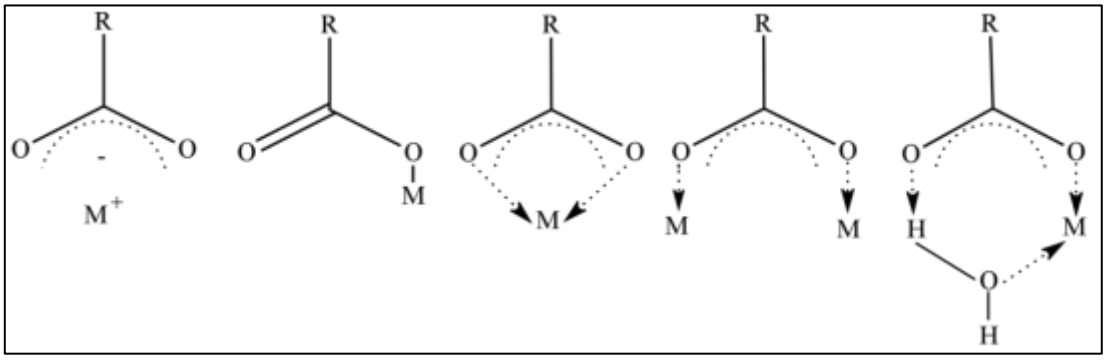

Figure 3.12: Types of interactions between a carboxylate ligand and metal ion with respective differecnes in wavenumbers between the anti-symmetric and symmetric C=O bands. (a) ionic ~151 cm^{-1}; (b) monodentate: ~260 cm^{-1}; (c) bidentate chelating ~102 cm^{-1}; (d) bidentate bridging: ~163 cm^{-1}; and (e) pseudo-bridging: ~197 cm^{-1} [15, 20].

The difference between the anti-symmetric and symmetric bands (1578 cm^{-1} and 1421 cm^{-1} respectively) of C=O bands here is 157 cm^{-1} falling within this range suggesting that this type of interaction is also present here (Figure 3.12 d). In the IR spectra, the lowering of the acidic O-H band, further confirms the deprotonation and complexation of the carboxylate group. Furthermore, looking at the shoulder at 1719 cm^{-1} suggests the presence of some free or uncomplexed carboxylate acid/acetate that remain within the precursor material. This may be unlikely since any free or unbound acids are expected to be lost during the rigorous drying process to prepare the precursor. It is plausible that another type of chelate is also present, as evidenced by the shoulder at 1348 cm^{-1}. This difference can be attributed to the possible presence of monodentate interactions between the carboxylate ligand and metal ion [20]. Consequently, that would mean the formation of at least two different chelates are present in the sample.

The peak at 1348 cm^{-1} is typical of the deformation mode of C-H. Though this does provide evidence of the formation of M-carboxylate complexes where M = Li or Mn in the precursor, the specific type of interaction is not absolute. Formation of these complexes is however important to allow better homogeneity and lower the temperature of synthesis of the final $LiMnPO_4$ product which thereby affords a shorter diffusion path length to crystalline $LiMnPO_4$ when compared to solid-state reactions. Further information on the nature of the $LiMnPO_4$ precursor by observing the stretching and deformation vibrations of the P-H bond. The peak at 2406 cm^{-1} is typical of the stretching vibration of the P-H bond [26]. The existence of one peak in this region (2222 cm^{-1} to 2505 cm^{-1}), suggest the presence of only one conformation of the phosphonate group [15, 27]. The deformation modes of P-H are usually around 990 cm^{-1}, however, P-O-C stretches are also found in this region and can overlap with this band [15, 27]. For this reason, it is difficult to discuss any structural considerations using the P-H bands.

The P=O stretching vibration would give a strong band between 1140 cm^{-1} to 1320 cm^{-1} for most P=O containing compounds and specifically for free phosphonate ligands at around 1250 cm^{-1} to 1275 cm^{-1} [15, 27]. This band is very strong in DHP at 1256 cm^{-1} (Figure 3.5), consistent with uncomplexed phosphonate ligands as expected. In the precursor, on the other hand, a relatively weak shoulder is present at 1220 cm^{-1}. This suggests that the majority of the phosphoryl groups participate in complexes [15]. Interestingly, the bands at 996 cm^{-1} (ν_1; symmetrical), 1048 cm^{-1} and the shoulder at around 1110 cm^{-1} (ν_3; anti-symmetrical) are indicative of the P-O-(C) and C-O-(P) stretching vibrations of partially crystalline hydrogen phosphonates. The complicated mixture and overlapping of peaks makes it difficult to differentiate between both these types of bonds. The shape of the bands can give an indication of the order in the material: amorphous or crystalline. Here, the shape of these bands, that is, how broad or narrow it is, indicate that the precursor is partially crystalline in nature. Vibrations related to crystalline PO_4^{3-} group also appear in this region, however, this is unlikely at the low temperatures of 130°C at which the precursor was dried [28-35]. The band at 885 cm^{-1} is typical of the wagging motion of the P-H band [27].

The broadness of the bands indicates the presence of organic residues or formation of nanocrystalline material which is consistent with the low temperature used. However, the splitting of the bands such as this is possible at higher temperatures for solid-state methods whereas at lower temperatures the P-O stretching and bending modes are relatively broad [36]. The number and positions of the bands are influenced by many factors. In the case of crystalline materials, it can observe the influence of crystalline field resulting in the band splitting—some bands can be split into two or more bands. Positions of the bands also depend on the kind of cations surrounding the phosphonate group [37].

The P-O stretching vibration bands are broad, indicating that the phosphonate groups and metal ions inside the sample are not as well oriented, coordinated or chemically bounded to each other (amorphous character) compared to highly crystalline material. With increasing temperature, however, these bands are expected to split into more bands as the phosphonate is transformed into the phosphate group (PO_4^{3-}). The peaks below 500 cm^{-1} could be related to translational modes of Li and Mn. The rest of the peaks could include the deformation modes but are difficult to assign due to the complicated constituents of the precursor. In summary, the IR spectrum of the precursor gives evidence of the formation of metal complexes to both phosphonate and carboxylate species and the stable presence of phosphorous within the material.

3.3.3.2. Interpretation of the vibrational characteristics of the $LiMnPO_4$ precursor using Raman spectroscopy

Figure 3.13 shows the Raman spectrum of $LiMnPO_4$ precursor dried at 130°C excited by the 1064 nm laser.

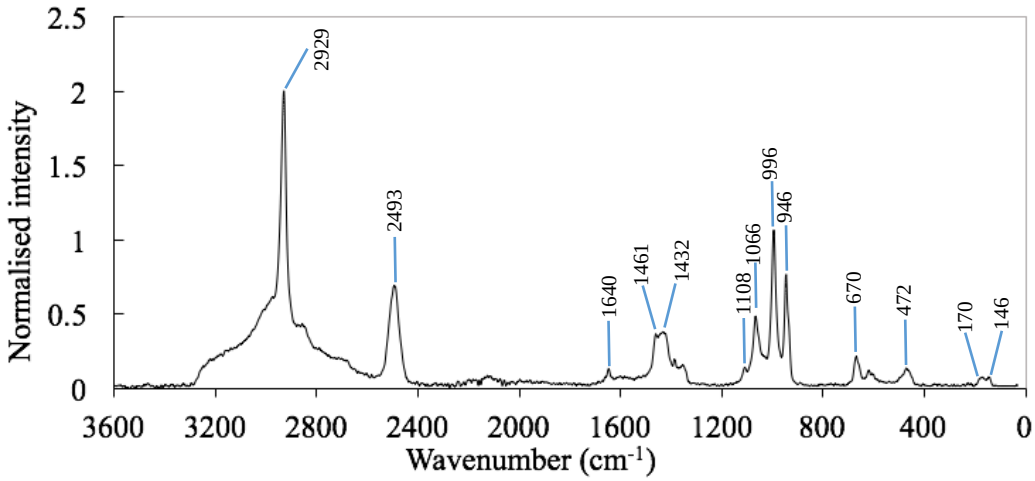

Figure 3.13: Raman spectra of the $LiMnPO_4$ precursor dried at 130°C.

Table 3.5: Assignment of Raman bands of the $LiMnPO_4$ precursor dried at 130°C.

Peak	Frequency range (cm^{-1})	Peak Assignment	Intensity	Mode
1	2929	C-H (CH_3 group, sharp)	strong	symmetric stretch
2	2493	P-H (broad)	medium	symmetric stretch
3	1640	O-H (broad)	weak	bending
4	1461	C=O (sharp)	weak	symmetric stretch
5	1432	C=O (sharp)	weak	anti-symmetric
6	1108	P=O (shoulder)	weak	stretch
7	1066	P=O (sharp)	medium	stretch
8	996	P=O (sharp)	medium	stretch
9	946	P=O (sharp)	medium	stretch
10	670	P-O (broad)	weak	bending/rocking
11	472	P-O (broad)	weak	bending/rocking
12	170	Mn-O or Li-O	weak	translational
13	146	Mn-O or Li-O	weak	translational

The symmetrical band of aliphatic ν(C-H) stretching vibrations is seen as sharp band at 2929 cm^{-1}. The slightly broad and medium band at 2493 cm^{-1} is consistent with the stretching mode of P-H [15]. This peak is stronger in the Raman spectrum than the corresponding IR spectrum and is consistent with the IR data indicating the presence of one conformation of the phosphonate group. The very weak broad band at 1640 cm^{-1} is typical of the bending mode of δ(H_2O). The bands around 1461 cm^{-1} and 1432 cm^{-1} could possibly be a combination of weak stretching vibrations of the ν(C=O) group participating in two types of chelates, which are perturbed by the bending modes of δ(C-H) moieties.

The peaks at very low wavenumber of 146 cm^{-1} and 170 cm^{-1} are typical of lattice vibrations and indicate the tentative presence of Mn-O or Li-O bonding modes consistent with the IR data depicting the formation of a metal carboxylate-phosphonate precursor material. Translational vibrations of MnO_6 and LiO_6 octahedra are observed in the low-wavenumber region (below 300 cm^{-1}) [38]. The identification of partially crystalline phosphonate in the IR spectrum is supported here in the Raman spectrum. The resonances found from 1108 cm^{-1} to 946 cm^{-1} can be attributed to the P-O group [15]. The bands between 400 cm^{-1} to 700 cm^{-1} are attributed to bending and rocking modes of the P-O units. Overall the Raman spectrum is in agreement with the IR data and shows evidence for the formation of complexes.

3.3.3.3. Powder X-ray diffraction

Powder x-ray diffraction (PXRD) was done is used to determine if there is any long-range order in the precursor. The X-ray powder diffraction of the precursor was measured by a Bruker D8 Advance Powder Diffractometer using CuKα (λ = 1.5618 Å) radiation as the x-ray light source with applied voltage and current of 40 kV and 40 mA respectively. The Diffractometer is equipped with a LynxEye detector which is much faster and sensitive than a scintillation counter.

The XRD patterns were measured in Bragg-Brentano geometry, in which the intensity of the diffracted X-ray is detected as a function of the diffraction angle of a detector. The diffraction patterns were recorded over the angular range, 2θ, of 5° to 60° with 0.02° per step and a step time of 5 seconds per step. All patterns were collected at room temperature. The pattern obtained is a plot between intensity versus 2θ angle. Raw data processing and crystalline phase compositions were determined using Bruker's Eva software and the Powder Diffraction File (PDF) database from the International Centre for Diffraction Data (ICDD) respectively.

Figure 3.14 shows the X-ray diffraction pattern of the $LiMnPO_4$ precursor which was dried at 130°C. It demonstrates several broad peaks indicating that it is partially crystalline in nature, perhaps due to ordered nature of the metal phosphonates (see Figure 3.1). However, it is likely that the crystalline phases present are related to the diffraction patterns of more than one crystalline phase [14-16]. This is supported by the IR and Raman data which also indicate the presence of crystalline phase in the precursor.

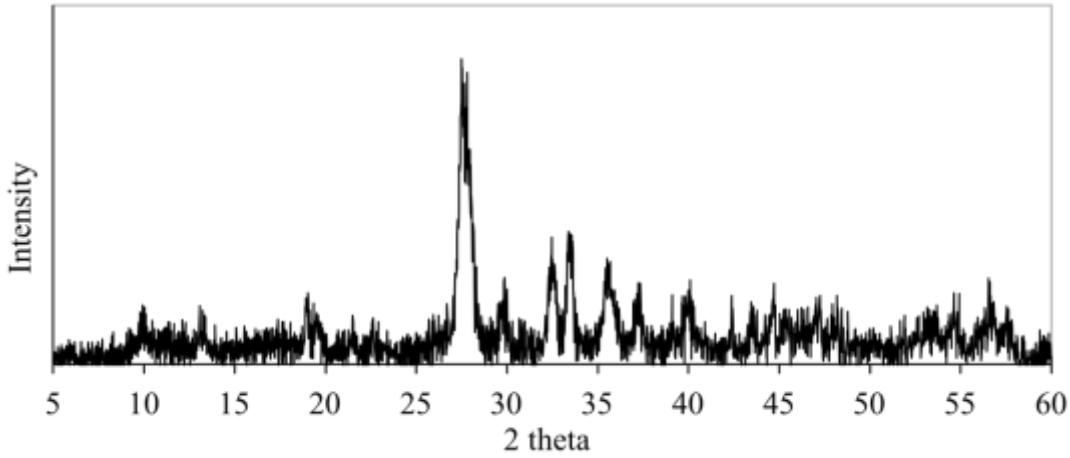

Figure 3.14: XRD pattern of the $LiMnPO_4$ precursor dried at 130ºC. The peaks can not be assigned to any pattern.

The presence of metal acetate chelates detected by the IR spectroscopy in the spectral range 1600 – 1350 cm^{-1} and the presence of medium intensity peak at 2493 cm^{-1} detected by the Raman spectroscopy suggests that the phosphonate structure is stable at 130°C. This, X-ray diffraction data and vibrational spectra suggest that while the nature of the crystallites is unknown it is most likely to be mixed phase acetate-phosphonates containing Li^+ and Mn^{2+} in unknown ratio. Therefore, it can be concluded that the precursor has both amorphous and nanocrystalline components and heat-treatment in air at 130°C is not sufficient to induce decomposition of the phosphonate precursor and crystallisation of the phosphate product, $LiMnPO_4$. The DSC/TGA data demonstrates that mixed metal acetate-phosphonates are stable to about 250 – 300°C depending on the atmosphere used (Section 3.3.4).

3.3.3.4. Morphology

The morphology of the precursor was examined by a field-emission electron microscope (JEOL 7001F) (Figure 3.15).

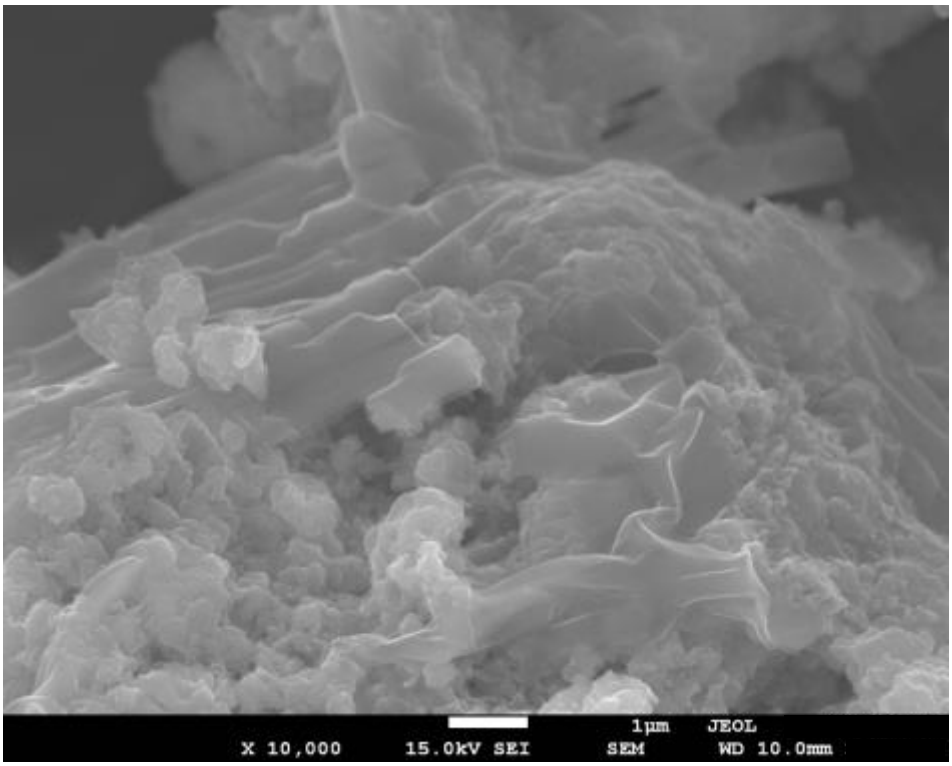

Figure 3.15: SEM image of the precursor at 10,000x magnification

The SEM image of the precursor at 10,000x magnification shows that the particle morphology is mostly plate-like stacked on top each other.

3.3.4. Thermal analysis

The decomposition behaviour of the $LiMnPO_4$ precursor dried at 130ºC in air and argon and the evolution of the gaseous products during heating was investigated by a NETZSCH Jupiter STA 449C Simultaneous Differential Scanning Calorimeter/Thermogravimetric Analyser (DSC/TGA). To investigate the molecular state of the IR active gaseous products of decomposition, the thermoanalyser was connected to a temperature-regulated Bruker TGA IR gas cell (120 mm long with an internal diameter of 8 mm) attached to a Bruker Vertex 70 mid IR spectrometer *via* a 0.8 m long heated transfer line with an external diameter of 3.5 cm and an internal diameter of 2 mm. The gas cells are equipped with a liquid nitrogen (LN_2) cooled Mercury-Cadmium-Telluride (MCT) detector which has higher sensitivity and better linearity than standard Deuterated Tri Glycine Sulfate (DTGS) detectors. Both the gas cell and transfer line are kept at 200°C to minimize condensation of the volatile decomposition products.

3.3.4.1. Decomposition profile of $LiMnPO_4$ precursor in dynamic air and argon atmospheres

Approximately 10 mg of sample was placed in an alumina (Al_2O_3) crucible covered using a lid with a hole. These crucibles are ideal for the required measurement because it has high melting point and good chemical stability. An empty crucible is placed as the reference which is required for DSC measurements. The sample carrier was equipped with an S-type thermocouple (Pt/PtRh) with a temperature range of 25ºC to 1650ºC. The $LiMnPO_4$ precursor was heated non-isothermally from ambient temperature to 800ºC at a heating rate of 10ºC min^{-1} under a dynamic air (purity > 99.999%) or argon (purity > 99.999%) atmosphere of 25 mL min^{-1} with an isothermal step at 110ºC for 15 minutes to remove absorbed moisture during sample handling.

Prior to this, a baseline correction measurement was performed using the same temperature program and gas atmosphere with empty Al_2O_3 crucibles in both the sample and reference pans. During the evolved gas analysis, spectral resolution was 2 cm^{-1} and 64 interferograms were co-added for each IR spectrum. Prior to each measurement, the sample chamber was evacuated three times to 10^{-2} Pa and then purged with the respective gas required.

The thermal data obtained after heating the sample in air and argon is shown in Figure 3.16 and 3.17. For clarity, the graphs are shown separately. The TGA data (blue) represents the mass change of the sample as a function of temperature in air or inert atmosphere. The DSC component (red) supplements the TGA data by providing information on phase changes in the sample that involve absorption (endothermic reaction) or evolution of heat (exothermic reaction) as a function of temperature. This is accomplished by manipulating the heat-flow between the sample and the reference in order to keep both at the same temperature.

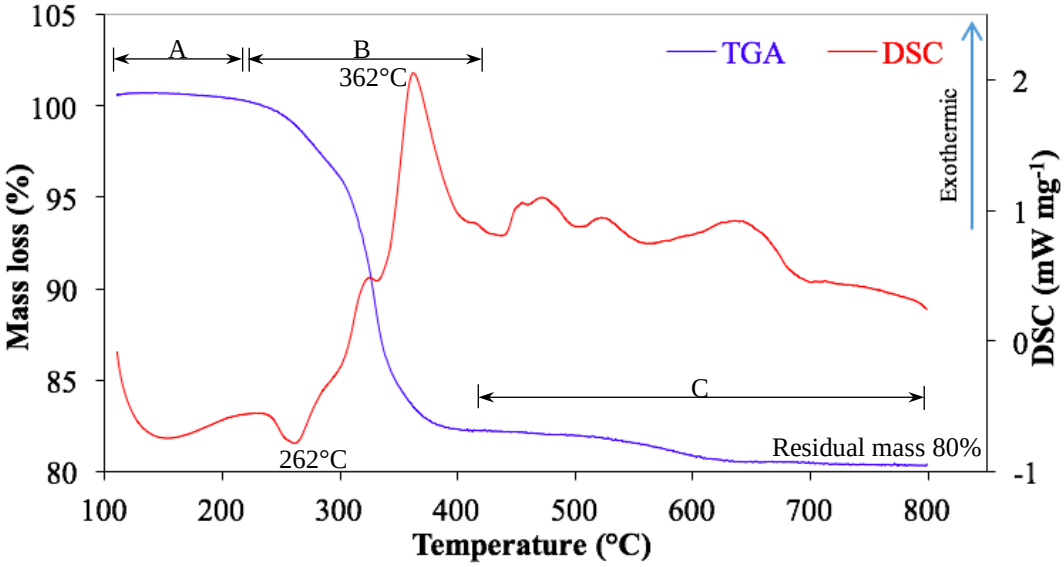

Figure 3.16: Non-isothermal TGA-DSC traces of the $LiMnPO_4$ precursor heated in air from ambient to 800°C. A, B and C represent the three distinct mass loss steps.

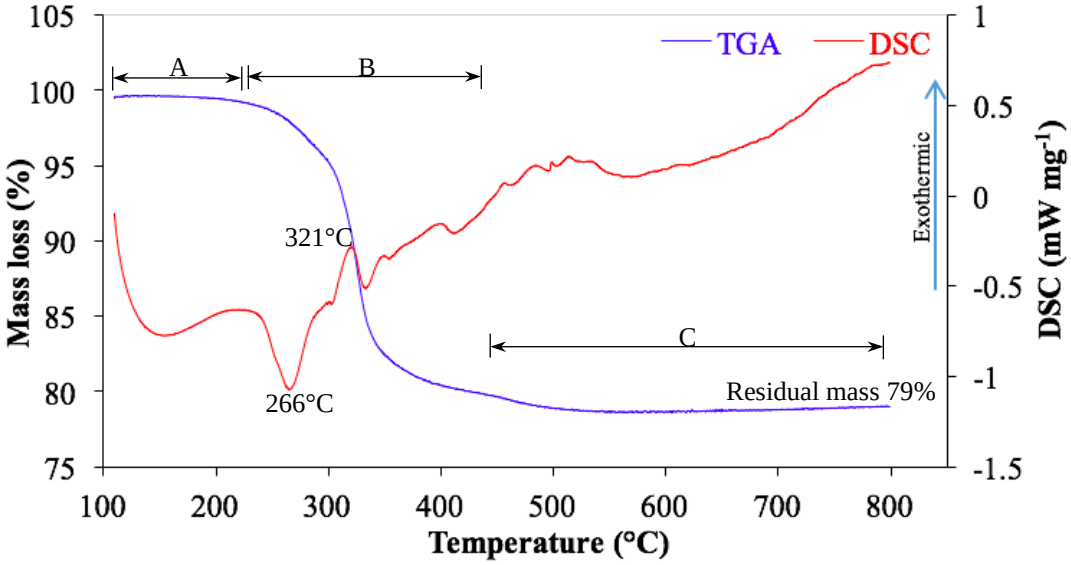

Figure 3.17: Non-isothermal TGA-DSC traces of the $LiMnPO_4$ precursor heated in argon from ambient to 800°C. A, B and C represent the three distinct mass loss steps.

The TGA graphs show three distinct mass losses in both air and argon measurements at distinct temperature intervals (Figure 3.16 and 3.17). The data for the first mass loss step below 110ºC is excluded as any loss below that is attributed to the evolution of adsorbed molecules such as water. Between 110ºC and 200ºC (A), there is a slight mass loss in both air and argon associated with the drying of the material and removal of the crystalline water. This corresponds to the broad endothermic peak at around 150ºC.

The major mass loss occurs between 200ºC and 400ºC in both air and argon (B) corresponding to mass losses of approximately 18% and 19% respectively associated with the decomposition of the sample. At 262ºC in air and 266ºC in argon, there is a sharp endothermic peak where mass loss occurs in the corresponding TGA graph. When decomposition occurs in air, there is a distinct exothermic peak observed at 362ºC. This exothermic peak is characteristic of the oxidative decomposition of part of the organic ligands in the precursor.

In the argon measurement, a similar mass loss occurs between 200ºC and 400ºC (B), however, only a relatively weak exothermic peak appears at about 321ºC due to the pyrolysis of the organic moieties. These observations suggest that the thermal energy or heating above 200ºC is sufficient to decompose the organic ligands in the precursor and depending on the atmosphere the decomposition is either oxidative in air or pyrolysis in an inert atmosphere such as argon. Also, it is still possible for oxidative decomposition to occur in an inert atmosphere. This can occur if some of the organic ligands (ethoxy, glycol and acetate) in the precursor are to release oxygen during the drying process thus allowing a small amount of oxidation to occur.

At around 400ºC to 550ºC, both measurements show weak exothermic peaks which are not associated with any major mass-loss events. This indicates the occurrence of physical events in that temperature interval. The weak DSC peaks in this interval can therefore be assigned to the crystallisation of the $LiMnPO_4$ phase. From 400ºC to 500ºC, the mass losses are gradual indicating that some organic ligands which were not decomposed at lower temperatures are being removed from the sample. This is not surprising given the short residence time during the non-isothermal heating. Above 500ºC (C), there are minor and gradual mass-loss events. The residual masses at the end temperature of 800ºC differ slightly with 80% and 79% of the material heated in air and argon respectively.

The use of air during synthesis of $LiMnPO_4$ from the precursor will not lead to oxidation of Mn^{2+} to Mn^{3+} unlike $LiFePO_4$ which is prone to oxidation. The electronic configuration of the Mn^{2+} ion is [Ar] $3d^5$ where the 3d orbital in Mn^{2+} is half-filled thus making Mn^{2+} stable. This $3d^5$ configuration is more stable than the $3d^4$ configuration of its oxidation product, Mn^{3+}, suggesting that Mn^{2+} is more stable than Mn^{3+}. Therefore, $LiMnPO_4$ can be produced in air unlike $LiFePO_4$ which is easily oxidised.

3.3.4.2. Simultaneous analysis of the evolved gas using infrared spectroscopy

TGA is a quantitative technique and will not give information as to the identity of evolved materials. By linking the TGA to a secondary analytical device such as Fourier Transform Infrared Spectroscopy (FTIR), however, it is possible to identify the evolved species. More information on the thermal profile of the $LiMnPO_4$ precursor can be obtained by studying the gaseous products evolved during the decomposition of the precursor in air and argon on a real-time basis. This is accomplished using gas-phase FT-IR spectroscopy which is coupled to the TGA-DSC instrument. Figure 3.18 shows the three-dimensional (3-D) graph obtained during the precursor decomposition in air. For illustration purposes, with the wavenumber and absorbance are plotted on the x and y-axis respectively while the and temperature is plotted along the z-axis. Similarly, a 3-D graph for the sample heated in argon was obtained.

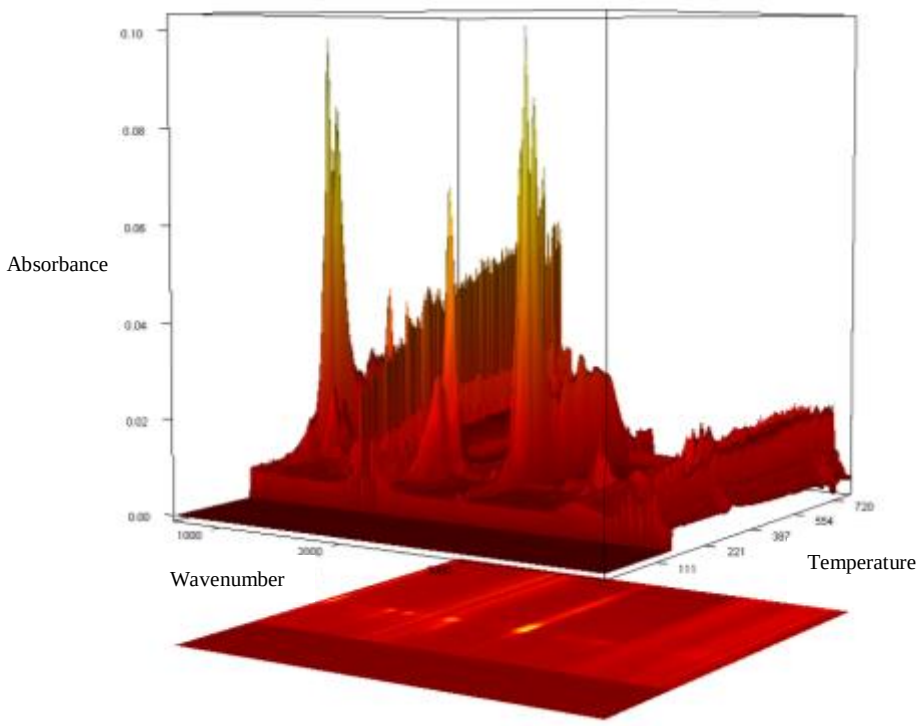

Figure 3.18: 3-D representation of the FT-IR spectra of the volatile species from the $LiMnPO_4$ precursor during non-isothermal heating in air.

Selected two-dimensional (2-D) IR spectra can be extracted from this 3-D graph to show what gaseous products have evolved from the samples at selected temperatures based on the DSC and TGA data shown in the Figure 3.19. The gas-IR analysis of the species produced during the first minor mass-loss step at ~150ºC demonstrates a broad band centred at about 3300 cm^{-1} and another centred at about 1650 cm^{-1}, characteristic of stretching and bending modes of water molecules (the spectrum is not shown here). There is also a doublet present at 2360 cm^{-1} and 2335 cm^{-1} which is typical of gas phase CO_2. The first 2-D spectrum was extracted from ~225ºC, which corresponds roughly to the onset of mass-loss, continues to show the broad O-H band and doublet of CO_2. The sharp band at around 668 cm^{-1} corresponds to the bending deformation of CO_2. At this temperature, there are also peaks observed at ~1700 cm^{-1} which indicates the beginning of the evolution of the carboxyl-group containing species. The band at 1183 cm^{-1} is difficult to assign but could belong to C-O groups evolving from the sample.

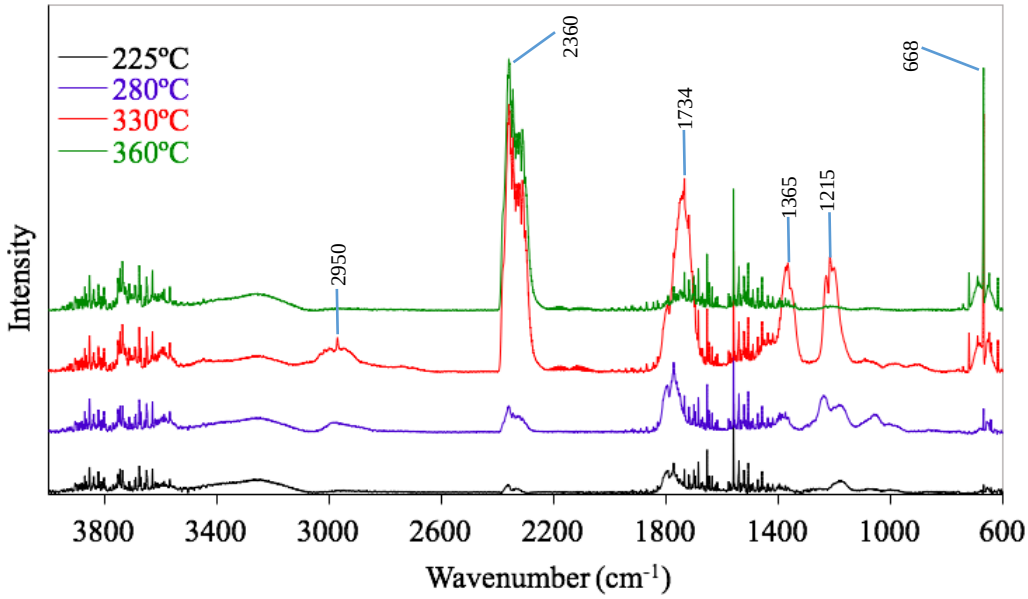

Figure 3.19: Gas-IR analysis of the volatile IR active species evolved at 225, 280, 330, and 360°C during heating in air.

Table 3.6: Assignment of gas-IR bands of the volatile IR active species when the $LiMnPO_4$ precursor is heated in air.

Peak	Frequency range (cm^{-1})	Peak Assignment	Intensity	Mode
1	2950	C-H (CH_3 group, broad)	weak	anti-symmetric stretch
2	2360	C-O (CO_2 group, sharp)	strong	anti-symmetric stretch
3	1734	C=O (sharp)	strong	anti-symmetric stretch
4	1365	C-O (sharp)	medium	stretch
5	1215	unassigned	medium	–
6	668	C-O (CO_2 group, sharp)	strong	bending

As the temperature increases to 280ºC, the bands that were present are more intense. The peak at 1183 cm^{-1} has evolved into a doublet at 1183 cm^{-1} and 1237 cm^{-1}. There is also a smaller band at around 1058 cm^{-1} and a weaker band appearing at around 1350 cm^{-1}. This temperature corresponds to the onset of the mass-loss (Figure 3.16).

The major mass-loss in air occurs between 200ºC and 400ºC during which carbon, hydrogen and oxygen containing species are released. By performing the first derivative of the sloping curve, the point at which the rate of change of mass-loss with respect to temperature is at a maximum can be determined. This corresponds to a temperature of ~330ºC which as shown in the extracted 2-D spectra which appear to be the most intense peaks for the decomposition of the precursor. The cluster of bands centred around 2950 cm^{-1} is typical of the anti-symmetrical C-H vibrations of CH_3 and CH_2 groups. These evolution groups are possibly related to partial oxidative decomposition of acetate and ethylene glycol containing ligands in the precursor.

Some of the gaseous, partially oxidised organics undergo further oxidation which is consistent with the significant increase in the characteristic vibrations of CO_2 at around 2360 cm^{-1} and the bending mode at 668 cm^{-1}. The intensity of the carboxyl group containing species at around 1734 cm^{-1} has also increased. The simultaneous evolution of the CH_3 and C=O groups correspond to decomposition of acetate groups prior to the oxidation. The presence of bands centring around 1215 cm^{-1} and the increase in the intensity of the band at 1365 cm^{-1} suggest the decomposition of other organic ligands present in the precursor.

At around 360ºC, where the TGA graph showed a strong exothermic peak typical of the combustion process characteristic of the bands for the characteristic bands to CO_2 at 2360 cm^{-1} and 668 cm^{-1}. These bands are equally intense as it was at 330ºC. However, the intense band of C=O can no longer be observed. The rest of the bands at 330ºC are also not visible here. Therefore, the decomposition of the organic moieties occurs gradually between 225ºC and around 330ºC, where most of the carboxylate ligands are decomposed. Above 330ºC, evolution of CO_2 occurs probably due to the slow oxidation of the carbon residue in the dynamic air atmosphere and any remaining organic ligands in the precursor. Also, the extremely rapid oxidation of functional groups at 330ºC, may have prevented the CO_2 from reaching the detector hence showing a delayed response. After 360ºC, the bands attributed to CO_2 gradually reduce to weak bands as seen at 225ºC. Between 360ºC and 800ºC, the level of CO_2 increases slightly at ~470, ~520, ~575 and ~635ºC, corresponding to the weak exothermic peaks shown in the DSC trace in Figure 3.16. Therefore, the analysis of the gaseous species produced from the precursor demonstrates that decomposition precedes (< 330ºC) the oxidation (> 360ºC) of the organic ligands even during heating in air.

When the heating was carried out in argon (Figure 3.17), at 150ºC the spectra are similar to that of the measurement carried out in air (3-D plot not shown here). At the onset of mass-loss at around 225ºC, the CO_2 bands are present but not the extra bands that appeared at the same temperature in air. It is only at ~270ºC that some very weak peaks can be seen at 1244 cm^{-1} and 1174 cm^{-1}.

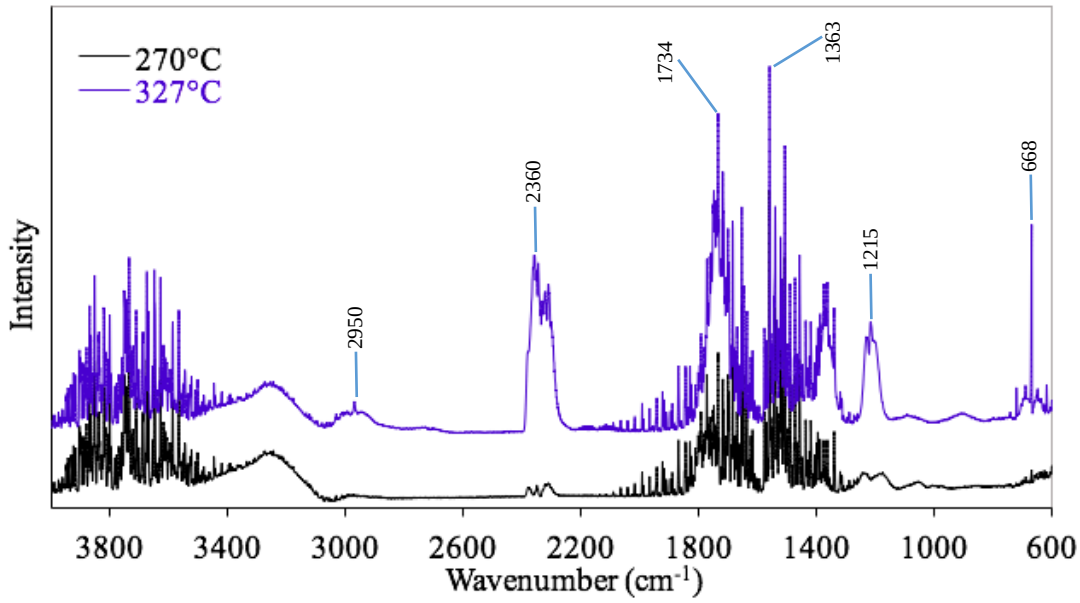

Figure 3.20: Gas-IR analysis of volatile IR active species evolved at 270ºC and 327ºC

Table 3.7: Assignment of gas-IR bands of the volatile IR active species when the $LiMnPO_4$ precursor is heated in argon.

Peak	Frequency range (cm^{-1})	Peak Assignment	Intensity	Mode
1	2950	C-H (CH_3 group, broad)	weak	anti-symmetric stretch
2	2360	C-O (CO_2 group, sharp)	strong	anti-symmetric stretch
3	1734	C=O (sharp)	strong	anti-symmetric stretch
4	1363	C-O (sharp)	medium	stretch
5	1215	unassigned	medium	–
6	668	C-O (CO_2 group, sharp)	strong	bending

The major mass-loss region is between 200ºC and 400ºC where at 327ºC the rate of mass-loss with respect to temperature is at a maximum. The broad bands between 3100 and 3500 cm^{-1} are assigned to O-H stretches and indicate the evolution of water molecules during the decomposition. The presence of anti-symmetrical C-H vibrations of CH_3 and CH_2 groups at around 2950 cm^{-1} indicate the decomposition of acetate and ethylene glycol groups in the precursor. Similar to the sample heated in air, there is a significant increase in the characteristic vibrations of CO_2 (2360 cm^{-1} and 668 cm^{-1}) as well as that of the carboxyl group (1734 cm^{-1}). Here the acetate groups are decomposed as indicated by the simultaneous evolution of CH_3 and C=O groups. Further decomposition of organic ligands is indicated by the peaks around 1215 cm^{-1} and the increase in the intensity of the band at 1363 cm^{-1}. Above 327ºC only CO_2 bands are present. It is likely that during pyrolysis the evolution of oxygen containing species leads to partial oxidation of the ligands, which in turn leads to the evolution of CO_2 molecules.

The step-wise chemistry of the decomposition is postulated as follows:

i. Firstly, the decomposition of ethylene glycol containing ligands which is detected through the gas-IR showing CH_2 vibrations. The main evolution of such ligands occurs below 300°C.
ii. Secondly, above 300°C the decomposition of acetate ligands commences giving rise to methyl groups, carboxylic groups and to CO_2 groups. The evolution of CO is also possible here. The release of O_2 during decomposition in argon also leads to the evolution of the groups, albeit to a lower extent than the decomposition in air.
iii. Some of the carbon ligands remain in the solid material and contribute to the carbon content. This would be more evident when decomposed in argon. These carbons would most likely be sp^3 and hence would not contribute to the conductivity of the sample. In other words, they are inert in terms of conductivity.

Overall, the nature of the atmosphere does not seem to have a significant effect on the formation of the final $LiMnPO_4$ product, although the onset of evolution of gaseous species in argon begins at higher temperature (~330ºC) than in air (~280ºC). The lower intensity of the CO_2 in argon implies the existence of more carbonaceous residues remaining after the decomposition steps in the sample whereas when heated in air carbon is expected to oxidise to a larger extent. Since heating was done under non-isothermal conditions, it is expected that an isothermal temperature program at around 280ºC should be adequate to decompose the organic ligands in the precursor.

3.3.5. Modulating crystalline phase purity of $LiMnPO_4$

As already described in Section 3.2.2, stoichiometric quantities of Li, Mn, and P precursors was used in the sol-gel process to produce the $LiMnPO_4$ precursor. Following thermal treatment, it was expected that the precursor would transform into phase pure crystallites of $LiMnPO_4$. Interestingly, this study has revealed that different heating regimes and temperatures can modulate the decomposition pathways and the phase purity of the crystallites formed. Subsequently, this might have a direct impact on the minimum temperature required to produce phase pure $LiMnPO_4$. The focus in this section is to produce phase-pure $LiMnPO_4$ to be used for subsequent studies on electrochemical performance.

3.3.5.1. X-ray diffraction study of the formation of the $LiMnPO_4$ in air

Based on the decomposition profiles of the precursor, determined by non-isothermal thermal analysis, samples were synthesised at 400, 500 and 600ºC by heating the precursor synthesised at 130ºC in air, for 2 hours using the TGA component of the thermal analysis instrumentation. This allowed the temperature, heating rate (10ºC min^{-1}) and gas flow rate (25 mL min^{-1}) to be controlled. Powder X-ray diffraction was obtained using the same method as described in Section 3.3.3.3. The powder X-ray diffraction technique was employed to determine the extent of crystallinity and crystalline phases present in the product (Figure 3.21). No peaks were present below 15º so the range from 2º up to 15º is excluded.

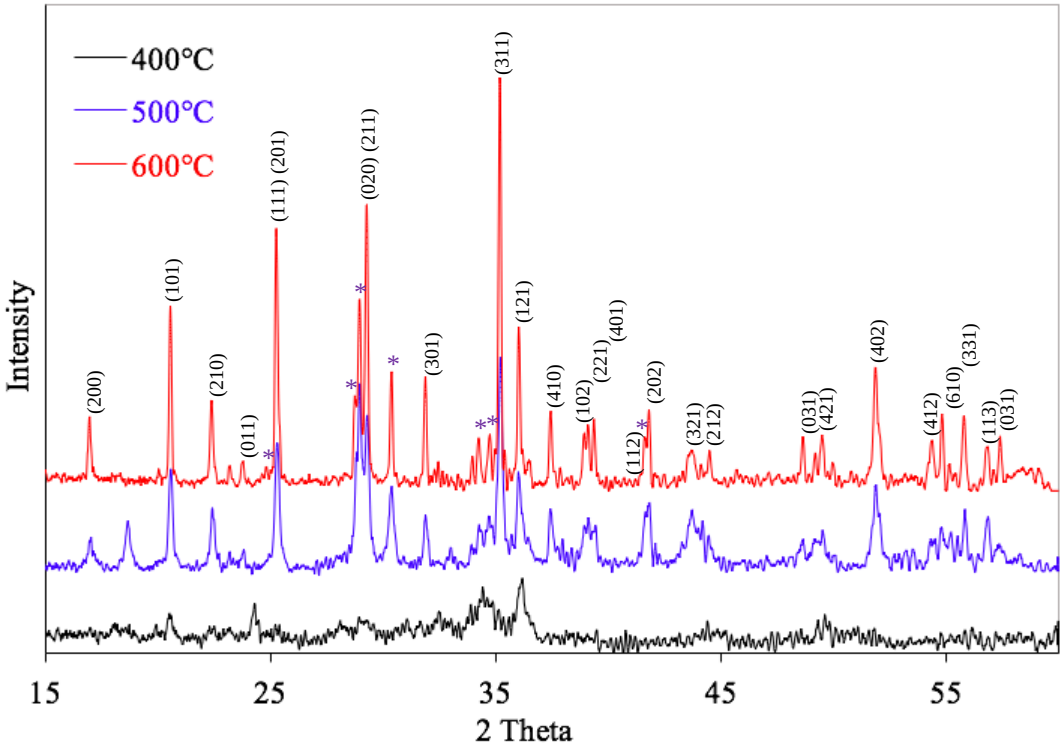

Figure 3.21: XRD pattern of $LiMnPO_4$ prepared at 400, 500 and 600ºC in air. The patterns indicate the formation of a product containing $LiMnPO_4$ and a phase marked (*) due to manganese pyrophosphate, $Mn_2P_2O_7$.

Figure 3.14 showed that the precursor at 130ºC was para crystalline with the possible co-existence of crystalline and amorphous structures. At 400ºC the relative quantity of crystalline phases is reduced. The pattern from 15° to 60° shows broad bumps and noise typical of amorphous materials. A few very broad peaks were visible but could not be assigned to any specific crystallographic pattern. This is not surprising because in the temperature interval ~250 to ~400ºC, the decomposition of the precursor occurred, as seen by the DSC-TGA-gas IR data. When the temperature is increased to 500ºC, the crystallinity improves at the expense of product purity. The crystalline phases present confirm a mixed-phase final product consisting of $LiMnPO_4$ and $Mn_2P_2O_7$ (Figure 3.21). At 500ºC, the intensity ratios of the $LiMnPO_4$ and $Mn_2P_2O_7$ peaks, are similar. For example, the peak at 35.20° assigned to $LiMnPO_4$ and the peak at 29° for $Mn_2P_2O_7$ are similar in intensity.

Interestingly, the intensity ratio of these two peaks at 600ºC is reduced. Thus, this indicates that at 600ºC, the quantity of $Mn_2P_2O_7$ has reduced relative to $LiMnPO_4$. This would also suggest that the lithium is present in the material in amorphous form and that higher sintering temperatures may be required to allow the diffusion of the Li into the crystalline $Mn_2P_2O_7$ particles. Semi-quantitatively, at 500ºC the ratio of $LiMnPO_4$ to $Mn_2P_2O_7$ is 68.3% to 31.7% respectively. At 600ºC, the ratio is 72.6% to 27.4% for $LiMnPO_4$ and $Mn_2P_2O_7$ respectively. As the temperature is increased from 400ºC to 600ºC, the shape of the peak is observed to be narrower and sharper. This indicates the improving crystallinity of the final product as well as an increase in the crystal size.

Next, it was necessary to determine at what temperature the transformation of $Mn_2P_2O_7$ to $LiMnPO_4$ can be completed. The final temperature applied in the thermogravimetric analyses was used as the lowest temperature (800ºC) with further samples prepared at 900ºC and 1000ºC. All samples were heated in air for 2 hours (Figure 3.22).

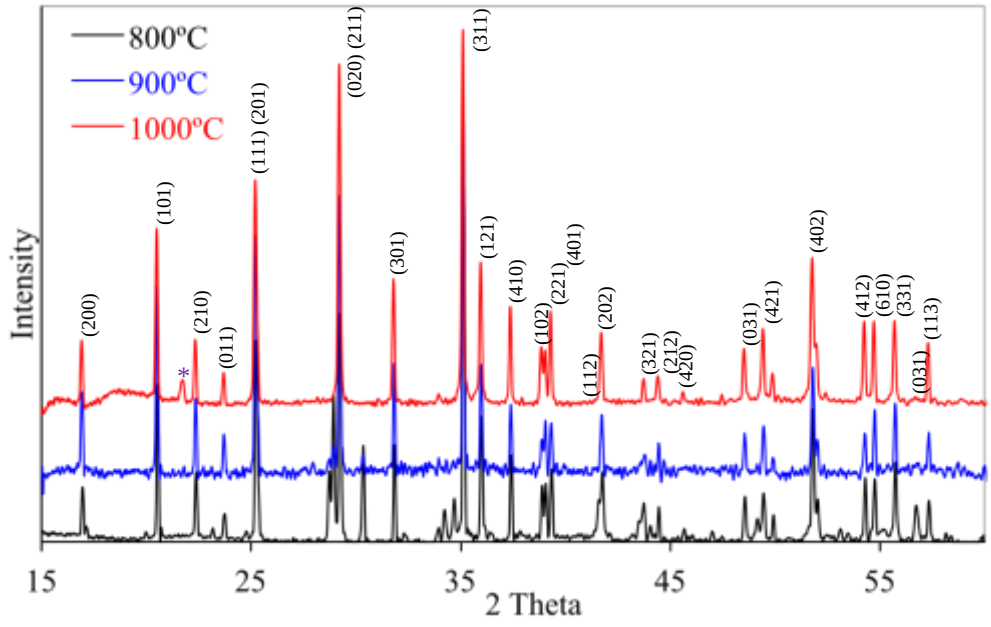

Figure 3.22: XRD pattern of $LiMnPO_4$ prepared at 800, 900 and 1000ºC in air. At 900ºC and 1000ºC the bands conformed to phase pure $LiMnPO_4$. At 800ºC, $Mn_2P_2O_7$ peaks were still present at very low relative intensities. An unidentified peak in the XRD pattern at 1000ºC is marked (*)

The samples prepared at 800, 900 and 1000°C showed patterns consistent with highly crystalline orthorhombic structure of $LiMnPO_4$ (space group *Pnma*(62), ICDD PDF card # 074-0375). At 800°C, the peaks were sharper and narrower compared to the sample produced between 400°C and 600°C. This is expected as higher temperatures promote the growth of crystalline particles. Thus, the particles at 800°C are expected to be larger with a lower surface area. The peaks attributed to $Mn_2P_2O_7$ are still present here and the ratio of intensity of the peaks at 35.20° assigned to $LiMnPO_4$ and the peak at 29° for $Mn_2P_2O_7$ have not decreased significantly to that at 600°C. Thus, between 600°C and 800°C, the two crystallographic domains appear stable and only the growth and size of the crystals are largely affected. At 900°C, however, the ratio between these two peaks has been reduced significantly. This reduction in relative intensity indicates that the quantity of $Mn_2P_2O_7$ has been reduced significantly at 900°C. At 1000°C, no $Mn_2P_2O_7$ can be detected within the detection limits of the XRD instrumentation. The very sharp and narrow peaks here also show that the $LiMnPO_4$ crystallites are well formed. There is a peak appearing here at around 22° only in the sample prepared at 1000°C which was unassigned, however, tentatively it may belong to a phase of MnO.

3.3.5.2. X-ray diffraction study of the formation of the $LiMnPO_4$ in argon.

Samples were prepared at 400, 500 and 600°C in argon using the same set-up and method as described in Section 3.3.5.1. Powder x-ray diffraction was obtained using the same method as described in Section 3.3.3.3 (Figure 3.23). Similarly, the region below 15° is excluded. The samples were prepared in argon gas to understand the influence of inert atmosphere on the synthesis of the $LiMnPO_4$ at lower temperatures.

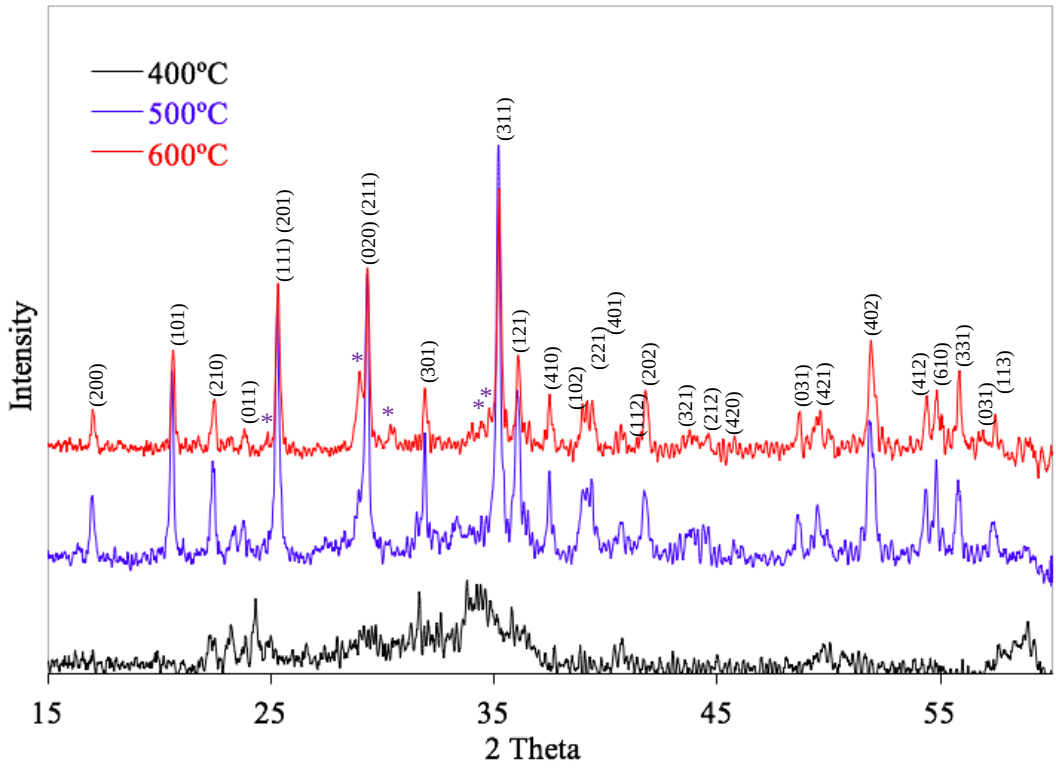

Figure 3.23: XRD pattern of the $LiMnPO_4$ prepared at 400, 500 and 600°C in argon. Most of the peaks conform to phase pure $LiMnPO_4$. The peaks marked (*) are contributed from the presence of manganese pyrophosphate, $Mn_2P_2O_7$.

Similar to the sample heated in air, at 400°C the sample was almost completely amorphous. Post-processing of the data using background subtraction, removal of K-$\alpha_2$lines and smoothing function reveals peaks which are broad and therefore are not assigned. Thus, the material has gone from partially crystalline to amorphous. The samples are crystalline at 500°C and 600°C. Most the peaks conform to the standard pattern of $LiMnPO_4$ (PDF card # 074-0375). Peaks relating to $Mn_2P_2O_7$ are present here as well in very small quantities compared to the corresponding sample prepared in air. However, at 600°C, the peaks related to $Mn_2P_2O_7$ increased slightly relative to $LiMnPO_4$ sample prepared at 500°C. The opposite occurred in air where the peak slowly reduced between 500°C and 600°C. As expected, the peaks of the samples prepared in argon were slightly broader than those in air which indicates the crystallites are slightly smaller. It is well-known that this occurs due to the pyrolysis process which leaves residual carbon in the material. This residual carbon then restricts the growth of the crystals due to more difficult diffusion of ionic species through the carbon containing phase.

The phase-evolution of the samples prepared at the higher temperatures of 800, 900 and 1000°C are shown in Figure 3.24.

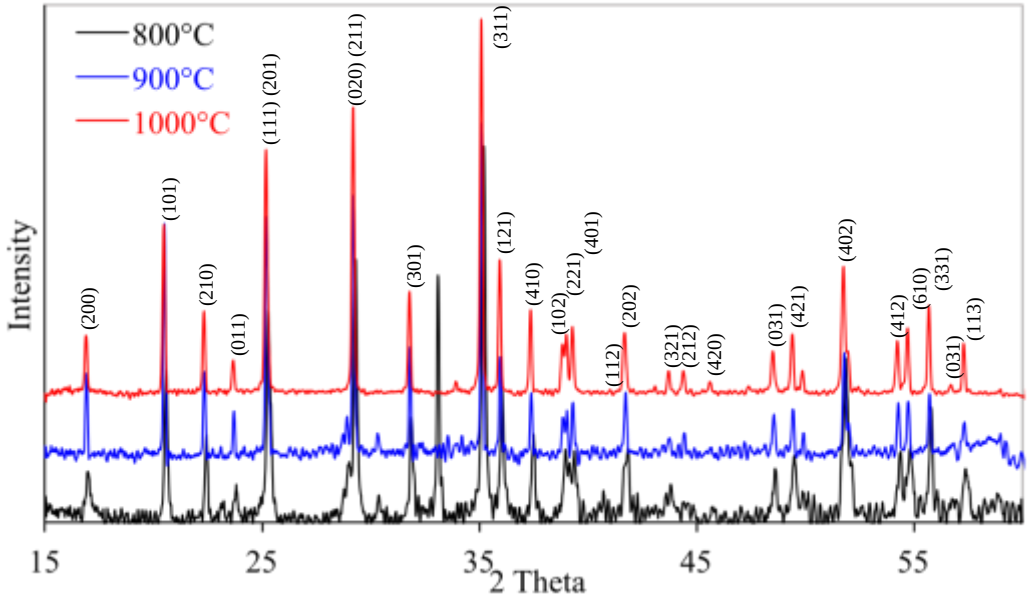

Figure 3.24: XRD pattern of $LiMnPO_4$ prepared at 800, 900 and 1000°C in argon. At 900°C and 1000°C the bands conformed to phase pure $LiMnPO_4$. At 800°C, $Mn_2P_2O_7$ peaks were still present at very low relative intensities.

Similar to the samples prepared in air, the samples prepared at 800, 900 and 1000°C showed patterns consistent with highly crystalline materials. At 800°C, the peaks were sharper and narrower compared to the samples produced between 400°C and 600°C. At 800°C, multiple crystalline phases can be seen. Peaks attributed to highly crystalline $LiMnPO_4$ is present as well as a relatively small quantity of $Mn_2P_2O_7$. The peak that appeared at 22° for the sample produced in air at 1000°C is not attributed to $LiMnPO_4$ nor $Mn_2P_2O_7$ and is absent from any of the samples produced in argon. There is tentative evidence of this peak being a form of MnO.

Overall, the diffraction patterns show improved purity compared to samples produced in air. Nevertheless, the temperature required to get phase-pure $LiMnPO_4$ is too high for application in Li-ion batteries. When using conventional solid-state synthesis, high temperatures are required to allow the diffusion of the lithium, manganese and phosphate groups to be completed. Since higher temperatures lead to increasing crystalline particle size, the ability of Li-ions to diffuse through the material becomes much more difficult due to the longer diffusion distances. From an electrochemical perspective, slow diffusion of Li-ions severely limits the rate capability of the cell. On the other hand, at lower temperatures, incomplete diffusion will lead to regions that are unreacted or the formation of impure phases [5].

Although, crystalline material was formed at lower temperatures here, the presence of the $Mn_2P_2O_7$ impurity is not ideal because its effect on the electrochemical performance at this stage is unknown. The aim is to evaluate the performance of phase-pure $LiMnPO_4$ prepared using the novel synthetic method described here. Therefore, the next section will investigate how phase-pure $LiMnPO_4$ can be produced at lower temperatures.

3.3.5.3. Effect of an intermediate decomposition temperature on the phase purity of $LiMnPO_4$ product

Research done in the past have also reported the appearance of impure phases when preparing $LiMnPO_4$ [40-41]. Usually, this can be overcome by, for example, in the case where there is excess manganese and there is a deficiency in lithium [40]. To better understand the formation of mixed phase manganese phosphates below 800ºC, samples were prepared with 10% and 20% lithium deficiency so that more Mn was in the system. Also, samples were prepared with excess 10%, 20% lithium and with 100% excess lithium. All samples were heated in air or argon to 800°C with a hold time of 2 hours. The residue that remained was collected and X-ray diffraction patterns were obtained (not shown here). All samples showed the traces of $Mn_2P_2O_7$ impurity similar to those with stoichiometric ratios. Hence, the presumption that lithium is leached or lost during the synthesis process is not true and there are other factors could be contributing to the existence of the impurity phase.

Based on DSC/TGA analyses, below 300°C, most organic ligands should be decomposed at a temperature below 300ºC. To investigate the effect of an intermediate isothermal heat-treatment prior to crystallisation of the $LiMnPO_4$ at higher temperatures, two sets of samples were decomposed for 2 hours at 250ºC and 300ºC, respectively. It is hypothesised that the removal of the organic components at a lower temperature without inducing the formation of highly crystalline phases, may allow phase-pure $LiMnPO_4$ to be produced at temperatures significantly lower than 900°C. A similar approach was successfully employed by Milev *et al*. [15, 17] for the low temperature synthesis of an unrelated calcium phosphate system. It was aimed at an intermediate temperature which is low enough to decompose most of the organics in the samples without causing crystallisation of large-size non-stoichiometric Li-rich and Mn-rich phases. Due to kinetic limitations, such large-sized crystals would require much higher temperatures for the respective Li-rich and Mn-rich species to diffuse and form the phase-pure $LiMnPO_4$ product as seen in Figures 3.21 – 3.24. Further, based on the thermal analysis, two temperatures were chosen; 250°C and 300°C as candidates for an intermediate heat treatment. The atmosphere combination of air – argon for the first and second heating steps respectively were chosen. Argon was required during the second heating step to retain the carbon in the samples. The initial atmosphere should be air to pre-decompose the precursor. Finally, for the lowest crystallisation temperature of $LiMnPO_4$ while maintaining sufficient carbon in the final product to improve the electronic conductivity of the material, the following combination was chosen: intermediate treatment in air followed by crystallisation of the product in argon.

The XRD patterns for samples prepared at the intermediate temperatures of 250°C and 300°C in air are shown in Figure 3.25.

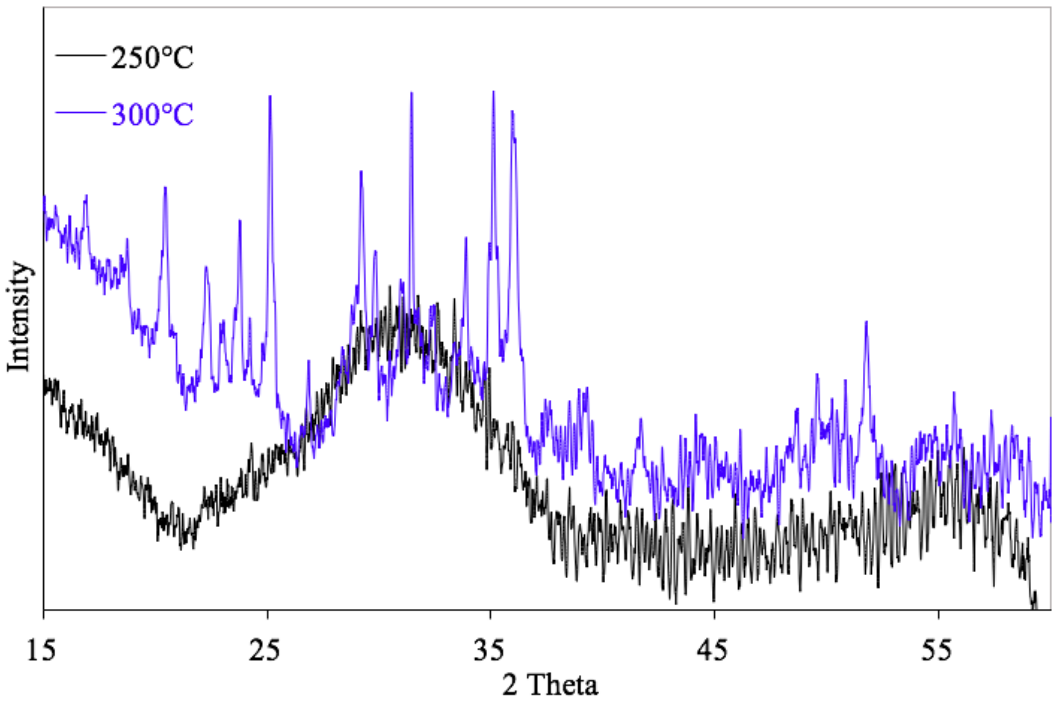

Figure 3.25: XRD pattern of the $LiMnPO_4$ prepared by heating for 2 hours at 250°C and 300°C in air. The structure at 250°C is amorphous and by 300°C crystals are starting to form. The peaks can not be assigned to any pattern.

At 250°C for 2 hours, the samples are X-ray amorphous. Increasing the temperature by 50°C allows crystals to start forming. The broad peaks at 300°C for 2 hours indicate poor crystallisation. The $LiMnPO_4$ samples were prepared using the intermediate heating temperatures of either 300°C (Figure 3.26) or 250°C (Figure 3.27) followed by the second heating step (400, 500 and 600°C) in argon to verify the hypothesis proposed in the previous paragraph.

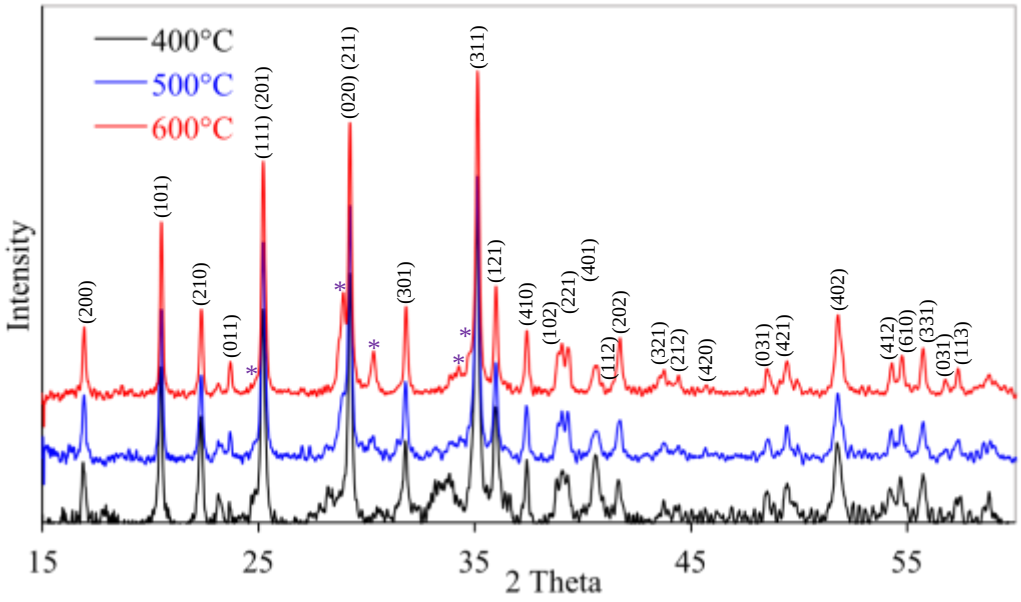

Figure 3.26: XRD pattern of the $LiMnPO_4$ prepared at the intermediate heating step of 300°C in air and subsequently heated to 400, 500, and 600°C in argon. The peaks marked (*) are contributed from the presence of manganese pyrophosphate, $Mn_2P_2O_7$.

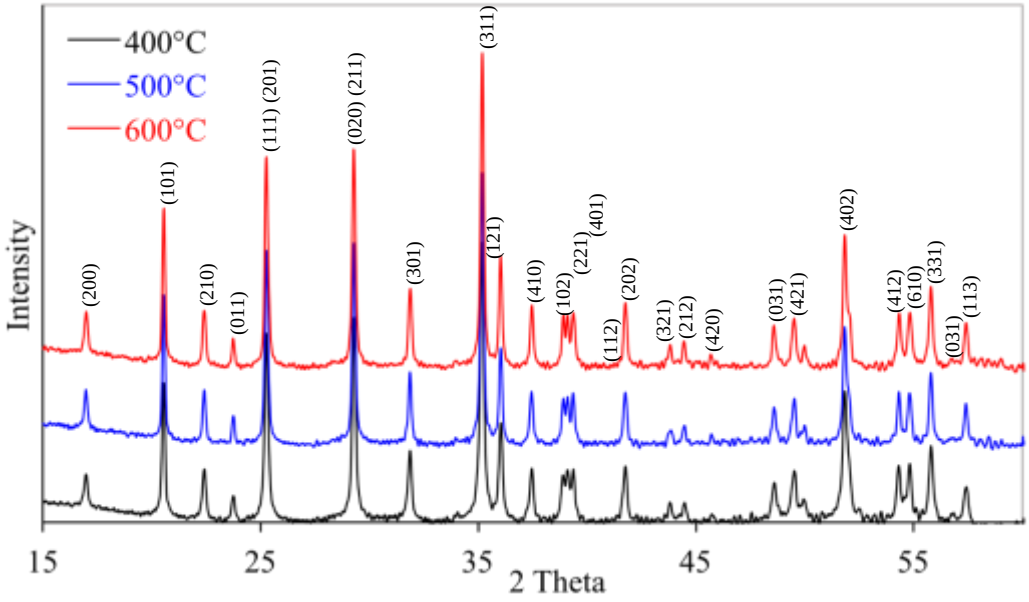

Figure 3.27: XRD pattern of the $LiMnPO_4$ prepared at the intermediate heating step of 250°C in air and subsequently heated to 400, 500, and 600°C in argon.

The samples prepared with the intermediate heating temperature of 300°C produced x-ray diffraction patterns consistent with the pattern for $LiMnPO_4$ (Figure 3.26). However, impurities were still detected at all three secondary temperatures. Hence, using an intermediate temperature of 300°C, the reaction again forms some $Mn_2P_2O_7$ as the intermediate phase before the reaction reaches equilibrium $LiMnPO_4$ product. Taking into account the thermodynamics of a diffusion controlled growth, higher temperatures are necessary to allow the completion of the reaction through these intermediary phases.

However, samples prepared with the intermediate temperature of 250°C, produced phase-pure $LiMnPO_4$ at 400°C and above at any temperature (Figure 3.27). Therefore, 250°C is considered an optimal intermediate temperature for this specific system, to produce pure samples and significantly improves the formation kinetics of $LiMnPO_4$ product.

3.3.5.4. Mechanism of low temperature $LiMnPO_4$ synthesis

What may be occurring in the precursor material is similar to the reactions in a solid-state reaction, where crystallisation of the final product requires long-range diffusion of species. The kinetics of this diffusion would be dependent on the degree of mixing and sizes of the powder particles. In typical solid-state reactions, the starting mixture is usually inhomogeneous with larger particles. Thus, mechanical mixing and higher temperatures are required to produce crystalline materials. Here, the solution-state method, uses the constituents which are mixed at a molecular level so diffusion path-length is expected to be shorter. However, this could also mean that other stable phases other than the main phase could be formed depending on the kinetics of diffusion.

In this case, these stable phases (mainly $Mn_2P_2O_7$) and perhaps Li-rich amorphous phase, tend to grow in isolation to larger sizes at medium to high temperatures (~400 to 800ºC), before it becomes energetically more favourable for those two phases to react and produce $LiMnPO_4$ product at 900ºC by an Ostwald ripening process (Figure 3.28). Therefore, the particles in the precursor would undergo a reaction similar to the well-known solid-state reaction initially at the points of contact between the particles and then continue successively by inter-diffusion of the constituent's ions through the desirable product phase, in this case, $LiMnPO_4$. Initially, this reaction is expected to be rapid because of the shorter diffusion paths, but as the reaction proceeds the reaction rate decreases as the ions have to diffuse longer distances to give rise to the phase pure product. Below 800ºC, what could happen in some cases is that several unwanted phases, such as $Mn_2P_2O_7$, are produced, as the solid-state reaction occurs with other particles away from the product phase, thus seemingly showing a deficiency in the amount of lithium.

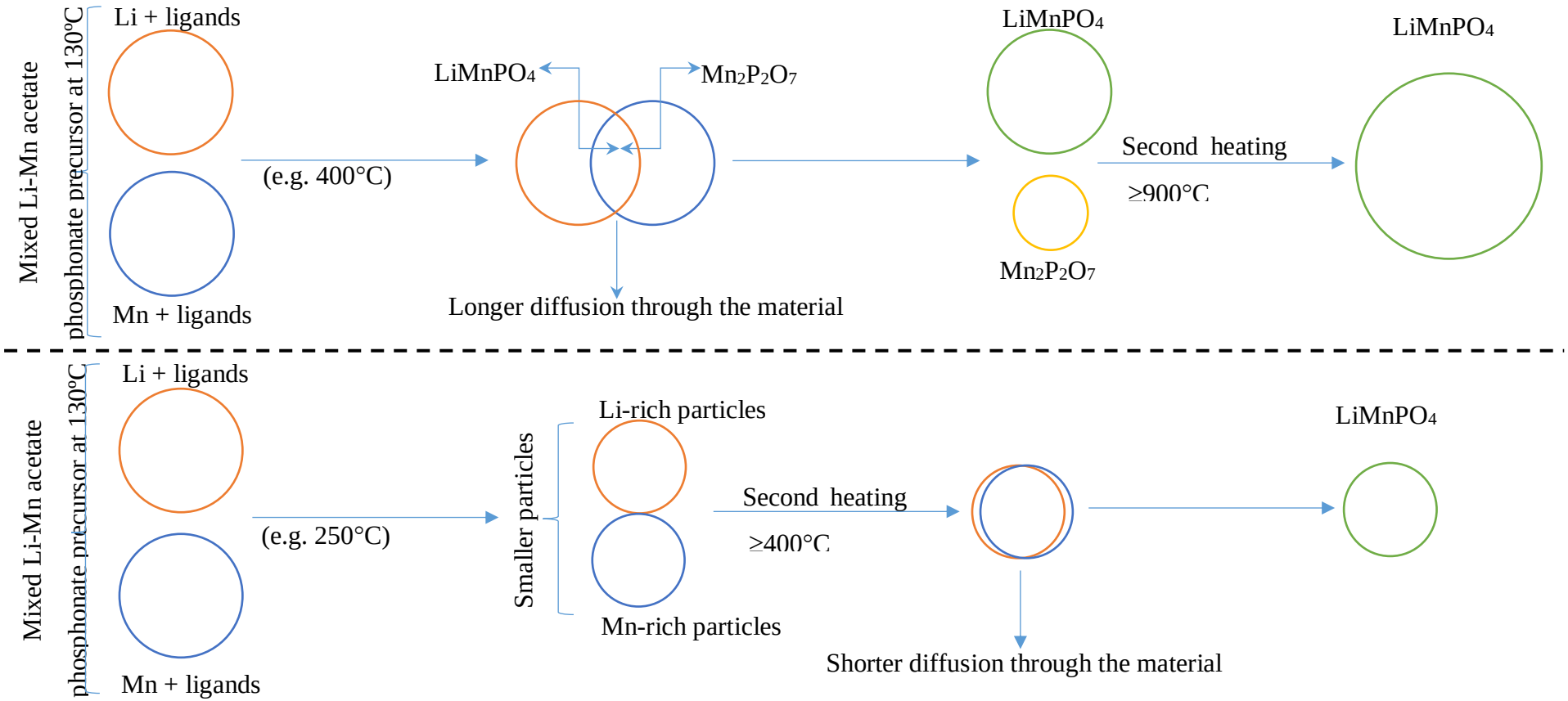

Figure 3.28: Schematic showing the - TOP: diffusion of cations with organic ligands heated using a single-step heating method. Due to the longer diffusion distance, $Mn_2P_2O_7$ is produced. A very high secondary temperature (~900°C) is required to reach equilibrium. BOTTOM: inclusion of an intermediate heating step which decomposes the organic ligands and reduces the distances between the Li and Mn containing particles, thereby producing pure and highly crystalline $LiMnPO_4$ at lower temperatures due to the shorter diffusion path-lengths for Li-rich and Mn-rich species.

If, however, an intermediate heat treatment is employed, the size of the respective Li-rich and Mn-rich domains is small and at this temperature, the thermal energy is not sufficient to facilitate the long-range diffusion of the ionic species and the material remains amorphous and presumably homogeneous at nanoscale level (here at 250ºC). The subsequent heat treatment, at or above 400ºC, gives rise to phase-pure $LiMnPO_4$ directly, without the formation of intermediate phases (Figure 3.28). Therefore, the use of this intermediate temperature has reduced the temperature required by 500°C, i.e. from 900°C to 400°C.

However, if the intermediate temperature is not optimal (here 300ºC), the decomposition of the ligands occurs simultaneously with the localised growth of unknown crystalline product(s) which would then require elevated temperatures to decay and form the energetically more favourable $LiMnPO_4$ product. These impurities in turn increase the diffusion distances, thus much higher temperatures are required to produce phase-pure material. Typically, in the conventional solid-state route, samples are repeatedly ground and heated for longer periods at higher temperatures. The drawbacks of this have been discussed before and summarised in Chapter 2. However, here it is shown that these diffusion distances can be reduced by introducing an intermediate temperature that would allow most of the organic ligands to be removed before it is heated at a higher temperature which would in turn allow the crystals to grow relatively uninhibited. In other words, the intermediate heat-treatment temperature should be sufficient to decompose the organic ligands but not high enough to cause longer range diffusion of Li-, Mn- and P-rich species and the evolution of any intermediate phases prior to the formation $LiMnPO_4$ product.

More work on refining and determining the kinetics of the method will be listed in future works. An interesting outcome of this research was the preliminary finding that the purity could be modulated by simply introducing an intermediate decomposition temperature before the final heating step to prepare phase-pure $LiMnPO_4$. Another aspect that was looked at was attempting to maintain the morphology of the precursor. It is anticipated that very high temperatures of 800°C to 1000°C causes the particles to fuse together. At lower temperatures, the morphology can be maintained better. As such, an intermediate temperature was chosen initially for this purpose. The next chapter describes the preparation of $LiMnPO_4$ and $LiMnPO_4$ carbon composites ($LiMnPO_4$/C) at different temperatures using the novel sol-gel methodology described in this chapter.

3.3.5.5. Kinetic analysis of the evolution of $LiMnPO_4$ by DSC/TGA

For the benefit of the reader, information on how the kinetics postulated here can be confirmed is included. The reactions of solids can be monitored under non-isothermal conditions in which a sample is heated at a constant heating rate. The rate of a single-step reaction is then expressed by $\beta \frac{d\alpha}{dT} = Aexp\left(-\frac{\Delta E}{RT}\right) f(\alpha)$, where β = dT/dt is the heating rate, dα/dT is the temperature dependence of the conversion α, T is temperature (K), A is Arrhenius factor (s^{-1}), ΔE is apparent activation energy (J/mol), $f(\alpha)$ is empirical differential conversion function, and R is the gas constant (J/molK). The $f(\alpha)$ functions are derived based on various models of the reaction interface movement, and the corresponding mathematical expressions are well-known in the literature [42].

The kinetic analysis involves curve fitting based on the kinetic parameters ΔE, A values and selection of the $f(\alpha)$ function that gives best approximation of experimental data. However, under non-isothermal conditions both T and α change simultaneously, and the curve fitting to data obtained from one heating-run experiment usually fails to achieve clean separation between the kinetic parameters [43]. Less ambiguous determination of the three kinetic parameters can be achieved by iso-conversion methods, which are based on the above equation but combine at least three non-isothermal measurements to derive ΔE and A estimates [44, 45]. Further, to derive unambiguous reaction model, the data obtained by the iso-conversion method is followed by multi-curve fitting by non-linear regression (NLR) method [46-49].

In practice, the thermal behavior of the partially decomposed precursors obtained after heating for 2 hours at 250°C in air can be monitored by simultaneous DSC or TGA measurements at four different heating rates; 2.5, 5, 10 and 20 deg min^{-1} in Argon flowing at 25 mL min^{-1}, according to a procedure described elsewhere [50]. The kinetic analysis involves the following steps: (i) DSC data collection under four different heating rates, (ii) computation of (ΔE) and Arrhenius factor ($\log A$) parameters according to iso-conversion method in the temperature interval 250 – 600 °C, (iii) differential conversion function $f(\alpha)$ determination by NLR using starting values of ΔE and $\log A$ calculated according to iso-conversion method, (iv) determining of mechanism from the above data. Once the kinetic parameters are identified, optimization of the time-temperature-transformation conditions can be achieved for the formation of phase-pure nanocrystalline $LiMnPO_4$ particles. The kinetic studies, together with additional Transition electron microscopy (TEM) measurements and high temperature X-ray diffraction analysis is expected to provide additional support for the proposed in Chapter 3 section 3.5.4 and Figure 3.28 two-step mechanism for low temperature formation of $LiMnPO_4$ product.

3.5. Summary and conclusions

In this chapter, a novel sol-gel approach using for the first time the phosphonate intermediates to prepare a $LiMnPO_4$ precursor material has been accomplished. Optimisation of the synthetic approach led to a reduction of the synthetic temperature by 500ºC; i.e., from 900ºC to 400ºC, which is much lower than that required by the solid-state approach and is comparable to the synthetic temperatures used by the hydrothermal method where the pressure is also a variable. Thus far, this is the first study to show the ability to produce the combination of high crystallinity and phase purity of $LiMnPO_4$ at a low temperature of 400ºC using a sol-gel method.

Important findings were made pertaining to the importance of an intermediate decomposition temperature in producing phase pure $LiMnPO_4$ and the ability to modulate this purity as required. Here it is clearly shown that the different crystalline phases can exist even without the loss of Li ions. More importantly, the phase purity of $LiMnPO_4$ has been achieved by applying a relatively facile process of heating the precursors at a temperature that is adequate to remove the organic residues without inducing crystallisation. This way, the smaller lithium and manganese containing particles sinter together much easily during the second heating and therefore the formation of the thermodynamically stable crystalline $LiMnPO_4$ phase occurs at low temperatures. The temperature regime and atmosphere that is employed modulates the purity of the final crystalline material. The work here suggests that this is probably achieved by changing the kinetics of the solid-state diffusion using a two-step heating regime. Any optimisation is subject to future work depending ultimately on its electrochemical performance.

3.6. References

1. Brinker C, Scherer G. Sol-gel science: the physics and chemistry of sol-gel processing. London Academic Press; 1990.

2. Mackenzie J, Bescher E. Chemical routes in the synthesis of nanomaterials using the sol–gel process. Accounts of Chemical Research. 2007;40(9):810-8.

3. Hench L, West J. The sol-gel process. Chemical Reviews. 1990;90(1):33-72.

4. Kakihana M. Invited review "sol-gel" preparation of high temperature superconducting oxides. Journal of Sol-Gel Science and Technology.6(1):7-55.

5. Cushing B, Kolesnichenko V, O'Connor C. Recent advances in the liquid-phase syntheses of inorganic nanoparticles. Chemical Reviews. 2004;104(9):3893-946.

6. Corriu R. Molecular chemistry of sol-gel derived nanomaterials. Nguyên T, editor. Chichester: Wiley; 2009.

7. Soltanmohammad S, Asgari S. Characterization of $LiCoO_2$ nanopowders produced by sol-gel processing. Journal of Nanomaterials. 2010;2010(55):1-8.

8 Ma J, Li B, Du H, Xu C, Kang F. Inorganic-based sol–gel synthesis of nano-structured $LiFePO_4$/C composite materials for lithium ion batteries. Journal of Solid State Electrochemistry. 2011;16(4):1353-62.

9. Lee S, Cho S, Cho S, Park G, Park S, Lee Y. Synthesis of $LiFePO_4$ material with improved cycling performance under harsh conditions. Electrochemistry Communications. 2008;10(9):1219-21.

10 Yang R, Kang E, Jiang B, Ahn J. Effect of complexing agents on the electrochemical performance of $LiFePO_4$/C prepared by sol-gel method. Nanoscale Research Letters. 2012;7(1):40.

11 Duncan H, Abu-Lebdeh Y, Davidson I. Study of the cathode–electrolyte interface of $LiMn_{1.5}Ni_{0.5}O_4$ synthesized by a sol–gel method for Li-ion batteries. Journal of The Electrochemical Society. 2010;157(4):A528-35.

12 Pan A, Liu J, Zhang J, Cao G, Xu W, Nie Z, et al. Template free synthesis of LiV_3O_8 nanorods as a cathode material for high-rate secondary lithium batteries. Journal of Materials Chemistry. 2011;21(4):1153-61.

13 Pan A, Zhang J, Cao G, Liang S, Wang C, Nie Z, et al. Nanosheet-structured LiV_3O_8 with high capacity and excellent stability for high energy lithium batteries. Journal of Materials Chemistry. 2011;21(27):10077-84.

14 Milev A, Kannangara G, Ben-Nissan B, Wilson M. Temperature effects on a hydroxyapatite precursor solution. The Journal of Physical Chemistry B. 2004;108(18):5516-21.

15. Milev A, Kannangara G, Wilson M. Template-directed synthesis of hydroxyapatite from a lamellar phosphonate precursor. Langmuir. 2004;20(5):1888-94.

16 Milev A, Kannangara G, Wilson M. Strain and microcrystallite size in synthetic lamellar apatite. The Journal of Physical Chemistry B. 2004;108(34):13015-21.

17 Milev A, McCutcheon A, Kannangara G, Wilson M, Bandara T. Precursor decomposition and nucleation kinetics during platelike apatite synthesis. The Journal of Physical Chemistry B. 2005;109(36):17304-10.

18. Musumeci A, Frost R, Waclawik E. A spectroscopic study of the mineral paceite (calcium acetate). Spectrochimica Acta Part A: Molecular and Biomolecular Spectroscopy. 2007;67(3–4):649-61.

19. Musumeci A, Frost R. A spectroscopic and thermoanalytical study of the mineral hoganite. Spectrochimica Acta Part A: Molecular and Biomolecular Spectroscopy. 2007;67(1):48-57.

20. Nara M, Torii H, Tasumi M. Correlation between the vibrational frequencies of the carboxylate group and the types of its coordination to a metal ion: an ab initio molecular orbital study. The Journal of Physical Chemistry. 1996;100(51):19812-7.

21. Keeler J. Chemical structure and reactivity: an integrated approach. 2nd ed. Wothers P, editor: Oxford University Press; 2014.

22. Zhang S. Raman spectroscopy and its application in nanostructures. Chichester, West Sussex: Wiley, Interscience; 2012.

23. Larkin P. Infrared and Raman spectroscopy principles and spectral interpretation. Science Direct, editor. Boston: Elsevier; 2011.

24 Mehrotra R, Bohra R. Metal Carboxylates: Academic Press; 1983.

25 Nakamoto K. Infrared and Raman Spectra of Inorganic and Coordination Compounds Part B, Applications in Coordination, Organometallic, and Bioinorganic Chemistry. 6th ed. Hoboken: John Wiley & Sons, Inc.; 2009.

26 Meyrick C, Thompson H. Vibrational spectra of alkyl esters of phosphorus oxy-acids. Journal of the Chemical Society. 1950(0):225-9.

27. Lin-Vien D, Colthup N, Fateley W, Grasselli J. Organophosphorus Compounds. San Diego: Academic Press; 1991.

28. Rivera-Munoz E. Hydroxyapatite-based materials: synthesis and characterization In: Fazel-Rezai R, editor. Biomedical Engineering - Frontiers and Challenges. Croatia: InTech; 2011.

29. Contreras C, Sugita S, Ramos E. Preparation of sodium aluminate from basic aluminium sulfate. Advances in Technology of Materials and Materials Processing Journal. 2006;8(2):122-9.

30. Norberg N, Kostecki R. FTIR spectroscopy of a $LiMnPO_4$ composite cathode. Electrochimica Acta. 2011;56(25):9168-71.

31 Bushiri M, Jayasree R, Fakhfakh M, Nayar V. Raman and infrared spectral analysis of thallium niobyl phosphates: $Tl_2NbO_2PO_4$, $Tl_3NaNb_4O_9(PO_4)_2$ and $TlNbOP_2O_7$. Materials Chemistry and Physics. 2002;73(2–3):179-85.

32. Bachouâ H, Othmani M, Coppel Y, Fatteh N, Debbabi M, Badraoui B. Structural and thermal investigations of a Tunisian natural phosphate rock. Journal of Materials and Environmental Science.5(4):1152-9.

33. Frost R, Xi Y, Scholz R, López A, Belotti F, Chaves M. Raman and infrared spectroscopic characterization of the phosphate mineral lithiophilite—$LiMnPO_4$. Phosphorus, Sulfur, and Silicon and the Related Elements. 2013;188(11):1526-34.

34. Julien C, Mauger A, Zaghib K, Gendron F, editors. High performance of lithium iron phosphates for HEV with quality control made by magnetometry. Proceedings of the Materials Research Society 2006; Boston, Massachusetts.

35. Korona K, Papierska J, Kamińska M, Witowski A, Michalska M, Lipińska L. Raman measurements of temperature dependencies of phonons in $LiMnPO_4$. Materials Chemistry and Physics. 2011;127(1–2):391-6.

36 Liu C, Wu X, Wu W, Cai J, Liao S. Preparation of nanocrystalline $LiMnPO_4$ via a simple and novel method and its isothermal kinetics of crystallization. Journal of Materials Science. 2011;46(8):2474-8.

37. Jastrzębski W, Sitarz M, Rokita M, Bułat K. Infrared spectroscopy of different phosphates structures. Spectrochimica Acta Part A: Molecular and Biomolecular Spectroscopy. 2011;79(4):722-7.

38. Kellerman D, Medvedeva N, Mukhina N, Semenova A, Baklanova I, Perelyaeva L, et al. Vanadium doping of $LiMnPO_4$: Vibrational spectroscopy and first-principle studies. Chemical Physics Letters. 2014;591:21-4.

39. Xiao J, Chernova N, Upreti S, Chen X, Li Z, Deng Z, et al. Electrochemical performances of $LiMnPO_4$ synthesized from non-stoichiometric Li/Mn ratio. Physical Chemistry Chemical Physics. 2011;13(40):18099-106.

40 Luo Y, Xu X, Zhang Y, Pi Y, Yan M, Wei Q, et al. Three-dimensional $LiMnPO_4{\cdot}Li_3V_2(PO_4)_3$/C nanocomposite as a bicontinuous cathode for high-rate and long-life lithium-ion batteries. ACS Applied Materials & Interfaces. 2015;7(31):17527-34.

41. El khalfaouy R, El knidri H, Belaabed R, Addaou A, Laajeb A, Lahsini A. Synthesis and characterization of $LiMnPO_4$ material as cathode for Li-ion batteries by a precipitation method and solid-state blending. Journal of Materials and Environmental Science. 2016;7(1):40-9.

42. Schmalzried H. Chemical kinetics of solids. John Wiley & Sons; 2008.

43. Vyazovkin S. Computational aspects of kinetic analysis.: Part C. The ICTAC Kinetics Project—the light at the end of the tunnel? Thermochimica Acta. 2000;31;355(1):155-63.

44. Ozawa T. Non-isothermal kinetics and generalized time. Thermochimica Acta. 1986;100(1):109-18.

45. Ozawa T. Estimation of activation energy by isoconversion methods. Thermochimica Acta. 1992;203:159-65.

46. Opfermann J. Kinetic analysis using multivariate non-linear regression. I. Basic concepts. Journal of thermal analysis and calorimetry. 2000;60(2):641-58.

47. Opfermann J, Kaisersberger E, Flammersheim H. Model-free analysis of thermoanalytical data-advantages and limitations. Thermochimica Acta. 2002;391(1):119-27.

48. Vyazovkin S, Wight C. Isothermal and nonisothermal reaction kinetics in solids: in search of ways toward consensus. The Journal of Physical Chemistry A. 1997;101(44):8279-84.

49. Flammersheim H, Opfermann J. Kinetic evaluation of DSC curves for reacting systems with variable stoichiometric compositions. Thermochimica acta. 2002;388(1):389-400.

50. Milev A, McCutcheon A, Kannangara K, Wilson M, Bandara T. Precursor decomposition and nucleation kinetics during platelike apatite synthesis. The Journal of Physical Chemistry B. 2005;109(36):17304-10.

CHAPTER 4

Preparation and Characterisation of Pristine and Carbon Coated $LiMnPO_4$

This chapter investigates the synthesis, physical characterisation and electrochemical behaviour of pristine and carbon coated $LiMnPO_4$. A brief introduction to the use of carbon as a suitable conducting agent is provided. The preparation of pristine and carbon coated samples from the $LiMnPO_4$ precursor at several temperatures is then described. The effect of temperature on the purity and crystallinity of the prepared samples is investigated by X-ray diffraction technique. Vibrational spectroscopic techniques (FT-IR and Raman) are used to investigate the local structural changes upon heating under inert conditions at four different temperatures. The above characterisation techniques are complemented with surface area measurements using the Brunauer-Emmett-Teller (BET) method and morphological examinations using scanning electron microscopy (SEM).

Following physical characterisation, the electrochemical performance of native $LiMnPO_4$ and carbon coated samples are evaluated using cyclic voltammetry (CV) and galvanostatic charge/discharge experiments at temperatures of 0°C, 20°C and 40°C. Firstly, a brief introduction to these techniques is provided. This is followed by the procedure used to prepare and assemble the cathode material and test coin cells respectively. Next, the CV and charge/discharge data are evaluated to determine the performance of the cathode in the test cells. Finally, the electrochemical behaviour is rationalised by correlating it to the physical properties discussed earlier in the chapter.

4.1. Introduction

As discussed in Chapters 1 and 2, research interest is focused on finding alternative active materials to replace the commercialised $LiFePO_4$ which is limited by its lower operating voltage. Consequently, using $LiMnPO_4$ is attractive due to its redox potential of 4.1 V *vs.* Li/Li^+, approximately 0.65 V higher than the potential of $LiFePO_4$ while retaining the advantage of low cost, abundance of raw materials and low environmental impact [1]. However, employing $LiMnPO_4$ as an electrode material is hampered due to its intrinsically poor electronic conductivity and similar to $LiFePO_4$, slow one-dimensional Li-ion diffusion kinetics within the bulk [2, 3]. To harness the full potential of $LiMnPO_4$ in an electrochemical cell, it is necessary to have fast and relatively seamless diffusion of electrons and lithium ions especially for more demanding applications.

Due to this innately poor bulk properties, it is essential to manipulate and optimise the physical characteristics of $LiMnPO_4$ to enhance its electrochemical properties. The most common strategies used include reducing the particle size to a nanometre domain and the addition of a suitable conducting agent [4]. Inhibiting crystal growth or promoting growth in certain crystallographic directions can lead to smaller/thinner particle sizes which reduces or enhance the diffusion path length for Li-ions and electrons. Also, the shorter pathway reduces the likelihood of encountering blockages and defects in the lattice. To improve electronic conductivity, modifying the surface of the particles to include a conductive species can provide a continuous pathway for electrons to flow. For example, a coating or layer of conductive carbon would allow electrons to flow through the crystal lattice thus improving the electronic contact between the particles (Figure 4.1).

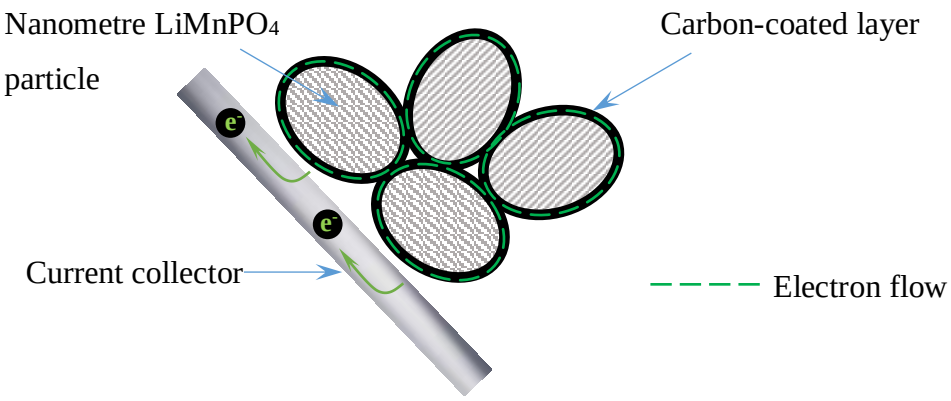

Figure 4.1: Simplified schematic of the ideal structure of $LiMnPO_4$ nanoparticles with a thin and continuous coating of carbon to provide uninterrupted path for electron flow. Adapted from ref. [5].

In addition to improving the electrical conductivity of the material, the addition of carbon has other advantageous effects including: (1) suppressing the undesirable growth of particles during the formation of $LiMnPO_4$ when heating at elevated temperatures and thus improving the surface area to volume ratio; (2) helping minimise agglomeration of particles; (3) reducing the likelihood of the cathode material dissolving in the electrolyte especially with nanosized materials which have greater reactivity by acting as a barrier between the active particles and electrolyte; (4) acting as a reducing agent which was especially important for producing $LiFePO_4$ and; (5) contributing to mechanical stability by better accommodating the volume change upon repeated Li-ion insertion and extraction [4, 6].

Using carbon coating to improve the electrochemical performance of a cathode material was first investigated by Ravet *et al.* [7]. They showed that $LiFePO_4$ coated with carbon demonstrated significantly improved capacity, kinetics and stability compared to samples without any coating [7]. Later studies show that if the particle size of $LiFePO_4$ is optimised, carbon coating can be avoided [8]. However, due to the much inferior electronic conductivity of $LiMnPO_4$, carbon coating is necessary for the material to show reasonable performance [3, 9, 10].

There are different ways to add carbon to the phosphate material. Carbon or carbon containing precursors can be physically deposited on the synthesised $LiMnPO_4$ by mechanical grinding and subsequently firing at higher temperatures to form $LiMnPO_4$/C composites [1, 11-18]. Alternatively, to allow better mixing of carbon with the active material, it can be added directly (*in situ*) to the reaction mixture containing the Li, Mn and P precursors in both solid-state and solution based synthesis [19, 20]. To this effect, *in situ* addition would enable a more uniform dispersion and homogenous distribution of carbon and the active material [21]. Also, indirect kinetic improvements may come from the restriction of the growth of active particles during the synthesis caused by residual carbon in between the grains [4]. This phenomenon is caused by the space steric effect of amorphous carbon which increases the diffusion activation energy of reactants and hence slows down the growth rate of grains [22].

Carbon can be added directly such as in the form of acetylene black [16, 18]. However, if carbon is added in direct form, it can settle and agglomerate during synthesis and therefore will require constant mixing. The major challenge is dispersing the carbon well with the precursors. A possible solution is to functionalise the carbon material to improve its dispersion throughout the material. Alternatively, it is more effective to introduce an organic precursor or carbon containing ligands into the reaction mixture. $LiMnPO_4$ or its precursor can be coated with organic ligands and heated to an elevated temperature to pyrolyse the organic layer to form a layer of conductive carbon on the active material. The advantage of adding a carbon precursor compound is that it can be dissolved into the reaction solution and thus homogenously distributed throughout the mixture.

In the literature, the use of various organic materials has been reported. For example, sucrose [13, 17, 20, 23, 24], glucose [13, 25], citric acid [13, 26], ascorbic acid [13] and carboxy methyl cellulose (CMC) [27] are amongst those commonly used organic compounds. Sucrose is among the most widely used carbon precursors for achieving excellent carbon coating. As such, it is chosen as the carbon source for coating the $LiMnPO_4$ produced here *via* the novel sol-gel method. It is however important to note that the quality of coating is also dependant on the synthetic method used and the physical characteristics of $LiMnPO_4$.

While the addition of carbon is necessary to improve the performance of $LiMnPO_4$ based cells, it can have some detrimental effects. Though sp^2-bonded carbon (graphite-like carbon) is an excellent electrical conductor, it is an electrochemically inactive material and contributes to the 'dead weight' in a battery. Hence, a carbon coating reduces the capacity and volumetric energy by reducing the tap density of the active material [28]. Also, substantive loadings of carbon are often required to achieve respectable specific energy densities that are closer to the theoretical value of 171 mA g^{-1}. It must be noted that carbon coating does not improve the intrinsic electrical conductivity of the material but rather the extrinsic electrical conductivity. To explain further, carbon coating mainly improves the electrical contact between the active particles and subsequently to the current collector. Thus, it creates a current distribution network which facilitates current collection at an improved charge and discharge kinetics from the particles [4]. The physical characteristics of the prepared $LiMnPO_4$ can affect this network leading to lower than expected electrochemical properties. Moreover, while it can improve electron transfer kinetics, it can also have an adverse effect on the diffusion of Li-ions through the material. Ideally, the carbon layer should be thin enough to prevent any obstruction of Li-ions from diffusion across it while also allowing a continuous path for electrons to flow.

An important consideration is also the 'quality' of the carbon coating on the $LiMnPO_4$ phase, which is determined by the ratio between sp^2 and sp^3 hybridised carbons. The formation of sp^3 bonded carbon during the decomposition and subsequent carbonisation of the carbon containing precursors may not contribute to electron conductivity. In sp^3 configured carbons, four sp^3 orbitals make a strong sigma (σ) bond to the neighbouring atom [29]. An example of sp^3 hybridised material is diamond, which is an electrical insulator. Here, there are no free electrons available to conduct electricity. Nevertheless, as mentioned, the presence of these carbons at the interfaces supress particle growth and hence reduces the diffusion distance for Li-ions. On the other hand, in the sp^2 configuration, a carbon atom forms three σ bonds and the p orbital forms a π bond [29]. An example of a material containing sp^2 hybridised carbon is graphite, which is an excellent electrical conductor. The carbon coating on a cathode active material can consist of a mixture of these types of bonding. Ideally, the carbon coating should consist mainly of sp^2 bonded carbons with delocalised π electrons which will improve the electron conductivity as well as modulate the crystal size. Thus, the physical properties, including electronic conductivity, of carbon structures is highly dependent on the ratio of sp^2 (graphite-like) to sp^3 (diamond-like) bonds.

In summary, carbon coating is essential to enhance the performance of $LiMnPO_4$ in an electrochemical cell. It can improve extrinsic electronic conductivity of the active material as well as supress undesirable particle growth. However, it can also reduce the density of the active material and obstruct the diffusion of Li-ions. An ideal situation is to produce a thin layer of carbon coating on the active material that consists of a higher ratio of sp^2 to sp^3 hybridised carbon. In practice, however, its impact can be difficult to predict precisely because of other factors including the morphology of the active material it is coating. This chapter looks at the effect of sucrose derived carbon coating (3% and 5% carbon) on the physical and electrochemical characteristics of $LiMnPO_4$ prepared according to the novel synthetic procedure described in Chapter 3.

4.2. Experimental

This section describes the preparation of native and carbon coated $LiMnPO_4$ product at different temperatures according to the procedure described in Chapter 3. Next, the method of incorporating the $LiMnPO_4$ material into a cathode material and assemble into a test cell is described. The $LiMnPO_4$ products are physically characterised by vibrational spectroscopic techniques (IR and Raman), Powder X-ray diffraction (PXRD) and field emission scanning electron microscopy (FE-SEM) to determine the local and long range structural changes to the final product. This is followed by electrochemical characterisation using cyclic voltammetry and galvanostatic charge/discharge measurements.

4.2.1. Materials

The materials used for the preparation of the $LiMnPO_4$ precursor are as described in Chapter 3 (Section 3.2.1). For the preparation of the electrochemically active cathode and for the assembly of the electrochemical cell, sucrose ($C_{12}H_{22}O_{11}$, purity > 99.7%), lithium metal (purity 99.9%) and sodium carboxymethyl cellulose ($[C_6H_7O_2(OH)_x(OCH_2COONa)_y]_n$, molecular weight [$M_w$] = 90,000 kDa) were obtained from Sigma-Aldrich Pty. Ltd (Castle Hill, NSW). TIMCAL C-NERGY™ SUPER C65 conductive carbon black required for the preparation of the electrode slurry, aluminium foil (purity 99.3%) used as the cathode current collector, and the components required to assemble CR2032 coin cells (cap, can, spacer and spring) were purchased from MTI Corp. (Richmond, CA, USA). A sheet of Celgard® 2500 polypropylene separator was provided by Celgard Inc. (Charlotte, North Carolina, USA). A commercial electrolyte (Purolyte® A5 series) was formulated by Novolyte Technologies (Independence, Ohio, USA), which contained a 1:1 by weight mixture of ethylene carbonate and dimethyl carbonate with 1.0 M lithium tetrafluorophosphate ($LiPF_6$).

4.2.2. Synthesis of native and carbon-coated $LiMnPO_4$ from precursor

The $LiMnPO_4$ and $LiMnPO_4$/C precursors were prepared as described in Chapter 3 (Section 3.2.2) with a modification for carbon coated samples to accommodate the addition of sucrose. To achieve the theoretically predicted 3 and 5 wt% carbon coating, approximately 2.35 g and 4.00 g of sucrose respectively was introduced during the initial mixing stage at ambient temperature. The mixing time was increased to allow the sucrose to dissolve fully in the solution. Further, the bottle was placed in the oven for 5 mins at 70°C and mixed again to fully dissolve the sugars. The resulting $LiMnPO_4$ and $LiMnPO_4$/C precursors were pre-decomposed in air at an intermediate heating step at 250°C as described in Chapter 3 (Section 3.3.5.3). All the samples were also dry ball-milled at 400 rpm using the same procedure as described in Chapter 3 (Section 3.2.2) to keep the particle size small before the final heat treatment.

The final $LiMnPO_4$ and $LiMnPO_4$/C products were prepared by isothermal heating at 400, 500, 600 and 700ºC for 2 hours using a quartz-glass tube mounted in a single-zone tube-furnace (Lindberg/Blue Mini-Mite™). The samples were heated in an inert argon (Ar) atmosphere (purity > 99.999%). This system provides a controlled dynamic atmosphere with a constant flow rate during heat treatment. Any gases evolved from the substrates during heating is removed from the system when passed through the oil trap. A schematic of this experimental set-up is shown in Figure 4.2.

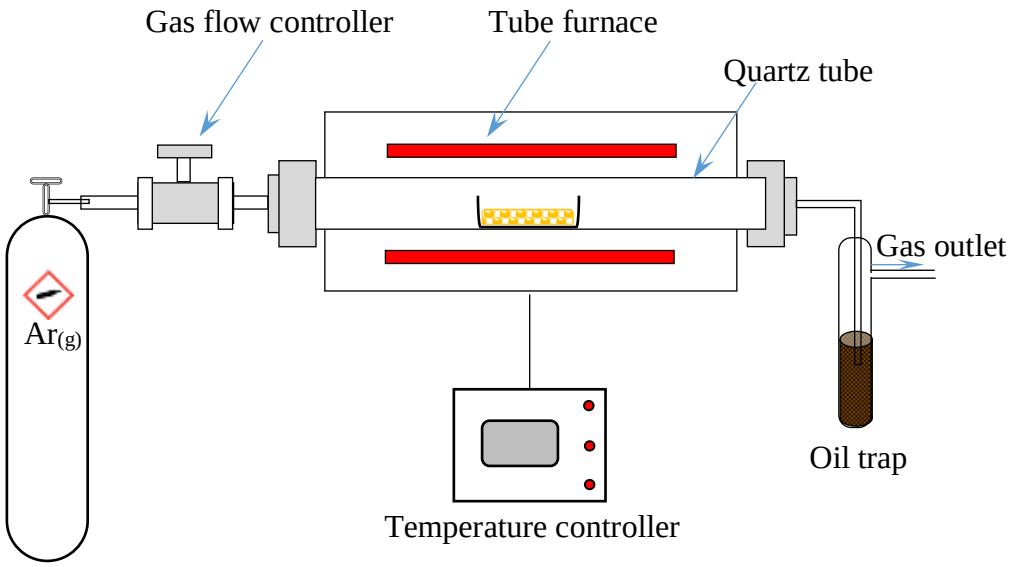

Figure 4.2: Schematic illustration of the quartz-glass tube furnace setup.

An appropriate quantity of precursor material was measured into an alumina boat and placed in the middle of the heating zone of the tube furnace. The tube furnace was firstly purged with argon gas at ambient temperature for 30 minutes at a rate of 1.0 L min^{-1} to remove residual air from the quartz tube. The gas flow rate was then decreased and kept constant at 25 mL min^{-1} throughout heating from ambient to desired temperature (10°C min^{-1}), isothermal heating for 2 hours and finally during cooling to ambient temperature. The samples prepared are summarised in Table 4.1. The sample sets will be referred to as S1, S2 and S3 samples; denoting a theoretical carbon content of 0, 3 and 5% respectively.

Table 4.1: Summary of samples prepared at different carbon contents and temperatures. S1 are sucrose free samples, S2 and S3 samples contain two different amounts of sucrose.

Sample set	Temperature (°C)	Theoretical carbon content (%)	# of samples
1	400	0	4
	500		
	600		
	700		
2	400	3	4
	500		
	600		
	700		
3	400	5	4
	500		
	600		
	700		
		Total samples	12

4.2.3. Cathode preparation

To improve the electrochemical performance of $LiMnPO_4$, it is understood that ball-milling of the samples is required. Depending on the initial nature of the samples, this is done to 1) reduce particle size with minimum agglomeration; 2) to improve the homogeneity of the samples and; 3) increase the overall surface area of the samples. All samples were wet-ball milled at 400 rpm in an 80 mL zirconium oxide (ZrO_2) jar containing ethanol and water (1:1 by volume) with a mass ratio of 1:20 of sample to ZrO_2 balls.

Electrodes for the electrochemical measurements were fabricated by mixing electroactive material (70 wt%), conductive carbon black (20 wt%) and low viscosity sodium carboxymethyl cellulose (CMC) binder (10 wt%) in a solvent consisting of a 50:50 ratio of water to ethanol. The resulting slurry was then mixed in a planetary ball mill (Fritsch pulverisette 6) for 40 minutes at 100 rpm with 10 x 5mm and 1 x 20mm diameter ZrO_2 balls. This was done to ensure uniform dispersion of the active material, binder and carbon black. A sheet of aluminium foil was sanded with 600 grit sandpaper and washed with absolute ethanol to improve the adhesion properties of the foil. The mixed slurry was then cast onto this aluminium foil using a K-hand coater set (RK PrintCoat Instruments Ltd) employing an orange K bar which can apply wet film deposits of 60 µm. The electrode sheet was then air dried in a fume hood until touch-dry. It was then transferred to an oven set at 100°C for 1 hour. Finally, the sheet was placed in a vacuum oven (0.5 bar) and kept overnight to remove any trace amounts of solvent. The cathode was prepared by cutting 15 mm diameter disks from the prepared electrode sheets using a precision disk cutter (MTI Corp.). The cathodes were then stored in sealed bags and placed in a desiccator to be used later for battery preparation.

4.2.4. Coin cell assembly

The electrodes were transferred into an Ar-filled glovebox where CR2032 coin cells were assembled. The oxygen and water content in the glovebox were both maintained below 2 ppm. The cell was assembled by placing the lithium metal (19 mm diameter) which was used as the anode at the base of the can while the prepared $LiMnPO_4$ or $LiMnPO_4$/C was used as the cathode (15 mm diameter). In between the electrodes, Celgard® 2500 polypropylene membrane was placed as the separator (19 mm diameter). The electrolyte comprising of a 1.0 M solution of $LiPF_6$ in ethylene carbonate and dimethyl carbonate mixture (1:1 w/w) was added to the coin cells before sealing the cell with a hydraulic crimping press (MTI Corp.). The assembling order is shown in Figure 4.3. The coin cell was then checked for short circuits by measuring the cell voltage using a multimetre. If acceptable, they were taken out of the glove box for electrochemical measurements.

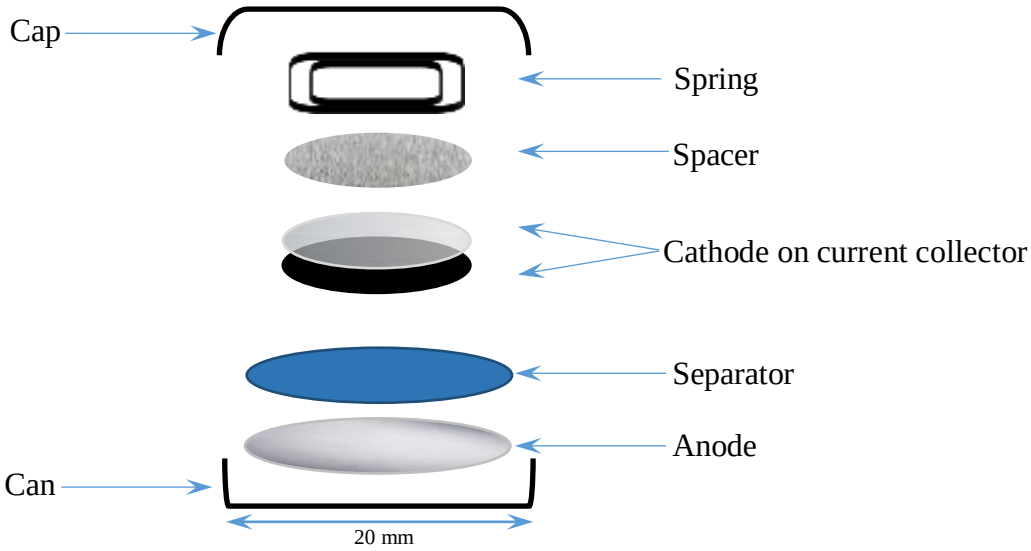

Figure 4.3: Schematic representation of coin test cell assembly process showing the order of the components to construct the cell.

4.2.5. Electrochemical characterisation

Electrochemistry is the study of the relationship between chemical response of a system when subjected to an electrical stimulation [30]. In an electrochemical experiment, two of the main parameters studied is the potential (*E*) and current (*I*). The response of a system to an electrochemical stimulus depends on which parameter is used as the excitation signal. When plotting different parameters in several ways, a wealth of information about the properties of a material can be derived.

The most widely used experiments to study electrochemical systems include cyclic voltammetry (CV), galvanostatic charge/discharge and electrochemical impedance spectroscopy (EIS). Here, electrochemical characterisation was performed on a five channel Biologic VSP Potentiostat System equipped with 3 standard VSP-01 potentiostat channels and 2 VSP-01/Z EIS capable channels controlled by the ECLab®. software. For all the measurements, a three-electrode system is used. This system is composed of the working electrode (WE), counter electrode (CE) and the reference electrode (RE) (Figure 4.4). A schematic of the set-up is shown below.

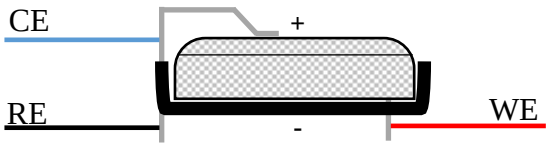

Figure 4.4: Schematic representation of the three-electrode system. The negative terminal or cathode is designated as the WE while the CE and RE are connected to the positive terminal or the lithium anode.

Three-electrode systems have an evident experimental benefit over the two-electrode configuration by measuring only one half of the cell. In two-electrode cells that contain a WE and a RE, current flows through the RE during measurements. A significant current flow can then alter the chemical composition of the RE and cause its potential to move away from the expected standard value. This can be circumvented using a three-electrode configuration which incorporates a CE. In this set-up, the current flows between the WE and the CE. The role of the CE is to ensure that current does not run through the RE, since such a flow would change the potential of the RE. In practice a small amount of current does flow through the RE resulting in a negligible potential change. Since voltage cannot be measured for a single isolated electrode, this provides an electrode with a standard value that the potential difference of the WE can be referenced to. Therefore, the potential changes of the WE are measured independent of changes that may occur at the CE. This separation allows for an electrochemical reaction to be studied with confidence and accuracy. In the potentiostatic mode, the potentiostat controls the voltage of the CE against the WE so that the potential difference between the WE and the RE is definite, and corresponds to the value required by the user, i.e. V is constant. In the galvanostatic mode, the current flow between the WE and the CE is controlled, i.e. I is constant.

Here, cyclic voltammetry (CV) was applied between 3.0 V and 4.7 V with scan rates of 0.05, 0.5 and 1.00 mV s^{-1}. To determine the charge-discharge cyclic performance, the coin cells were cycled galvanostatically between 3.0 V and 4.7 V (*vs.* Li/Li^+) at a constant current (CC) of C/50 based on a theoretical specific capacity 1C = 171 mA.h g^{-1}. The electrochemical capacity is calculated based on the amount of the active material. Relaxation time before the commencement of the measurements was 2 hours. The CV and charge-discharge behaviour was both evaluated at 3 temperatures: 0, 20 and 40ºC. All measurements were carried out in a temperature controlled environmental chamber (ACS Discovery).

4.3. Results and discussion

This section, at first, deals with a discussion on the physical characteristics of native and carbon-coated $LiMnPO_4$ prepared at 400, 500, 600 and 700ºC. The preliminary electrochemical performance will then be evaluated using cyclic voltammetry (CV) and galvanostatic charge and discharge cycling.

4.3.1. Physical characterisation of $LiMnPO_4$/C

The physical properties of the samples as a function of temperature and carbon content were monitored using XRD, IR, Raman, FE-SEM and BET surface area analysis.

4.3.1.1. Determination of carbon content

The amount of carbon to be deposited on the electroactive material from sucrose is calculated to be 3 and 5% by weight (S2 and S3). One set of precursor samples was prepared without the addition of sucrose (S1). However, the total carbon content in the samples may be different when the presence of other organic ligands in the samples are considered. Although most of the ligands are expected to be decomposed during heating in air at 250ºC, some may remain which would add extra carbon on the samples. The thermogravimetric analyser (TGA) was used to determine the carbon content in the samples. The samples were heated in air to 1000ºC while the weight-loss was measured. The weight loss of the samples below 250°C was due to the evaporation of adsorbed moisture, whereas the weight-loss in the interval 250ºC 1000ºC was attributed to the decomposition of residual carbon.

The carbon content of the respective samples is shown in Table 4.2. The respective TGA curves are given in Appendix A.

Table 4.2: Approximate carbon content of S1, S2 and S3 samples, synthesised at different temperatures as determined by thermogravimetric analysis.

Sample #	% Carbon content				Theoretical carbon content (%)
	Temperature (°C)				
	400	500	600	700	
1	6.0	5.0	5.0	5.0	0
2	8.0	7.0	7.0	7.0	3
3	9.0	8.0	8.0	8.0	5

The amount of carbon contribution from the ligands used in the reaction is quite significant. The samples prepared at 400°C contained a slightly higher amount due to the extra organic material that would be present at that temperature. It is important to know the carbon content in each sample to calculate the capacity of the electroactive materials in a test coin cell.

4.3.1.2. Powder x-ray diffraction

Powder X-ray diffraction (PXRD) was employed to determine the phase purity of the final products. The PXRD patterns were followed along the increasing temperature range. The parameters used to acquire the patterns are the same as described in Chapter 3 (Section 3.3.3.3.). The patterns obtained for S1, S2 and S3 samples are shown in Figures 4.5 – 4.7.

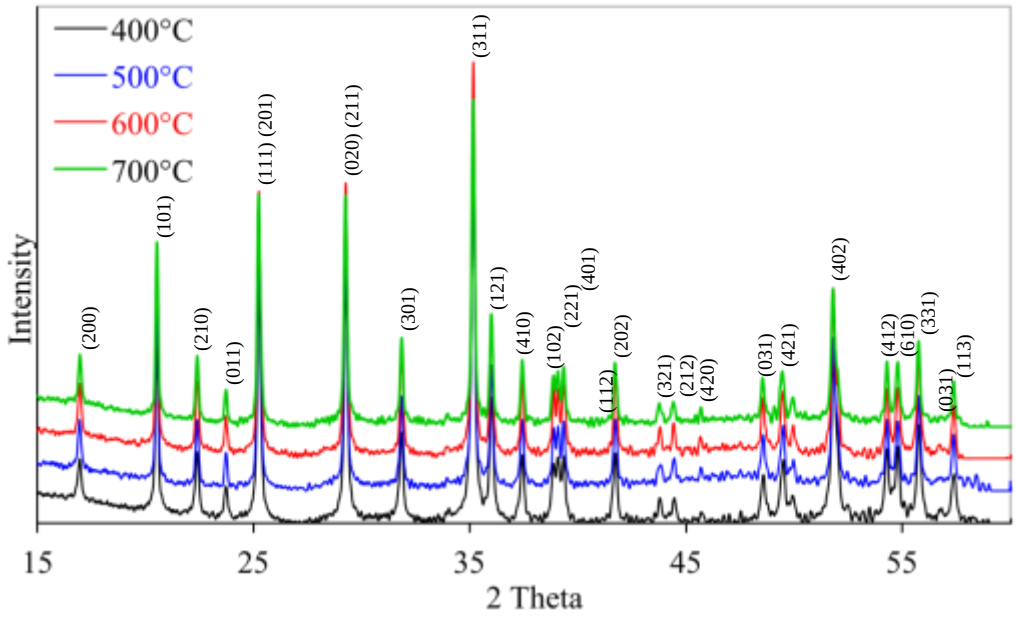

Figure 4.5: PXRD pattern of the S1 samples prepared at 400°C, 500°C, 600°C and 700°C in argon.

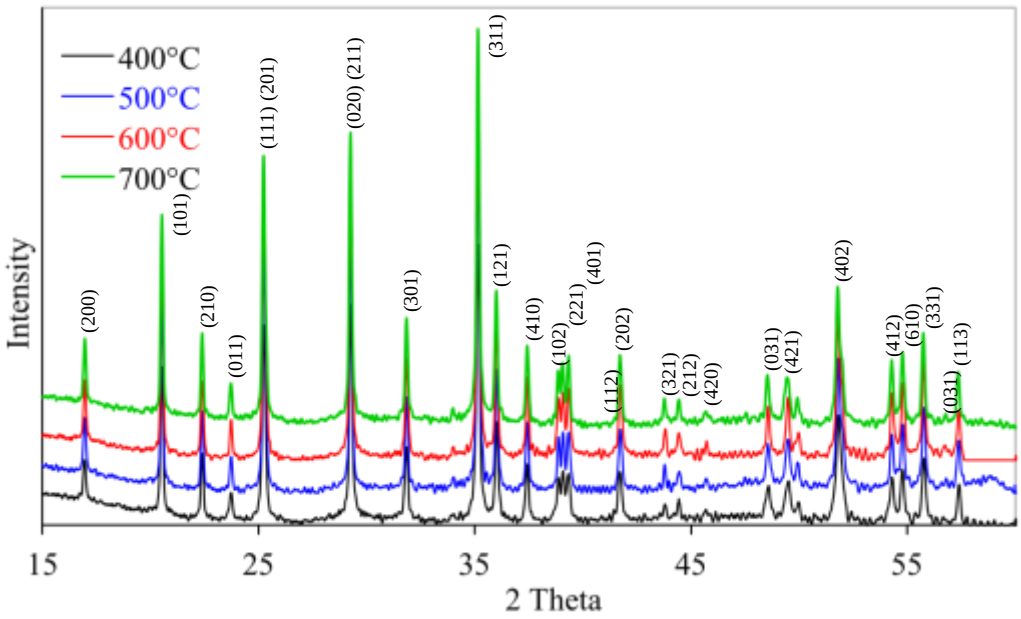

Figure 4.6: PXRD pattern of the S2 samples prepared at 400°C, 500°C, 600°C and 700°C in argon.

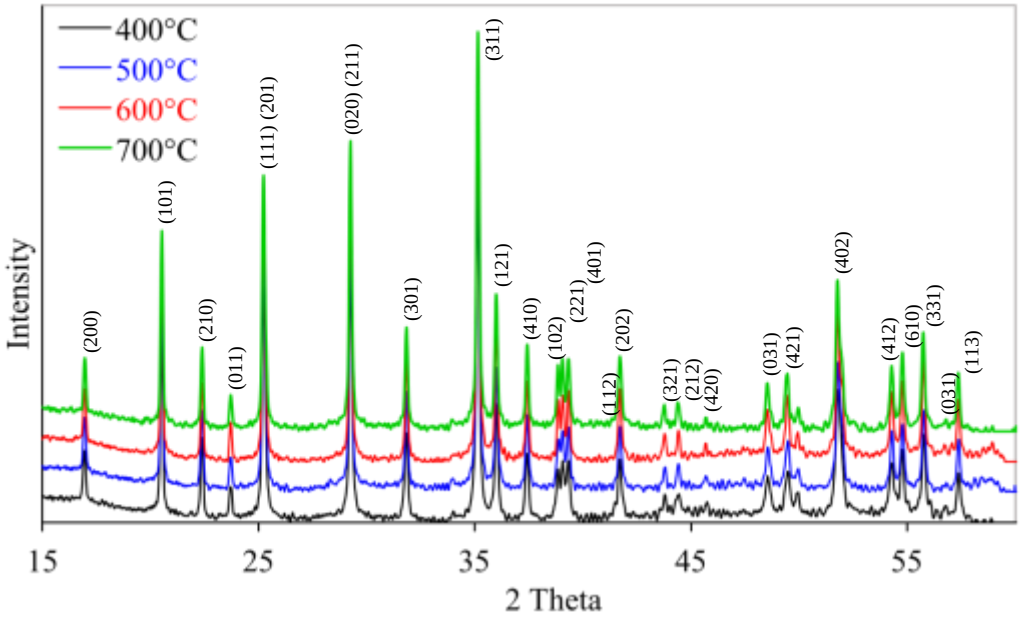

Figure 4.7: PXRD pattern of the S3 samples prepared at 400°C, 500°C, 600°C and 700°C in argon.

All the samples produced in S1, with no additional carbon from sucrose, were highly crystalline in nature. The method developed in Chapter 3 allowed the material produced at temperatures as low as 400°C to be highly crystalline. All the samples are well crystallised in the single-phase orthorhombic olivine structure with a *Pnma* space group. The diffraction peaks are in excellent agreement with the diffraction pattern of the standard $LiMnPO_4$ material (JCPDS No. 74-0375). The diffraction peaks are slightly narrower and intense as the temperature was increased, indicating the slight improvement in crystallinity of the material at higher temperatures. However, overall, the increase in temperature does not seem to have a significant impact either on the width of the peaks or the intensity. The same trend is observed for samples from S2 and S3. For corresponding samples at the same temperature, this may be due to the presence of relatively similar amounts of carbon as shown in Table 4.2. Moreover, when the temperature is increased from 400°C to 700°C, the insignificant increase in peak width and intensity is also due to the presence of carbon between the crystals which may inhibit the crystal growth as discussed in Chapter 2.

As mentioned in Chapter 2, the Li-ion diffusion pathway in the olivine structured lattice of $LiMnPO_4$ is known to be along the *b* (010) direction or the a–c planes, where the Li-ions 'hop' between the octahedral sites *via* a hollow tetrahedral path formed by the edge-sharing LiO_6 octahedra [31, 32]. Therefore, growth in this crystallographic direction is more favourable for enhanced electrochemical performance [3]. The Miller indices of the peak have been assigned in Figure 4.5. Two of the most intense peaks are the (020) and (311) peaks. Ideally, growth along the (020) direction is preferred. Having more a-c planes is advantageous because Li ions are confined to move only parallel to the *b* axis [33, 34]. This crystal orientation would be optimal for faster ionic diffusion and good kinetics of Li-ion extraction and insertion. Consequently, the crystal orientation of the material can affect the Li-ion diffusion rate.

In all the samples, the strongest peak is along the (311) direction with the (020) being the next strongest peak. The ratio of relative intensity between the (020) and (311) peaks were calculated to see if there were any significant differences in the preferred crystal orientation when: (1) the temperature is increased from 400℃ to 700℃; and (2) between S1, S2 and S3 samples. For S1 samples, the ratio of (020) to (311) for all the samples ranged from 0.70 to 0.74 with the slight increase observed at higher temperatures. For S2 samples, the ratio ranged from 0.73 to 0.79. Likewise, in S3 samples, it ranged from 0.73 to 0.77. In standard XRD patterns of $LiMnPO_4$, the most intense peak is the (311) band and the peak intensity ratio of (020) and (311) is 0.78. The XRD patterns of the samples here closely matched this data [15].

These results show that the heat treatment at increased temperatures do not affect the crystal orientation of the material as the ratio of intensity at 400℃ does not differ significantly to that at 700℃ for the samples. No significant differences are observed among them as well which is consistent with the similar quantities of carbon present as shown in Table 4.2. Since the (010) direction is the most facile pathway for lithium ion diffusion in olivine type of crystals, the diffusion of Li-ions in this case may be limited due to the greater preferred growth along the (311) plane seen here. Since different crystallographic planes have different interfacial energies, it can be concluded that the synthetic conditions employed are more suited to the formation of (311) crystallographic planes more than the (020) planes.

No impurity phases such as Li_3PO_4 and $Mn_2P_2O_7$ were detected in any of the prepared samples. This does give an indication that the use of a two-stage heating method can improve the purity of the material regardless of the additional mass from sucrose. Furthermore, no carbon peak is observed in the XRD patterns due to the relatively smaller amount (carbon ~5 – 9 wt.%), indicating the amorphous nature of the carbon obtained from the pyrolysis of sucrose and other ligands in the samples. Also, usually at temperatures of 400°C (at constant pressure), the carbon is amorphous and an ordered structure starts to form around 500°C [16, 35]. The presence of carbon can be observed by Raman spectroscopy shown later. Overall, all the peaks shown are strong and narrow indicating the high crystallinity of the prepared samples. Also, the relative intensity of the peaks is remained unchanged as the temperature was increased. The XRD results demonstrated the feasibility of synthesizing pure $LiMnPO_4$ phase and its carbon composites *via* this method.

4.3.1.3. FT-IR analysis

The XRD method provides data about the crystal structure and phase composition of the material. FT-IR spectroscopy can be used to confirm the formation and stability of the phosphate, PO_4^{3-} bond in $LiMnPO_4$. The FT-IR, in this case can be used to systematically monitor the variations of these structural characteristic groups and vibrational bonds across the different sample sets prepared at different temperatures. It is also a sensitive method to determine phase composition. The location of the absorbed maximum can indicate material composition, so even slight variations of the composition influence energy of material bonding and as such the frequency of the vibrations [36]. It is probably circumspect however, given the variable nature of the carbons derived from the sucrose and/or from the carbon containing ligands not to exclude C–O and C–H assignments for some carbons that possess a large number of defects and is exposed to heteroatoms. Our view is that these bonds will give rise to characteristic vibrations which could be observed using infra-red and/or Raman spectroscopy [37].

Infrared-attenuated total reflection (IR-ATR) spectroscopy of the three sample sets was carried out on a Bruker Vertex 70 FT-IR spectrometer equipped with a PLATINUM Diamond ATR accessory. The background and sample data were acquired at a resolution of 4 cm^{-1} from 4000 cm^{-1} to 400 cm^{-1} and averaged for 256 scans to establish an acceptable signal to noise ratio. The IR spectra were all baseline corrected and normalised to 2.0 absorbance units (a.u.)

Figures 4.8 to 4.10 show the IR spectra of S1, S2 and S3 samples at four different temperatures, 400, 500, 600 and 700°C. No peaks were observed at wavelengths greater than 1500 cm^{-1} other than an absorption band of very weak intensity within the range 1950 - 2100 cm^{-1} for some of the samples which is associated with combinations of (PO_4) v_3, v_1 modes. [36]. Therefore, the wavelengths shown here are within 1500 cm^{-1} to 400 cm^{-1} for clarity.

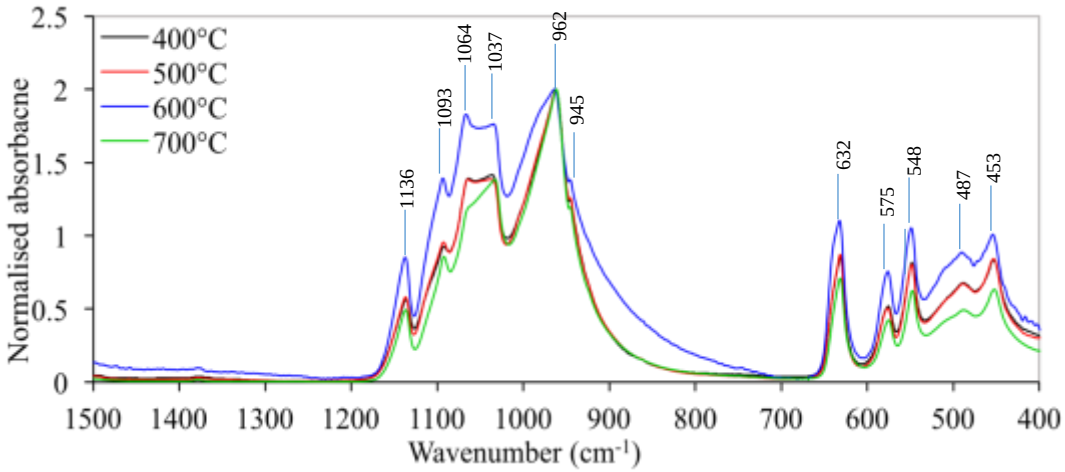

Figure 4.8: IR spectra of S1 samples prepared at 400°C, 500°C, 600°C and 700°C.

Table 4.3: Assignment of IR bands of S1 samples prepared at 400°C, 500°C, 600°C and 700°C.

Peak	Frequency range (cm^{-1})	Peak Assignment	Intensity	Mode
1	1136	P-O (PO_4^{3-}, sharp)	medium	anti-symmetric stretch
2	1093	P-O (PO_4^{3-}, sharp)	medium	anti-symmetric stretch
3	1064	P-O (PO_4^{3-}, broad)	strong	anti-symmetric stretch
4	1037	P-O (PO_4^{3-}, broad)	strong	anti-symmetric stretch
5	962	P-O (PO_4^{3-}, sharp)	strong	anti-symmetric stretch
6	945	P-O (PO_4^{3-}, shoulder)	medium	symmetric stretch
7	632	P-O (PO_4^{3-}, broad)	medium	bending
8	575	P-O (PO_4^{3-}, broad)	medium	bending
9	548	P-O (PO_4^{3-}, broad)	medium	bending
10	487	Li-O (LiO_6)	weak	bending cage
11	453	Li-O (LiO_6)	weak	bending cage

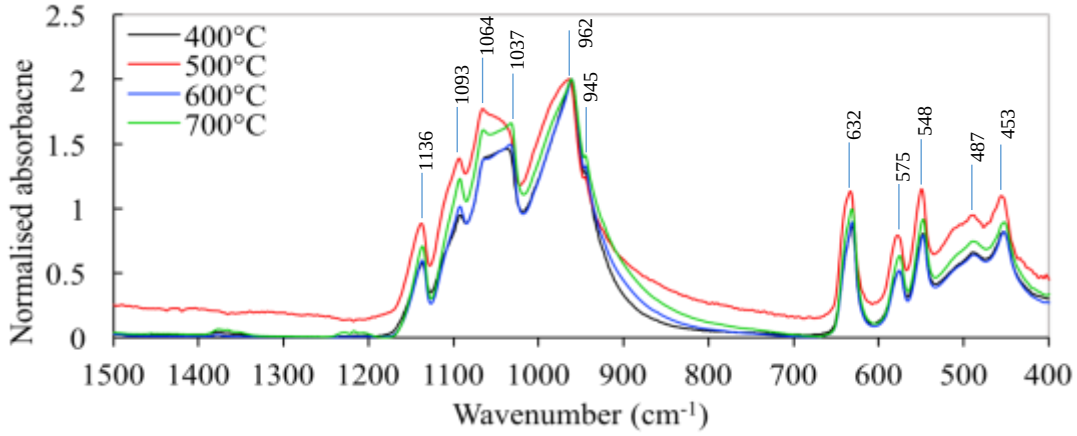

Figure 4.9: IR spectra of S2 samples prepared at 400°C, 500°C, 600°C and 700°C.

Table 4.4: Assignment of IR bands of S2 samples prepared at 400°C, 500°C, 600°C and 700°C.

Peak	Frequency range (cm^{-1})	Peak Assignment	Intensity	Mode
1	1136	P-O (PO_4^{3-}, sharp)	medium	anti-symmetric stretch
2	1093	P-O (PO_4^{3-}, sharp)	medium	anti-symmetric stretch
3	1064	P-O (PO_4^{3-}, broad)	strong	anti-symmetric stretch
4	1037	P-O (PO_4^{3-}, broad)	strong	anti-symmetric stretch
5	962	P-O (PO_4^{3-}, sharp)	strong	anti-symmetric stretch
6	945	P-O (PO_4^{3-}, shoulder)	medium	symmetric stretch
7	632	P-O (PO_4^{3-}, broad)	medium	bending
8	575	P-O (PO_4^{3-}, broad)	medium	bending
9	548	P-O (PO_4^{3-}, broad)	medium	bending
10	487	Li-O (LiO_6)	weak	bending cage
11	453	Li-O (LiO_6)	weak	bending cage

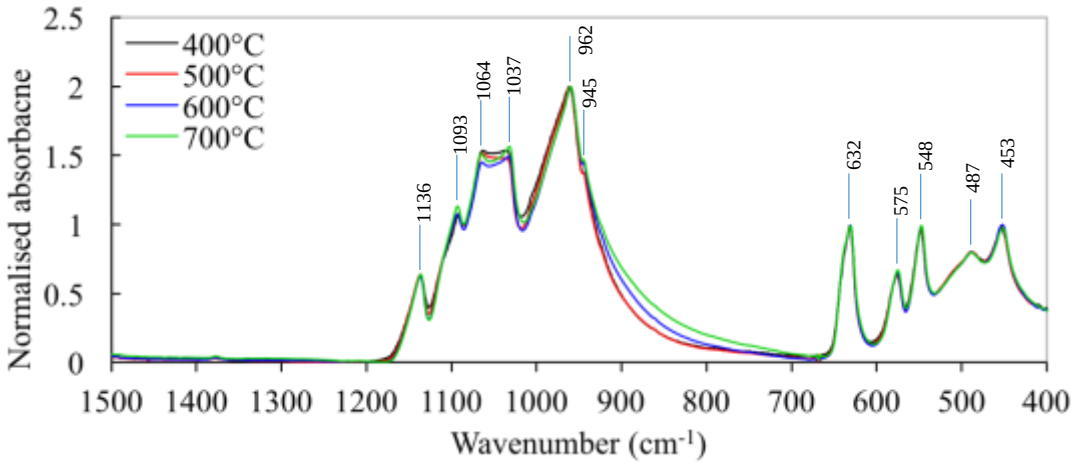

Figure 4.10: IR spectra of the S3 samples prepared at 400°C, 500°C, 600°C and 700°C.

Table 4.5: Assignment of IR bands of S3 samples prepared at 400°C, 500°C, 600°C and 700°C.

Peak	Frequency range (cm^{-1})	Peak Assignment	Intensity	Mode
1	1136	P-O (PO_4^{3-}, sharp)	medium	anti-symmetric stretch
2	1093	P-O (PO_4^{3-}, sharp)	medium	anti-symmetric stretch
3	1064	P-O (PO_4^{3-}, broad)	strong	anti-symmetric stretch
4	1037	P-O (PO_4^{3-}, broad)	strong	anti-symmetric stretch
5	962	P-O (PO_4^{3-}, sharp)	strong	anti-symmetric stretch
6	945	P-O (PO_4^{3-}, shoulder)	medium	symmetric stretch
7	632	P-O (PO_4^{3-}, broad)	medium	bending
8	575	P-O (PO_4^{3-}, broad)	medium	bending
9	548	P-O (PO_4^{3-}, broad)	medium	bending
10	487	Li-O (LiO_6)	weak	bending cage
11	453	Li-O (LiO_6)	weak	bending cage

The IR and Raman vibrations of metal-phosphates including $LiMnPO_4$ can be divided into internal (the PO_4^{3-} tetrahedron) and external (lattice) vibrations. These types of vibrations are generally within distinctive wavenumber ranges; (1) lattice modes < 400 cm^{-1}, 2) bending vibrations (ν_4; asymmetrical and ν_2; symmetrical) of the valence bonds of PO_4^{3-} tetrahedron between 400 – 700 cm^{-1}; and (3) stretching vibrations (ν_3; asymmetrical and ν_1; symmetrical) of the valence bonds of PO_4^{3-} tetrahedron between 900 – 1250 cm^{-1} [38-43]. Here, monitoring of any changes in these regions is useful to investigate if increased temperatures induce local structural changes.

The IR spectral features of $LiMnPO_4$ have been previously assigned based on group theory analysis, isotope studies, and direct comparison to similar olivine structures ($LiMPO_4$; M = Fe, Mg, Ni) [44-48]. In these investigations, the vibrational spectra have been assigned on the assumption that the vibrations can be divided into internal modes (stretching and deformation vibrations of the PO_4^{3-} groups) and external modes (translational vibrations of the cations and the liberations of the PO_4^{3-} groups). This assumption is based on the fact that the chemical bond between P and O is much stronger than that between Li/Mn and O. Consequently, the vibrating frequency of the PO_4^{3-} groups is virtually indistinguishable in different compounds and does not differ much from that of the free tetrahedral PO_4^{3-} [49].

The internal vibrations originate from the fundamental P-O modes of the free PO_4^{3-} tetrahedron. The free PO_4^{3-} ion under ideal T_d symmetry has four normal modes: ν_1, ν_2, ν_3 and ν_4 (ν_1 = 990 – 920 cm^{-1}, ν_2 = 465 – 320 cm^{-1}, ν_3 = 1155 – 950 cm^{-1} and ν_4 = 650 – 475 cm^{-1}). All these modes are Raman active whereas ν_3 (antisymmetric O-P-O stretching vibration) and ν_4 (antisymmetric O-P-O bending vibration) are the only infrared active modes. In the vibrational spectra of crystalline substances containing PO_4^{3-}, the frequencies of the corresponding vibrations vary as a function of the nature of the cations and the crystal structure. The latter determines the symmetry of the PO_4^{3-} groups in the crystal lattice and can lead to the splitting of the degenerate modes and of the resonance interaction of the vibrations, which increases the number of bands in the spectra. Applied to $LiMPO_4$ compounds, upon incorporating in the crystal lattice of M^{2+} and Li^+, the T_d symmetry of the free phosphate ion is reduced and the symmetric stretching and bending modes become IR active. Consequently, additional IR spectral features due to the phosphate group appear. The theoretically predicted IR and Raman bands are used as a tool to investigate the purity and the structure of the $LiMPO_4$ material.

The IR spectra of S1 samples (Figure 4.8) showed similar patterns for all the samples regardless of the temperature used. The peak locations for all temperatures were the same with the only slight differences being the shape and breath of the peaks. Usually at lower temperatures the peaks are expected to be broader and less splitting corresponding to the lower degree of crystallinity. Here, the IR data is consistent with the XRD patterns that samples produced at 400°C are highly crystalline. The vibrations here are sharp and very well defined.

The IR spectra of S1 samples prepared at 400, 500, 600 and 700°C all demonstrate five bands due to the $LiMnPO_4$ phase at 1136, 1093, 1064, 1037 and 962 cm^{-1}. These are assigned to asymmetrical ν_3 P-O stretches in the PO_4^{3-} anion whereas the shoulder at ~ 945 cm^{-1} observed on the low-frequency side of the resonance at 962 cm^{-1} absorptions is assigned to the ν_1 symmetrical stretches. The three IR bands at 548, 575 and 632 cm^{-1} are assigned to asymmetrical PO_4^{3-} bending vibrations whereas the bands at 487 and 453 cm^{-1} are assigned to so called Li-ion "cage modes" in LiO_6 octahedral units induced by the contributions of ν_2 bending modes and Li-ion vibrational character [43, 44]. The external modes, i.e. below 400 cm^{-1} composed of Li^+, Mn^{2+} and PO_4^{3-} translations and rotations would also be consistent here in line with the stability of the material from 400 to 700°C.

The S2 and S3 samples (Figure 4.9 and 4.10) all show similar results to peak positions at the same wavelengths. The bands are located at the same wavelength and similar intensities as the temperature is increased for all the sample sets. This provides conclusive evidence that the PO_4^{3-} group is very stable in this system. The use of an intermediate heating step eliminated the $Mn_2P_2O_7$ impurity that was in the system as discovered in Chapter 3. This was proven using XRD. FT-IR is however a far more sensitive technique. The absence of asymmetric and symmetric stretching modes at around 763 and 954 cm^{-1} respectively, as well as the terminal stretching mode of $P_2O_7^{4-}$ ions at 1226 cm^{-1}, shows that the material produced is phase-pure [50]. Thus, there is no spectroscopic evidence to confirm the presence of $Mn_2P_2O_7$ impurities in the final product. This is consistent with the XRD data.

To summarise, the IR data is supportive and consistent with XRD data on the production of phase pure $LiMnPO_4$ from 400°C. These results tie in with that reported in Chapter 3 on how the purity of $LiMnPO_4$ can be modulated based on the introduction of an intermediate heating step.

4.3.1.4. Raman analysis

The surface carbon structure in the $LiMnPO_4$/C was investigated by Raman spectroscopy. The Raman spectra of the samples were collected using a Bruker Senterra III Raman spectrometer using a 532-nm excitation laser focussed through an Olympus objective lens with objective 50x magnification. The spot size of the laser beam on the sample surface was focussed to a 50 x 1000 μm^2 area. The laser power used for all measurements was 2.0 mW. The spectra were recorded in air, at room temperature with an exposure time of 10 s, an accumulation number of 10 scans. All spectra were normalised to the intensity of the peak at ~1600 cm^{-1}. Peak positions, peak intensities, full widths at half maximum (fwhm) were determined by software, OPUS version 7 (Bruker). The peak positions and their fwhm and the I_D/I_G intensity ratio obtained from the fitting to each spectrum are employed to quantify the changes which occurred in the samples upon heating at 500, 600 and 700ºC.

The Raman spectra for S1, S2 and S3 samples are shown in Figures 4.11 to 4.13. The peaks and assignment have also been tabulated in Tables 4.6 to 4.8. All samples prepared at 400ºC were excluded because no peaks were visible due to the high level of fluorescence emitting from the sample when subjected to the excitation laser. This fluorescence occurred because of the higher quantity of organic ligands present in these samples which absorb the incident laser and emit fluorescence signal. Also, due to the screening effect of carbon, none of the peaks related to the $LiMnPO_4$ material are seen [51]. Unlike the FT-IR and XRD patterns, the Raman spectra are showing important differences between the samples produced at different temperatures.

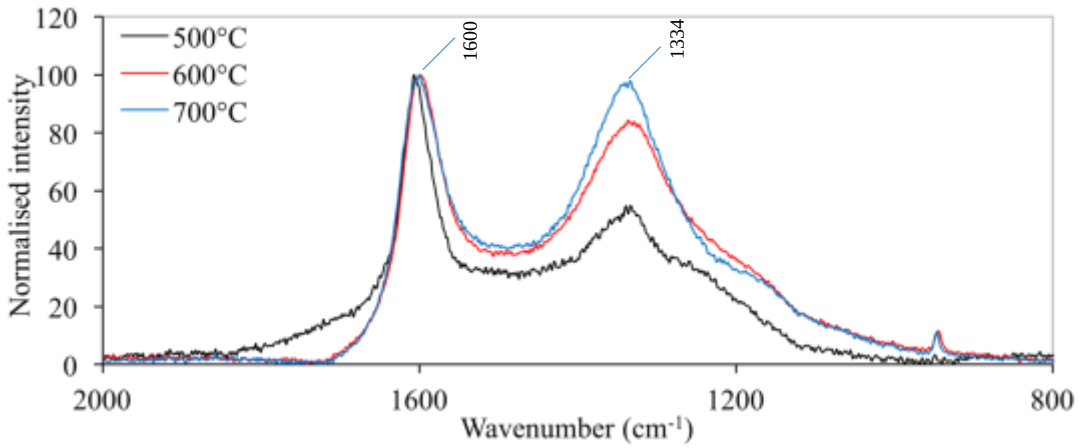

Figure 4.11: Raman spectra of S1 samples prepared at 500°C, 600°C and 700°C.

Table 4.6: Assignment of Raman bands of S1 samples prepared at 500°C, 600°C and 700°C.

Temperature (°C)	Peak	Frequency range (cm^{-1})	Peak Assignment
500	1	1607	G-band
	2	1334	D-band
600	1	1600	G-band
	2	1335	D-band
700	1	1600	G-band
	2	1337	D-band

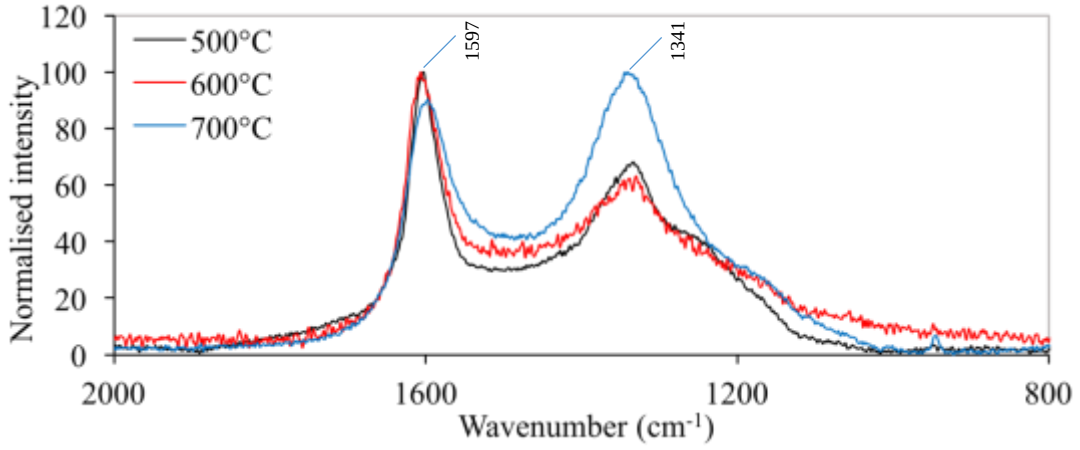

Figure 4.12: Raman spectra of S2 samples prepared at 500°C, 600°C and 700°C.

Table 4.7: Assignment of Raman bands of S2 samples prepared at 500°C, 600°C and 700°C.

Temperature (℃)	Peak	Frequency range (cm^{-1})	Peak Assignment
500	1	1607	G-band
	2	1330	D-band
600	1	1607	G-band
	2	1330	D-band
700	1	1599	G-band
	2	1335	D-band

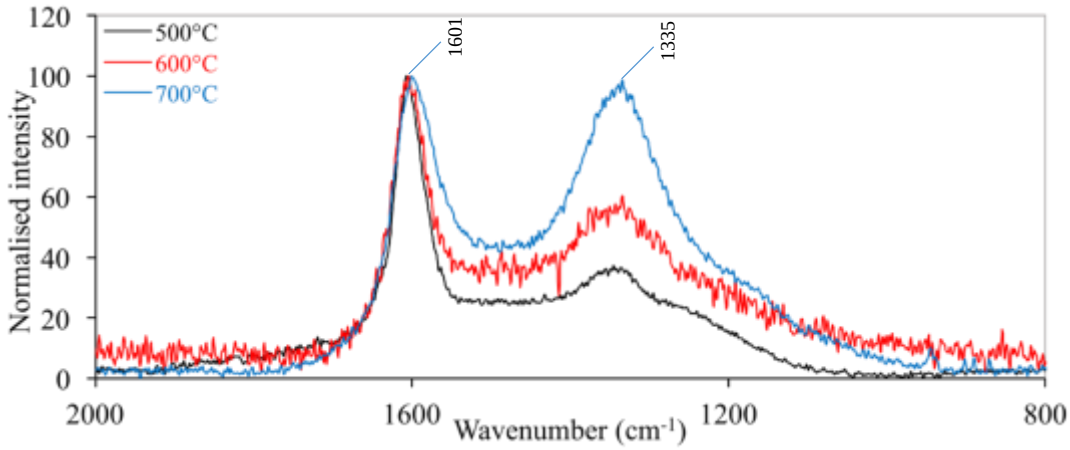

Figure 4.13: Raman spectra of S3 samples prepared at 500°C, 600°C and 700°C.

Table 4.8: Assignment of Raman bands of S3 samples prepared at 500°C, 600°C and 700°C.

Temperature (℃)	Peak	Frequency range (cm^{-1})	Peak Assignment
500	1	1608	G-band
	2	1334	D-band
600	1	1605	G-band
	2	1335	D-band
700	1	1602	G-band
	2	1334	D-band

Due to the presence of carbon coating on the samples, the bands that would be assigned to Raman signal of $LiMnPO_4$ are not intense enough to be seen in the Raman spectra. As discussed earlier, the quality and type of carbon coating is an important factor in determining its effectiveness and will have a major influence on improving the extrinsic electronic conductivity of $LiMnPO_4$. The source of carbon and the temperature the material is heated at are both important in determining the quality and type of carbon coating. Disordered carbons are less conductive than graphite, and conductivity depends on the size and number of graphene domains. The carbon structure with higher graphite-like structure or ratio of sp^2 hybridized carbon to disordered carbon or sp^3 hybridized carbon improves electrical conductivity.

Raman spectra of graphitic carbons consist of a G band peak at ~1575 – 1600 cm^{-1} and peak at around 1330 – 1345 cm^{-1}, corresponding to disorder induced features (called D band) [52-54]. Interpretation of the Raman spectral data needs to be done with care due to information being lost as a result of the broadening of the D and the G bands. The relative intensities of the D and G band peaks called the I_D/I_G ratio can be used to estimate the degree of order. The fwhm of the bands can also be measured and interpreted. The main spectral positions of all samples were similar to sp^2 bonded graphitic materials already reported in the literature (Figures 4.11 – 4.13). However, some variation in the relative intensities was observed. The main features observed in the Raman spectra of our samples as per the usual are a G band peak at 1575 – 1600 cm^{-1}, corresponding to ordered graphite structure and D band peaks at around 1335 cm^{-1}corresponding to disorder induced features. [53, 55-57]. The main effects on Raman spectral features upon heating are; (i) the G band peak moves from ~1610 cm^{-1} to ~1590 $^{-1}$ while its fwhm increases (ii) D band peak intensities and fwhm increase but no significant peak shifts are observed.

The G band of graphite is characteristic of all sp^2 sites, including alkenic C=C sites and not only those in aromatic rings [58, 59]. It always lies in the range 1500 – 1630 cm^{-1}, as it does in spectra of other aromatic and alkenic solids [53, 55-57]. Nevertheless, differences can be delineated. The unconjugated alkenic C=C bonds are shorter than aromatic bonds, so they have higher vibration frequencies. Thus, during gradual transformation from sp^2 bonded chains to sp^2 bonded conjugated hexagonal rings upon heating, a shift in the G band to lower wave numbers is therefore expected. Moreover, it is well established that the width of the G band peak is proportional to the bond-angle or bond-length disorder at the sp^2 sites.

In other words, improving the conjugation, which results in electron delocalisation effect, seems to be the mechanism capable of down-shifting the G Raman peak from ~1610 cm^{-1} to ~1600 cm^{-1} [37]. The reorganisation upon heating leads to a chemical transition from non-aromatic to aromatic and the π states become increasingly delocalised, i.e. some of the alkenic C=C chains change gradually to hexagonal rings. During heating at higher temperatures (700^{o}C), the delocalization of the π electrons in the nanosized carbonaceous domains leads to a weakening of the in-plane C=C bonds, thus leading to the ~10 cm^{-1} down-shift of the G band Raman peak. Because of the close link between the electric conductivity and delocalisation of the π electrons, the optimisation of the heat-treatment of the $LiMnPO_4$/carbon composite is critical to the rate capability of the cathode material.

On the other hand, the D band intensity is proportional to the carbons only in the aromatic rings in clusters with small sizes, while the D band broadening is proportional to the distribution of clusters containing hexagonal aromatic rings with different orders and dimensions. In other words, the D band intensity is proportional to the number of hexagonal aromatic rings in the cluster whereas carbons in non-aromatic bonds do not contribute to the intensity of the D band [58-61]. That is, if there is any change in total disorder where there would be no change in the intensity of the D, but if the distribution of disordered regions changes, this would still be reflected in D line broadening [57-62]. For the samples prepared here, we note that the D band peak intensity and fwhm increase with increasing temperature. This suggests that less ordered clusters are formed first but also, they become less randomly distributed. As mentioned, this does not denote that there was an increase in the amount of non-aromatic bonds.

The intensity ratio of the D-band to the G-band, $R = I_D/I_G$, has been used to get an idea of the carbon quality by estimating the degree of graphitisation. A similar strategy has been used with S1, S2 and S3 samples and are reported in Table 4.9.

Table 4.9: Degree of graphitisation for samples produced from 500-700°C

Sample set	Temperature (°C)	I_D	I_G	I_D / I_G
1	500	55	100	0.55
	600	85	100	0.85
	700	99	100	0.99
2	500	45	100	0.45
	600	63	100	0.63
	700	100	90	1.11
3	500	37	100	0.37
	600	60	100	0.6
	700	100	94	1.06

As mentioned, the D-band peak intensity increased as the temperature was increased from 500-700ºC which is unusual. Generally, the intensity of the D-band peak decreases at higher temperatures. The degree of graphitisation is highest at 500°C and lowest at 700°C. Thus, the I_D/I_G ratios are accordingly consistent with the increasing intensity of the D-band. However, generally, I_D/I_G ratios are lowered as temperature is increased which would be beneficial for better electrochemical performance if graphitisation is one of the main factors underpinning electrical conductivity. These results indicate that there are more structural defects present at 700ºC than at lower temperatures which could in turn affect its electrochemical properties. The electrochemical performance of S1, S2 and S3 samples are presented in section 4.3.2.2.

An alternate explanation for this unexpected result has been suggested by Benard *et al.* [63]. The change in the I_D/I_G ratios are not only related to the degree of graphitisation but can also be related to the pyrolysis state. Benard *et al.* [63] indicated that the intensity of the D band peak is related to the pyrolysis state. There are two regimes, the first of which is pyrolysis where the I_D/I_G ratio increases with temperature (i.e. the intensity of the D band peak increases). This is then followed by graphitisation where the I_D/I_G ratio decreases with temperature (i.e. the intensity of the D band peak decreases). Ferrari and Robertson [59] also support the increase and decrease in the I_D/I_G ratio across these two regimes. Therefore, the intensity of the D band peaks first increase with temperature and then decreases as the temperature is further increased. It can be said that the increasing I_D/I_G ratio shown in Table 4.9 is due to being in this pyrolysis state. This is critical information as it indicates that the material is not yet in a graphitised stage and that the I_D/I_G ratio does not imply the extent of graphitisation in this case. However, it indicates that the carbon is approaching the state of graphitisation.

4.3.1.5. Morphology

The morphological characteristics of the samples were observed using a JEOL 7001F Field emission scanning electron microscope (FE-SEM) operating at an accelerating voltage of 15.0 kV. The morphology for sample sets 1, 2 and 3 are shown in Figures 4.14 to 4.16.

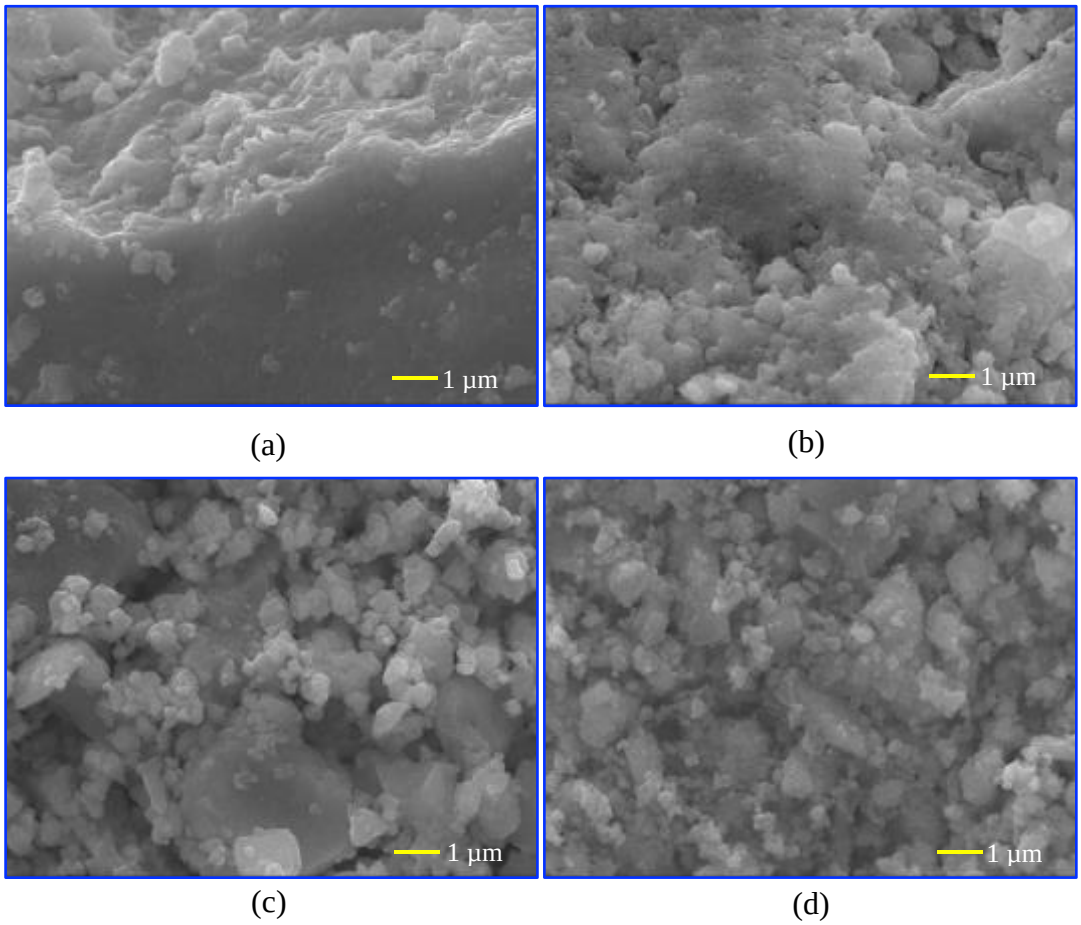

Figure 4.14: SEM images of S1 samples at (a) 400°C; (b) 500°C; (c) 600°C; and (d) 700°C. Images are taken at 10,000x magnification.

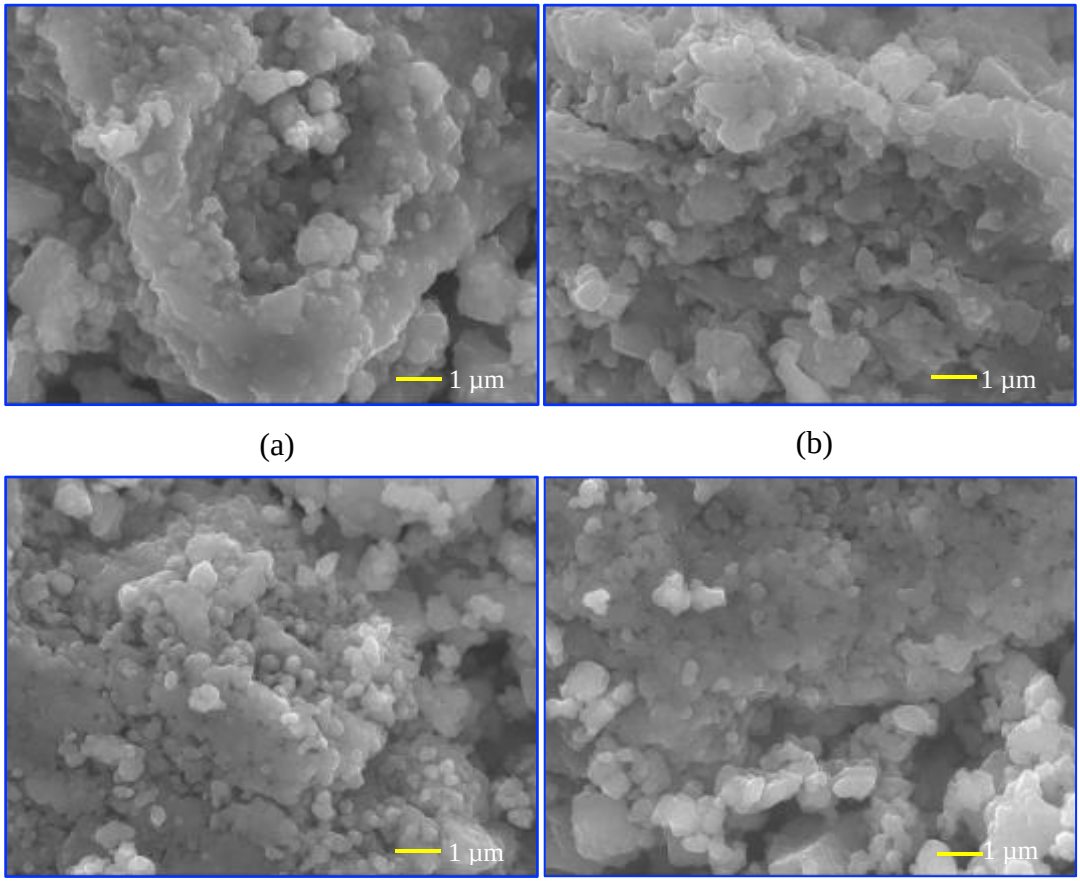

Figure 4.15: SEM images of S2 samples at (a) 400°C; (b) 500°C; (c) 600°C; and (d) 700°C. Images are taken at 10, 000x magnification.

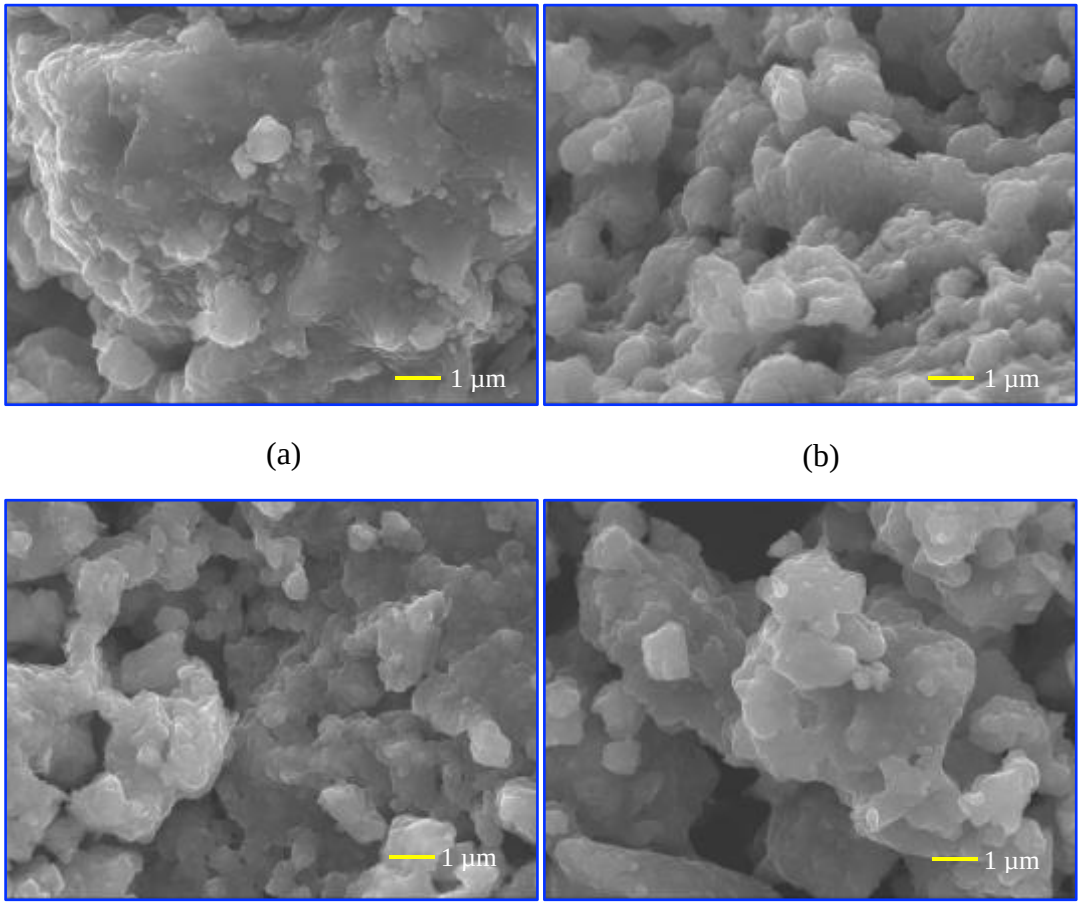

Figure 4.16: SEM images of S3 samples at (a) 400°C; (b) 500°C; (c) 600°C; and (d) 700°C. Images are taken at 10,000x magnification.

All the images are consistent with other characterisation methods used. There are not much observable differences between the morphology of the samples from 400°C to 700°C. Therefore, as the temperature is increased, the particle size and morphology remain relatively the same. The material prepared at 400°C is very stable as indicated by FT-IR and XRD.

4.3.1.6. Surface area analysis

The surface areas of the three sample sets were all measured on a Micrometrics ASAP 2020. The surface area was determined by the triple-point BET (Brunauer, Emmett, Teller) method with nitrogen as the adsorbate gas and helium as an inert non-adsorbable carrier. Samples were first degassed under vacuum at 350°C until a stable vacuum was reached. The tube was transferred to the analysis port and back filled with helium ready for analyses. Adsorption/desorption isotherms were then carried out under nitrogen gas at 77 K. BET surface analysis models were used to calculate the surface areas. The material was ball-milled in water-ethanol (1:1) solvent mixture, as a prerequisite for electrochemical testing to improve the surface area.

Table 4.10: BET surface area of unmilled and ball-milled samples in water-ethanol (1:1) medium.

Sample set	Temp (°C)	BET Surface Area (m^2/g)
S1 (unmilled)	400	11.95
	500	8.77
	600	4.20
	700	3.24
S1 (wet ball-milled)	400	31.93
	500	31.09
	600	28.24
	700	24.28
S2 (unmilled)	400	4.32
	500	6.03
	600	5.25
	700	3.92
S2 (wet ball-milled)	400	26.14
	500	28.92
	600	27.93
	700	25.32
S3 (unmilled)	400	2.16
	500	1.85
	600	2.01
	700	2.32
S3 (wet ball-milled)	400	27.56
	500	30.47
	600	36.22
	700	32.55

These data show that the surface area increases significantly and consistently across different samples upon milling (Table 4.10). Unmilled samples have very low surface areas ranging from 3.24 $m^2 g^{-1}$ to 6.03 $m^2 g^{-1}$. One unmilled sample from S1 prepared at 400°C had a much higher surface area of 11.95 $m^2 g^{-1}$. Milled samples had surface areas ranging from 24.28 $m^2 g^{-1}$ to 36.22 $m^2 g^{-1}$. Several previous studies have confirmed the need for ball-milling to increase the surface area and thus to promote an enhancement in the electrochemical performance of electroactive material [20, 27].

4.3.2. Electrochemical characterisation

4.3.2.1. Cyclic voltammetry

Voltammetry is a potentiodynamic electrochemical measurement technique widely used to gather qualitative information on electrochemical reactions including the location of the redox potential of the electroactive species, kinetics of electron transfers and phase transition of a voltaic cell. Here a potential is applied to the working electrode (relative to a reference electrode) at a constant sweep rate and the corresponding current that flows is monitored, that is, the flow rate of electrons is measured. The magnitude of the resulting current and its dependence on the applied voltage provide useful information. In cyclic voltammetry (CV), the voltage is swept between two values at a fixed rate. The scan rate unit is given as mV s^{-1}. Here, all the CV measurements were taken at three different rates (0.05, 0.5 and 0.1 mV s^{-1}) from 2.5 V to 4.7 V and at three temperatures (0, 20 and 40°C). For clarity, only the measurements at the slowest rate of 0.05 mV s^{-1} are included here. Also, due to the similarities in the data trends acquired which is consistent with the determination of carbon content in the material, only S3 samples at 0, 20 and 40°C is shown here (Figure 4.17 to 4.19).

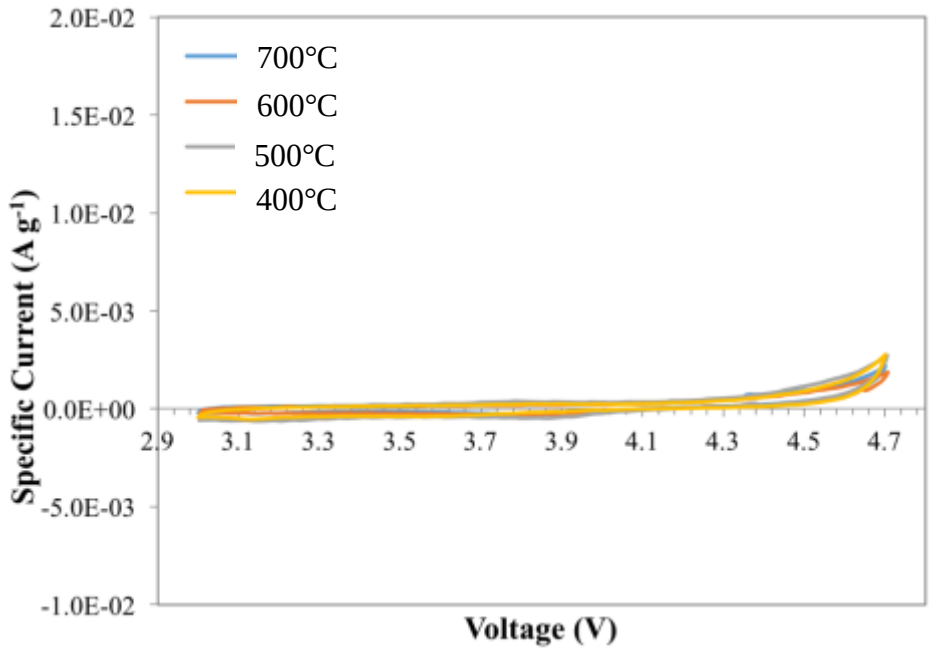

Figure 4.17: Cyclic voltammetry plots of S3 samples (400, 500, 600 and 700°C) measured at 0°C.

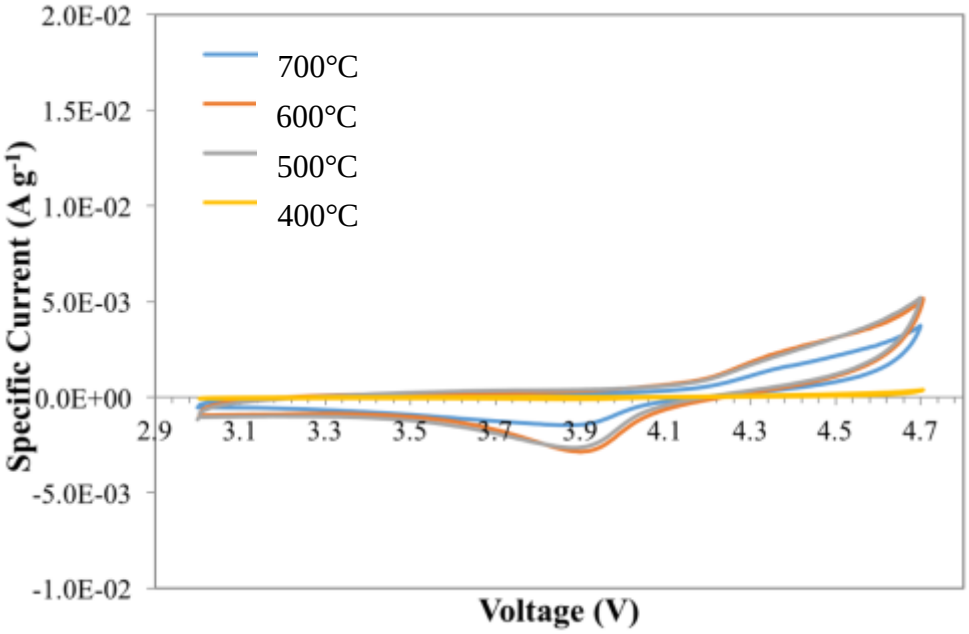

Figure 4.18: Cyclic voltammetry plots of S3 samples (400, 500, 600 and 700°C) measured at 20°C.

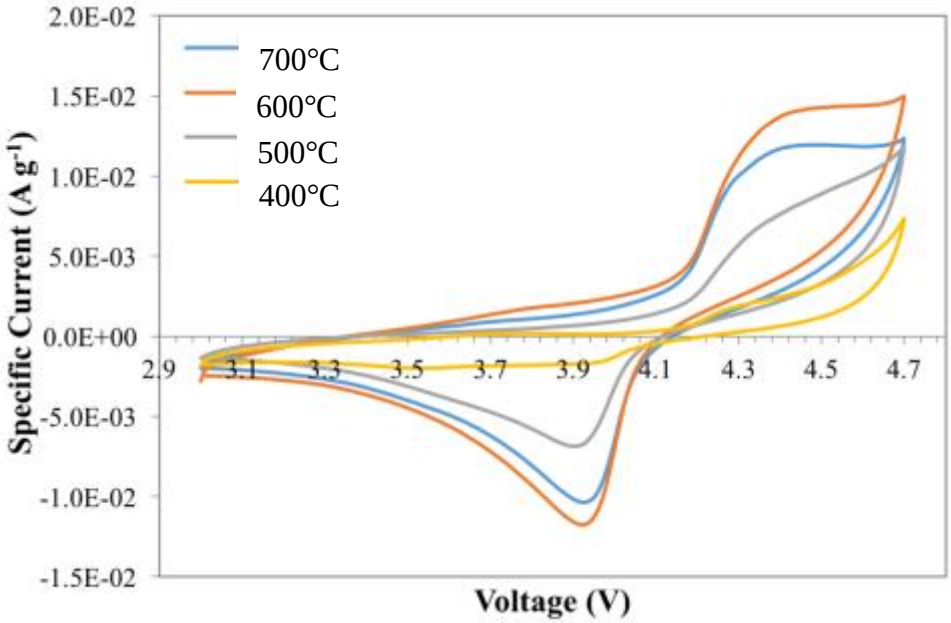

Figure 4.19: Cyclic voltammetry plots of S3 samples (400, 500, 600 and 700°C) measured at 40°C.

The CV measurements were obtained to investigate the reversibility of the electrochemical reaction of the $LiMnPO_4$/C material during cycling. The peak shown in the positive region of the y-axis of the Cartesian plane is the anodic peak, correlating to Li-ion extraction. Correspondingly, the peak in the negative region of the y-axis is the cathodic peak, correlating to the insertion of Li-ions into the active material. In this case, this corresponds to the oxidation and reduction peaks of $Mn^{2+/}Mn^{3+}$ redox couple *vs.* Li/Li^+ respectively. The CVs obtained at 0ºC do not show much electrochemical activity as evidenced by the lack of any observed redox peaks. The CVs run at 20ºC show better electrochemical activity when compared to the samples at 0ºC as evidenced by the appearance of redox peaks.

As the temperature increases from 0 to 40ºC, these peaks are higher in intensity and come closer in location. The oxidation and reductions peaks appear at ~4.3 V and ~3.9 V corresponding to the oxidation and reduction of $Mn^{2+/}Mn^{3+}$ redox couple respectively. This clearly indicates that Li-ion diffusion is enhanced, more charge/electrons are being transferred, and electrochemical polarisation is reduced at higher operating temperatures. This trend is logical and consistent to that reported in literature [33].

As expected, samples synthesised at the lowest temperature, are exhibiting traits of a low electrochemical performer. Samples prepared at 600 to 700ºC, have sharper and distinct peaks. The greater area under the curve of these CV measurements also indicates that more charge has transferred to and from the electroactive material. This is consistent with the Raman data in Section 4.3.1.4 which shows that the samples prepared at higher temperatures contained more ordered graphite-like coatings. This was demonstrated by the lower Raman shift of the G band for samples prepared at higher temperatures. To this end, it is expected that these samples will have the highest capacity. Similar trends were observed for S1 and S2 samples, however, overall, the S3 samples showed the best electrochemical activity most probably due to the higher amount of carbon present.

4.3.2.2. Galvanostatic charge/discharge cycling

Galvanostatic cycling also known as constant current (CC) was carried out to investigate the capability of materials to produce a capacity at a certain applied current. From these measurements, information regarding the capacity delivered as a function of current rate can be obtained. Here the cells were cycled between 2.5 V to 4.7 V *vs.* Li/Li^+ at a CC rate of C/50. The current rate is usually articulated as the C-rate which indicates the amount of charge that could be delivered within a certain hour. The calculated C-rates were based on the theoretical capacity of 171 mA.h g^{-1} for $LiMnPO_4$, but will vary slightly as the mass of active material on the electrodes between the samples are varied. Cells first underwent a conditioning cycle for each rate, before a subsequent cycle was used for calculating capacity. The equation for calculating the capacity is given in Equation 4.1.

$$Specific\ Capacity = C_{Sp} = \frac{I \times t}{m} \qquad \text{Equation 4.1}$$

Where *I* is the current in mA, *t* is the time taken to charge/discharge in hours, and *m* is the mass of active material on the electrode.

The capacity of the samples follows the same trends as the CVs. For continuity with the CV data presented, trends will be discussed based on the cycling of samples from S3 at 0, 20 and 40°C. The charge and discharge capacities were calculated and are presented in tabulated form (Table 4.11). An example of a graphical representation of the capacity is shown in Figure 4.20.

Table 4.11: The charge/discharge capacities of S3 samples (400, 500, 600 and 700°C) at 0, 20 and 40°C. The specific capacity is measured in mAh g^{-1}.

	Temp (°C)	700	600	500	400
Charge	**0**	4.1	2.8	4.5	5.5
	20	25.0	15.5	15.9	10.4
	40	139.6	133.3	66.0	50.8
Discharge	**0**	1.8	1.6	2.9	3.4
	20	10.2	11.4	13.0	6.5
	40	44.0	64.2	40.7	26.8

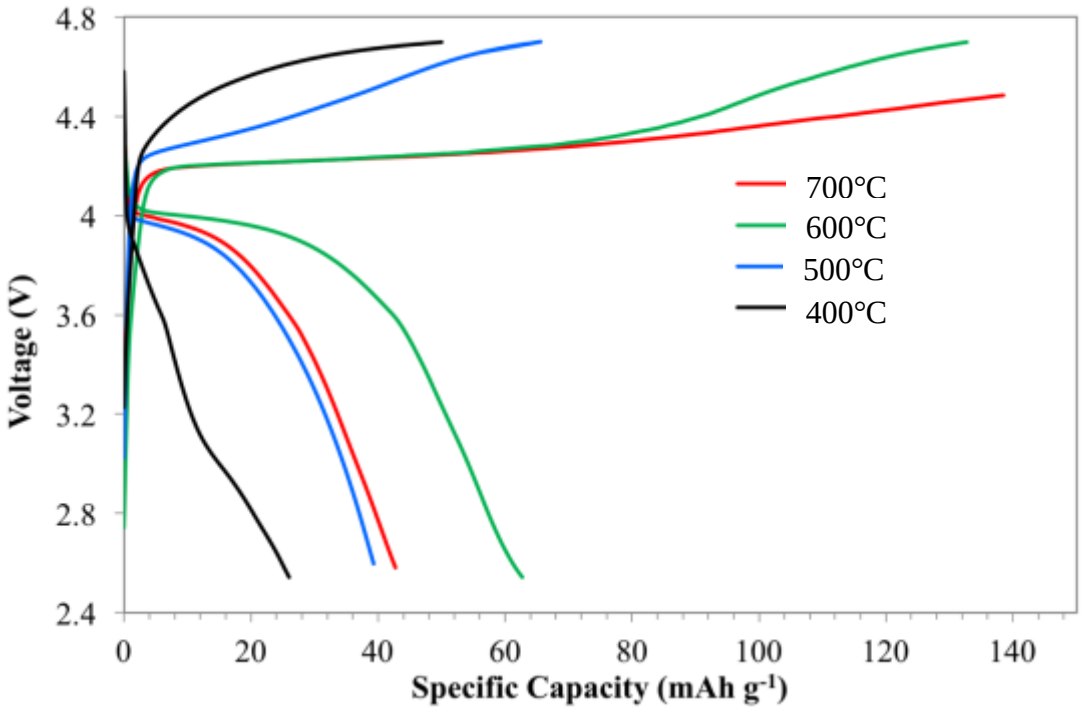

Figure 4.20: Charge/discharge curves for S3 samples (400, 500, 600 and 700°C) measured at 40°C.

The electroactive material exhibited the best capacities at 40ºC and expectedly increases from 0 to 40ºC. Samples prepared at 600 and 700ºC from S3 showed excellent capacities on charging exhibiting a charging capacity of 133.3 and 139.6 mA.h g^{-1} and a corresponding discharge capacity of 64.2 and 44.0 mA.h g^{-1} respectively. Unexpectedly, the discharge capacity at 600°C is higher than that of 700°C. Upon closer inspection, it can be seen on the graphical representation that during galvanostatic cycling, the voltage cut off at 4.5 V during the charging cycle instead of 4.7 V, which impacted on both the charge and discharge capacity. This occurred due to the maximum run time of the measurement parameters being exceeded. It is apparent that at 700 ºC, the charge and discharge capacities would exceed that of 600ºC if fully charged to 4.7 V. At these temperatures, the capacity is better than at 400°C and 500°C (Table 4.5). This is consistent with the CV measurements and correlates well with the physical characteristics of the carbon coating shown by Raman analysis. The discharge and charge plateaus are at ~3.9 V and ~ 4.3 V, consistent with the CV data. Considering that the physical characteristics from IR, XRD and SEM of samples prepared from 400 to 700°C were similar, it is likely that the low capacities at 400 and 500°C are due to the increase in the charge-transfer resistance caused by the presence of similar quantities but electrochemically inactive carbon particles.

The electrochemical performance is consistent with the Raman data which indicates greater delocalisation of π electrons caused as proven with the lower Raman shifts of the G band at higher temperatures. If the carbon was in state of graphitisation, which would then, in this case, decrease as the temperature went from 500ºC to 700ºC (increase in I_D/I_G ratio), then the electrochemical performance would be lower at 700ºC. This is not the case because the carbon is in pyrolysis state and the improved electrochemical performance at 700ºC is related to the greater delocalisation of π electrons caused by the transformation of alkenic C=C chains to aromatic hexagonal rings which improves the electronic conductivity.

4.4. Summary

The electrochemical performance of the $LiMnPO_4$ material is dependant and can be rationalised by the physical characteristics of the material. The physical characterisation of the electroactive material showed no major differences. However, the samples from 400 to 700ºC showed different electrochemical properties. Therefore, the differing electrochemical performance of the battery cells has been linked to the quality of carbon coating on the material rather than the electroactive material itself. Here, the best performing samples generally were those prepared at 600 and 700ºC. Raman spectra of the samples revealed that the quality of carbon deposited on the samples changed as the temperature was increased. The improved electrochemical performance is related to the greater delocalisation of π electrons caused by the transition of alkenic C=C chains to aromatic hexagonal rings which occurred at higher temperatures. The greater delocalisation of π electrons improves the electronic conductivity of the material as exhibited in samples prepared at 600 and 700ºC. Additionally, the capacity of the cells is strongly dependant on the temperature it is run since the samples ran at 40ºC showed better electrochemical properties compared to samples run at 0 and 20ºC.

4.5. References

1. Aravindan V, Gnanaraj J, Lee Y, Madhavi S. $LiMnPO_4$ - A next generation cathode material for lithium-ion batteries. Journal of Materials Chemistry. 2013;1(11):3518-39.

2. Drezen T, Kwon N, Bowen P, Teerlinck I, Isono M, Exnar I. Effect of particle size on $LiMnPO_4$ cathodes. Journal of Power Sources. 2007;174(2):949-53.

3. Choi D, Wang D, Bae I, Xiao J, Nie Z, Wang W, et al. $LiMnPO_4$ nanoplate grown via solid-state reaction in molten hydrocarbon for Li-ion battery cathode. Nano Letters. 2010;10(8):2799-805.

4. Li H, Zhou H. Enhancing the performances of Li-ion batteries by carbon-coating: present and future. Chemical Communications. 2012;48(9):1201-17.

5. Wang J, Sun X. Understanding and recent development of carbon coating on $LiFePO_4$ cathode materials for lithium-ion batteries. Energy & Environmental Science. 2012;5(1):5163-85.

6. Lin Y, Gao M, Zhu D, Liu Y, Pan H. Effects of carbon coating and iron phosphides on the electrochemical properties of $LiFePO_4$/C. Journal of Power Sources. 2008;184(2):444-8.

7. Ravet N, Chouinard Y, Magnan J, Besner S, Gauthier M, Armand M. Electroactivity of natural and synthetic triphylite. Journal of Power Sources. 2001;97:503-7.

8. Gaberscek M, Dominko R, Jamnik J. Is small particle size more important than carbon coating? An example study on $LiFePO_4$ cathodes. Electrochemistry Communications. 2007;9(12):2778-83.

9. Martha S, Grinblat J, Haik O, Zinigrad E, Drezen T, Miners J, et al. $LiMn_{0.8}Fe_{0.2}PO_4$: An advanced cathode material for rechargeable lithium batteries. Angewandte Chemie International Edition. 2009;48(45):8559-63.

10. Doi T, Yatomi S, Kida T, Okada S, Yamaki J. Liquid-phase synthesis of uniformly nanosized $LiMnPO_4$ particles and their electrochemical properties for lithium-ion batteries. Crystal Growth & Design. 2009;9(12):4990-2.

11. Chung S, Bloking J, Chiang Y. Electronically conductive phospho-olivines as lithium storage electrodes. Nature Materials. 2002;1(2):123-8.

12. Gao Z, Pan X, Li H, Xie S, Yi R, Jin W. Hydrothermal synthesis and electrochemical properties of dispersed $LiMnPO_4$ wedges. CrystEngComm. 2013;15(38):7808-14.

13. Li L, Liu J, Chen L, Xu H, Yang J, Qian Y. Effect of different carbon sources on the electrochemical properties of rod-like $LiMnPO_4$-C nanocomposites. RSC Advances. 2013;3(19):6847-52.

14. Shiratsuchi T, Okada S, Doi T, Yamaki J. Cathodic performance of $LiMn_{1-x}M_xPO_4$ (M = Ti, Mg and Zr) annealed in an inert atmosphere. Electrochimica Acta. 2009;54(11):3145-51.

15. Wang D, Buqa H, Crouzet M, Deghenghi G, Drezen T, Exnar I, et al. High-performance, nano-structured $LiMnPO_4$ synthesized via a polyol method. Journal of Power Sources. 2009;189(1):624-8.

16. Doan T, Bakenov Z, Taniguchi I. Preparation of carbon coated $LiMnPO_4$ powders by a combination of spray pyrolysis with dry ball-milling followed by heat treatment. Advanced Powder Technology. 2010;21(2):187-96.

17. Zhao M, Fu Y, Xu N, Li G, Wu M, Gao X. High performance $LiMnPO_4$/C prepared by a crystallite size control method. Journal of Materials Chemistry A. 2014;2(36):15070-7.

18. Moon S, Muralidharan P, Kim D. Carbon coating by high-energy milling and electrochemical properties of $LiMnPO_4$ obtained in polyol process. Ceramics International. 2012;38:S471-5.

19. Kim J, Cheruvally G, Ahn J, Hwang G, Choi J. Electrochemical properties of carbon-coated $LiFePO_4$ synthesized by a modified mechanical activation process. Journal of Physics and Chemistry of Solids. 2008;69(10):2371-7.

20. Ni J, Kawabe Y, Morishita M, Watada M, Sakai T. Improved electrochemical activity of $LiMnPO_4$ by high-energy ball-milling. Journal of Power Sources. 2011;196(19):8104-9.

21. Yang J, Xu J. Synthesis and characterization of carbon-coated lithium transition metal phosphates $LiMPO_4$ (M = Fe , Mn, Co, Ni) prepared via a nonaqueous sol-gel route. Journal of The Electrochemical Society. 2006;153(4):A716-23.

22. Ma J, Li B, Du H, Xu C, Kang F. Inorganic-based sol–gel synthesis of nano-structured $LiFePO_4$/C composite materials for lithium ion batteries. Journal of Solid State Electrochemistry. 2011;16(4):1353-62.

23. Wang L, Sun W, Li J, Gao J, He X, Jiang C. Synthesis of electrochemically active $LiMnPO_4$ via $MnPO_4 \cdot H_2O$ with different morphology prepared by facile precipitation. International Journal of Electrochemical Science. 2012;7(4):3591-600.

24. Cheng G, Zuo P, Wang L, Shi W, Ma Y, Du C, et al. High-performance carbon-coated $LiMnPO_4$ nanocomposites by facile two-step solid-state synthesis for lithium-ion battery. Journal of Solid State Electrochemistry. 2015;19(1):281-8.

25. Yang S, Ma R, Hu M, Xi L, Lu Z, Chung C. Solvothermal synthesis of nano-$LiMnPO_4$ from Li_3PO_4 rod-like precursor: reaction mechanism and electrochemical properties. Journal of Materials Chemistry. 2012;22(48):25402-8.

26. Fujita A, Isobe F, Kodera T, Ogihara T, editors. Synthesis and Electrochemical Properties of C/$LiMnPO_4$ Cathode Materials by Complex Polymerized Method. Key Engineering Materials. 2011;485:115-8.

27. Kotobuki M. Improved performance of hydrothermally synthesized $LiMnPO_4$ by ball-milling as a positive electrode for Li ion battery. ISRN Electrochemistry. 2013:1-5.

28. Chen Z, Dahn J. Reducing carbon in $LiFePO_4$/C composite electrodes to maximize specific energy, volumetric energy, and tap density. Journal of The Electrochemical Society. 2002;149(9):A1184-9.

29. Chu P, Li L. Characterization of amorphous and nanocrystalline carbon films. Materials Chemistry and Physics. 2006;96(2):253-77.

30. Wang J. Analytical electrochemistry: John Wiley & Sons; 2006.

31. Morgan D, Van der Ven A, Ceder G. Li conductivity in Li_xMPO_4 (M = Mn, Fe, Co, Ni) olivine materials. Electrochemistry Solid State Letters. 2004;7(2):A30-2.

32. Nishimura S, Kobayashi G, Ohoyama K, Kanno R, Yashima M, Yamada A. Experimental visualization of lithium diffusion in Li_xFePO_4. Nature Materials. 2008;7(9):707-11.

33. Pan X, Xu C, Hong D, Fang H, Zhen L. Hydrothermal synthesis of well-dispersed $LiMnPO_4$ plates for lithium ion batteries cathode. Electrochimica Acta. 2013;87:303-8.

34. Zhu J, Li W, Cheng F, Lu A. Synthesis of $LiMnPO_4$/C with superior performance as Li-ion battery cathodes by a two-stage microwave solvothermal process. Journal of Materials Chemistry A. 2015;3(26):13920-5.

35. Fujimoto D, Kuwata N, Matsuda Y, Kawamura J, Kang F. Fabrication of solid-state thin-film batteries using $LiMnPO_4$ thin films deposited by pulsed laser deposition. Thin Solid Films. 2015;579:81-8.

36. Berzina-Cimdina L, Borodajenko N. Research of calcium phosphates using Fourier transform infrared spectroscopy: INTECH Open Access Publisher; 2012.

37. Milev A, Tran N, Kannangara G, Wilson M. Unoccupied electronic structure of ball-milled graphite. Physical Chemistry Chemical Physics. 2010;12(25):6685-91.

38. Bushiri M, Antony C, Aatiq A. Raman and FTIR studies of the structural aspects of Nasicon-type crystals; $AFeTi(PO_4)_3$ [A= Ca, Cd]. Journal of Physics and Chemistry of Solids. 2008;69(8):1985-9.

39. Kravchenko V, Michailov V, Sigaryov S. Some features of vibrational spectra of $Li_3M_2(PO_4)_3$ (M= Sc, Fe) compounds near a superionic phase transition. Solid State Ionics. 1992;50(1):19-30.

40. Kravchenko V, Sigaryov S. Lithium disorder in the vicinity of the superionic phase transition in monoclinic and rhombohedral $Li_3In_2(PO_4)_3$. Journal of Materials Science. 1994;29(22):6004-10.

41. Bih H, Bih L, Manoun B, Azdouz M, Benmokhtar S, Lazor P. Raman spectroscopic study of the phase transitions sequence in $Li_3Fe_2(PO_4)_3$ and $Na_3Fe_2(PO_4)_3$ at high temperature. Journal of Molecular Structure. 2009;936(1):147-55.

42. Padhi A, Nanjundaswamy K, Masquelier C, Okada S, Goodenough J. Effect of structure on the Fe^{3+}/Fe^{2+} redox couple in iron phosphates. Journal of The Electrochemical Society. 1997;144(5):1609-13.

43. Norberg N, Kostecki R. FTIR spectroscopy of a $LiMnPO_4$ composite cathode. Electrochimica Acta. 2011;56(25):9168-71.

44. Paques-Ledent M, Tarte P. Vibrational studies of olivine-type compounds—II orthophosphates, arsenates and vanadates AIBIIXVO4. Spectrochimica Acta Part A: Molecular Spectroscopy. 1974;30(3):673-89.

45. Burba CM, Frech R. Raman and FTIR Spectroscopic Study of Li_xFePO_4 ($0 \leqslant x \leqslant 1$). Journal of The Electrochemical Society. 2004;151(7):A1032-8.

46. Salah A, Jozwiak P, Garbarczyk J, Benkhouja K, Zaghib K, Gendron F, et al. Local structure and redox energies of lithium phosphates with olivine-and Nasicon-like structures. Journal of Power Sources. 2005;140(2):370-5.

47. Burba C, Frech R. Vibrational spectroscopic investigation of structurally-related $LiFePO_4$, $NaFePO_4$, and $FePO_4$ compounds. Spectrochimica Acta Part A: Molecular and Biomolecular Spectroscopy. 2006;65(1):44-50.

48. Salah A, Jozwiak P, Zaghib K, Garbarczyk J, Gendron F, Mauger A, et al. FTIR features of lithium-iron phosphates as electrode materials for rechargeable lithium batteries. Spectrochimica Acta Part A: Molecular and Biomolecular Spectroscopy. 2006;65(5):1007-13.

49. Kellerman D, Medvedeva N, Mukhina N, Semenova A, Baklanova I, Perelyaeva L, et al. Vanadium doping of $LiMnPO_4$: Vibrational spectroscopy and first-principle studies. Chemical Physics Letters. 2014;591:21-4.

50. Julien C, Jozwiak P, Garbarczyk J, editors. Vibrational Spectroscopy of electrode materials for rechargeable lithium batteries IV. Lithium metal phosphates. Proceedings of the International Workshop ‘‘Advanced Techniques for Energy Sources Investigation and Testing, Sofia, Bulgaria; 2004.

51. Salah A, Mauger A, Zaghib K, Goodenough J, Ravet N, Gauthier M, et al. Reduction Fe^{3+} of impurities in LiFePO4 from pyrolysis of organic precursor used for carbon deposition. Journal of The Electrochemical Society. 2006;153(9):A1692-701.

52. Markevich E, Sharabi R, Haik O, Borgel V, Salitra G, Aurbach D, et al. Raman spectroscopy of carbon-coated $LiCoPO_4$ and $LiFePO_4$ olivines. Journal of Power Sources. 2011;196(15):6433-9.

53. Reich S, Thomsen C. Raman spectroscopy of graphite. Philosophical Transactions Royal Society of London A. 2004;362 (1824):2271-88.

54. Dresselhaus M, Dresselhaus G, Jorio A, Souza Filho A, Saito R. Raman spectroscopy on isolated single wall carbon nanotubes. Carbon. 2002;40(12):2043-61.

55. Matthews M, Pimenta M, Dresselhaus G, Dresselhaus M, Endo M. Origin of dispersive effects of the Raman D band in carbon materials. Physical Review B: Condensed Matter and Materials Physics. 1999;59(10):R6585-R88.

56. Pimenta M, Dresselhaus G, Dresselhaus M, Cancado L, Jorio A, Saito R. Studying disorder in graphite-based systems by Raman spectroscopy. Physical Chemistry Chemical Physics. 2007;9(11):1276-91.

57. Maultzsch J, Reich S, Thomsen C, Requardt H, Ordejon P. Phonon dispersion in graphite. Physical Review Letters. 2004;92(7):075501-04.

58. Ferrari A, Robertson J. Raman spectroscopy of amorphous, nanostructured, diamond-like carbon, and nanodiamond. Philosophical Transactions Royal Society of London A. 2004;362(1824):2477-512.

59. Ferrari A, Robertson J. Interpretation of Raman spectra of disordered and amorphous carbon. Physical Review B: Condensed Matter and Materials Physics. 2000; 61(20):14095-107.

60. Ferrari A, Raman spectroscopy of graphene and graphite: disorder, electron-phonon coupling, doping and nonadiabatic effects. Solid State Communications. 2007;143(1-2):47-57.

61. Ferrari A, Libassi A, Tanner B, Stolojan V, Yuan J, Brown L, et al. Density, sp^3 fraction, and cross-sectional structure of amorphous carbon films determined by x-ray reflectivity and electron energy-loss spectroscopy. Physical Review B: Condensed Matter and Materials Physics. 2000;62(16):11089-103.

62. Thomsen C, Reich S. Double resonant Raman scattering in graphite. Physical Review Letters. 2000;85(24):5214-17.

63. Bernard S, Beyssac O, Benzerara K, Findling N, Tzvetkov G, Brown Jr. G. XANES, Raman and XRD study of anthracene-based cokes and saccharose-based chars submitted to high-temperature pyrolysis. Carbon. 2010;48(9):2506-16.

CHAPTER 5

Evaluation of cell impedance using electrochemical impedance spectroscopy

The main objective of this chapter is to study impedance in the $LiMnPO_4$/C composite samples. Based on the capacity calculations in Chapter 4, sample set 3 was selected for more detailed analysis. Firstly, a brief introduction to electrochemical impedance spectroscopy (EIS) will be provided. Following this, the method of collecting and extracting information from EIS measurements will be described. The impedance data will be represented as both Nyquist and Bode plots. The semi-circle present in the Nyquist plot can then be modelled using equivalent circuits where the physiochemical processes occurring in an electrochemical cell can be represented by a network of resistors and capacitors. This model circuit will then be used to separate and quantify the three sources of polarisation (kinetic, ohmic and concentration). Next, the extraction of diffusion data will be described.

The obtained information will be correlated to the physical and electrochemical properties of the electroactive material. This will function as a diagnostic test to determine the limiting factors and bottlenecks that inhabit electrochemical performance. Lastly, possible ways to improve the performance of the electroactive material based on the impedance sources will be described. The conclusions can be used to improve the performance of $LiMnPO_4$ based cells.

5.1. Brief introduction to electrochemical impedance spectroscopy

Electrical resistance is the ability of a circuit to impede the flow of current carrying electrons [1-3]. This relationship can be described by Ohm's Law (Equation 5.1) where the resistance (*R*) measured in ohms (Ω), is directly and inversely proportional to voltage (*E*) and current (*I*) respectively, measured in Volts (V) and Amperes (A) respectively.

$$R = \frac{E}{I} \qquad \text{Equation 5.1}$$

In direct current theory (DC), resistance can be expressed by Ohm's law. This equation, however, only holds true for one element of a circuit - the ideal resistor. An ideal resistor obeys this law at any voltage and current. Also, the resistance is independent of frequency; i.e. frequency is 0, while the current and voltage signals through an ideal resistor are in phase. In alternating current (AC) though, resistance, *R*, is too simple to apply realistically to circuits containing multiple elements which exhibit much more complicated behaviour [2-6]. Here, there are other components which can restrict the flow of electrons such as capacitors and inductors. Consequently, a better concept termed impedance (*Z*), the AC equivalent of resistance, which is not constrained by the limitations of resistance, can be used. The analogous equation is shown below (Equation 5.2) [2, 7].

$$Z(i\omega) = \frac{E(\omega)}{I\ (\omega)} \qquad \text{Equation 5.2}$$

where Z (iω) is the impedance, i is the imaginary component and ω is the radial frequency. Z (iω) is a complex quantity with a magnitude and a phase shift dependent on the frequency of the signal. Hence, by varying the frequency of the applied signal, the impedance of the system as a function of frequency can be determined.

The interesting application here is that the resistors, capacitors, and inductors that hinder the flow of electrons in an AC circuit can be considered analogous to the slow electrode kinetics and diffusion that impede electron flow in an electrochemical cell. This analogy can use well-established AC circuit theory to characterise the electrochemical system by modelling the reaction using equivalent circuits to understand the physical phenomena occurring in the reaction. This is accomplished by using a technique called electrochemical impedance spectroscopy (EIS). Here, an electrochemical cell is subjected to a sinusoidal (sine wave) voltage perturbation of low amplitude (e.g. 10 mV) and varying frequency. At each frequency, the various processes evolve at different rates, allowing the separation and quantification of these sources of polarisation [3]. It is important to know that electrochemical dynamics in a cell are extremely non-linear. However, the advantage of using EIS is that the small excitation signal allows a linear voltage to current relation to be assumed; a so-called pseudo-linearity [3].

Looking at the capacities of the material across the different synthesis temperatures and at different temperature controlled environments shown in Chapter 4, the results are dissimilar. If an electrochemical cell is modelled as a circuit, we can get an idea of where the resistance to electron flow originates from. The aim is to understand the bottlenecks in the system so future work can be targeted to specific problems in a cell and thus lead to the production of better materials. This provides a holistic and systematic study to using a new method to synthesis electroactive materials. This chapter will look at the determining the impedances present in S3 samples (400, 500, 600 and 700ºC) measured at three different temperatures (0, 20 and 40ºC).

5.2. Experimental

EIS characterisation was performed on a Biologic VSP Potentiostat System equipped with 2 VSP-01/Z EIS capable channels controlled by the ECLab® software. For all the measurements, a three-electrode system is used. EIS were collected at 0, 20 and 40ºC in a special temperature controlled environmental chamber. The amplitude of the AC voltage applied was 10 mV and the frequency was varied within a range from 0.1 MHz to 0.006 Hz in automatic sweep mode from high to low frequencies. A fresh cell was prepared for each sample and used within 24 hours. The protocol used for all EIS measurements were as follows:

i. resting for 2 hours at the controlled temperature;
ii. conditioning charge/discharge cycling between 2.7 V and 4.7 V at a constant current of 0.23 mA;
iii. cell charged at a constant current of 0.02 mA to the first voltage required;
iv. cell held for 30 mins at voltage to be measured;
v. EIS measurement done at required voltage;
vi. the above steps are repeated from step (ii) at different voltage increments and then repeated for the discharge cycle.
vii. there were 9 voltage steps (3.60, 3.75, 3.90, 4.00, 4.15, 4.30, 4.40, 4.55 and 4.70 V) for both charge and discharge measurements.

The circuit parameters of the equivalent circuit were obtained by the least square fitting of the equivalent circuit to the experimental impedance profile using the Z-fit in ECLab® software.

5.3. Results and discussion

This section will represent EIS data as both Nyquist and Bode plots. This will be followed by modelling the data using an equivalent circuit to represent elements in the cell. The physical meaning of these models will then be applied to the cells being tested by identifying trends in the charge-transfer resistance (R_{CT}) and constant phase element (CPE). Finally, the diffusion will be extrapolated using the Warburg factor ($\Omega\ s^{-1}$).

5.3.1. EIS of $LiMnPO_4$ prepared at different temperatures.

This section looks at the EIS measurements of samples prepared at 400, 500, 600 and 700°C. The data will be presented in two ways, firstly as real and imaginary impedance components which are plotted against one another in Nyquist plots where information on electrolyte resistance, charge-transfer resistance and diffusion can be determined. Another is by graphing Bode plots, where the impedance and phase angle is plotted against frequency which can determine capacitive effects of electrochemical systems.

5.3.1.1. Nyquist plots

Impedance, $Z(\omega)$, can be expressed as a complex number, where the resistance is the real component, Z' and the combined capacitance and inductance is the imaginary component, Z''. If the real component is plotted on the x-axis against the imaginary part on the y-axis of a chart, we obtain a Nyquist plot (Figure 5.1).

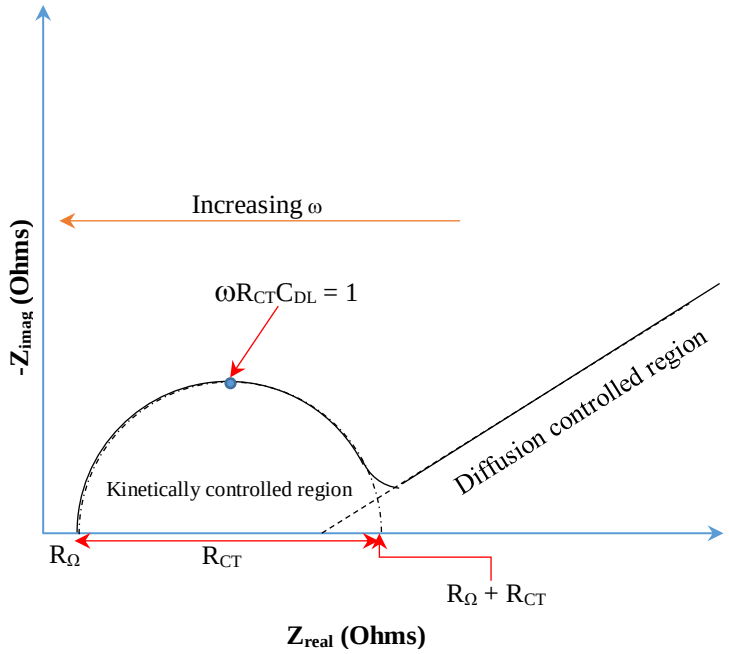

Figure 5.1: Ideal Nyquist plot. Adapted from ref. [2].

The ionic movement in the electroactive material, in this case, the Li-ion in $LiMnPO_4$, involves a sequence of steps including (1) Li-ion diffusion through the electrolyte; (2) charge transfer through the $LiMnPO_4$/electrolyte interface; and (3) Li-ion solid-state diffusion in the bulk of electroactive material [8]. Losses due to impedance that occur along these steps are investigated by EIS as they have different time constant, which is the basis of their separation [8].

The ohmic resistance (R_Ω), which is independent of the frequency, is attributed to the electrolyte resistance plus the accumulation of resistances from the components used to construct the cell. This is located at the first intersection of the semi-circle with the real axis (x-axis) (Figure 5.1). The extrapolated semi-circle in the mid to low frequency region, intersects the real axis to give the sum of the ohmic resistance (R_Ω) and the charge-transfer resistance (R_{CT}), i.e. $R_\Omega + R_{CT}$. Charge-transfer resistance (R_{CT}) is the opposition to the flow of electrons through the $LiMnPO_4$/electrolyte interface. Both R_Ω and R_{CT} are real quantities. The double layer capacitance (C_{DL}) can be roughly estimated from the maximum on the Z_{imag} axis of the semi-circle. Thus, the total impedance of the cell can be equated as the sum of the real quantities (R_Ω and R_{CT}) and imaginary quantity (C_{DL}).

Under applied conditions, the measured impedance data represented as Nyquist plots usually differ from theoretical behaviour. The time constant region (R_{CT} and C_{DL}) in a Nyquist plot does not usually show a perfect semi-circle shape where a perfect semi-circle would represent a perfect capacitor. This non-ideal behaviour may arise from several factors which affect capacitance such as coating heterogeneities [2]. This sloping semi-circle is hence an imperfect capacitor and is referred to as a constant phase element (CPE).

The Nyquist plots of the samples prepared at 400, 500, 600 and 700°C and measured under 40ºC are shown in Figure 5.2.

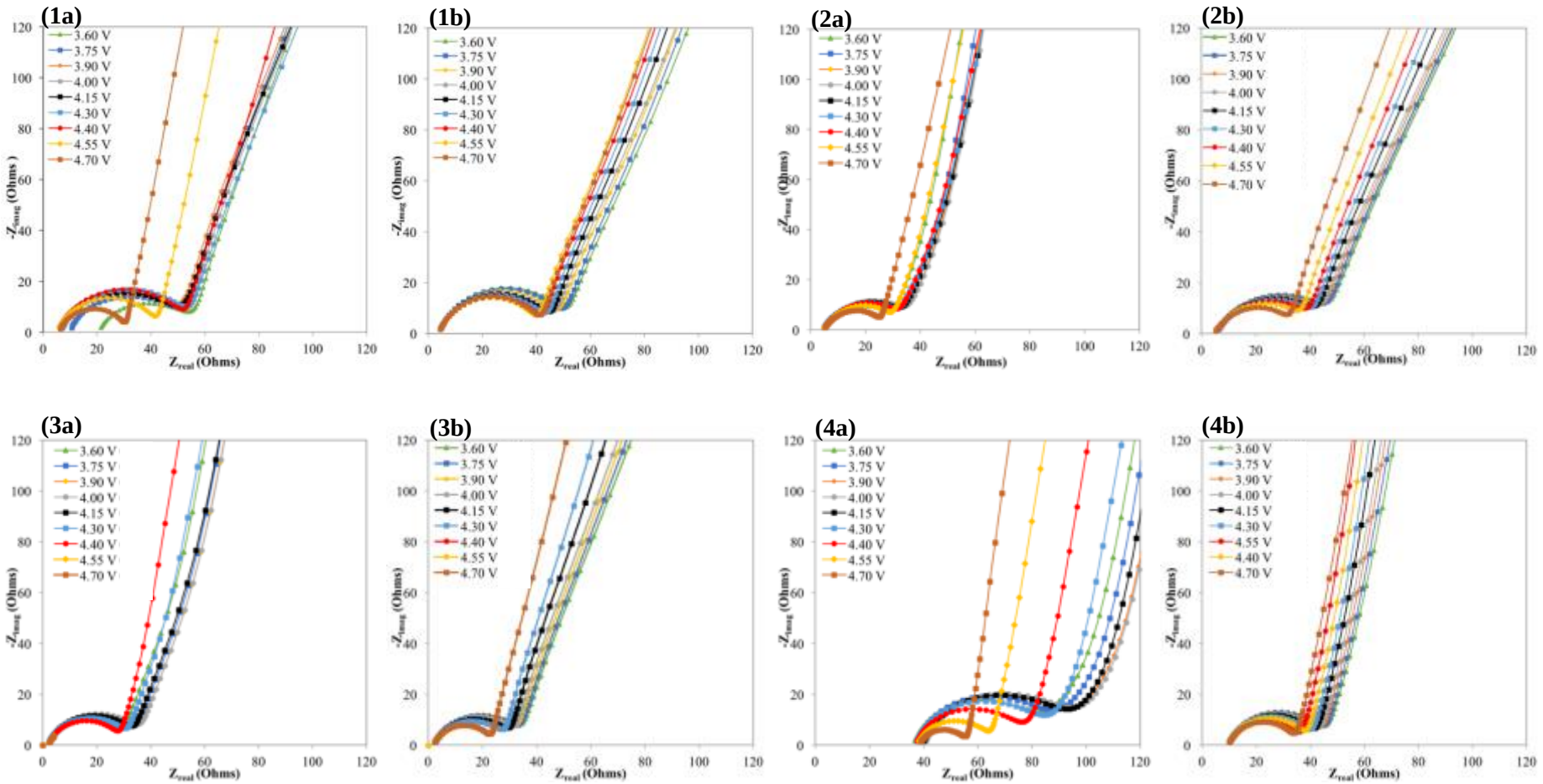

Figure 5.2: Nyquist plots of S3 samples at 40°C. 1: (a) 700°C charge, (b) 700°C discharge; 2: (a) 600°C charge, (b) 600°C discharge; 3: (a) 500°C charge, (b) 500°C discharge; 4: (a) 400°C charge; (b) 400°C discharge. Impedance are obtained at nine potentials ranging from 3.60 to 4.7 V. Nyquist plots do not depict frequency. However, the left side is towards higher frequency and right towards lower frequency.

In all the Nyquist plots, the high frequency domain shows a small perturbed semi-circle. As shown in Figure 5.2, the Nyquist plots consist of a sloping semi-circle in the high to intermediate frequency ranges and a straight line inclined at an angle to the real axis in the lower frequency range. The data has been plotted with the real axis at the same scale as the imaginary axis, so that the shape of the curve is not distorted. This shape is important in determining the presence of an ideal capacitor or a constant phase element (CPE).

The Nyquist plot itself is not tremendously meaningful, however, when modelled according to an equivalent circuit, greater physical meaning can be derived from it and sources of polarisation can be quantified. While the graph looks very simple, it is the result of a very complex response from the electrochemical system. It is best to use the simplest model possible to represent the physical electrochemical cell. In this case, a simple equivalent circuit called Randel's circuit (Figure 5.3) has been used as a theoretical model of the electrochemical interface to represent the physical components or experimental data of the electrochemical cells being tested.

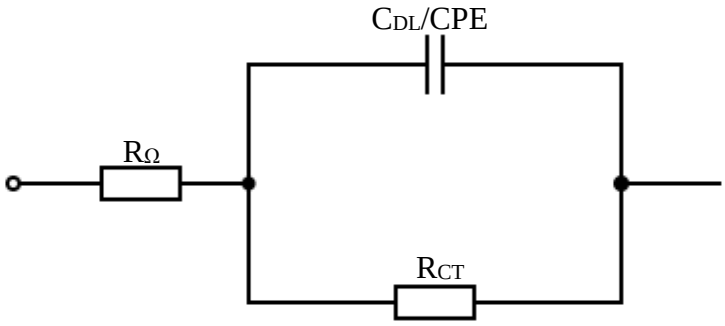

Figure 5.3: Randles circuit. Adapted from ref. [2].

The Randel's circuit is one of the simplest and most common cell models. It includes an ohmic resistance (R_Ω), a double layer capacitor (C_{DL}) or constant phase element (CPE) and a polarisation resistance (R_{CT}). Sometimes a Warburg element can also be added to this circuit to account for the diffusion of ions seen at lower frequencies. This circuit often the starting point for more complex models. The Warburg contributions can be seen in Figure 5.2 at lower frequencies. Z-fit in ECLab® software was used to determine if this equivalent circuit model fit to the experimental impedance profile. In all the cases, the Randel's circuit provided a good fit. After this, numerical values including the ohmic resistance (R_Ω), charge-transfer resistance (R_{CT}) and the constant-phase element (CPE) could be determined. The Warburg element was excluded and only the semi-circle in the high to mid frequency range was modelled. The EIS data can be explained by examining both the Nyquist plots and the modelling data presented in the tables below.

Table 5.1: Ohmic resistances (R_Ω) during charge/discharge at 40°C for samples prepared at 400, 500, 600 and 700°C.

Voltage (V)	R_Ω (Ω) during charging at 40°C				Voltage (V)	R_Ω (Ω) during discharging at 40°C			
	700°C	600°C	500°C	400°C		700°C	600°C	500°C	400°C
3.60	20.3	4.5	21.1	35.8	**4.70**	3.9	4.6	15.4	9.7
3.75	9.4	4.5	21.0	37.0	**4.55**	3.8	4.8	15.8	9.5
3.90	4.7	4.7	23.8	40.1	**4.40**	3.7	5.2	15.0	9.5
4.00	5.9	4.9	21.3	40.1	**4.30**	3.7	5.4	14.8	9.4
4.15	5.6	4.6	20.9	39.2	**4.15**	3.7	5.3	14.2	9.5
4.30	6.3	4.6	22.7	36.6	**4.00**	3.8	5.4	14.5	9.5
4.40	5.3	4.4	19.7	36.6	**3.90**	3.8	5.5	14.9	9.5
4.55	5.2	4.4	19.4	37.4	**3.75**	3.8	5.5	15.0	9.6
4.70	5.8	4.7	14.2	38.2	**3.60**	3.8	5.4	15.4	9.6

The ohmic resistance, R_Ω, is generally consistent at difference voltages (Figure 5.2 and Table 5.1). This is expected since R_Ω is independent of the frequency. As mentioned, this resistance originates from the electrolyte and various cell components.

Table 5.2: Charge-transfer resistances (R_{CT}) during charge/discharge at 40°C for samples prepared at 400, 500, 600 and 700°C.

Voltage (V)	R_{ct} (Ω) during charging at 40°C				Voltage (V)	R_{ct} (Ω) during discharging at 40°C			
	700°C	600°C	500°C	400°C		700°C	600°C	500°C	400°C
3.60	37.1	32.4	33.9	52.4	**4.70**	40.7	33.5	36.7	26.3
3.75	44.8	36.1	33.7	55.7	**4.55**	39.8	39.1	51.7	28.8
3.90	46.7	37.0	34.1	57.6	**4.40**	41.6	41.8	59.2	31.1
4.00	48.2	37.1	34.0	58.3	**4.30**	43.4	43.1	64.8	33.2
4.15	47.5	35.7	33.2	57.7	**4.15**	44.9	44.5	71.2	34.4
4.30	50.2	34.8	31.6	52.1	**4.00**	46.4	45.6	74.6	35.8
4.40	49.5	34.9	30.1	43.8	**3.90**	48.3	46.8	77.8	36.9
4.55	38.6	30.8	27.5	29.2	**3.75**	50.6	48.2	80.0	37.9
4.70	25.9	24.8	22.2	18.8	**3.60**	52.3	49.8	81.7	38.7

Table 5.3: Constant phase element (CPE) during charge/discharge at 40°C for samples prepared at 400, 500, 600 and 700°C.

Voltage (V)	CPE_{dl} ($F.sa^{-1}$) during charging at 40°C				Voltage (V)	CPE_{dl} ($F.sa^{-1}$) during discharging at 40°C			
	700°C	600°C	500°C	400°C		700°C	600°C	500°C	400°C
3.60	3.4E-05	1.0E-04	5.3E-05	2.4E-05	**4.70**	1.8E-05	7.0E-05	6.6E-05	2.7E-05
3.75	2.8E-05	8.5E-05	5.4E-05	2.2E-05	**4.55**	1.8E-05	6.4E-05	6.7E-05	2.9E-05
3.90	2.2E-05	7.9E-05	5.6E-05	2.1E-05	**4.40**	1.8E-05	5.8E-05	6.0E-05	2.9E-05
4.00	2.1E-05	7.9E-05	5.7E-05	2.2E-05	**4.30**	1.8E-05	5.4E-05	5.7E-05	3.1E-05
4.15	2.1E-05	8.3E-05	5.8E-05	2.4E-05	**4.15**	1.8E-05	5.1E-05	6.0E-05	2.9E-05
4.30	2.0E-05	8.9E-05	6.5E-05	2.8E-05	**4.00**	1.8E-05	4.9E-05	5.8E-05	2.8E-05
4.40	1.9E-05	8.8E-05	6.8E-05	3.4E-05	**3.90**	1.8E-05	4.7E-05	5.8E-05	2.8E-05
4.55	1.9E-05	8.4E-05	7.0E-05	4.0E-05	**3.75**	1.8E-05	4.6E-05	5.7E-05	2.8E-05
4.70	1.8E-05	7.9E-05	7.0E-05	4.6E-05	**3.60**	1.9E-05	4.7E-05	5.5E-05	2.8E-05

Table 5.4: Semi-circle depression, a, during charge/discharge at 40°C for samples prepared at 400, 500, 600 and 700°C.

semi-circle depression, a, during charging at 40°C					semi-circle depression, a, during discharging at 40°C				
Voltage (V)	700°C	600°C	500°C	400°C	Voltage (V)	700°C	600°C	500°C	400°C
3.60	0.709	0.690	0.762	0.762	**4.70**	0.782	0.696	0.715	0.773
3.75	0.726	0.702	0.761	0.773	**4.55**	0.779	0.696	0.696	0.766
3.90	0.747	0.708	0.758	0.779	**4.40**	0.778	0.702	0.701	0.764
4.00	0.748	0.707	0.758	0.775	**4.30**	0.778	0.705	0.701	0.757
4.15	0.749	0.703	0.758	0.767	**4.15**	0.778	0.709	0.692	0.762
4.30	0.756	0.700	0.749	0.753	**4.00**	0.777	0.711	0.694	0.763
4.40	0.762	0.701	0.751	0.736	**3.90**	0.776	0.713	0.692	0.763
4.55	0.774	0.704	0.749	0.732	**3.75**	0.775	0.714	0.691	0.764
4.70	0.789	0.705	0.740	0.732	**3.60**	0.773	0.711	0.693	0.764

All the spectra shown are dependent on the potential. The radius of the semicircle decreases when the voltage increases from 3.6 V to 4.7 V on the charging cycle, revealing the lowering of the charge-transfer resistance (R_{CT}). In other words, during Li-ion extraction, the charge transfer or Li-ion migration across the cathode/electrolyte interface improves since the corresponding resistance, R_{CT}, is reduced. One reason applied to explain the phenomena is that the ionic conductivity of the cathode materials increases with the state of charge (SOC). Also, on the discharge cycle, the opposite trend is observed where the radius of the semi-circle increases going from 4.7 V to 3.6 V. Therefore, the charge-transfer resistance increases as the cell is discharged or as Li-ions are inserted back into the cathode. Thus, there is greater resistance during discharge. This is consistent with the charge/discharge cycling capacity in Chapter 4 (Section 4.3.2.2) which showed that discharge capacities were lower than charge capacities. Also, the R_{CT} during charge from samples 400 to 700°C follows a general trend. Generally, the R_{CT} is higher at 400°C than at 700°C. This is consistent with the CV and charge/discharge behaviour showing poor electrochemical properties for the samples at 400°C. However, during discharge, the R_{CT} is somewhat higher at 700°C than at 400°C. This explains the greater loss of capacity at 700°C on discharge than for the sample prepared at 400°C. For instance, at 700°C measured at 40°C, the charge and discharge capacity was 139.6 mA.h g^{-1} and 44.0 mA.h g^{-1} respectively. This is a capacity loss of ~ 52%. For the corresponding sample at 400°C, the charge and discharge capacity was 50.8 mA.h g^{-1} and 26.8 mA.h g^{-1} respectively, a loss of ~ 31%.

All the semi-circles in the Nyquist plot were in a depressed shape. This indicated a deviation from the ideal capacitive behaviour. In this case, to obtain a good fit between the experimental data and the equivalent circuit model, a constant phase element (CPE) was used instead of the capacitor. The impedance from CPE can be described as:

$$Z_{CPE} = \frac{1}{Qa\ (i\omega)} \qquad \text{Equation 5.3}$$

where ω is the frequency, *a* defines the degree of deviation from the ideal capacitive behaviour and Q ($F.s^{a-1}\,cm^{-2}$) is the CPE parameter [8]. The value of the coefficient *a* does not change significantly as the cell is charged or discharged and across the different samples from 400 to 700°C. The CPE, on the other hand, decreases slightly as the samples are charged and varies little on the discharge. Overall, there are no significant variations to *a* and CPE as the potential is changed. This contrasts with the charge-transfer resistance (R_{CT}) which shows an evident trend.

5.3.1.2. Bode plots

The last section in the Nyquist plots is in the low frequency region which is represents the movement of Li-ions into the active material. Under semi-finite diffusion conditions, this region has equal contribution from Z_{real} and Z_{imag} [8]. Consequently, the phase angle is -45º which is called the Warburg impedance. However, the Nyquist plot shows that the 'linear' portion of the spectra deviates from this ideal -45º position. These differences are easier to visualise on a Bode plot (Figure 5.4). In bode plots, the phase changes can be seen. Here, the absolute value of the impedance (*Z*) and phase shifts are plotted as a function of frequency. The plots showed here are only to represent the phase shifts as a function of frequency and *Z* is excluded (Figure 5.4). Because the frequency spans orders of magnitude, they are plotted on a logarithmic scale. Looking at the lower frequency section, it can be clearly seen the significant variation of the phase angles at different voltages. This indicates different diffusion mechanisms throughout the material. This correlates to the sloping charge/discharge profile of the material seen in Chapter 4 (Section 4.3.2.2.)

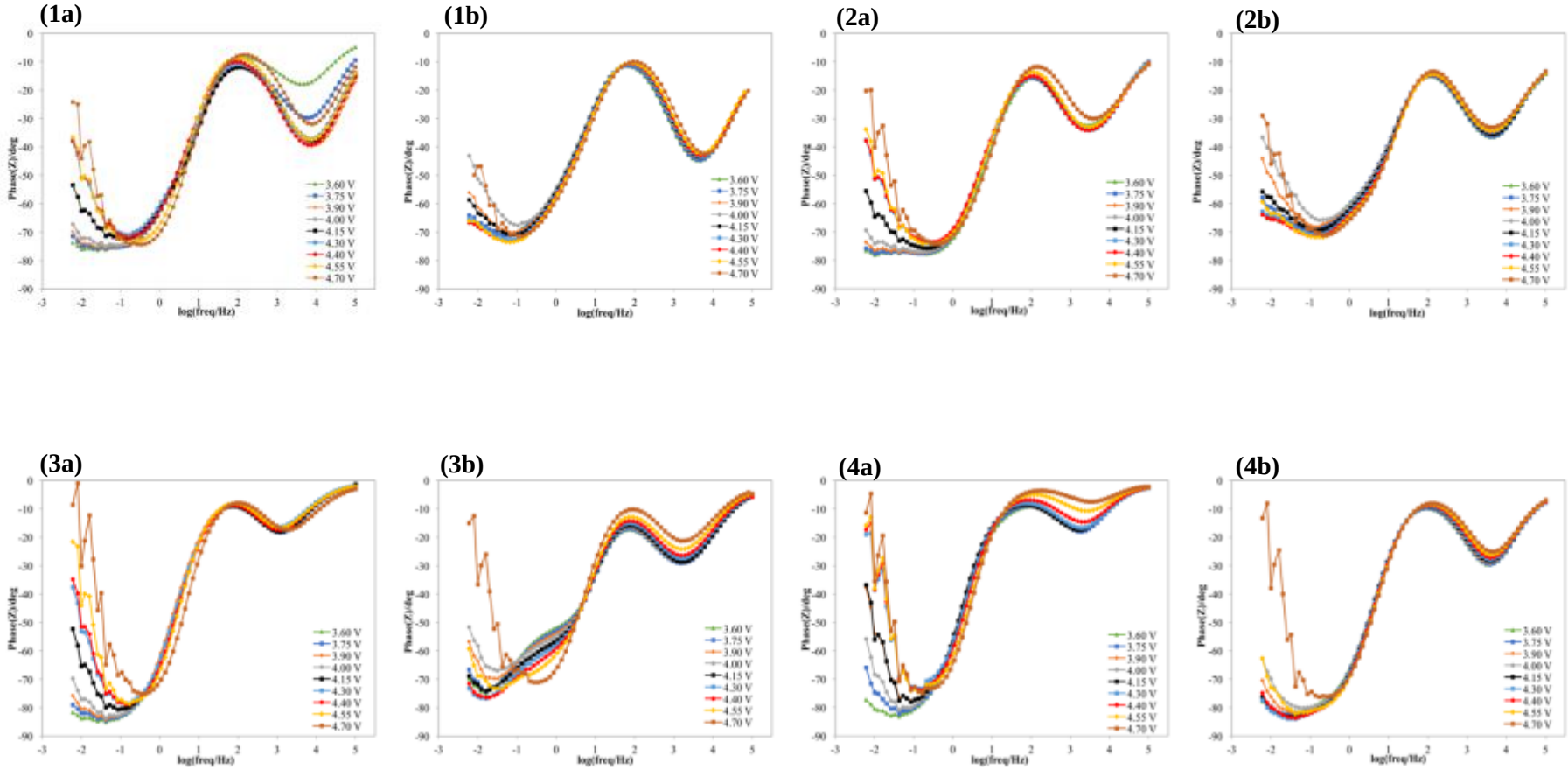

Figure 5.4: Bode plots of S3 samples at 40°C. 1: (a) 700°C charge, (b) 700°C discharge; 2: (a) 600°C charge, (b) 600°C discharge; 3: (a) 500°C charge, (b) 500°C discharge; 4: (a) 400°C charge; (b) 400°C discharge. Impedance are obtained at nine potentials ranging from 3.60 to 4.7 V.

The surface areas of the material were determined in Chapter 4 Section 4.3.1.6. The total surface area is a combination from the phosphate phase and the carbon phase. Due to the difficulty in determining the relative contribution of each of these phases to the total surface area, it is not suitable to use EIS data to calculate the Li-ion diffusion coefficient of the materials [8].

5.3.2. EIS of $LiMnPO_4$ prepared measured at 0, 20 and 40°C.

This section looks at the EIS measurements of samples prepared 700°C (S3) and EIS spectra collected at 0, 20 and 40°C.

5.3.2.1. Nyquist plots

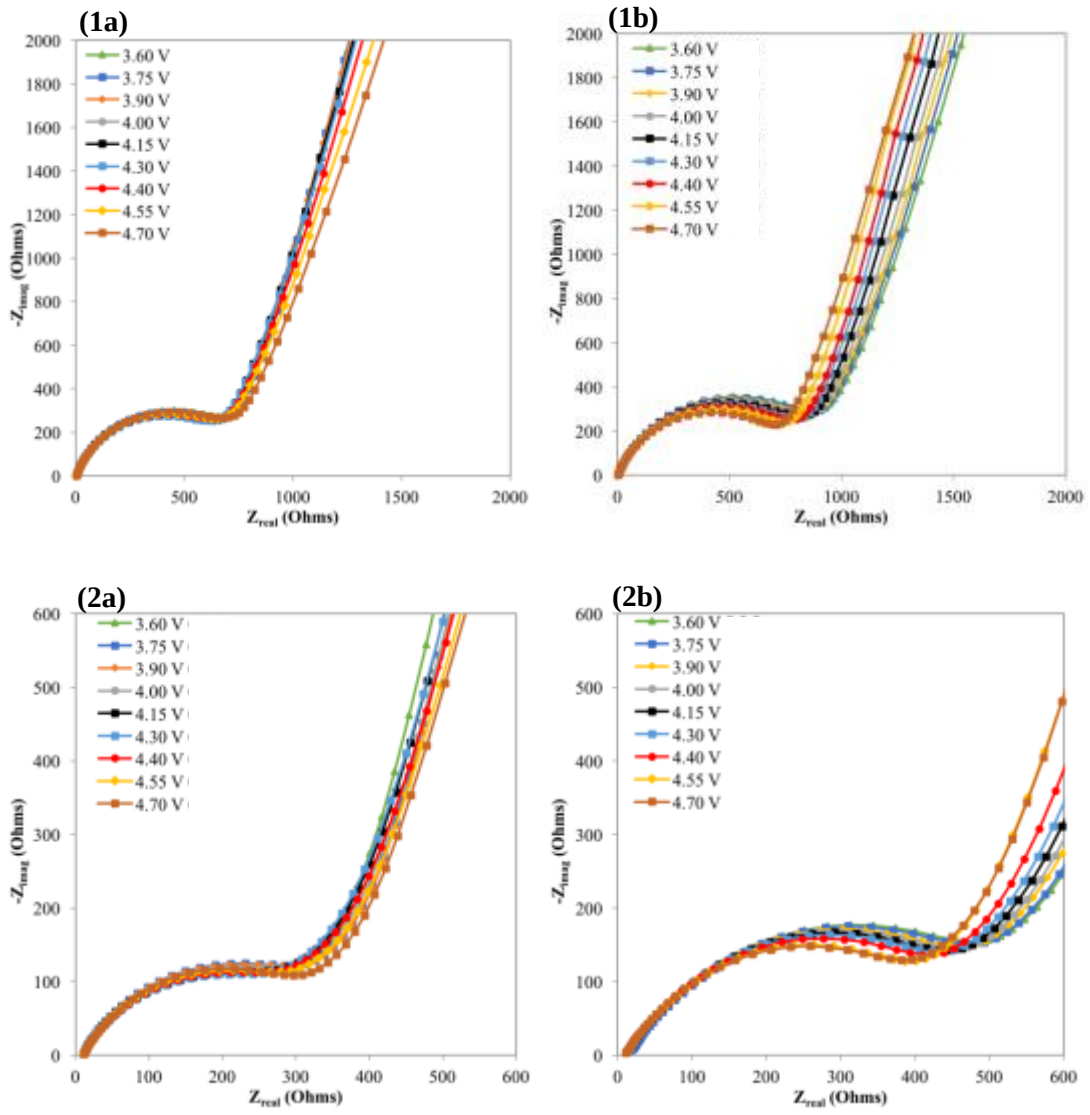

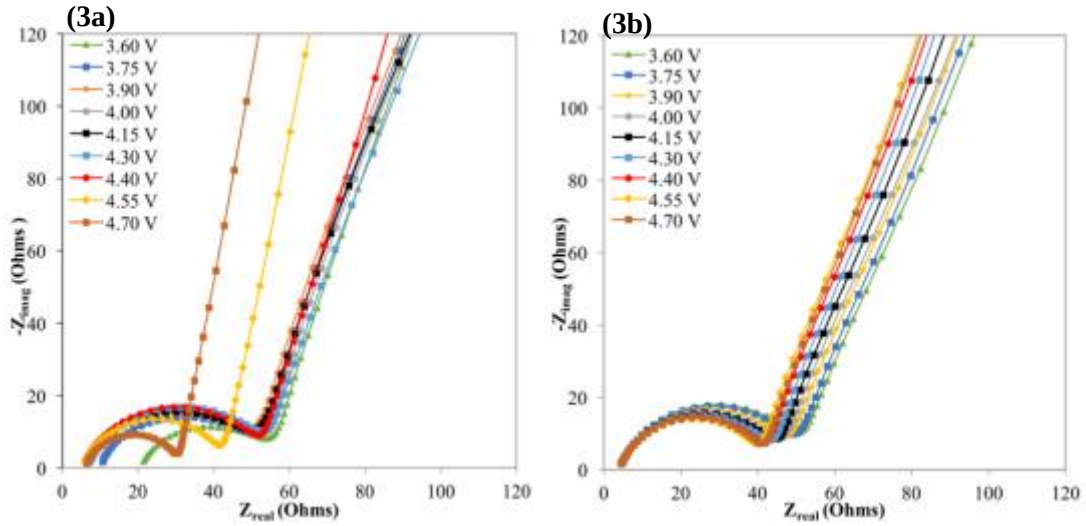

Figure 5.5: Nyquist plots of S3 samples at 0, 20 and 40ºC. 1: (a) 0ºC charge, (b) 0ºC discharge; 2: (a) 20ºC charge, (b) 20ºC discharge; 3: (a) 40ºC charge, (b) 40ºC discharge. Impedance are obtained at nine potentials ranging from 3.60 to 4.7 V. The left side is towards higher frequency and right towards lower frequency.

As in the previous section, Z-fit in ECLab® software was used to determine the equivalent circuit model fit to the experimental impedance profile. The simple Randel's circuit fit well to the experimental data. The modelling data are presented in the tables below and will be used to extract information from the EIS data.

Table 5.5: Ohmic resistances (R_Ω) during charge/discharge at 0, 20 and 40°C for samples set 3 (700°C).

Voltage (V)	R_Ω (Ω) during charging		
	40°C	20°C	0°C
3.60	20.28	10.13	3.84
3.75	9.42	9.81	3.84
3.90	4.74	9.81	3.83
4.00	5.94	9.64	3.83
4.15	5.59	9.53	3.82
4.30	6.31	9.42	3.81
4.40	5.30	9.47	3.83
4.55	5.24	9.59	3.79
4.70	5.84	10.24	3.80

Voltage (V)	R_Ω (Ω) during discharging		
	40°C	20°C	0°C
4.70	3.87	9.71	3.20
4.55	3.75	10.16	3.21
4.40	3.66	10.74	3.22
4.30	3.71	10.62	3.21
4.15	3.72	11.52	3.22
4.00	3.76	11.91	3.22
3.90	3.77	13.26	3.23
3.75	3.77	15.64	3.22
3.60	3.76	15.55	3.23

As in the previous section, the ohmic resistance, R_Ω, contributed from the electrolyte and cell components is generally consistent at difference voltages (Figure 5.5 and Table 5.5).

Table 5.6: Charge-transfer resistances (R_{CT}) during charge/discharge at 0, 20 and 40°C for samples set 3 (700°C).

Voltage (V)	R_{ct} (Ω) during charging			Voltage (V)	R_{ct} (Ω) during discharging		
	40°C	20°C	0°C		40°C	20°C	0°C
3.60	37	352	809	**4.70**	41	520	784
3.75	45	390	792	**4.55**	40	532	820
3.90	47	359	783	**4.40**	42	551	853
4.00	48	356	773	**4.30**	43	571	862
4.15	48	346	760	**4.15**	45	577	884
4.30	50	340	744	**4.00**	46	593	906
4.40	49	352	752	**3.90**	48	603	920
4.55	39	369	767	**3.75**	51	625	934
4.70	26	390	784	**3.60**	52	630	948

Table 5.7: Constant phase element (CPE) during charge/discharge at 0, 20 and 40°C for samples set 3 (700°C).

Voltage (V)	CPE_{dl} ($F.s^{a-1}$) during charging			Voltage (V)	CPE_{dl} ($F.s^{a-1}$) during discharging		
	40°C	20°C	0°C		40°C	20°C	0°C
3.60	3.4E-05	3.3E-05	1.3E-05	**4.70**	1.8E-05	5.0E-05	1.5E-05
3.75	2.8E-05	3.6E-05	1.3E-05	**4.55**	1.8E-05	5.0E-05	1.5E-05
3.90	2.2E-05	3.2E-05	1.3E-05	**4.40**	1.8E-05	4.5E-05	1.5E-05
4.00	2.1E-05	3.6E-05	1.3E-05	**4.30**	1.8E-05	4.5E-05	1.5E-05
4.15	2.1E-05	3.9E-05	1.4E-05	**4.15**	1.8E-05	4.3E-05	1.5E-05
4.30	2.0E-05	4.1E-05	1.4E-05	**4.00**	1.8E-05	4.3E-05	1.5E-05
4.40	1.9E-05	4.2E-05	1.4E-05	**3.90**	1.8E-05	4.3E-05	1.5E-05
4.55	1.9E-05	4.4E-05	1.5E-05	**3.75**	1.8E-05	4.4E-05	1.5E-05
4.70	1.8E-05	4.8E-05	1.4E-05	**3.60**	1.9E-05	4.4E-05	1.5E-05

Table 5.8: Semi-circle depression, a, during charge/discharge at 0, 20 and 40°C for samples set 3 (700°C).

Voltage (V)	semi-circle depression, a, during charging			Voltage (V)	semi-circle depression, a, during discharging		
	40°C	20°C	0°C		40°C	20°C	0°C
3.60	0.709	0.721	0.804	**4.70**	0.782	0.661	0.792
3.75	0.726	0.710	0.804	**4.55**	0.779	0.657	0.793
3.90	0.747	0.720	0.803	**4.40**	0.778	0.663	0.793
4.00	0.748	0.711	0.802	**4.30**	0.778	0.659	0.794
4.15	0.749	0.703	0.801	**4.15**	0.778	0.662	0.795
4.30	0.756	0.699	0.800	**4.00**	0.777	0.659	0.795
4.40	0.762	0.696	0.800	**3.90**	0.776	0.657	0.795
4.55	0.774	0.692	0.796	**3.75**	0.775	0.650	0.795
4.70	0.789	0.685	0.796	**3.60**	0.773	0.650	0.795

Since the trends at increasing and decreasing voltages during charge and discharge respectively have been discussed in the previous section, the focus here will be on the operating temperature of the electrochemical cells. The charge-transfer resistance (R_{CT}) increases significantly at 0 and 20ºC as opposed to the R_{CT} at 40ºC. In fact, going from 40ºC to 20ºC, R_{CT} has increased by as much as 10 times. From 20ºC to 0ºC, the RCT has more than doubled. This is consistent with the CV and charge/discharge cycling which indicated that the samples run at 0ºC exhibited the poorest electrochemical properties while at 20ºC the performance was slightly better. The significant decrease in the R_{CT} at 20ºC to 40ºC correlates with the electrochemical data in Chapter 4 which showed a significant leap in the electrochemical performance of the cells. Higher temperatures are expected to improve the performance of the cells; however, they can also deteriorate at higher temperatures. The temperature tolerance of cells is important especially in countries where temperatures can go from extreme cold to hot weather. Lithium metal phosphates in general are well-known to be tolerant to high temperatures.

Again, the sloping shape of the semi-circle indicated deviation from an ideal capacitor. The value of the coefficient *a* does not change significantly as the cell is operated under different temperature conditions from 0 to 40ºC. The CPE also shows very little variation across the different operating temperatures.

5.3.2.2. Bode plots

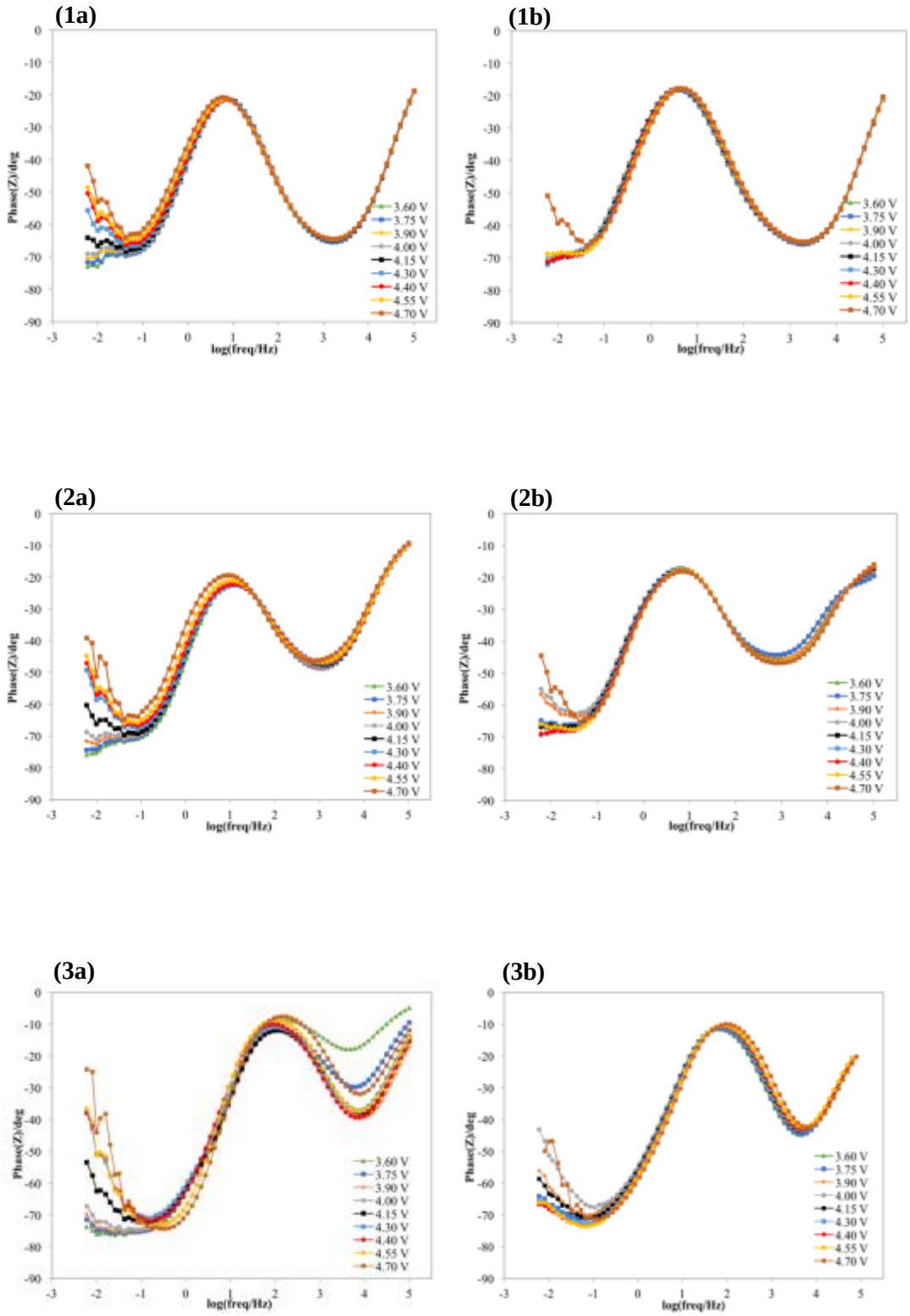

Figure 5.6: Bode plots of S3 samples at 0, 20 and 40°C. 1: (a) 0°C charge, (b) 0°C discharge; 2: (a) 20°C charge, (b) 20°C discharge; 3: (a) 40°C charge, (b) 40°C discharge. Impedance are obtained at nine potentials ranging from 3.60 to 4.7 V.

The bode plots of the samples at 0, 20 and 40°C show an interesting trend. During charging, the range of the phase angle increases from 0ºC to 40°C. However, during discharging, there is not much difference between the phase angle at 0, 20 and 40°C. However, the phase angles are still spread out indicating different diffusion mechanisms.

5.4. Summary

EIS spectra have been used to evaluate the origin of impedance in the electrochemical cells. It is clear that at for samples prepared at different temperatures (400, 500, 600 and 700ºC) and at different operating temperatures (0, 20 and 40ºC), the charge-transfer resistance (R_{CT}) is the major contributor to the overall impedance of the cell. This would mean that the limiting factor to the cells produced here and hence the $LiMnPO_4$ cathode material is the charge-transfer at the electrode/electrolyte interface. Here it is also seen that this resistance can be reduced significantly by increasing the temperature the cell is run at or by improving the quality of carbon. This explains why the samples prepared at 600 and 700ºC performed better than samples prepared at 400 and 500ºC. The electrochemical activity is then significantly improved by running the cells in a 40ºC temperature oven.

5.5. References

1. Meaden G. Electrical resistance of metals: Springer; 2013.

2. Orazem M, Tribollet B. Electrochemical impedance spectroscopy. John Wiley & Sons; 2011.

3. Chang B, Park S. Electrochemical impedance spectroscopy. Annual Review of Analytical Chemistry. 2010;19(3):207-29.

4. Retter, U, Lohse, H. Electrochemical impedance spectroscopy. In *Electroanalytical Methods*. Springer Berlin Heidelberg; 2005.

5. Randviir E, Banks C. Electrochemical impedance spectroscopy: an overview of bioanalytical applications. Analytical Methods. 2013;5(5):1098-115.

6. Olivier M, Poelman M. Use of electrochemical impedance spectroscopy (EIS) for the evaluation of electrocoatings performances: INTECH Open Access Publisher; 2012.

7. Macdonald, D. Reflections on the history of electrochemical impedance spectroscopy. Electrochimica Acta. 2006;51(8-9):1376-88.

8. Milev A, George L, Khan S, Parasuraman S, Kannangara G. Li-ion kinetics in $LiFePO_4$ nanocomposite prepared by a two-step process: the role of phase composition. Electrochimica Acta. 2016;209:565-73.

CHAPTER 6

Conclusions and future work

This dissertation investigated a novel sol-gel method to synthesis $LiMnPO_4$ which incorporated metal acetate precursors, acetic acid and ethylene glycol and diethyl hydrogen phosphonate as a new phosphate source. For the first time, a stable intermediate phosphonate species was used to prepare a precursor $LiMnPO_4$ material. Chapter 3 investigated how the purity of $LiMnPO_4$ can be modulated by including and varying an intermediate heating step. Here, it was reported that the optimisation of the synthesis led to the reduction of the required synthetic temperature by 500°C; from 900ºC to 400ºC. Highly crystalline and phase-pure $LiMnPO_4$ was produced at 400ºC. This is much lower than temperatures required by conventional solid-state routes and is comparable to the synthesis temperatures used by the hydrothermal method where the pressure is also a variable. So far, no study has shown the ability to produce the combination of high crystallinity and phase purity of $LiMnPO_4$ at a low temperature of 400ºC using solid and solution state methods where pressure is constant.

Chapter 4 investigated the physical characteristics of the prepared samples and subsequent electrochemical performance. Interestingly, the crystallinity and structure of the electroactive material was consistent from 400 to 700°C. Although the physical characteristics were similar, their electrochemical properties were different. The electrochemical performance was therefore attributed to the different levels of graphite-like sp^2 bonded carbon as shown by Raman spectroscopy, specifically the increase in delocalised π electrons caused by the transformation of alkenic C=C chains to aromatic hexagonal rings. This, although phase-pure and crystalline material was prepared at temperatures as low as 400ºC, the final electrochemical performance was based on the quality of carbon coating rather than the physical characteristics of the electroactive material. An ideal scenario would be the ability to coat a low temperature synthesised material with conductive coating or particles. However, currently, the carbon coating method is only effective when treated to higher temperatures.

Chapter 5 examined electrochemical impedance spectroscopic (EIS) data to evaluate the origin of resistances in the electrochemical cells. The major source of resistances was kinetically controlled specifically the charge-transfer resistance at the cathode/electrolyte interface. As expected, the kinetics of charge transfer improved dramatically at higher temperatures. The better quality of carbon coating on samples produced at higher temperatures also helped improve charge-transfer kinetics, however, the increase was not as dramatic as running cells at higher temperatures.

This study encompassed the synthesis, physical characterisation and electrochemical characterisation of $LiMnPO_4$, where areas of further study was determined to further contribute to this field. Future work emanating from this study includes:

1. To determine the activation energy of conductivity required to overcome the charge-transfer resistances. This can be obtained from EIS data collected over a larger range of temperatures than has been reported here.
2. The use of Potentiostatic Intermittent Titration Technique (PITT) will be used to measure the chemical diffusion coefficient of Li-ions.
3. To determine the kinetics of the formation of phase pure LiMnPO4 and how the temperature and atmosphere modulate the purity and mechanism using thermogravimetric analysis and transmission electron microscopy (TEM).

4. To investigate further the relationship between nanocrystalline graphite and the electrochemical performance of the electrode material. Specifically, to look at how the different changes occurring to graphite-like carbon as the temperature is increased (> 700°C).
5. To determine and monitor the temperature range when the material is at a stage of pyrolysis and the onset and range at which graphitisation begins and increases respectively. The effect on electrochemical performance within these two regimes will be explored.

Appendix A

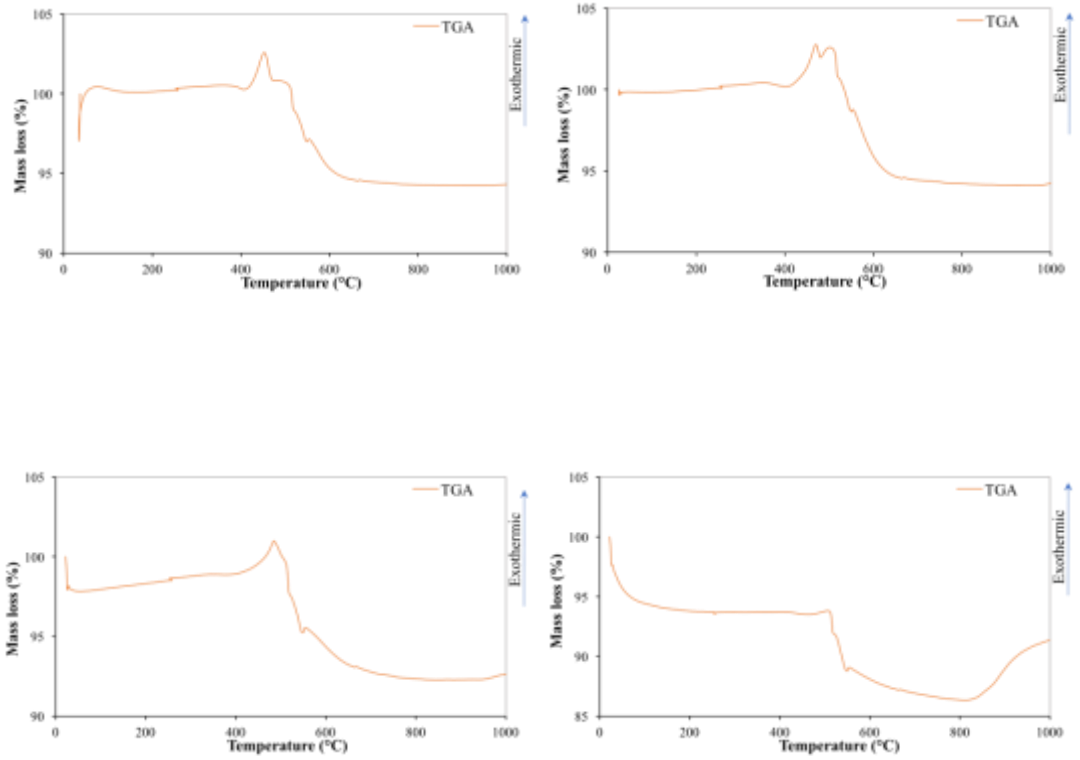

Figure A1: Thermogravimetric curves for the determination of carbon content of S1 samples; a) 400°C, b) 500°C, c) 600°C and d) 700°C.

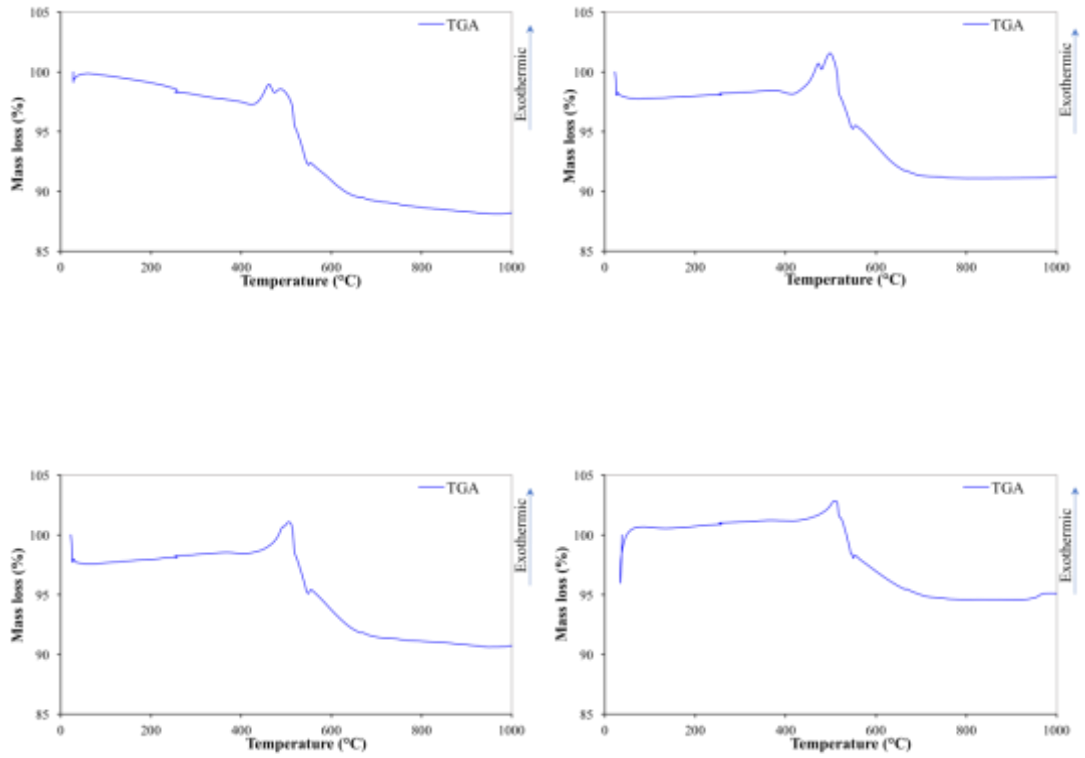

Figure A2: Thermogravimetric curves for the determination of carbon content of S2 samples; a) 400°C, b) 500°C, c) 600°C and d) 700°C.

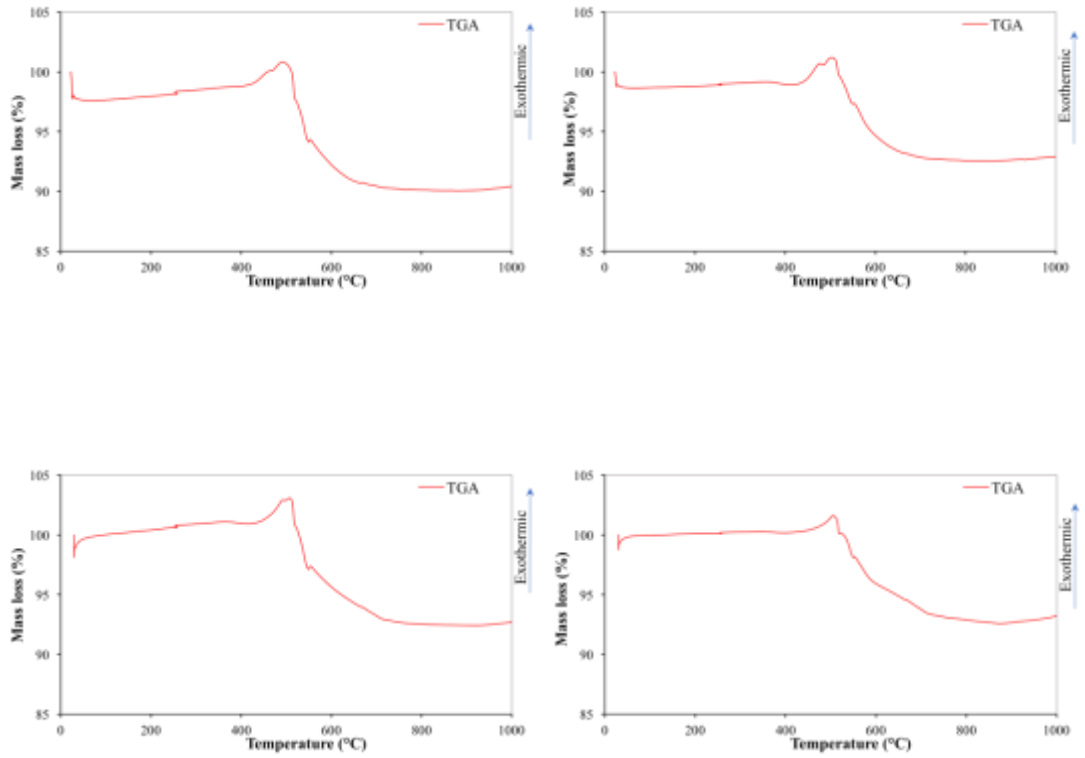

Figure A3: Thermogravimetric curves for the determination of carbon content of S3 samples; a) 400°C, b) 500°C, c) 600°C and d) 700°C.

Appendix B

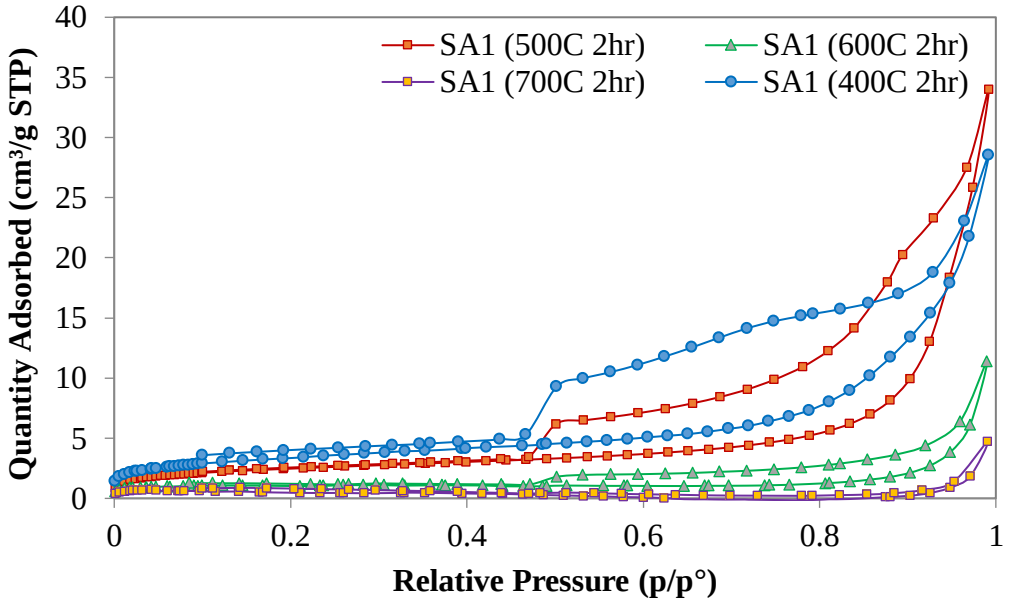

Figure B1: Adsorption curves of un-milled S1 samples

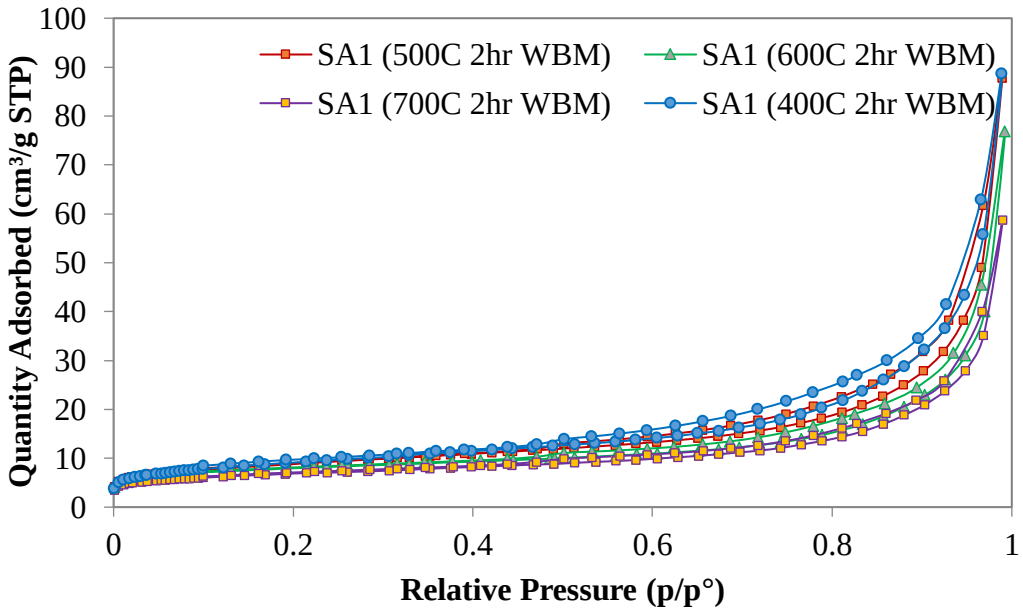

Figure B2: Adsorption curves of wet ball-milled S1 samples

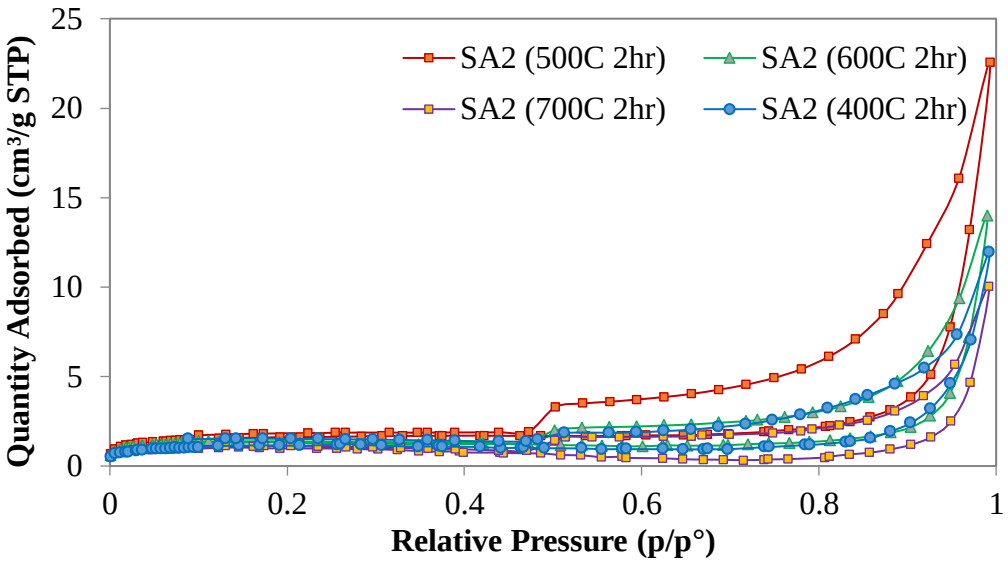

Figure B3: Adsorption curves of un-milled S2 samples

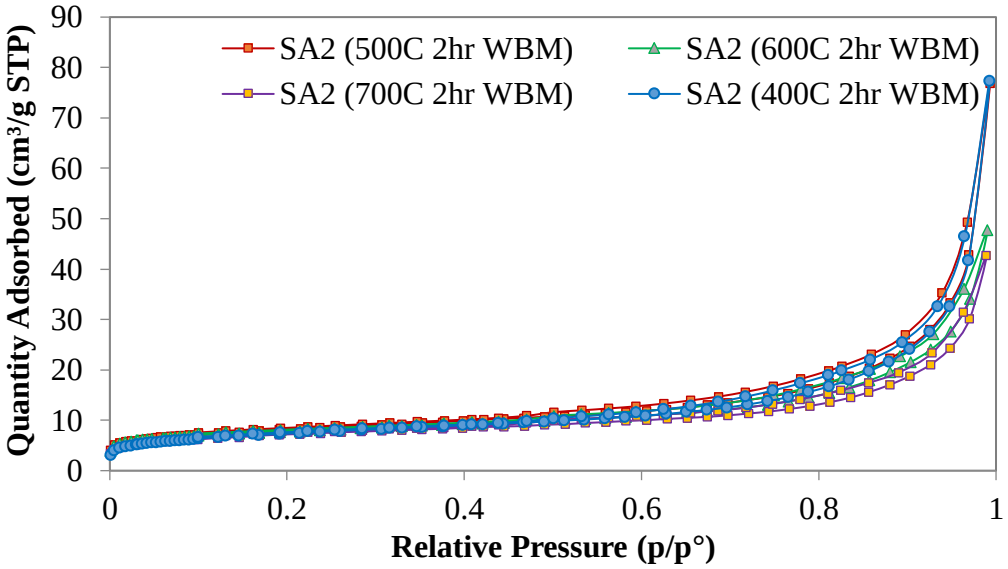

Figure B4: Adsorption curves of wet ball-milled S2 samples

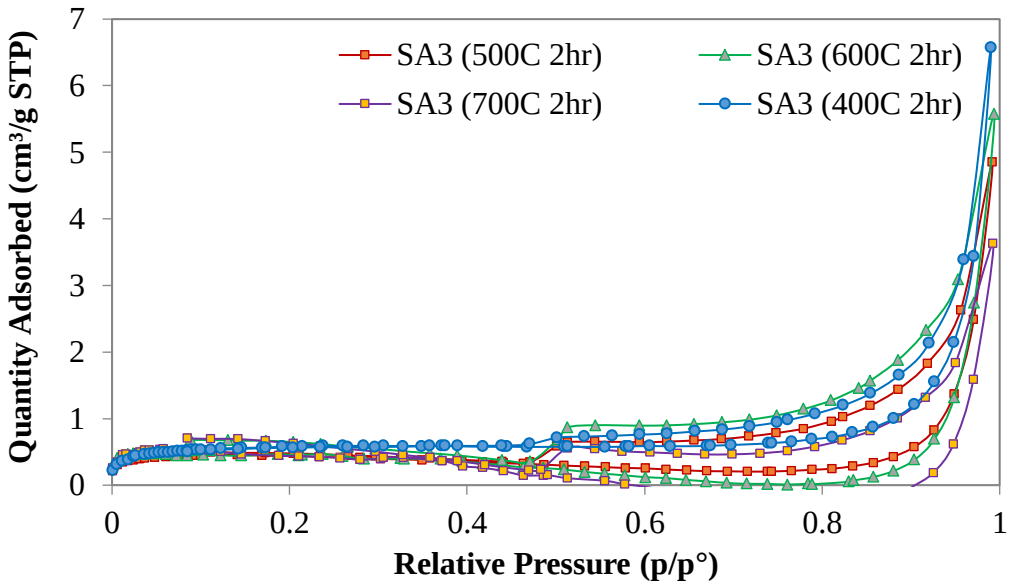

Figure B5: Adsorption curves of un-milled S3 samples

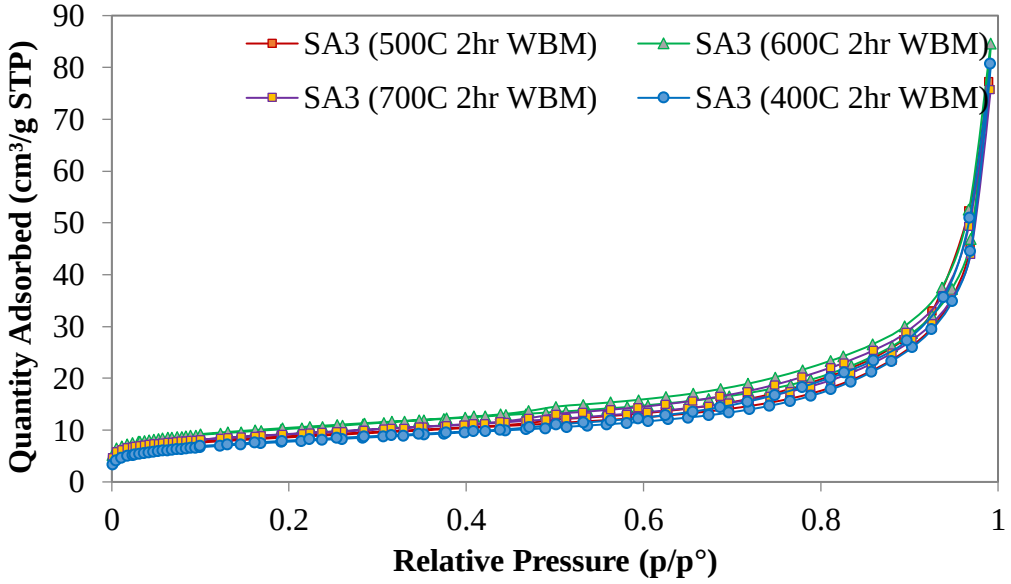

Figure B6: Adsorption curves of wet ball-milled S3 samples